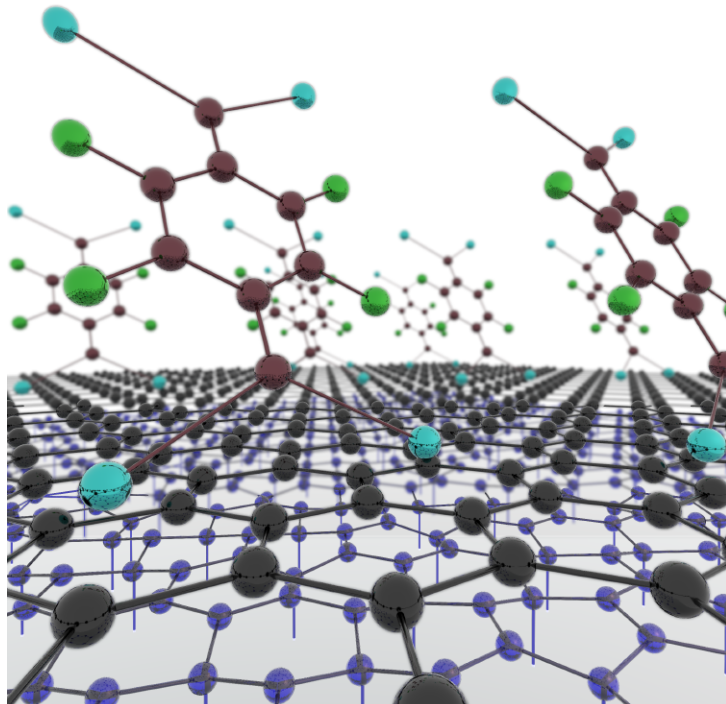




CHALMERS



Molecular Doping of Epitaxial Graphene For Device Applications

HANS HE

THESIS FOR THE DEGREE OF DOCTOR OF PHILOSOPHY

Molecular Doping of Epitaxial Graphene

For Device Applications

HANS HE

Department of Microtechnology and Nanoscience (MC2)
Quantum Device Physics Laboratory
CHALMERS UNIVERSITY OF TECHNOLOGY

Göteborg, Sweden 2020

Molecular Doping of Epitaxial Graphene
For Device Applications
HANS HE
ISBN 978-91-7905-309-3

© HANS HE, 2020

Doktorsavhandlingar vid Chalmers tekniska högskola
Ny serie nr. 4776
ISSN 0346-718X
Department of Microtechnology and Nanoscience (MC2)
Quantum Device Physics Laboratory
Chalmers University of Technology
SE-412 96 Göteborg
Sweden
Telephone: +46 (0)31-772 1000

Cover:
Artistic rendering of acceptor molecules F4TCNQ aggregated on the surface of epigraphene (black). The buffer layer can be seen below (purple).

Chalmers Reproservice
Göteborg, Sweden 2020

Molecular Doping of Epitaxial Graphene

For Device Applications

Thesis for the degree of Doctor of Philosophy

HANS HE

Department of Microtechnology and Nanoscience (MC2)

Quantum Device Physics Laboratory

Chalmers University of Technology

ABSTRACT

Epitaxial graphene grown on silicon carbide, or epigraphene, offers in principle a suitable platform for electronic applications of graphene which require scalable, reproducible, and high-quality material. However, one of the main drawbacks of epigraphene lies in the difficulty in tuning its carrier density due to strong interactions with the substrate.

This thesis introduces a novel molecular doping method which is especially suitable for 2D materials. This technique utilizes acceptor molecules mixed with a polymer, which results in a dopant blend that can be applied using simple spin-coating. It provides potent and homogeneous doping over wafer-scale, leading to doped epigraphene samples with exceptionally low charge disorder, comparable to state-of-the-art encapsulated or suspended graphene, in addition to record high carrier mobilities for epigraphene ($80\,000\,\text{cm}^2/\text{Vs}$ at 2 K). Molecular doping allows for controllable tuning of the carrier density of epigraphene, which opens up many different avenues for potential applications.

The doping method was successfully used to create practical graphene quantum resistance standards based on the quantum Hall effect. Doped epigraphene devices were compared to conventional GaAs devices by two independent metrology institutes, and it was confirmed that epigraphene meets the stringent criteria for use in precision quantum resistance metrology. Furthermore, the samples could consistently operate at relaxed measurement conditions with stable doping levels, which extend the device lifetimes to over three years and counting.

Doped epigraphene was also used to develop magnetic field sensors capable of operating from room temperature up to $T = 150\,\text{°C}$. With the doping level tuned close to neutrality, epigraphene Hall sensors were shown to rival, and even surpass, the best graphene-based Hall sensors reported in literature thus far, including having record-low magnetic field detection limits at room temperature. The Hall sensors also demonstrated promising performance at high temperatures, with the potential to one day outmatch industrial sensors in the automotive and military temperature ranges.

Lastly, doped epigraphene was used to create a proof-of-concept terahertz detector. Near charge neutrality, epigraphene develops a logarithmic temperature dependence of resistance which enables its use as a bolometric mixer. The device demonstrated highly sensitive and wide-band coherent detection of terahertz signals, with record-low power consumption requirements. It was found that initial device performance was limited by the measurement setup, and an optimized device could potentially allow for the creation of detector arrays which provide quantum limited detection across the entire terahertz range, which would revolutionize sensors used in next-generation space telescopes.

Keywords: Epitaxial Graphene, Molecular Doping, Metrology, Hall Effect, THz

Dedicated to my beloved wife

ACKNOWLEDGEMENTS

I would like to thank my supervisor Samuel Lara for supporting me throughout this whole journey. Thank you for dedicating much of your time and energy to coach me in the ways of experimental physics. I am grateful for your patience and lending me your expertise, and I appreciate that you always took the time to answer any and all questions. Secondly, I would like to thank my co-supervisor at RISE, Tobias Bergsten, for opening my eyes to the wonderful world of metrology, full uncertainties and error. I have learned much about the intricacies of precision measurements. I would also like to thank my co-supervisor and examiner Sergey Kubatkin, the leader of our research group. You gave me this invaluable opportunity to develop myself as a physicist and researcher, and I truly hope that my contributions prove useful to the group in the future. Through your leadership, wisdom, and experience, you have always steered me towards the right path. Furthermore, I would like to thank the rest of our group members whom I have worked with: Naveen Shetty, Kyung Ho Kim, Andrey Danilov, Sumedh Mahashabde, Ernst Otto, Domenico Montemurro, Tom Yager, Astghik Adamyan, and Arseniy Lartsev. Thanks for all the help you have graciously given me. Extra thanks to our previous master's students Maria Karani, Mohab O. Hassan, and David Barker for their contributions to this work. Special thanks to Gunnar Eklund and Karin Cedergren for your assistance in the labs at RISE, and help with metrology in general.

The majority of experiments in this work were performed inside the clean room and laboratories at Chalmers, and I want to give a shout-out to all the dedicated staff who work to ensure the smooth operation of the tools and machinery. Special thanks to Niclas Lindvall, Alexei Kalaboukhov, Bengt Nilsson, Mats Hagberg, Henrik Fredriksen, Johan Andersson, and Ulf Södervall, with whom I have interacted with extensively. Special thanks to Lars Jönsson for always keeping his workshop door open and accepting our requests, even trivial ones. Many thanks to Grigory Skoblin and August Yurgens for assisting in the hBN encapsulation of epigraphene.

Obviously, I would like to thank all of the wonderful co-workers and friends here at MC2 who make working here a treat. I have spent more than a decade at Chalmers now, and I do not regret it one bit because of all the people I have had the pleasure to meet. There are too many to name, but you know who you are.

Finally, I would like to extend my sincerest thanks to my family for their endless patience, loving care, and support. This would not have been possible without you by my side. Special thanks and love to my mother and brother.

ABBREVIATIONS

2D	Two-dimensional
2DEG	Two-dimensional electron gas
III-V	Compounds consisting of group III and V elements
AFM	Atomic force microscopy
C-face	Carbon face of silicon carbide
CCC	Cryogenic current comparator
CVD	Chemical vapor deposition
DOS	Density of states
EBL	Electron beam lithography
F4TCNQ	2,3,5,6-Tetrafluoro-tetracyanoquinodimethane
GaAs	Gallium arsenide
GIWAXs	Grazing-incidence wide-angle x-ray scattering
HEB	Hot electron bolometer
hBN	Hexagonal boron nitride
IPA	Isopropanol
LL	Landau level
NMI	National metrology institute
PMMA	Poly(methyl-methacrylate)
QHE	Quantum Hall effect
QHR	Quantum Hall resistance
SEM	Scanning electron microscopy
SiC	Silicon carbide
Si-face	Silicon face of silicon carbide
SIMS	Secondary-ion mass spectroscopy
TLM	Transfer length method
UHV	Ultra-high vacuum
vdP	Van der Pauw
vdW	Van der Waals

SYMBOLS

α	Fine structure constant
k_B	Boltzmann constant
h	Planck constant
e	Elementary charge
c	Speed of light in vacuum
τ	Scattering time
ℓ	Mean free path
m^*	Effective mass
E_F	Fermi energy
v_F	Fermi velocity
W	Sample width
L	Sample length
n	Charge carrier density
n_e	Electron charge carrier density
n_h	Hole charge carrier density
μ	Charge carrier mobility
l_B	Magnetic length
R_H	Hall coefficient
ν	Filling factor
ρ	Sheet resistance
R_{XX}	Longitudinal resistance
R_{XY}	Transverse resistance
λ	Wavelength
f	Frequunecy
ω	Angular frequency
ω_c	Cyclotron frequency
t	Time
B	Magnetic field
T	Temperature
P	Power
I	Current
V	Voltage
V_G	Gate voltage

THESIS

This thesis consists of an extended summary and the following appended papers:

- Paper A** T. J. B. M. Janssen, S. Rozhko, I. Antonov, A. Tzalenchuk, J. M. Williams, Z. Melhem, **H. He**, S. Lara-Avila, S. Kubatkin, and R. Yakimova. Operation of graphene quantum Hall resistance standard in a cryogen-free table-top system. *2D Materials* **2** (2015)
- Paper B** **H. He**, T. J. N. M. Janssen, S. Rozhko, A. Tzalenchuk, S. Lara-Avila, R. Yakimova, and S. Kubatkin. Fabrication of graphene quantum hall resistance standard in a cryogen-free table-top system. *Conference of Precision Electromagnetic Measurements (CPMEM)* (2016)
- Paper C** **H. He**, K. H. Kim, A. Danilov, D. Montemurro, L. Yu, Y. W. Park, F. Lombardi, T. Bauch, K. Moth-Poulsen, T. Iakimov, R. Yakimova, P. Malmberg, C. Müller, S. Kubatkin, and S. Lara-Avila. Uniform doping of graphene close to the Dirac point by polymer-assisted assembly of molecular dopants. *Nature Communications* **9** (2018)
- Paper D** **H. He**, S. Lara-Avila, K. H. Kim, N. Fletcher, S. Rozhko, T. Bergsten, G. Eklund, K. Cedergren, R. Yakimova, Y. W. Park, A. Tzalenchuk, and S. Kubatkin. Polymer-encapsulated molecular doped epigraphene for quantum resistance metrology. *Metrologia* **56** (2019)
- Paper E** **H. He**, N. Shetty, T. Bauch, T. Kaufmann, M. Cornills, R. Yakimova, and S. Lara-Avila. The performance limits of Epigraphene Hall sensors doped across the Dirac point. *Accepted by Applied Physics Letters* (2020)
- Paper F** S. Lara-Avila, A. Danilov, D. Golubev, **H. He**, K. H. Kim, R. Yakimova, F. Lombardi, T. Bauch, S. Cherednichenko, and S. Kubatkin. Towards quantum-limited coherent detection of terahertz waves in charge-neutral graphene. *Nature Astronomy* **3** (2019)

Other publications related to this thesis:

- Patent I** **H. He**, S. Lara-Avila, and S. Kubatkin. *Electrical contacts for low-dimensional materials* SE541523
- Patent II** **H. He**, S. Lara-Avila, and S. Kubatkin. *Assembling of molecules on a 2D material and an electronic device* SE541515

Publications not included in this thesis:

- Paper I** K. H. Kim, S. Lara-Avila, H. Kang, **H. He**, J. Eklof, S. J. Hong, M. Park, K. Moth-Poulsen, S. Matsushita, K. Akagi, S. Kubatkin, and Y. W. Park. Apparent Power Law Scaling of Variable Range Hopping Conduction in Carbonized Polymer Nanofibres. *Scientific Reports* **6** (2016)

- Paper II** K. H. Kim, S. Lara-Avila, **H. He**, H. Kang, Y. W. Park, R. Yakimova, and S. Kubatkin. Thermal stability of epitaxial graphene electrodes for conductive polymer nanofiber devices. *Crystals* **7** (2017)
- Paper III** K. H. Kim, S. Lara-Avila, **H. He**, H. Kang, S. J. Hong, M. Park, J. Eklof, K. Moth-Poulsen, S. Matsushita, K. Akagi, S. Kubatkin, and Y. W. Park. Probing variable range hopping lengths by magneto conductance in carbonized polymer nanofibers. *Scientific Reports* **8** (2018)
- Paper IV** K. H. Kim, **H. He**, M. Rodner, R. Yakimova, K. Larsson, M. Piantek, D. Serrate, A. Zakharov, S. Kubatkin, J. Eriksson, and S. Lara-Avila. Chemical Sensing with Atomically Thin Platinum Tempered by a 2D insulator. *Advanced Materials Interfaces* <https://doi.org/10.1002/admi.201902104> (2020)

CONTENTS

1	Introduction	1
1.1	What is Graphene?	1
1.2	Epitaxial Graphene	2
1.3	Initial Motivation	3
1.4	Research Scope	4
1.5	Thesis Outline	7
2	Theory & Concepts	9
2.1	Electrical Properties of Graphene	9
2.2	Epitaxial Graphene	12
2.3	Magnetotransport	16
3	Experimental Methods	29
3.1	Graphene Growth	29
3.2	Electron Beam Lithography	35
3.3	Molecular Doping Method	38
3.4	Electrical Characterization	40
4	Molecular Doping	47
4.1	Towards Charge Neutrality	48
4.2	Molecular Doping Schemes	49
4.3	Spontaneous Assembly	51
4.4	Tuning Carrier Density via Annealing	55
4.5	Macroscopic Homogeneity	58
4.6	Microscopic Homogeneity	60
4.7	Grazing-incidence Wide-angle X-ray Scattering	64
4.8	Redistribution of Dopants	66
4.9	Conclusions	69
5	Quantum Resistance Standard	71
5.1	Sample Preparation	72
5.2	Initial Characterization	73
5.3	Measurements at National Physical Laboratory	75
5.4	Measurements at Research Institutes of Sweden	77
5.5	Long-term Stability	79
5.6	Conclusions	80
6	Epigraphene Hall Sensors	81
6.1	Sample Preparation	82
6.2	Carrier Density Tuning	82
6.3	Device Linearity	83
6.4	Device Offset	85

6.5	Noise Characterization	86
6.6	Figures of Merit	87
6.7	Thermal Stability	89
6.8	Conclusions	92
7	Coherent THz Detection	95
7.1	Heterodyne Detection	96
7.2	DC Characterization of Epigraphene HEB	98
7.3	Diffusion Cooling	101
7.4	THz Mixer	104
7.5	Future Prospects	107
7.6	Conclusions	108
8	Summary & Outlook	109
A	Recipes	111
A.1	Growth	111
A.2	RCA cleaning	111
A.3	Electron Beam Lithography	112
A.4	Chemical Doping	114
A.5	Electrostatic Gating	115
B	Derivations	117
B.1	Integer Quantum Hall Effect	117
B.2	Tight-binding Graphene	119
References		121
I	Appended Papers	129
Paper A	129
Paper B	143
Paper C	147
Paper D	156
Paper F	169
Paper E	181

1 Introduction

1.1 What is Graphene?

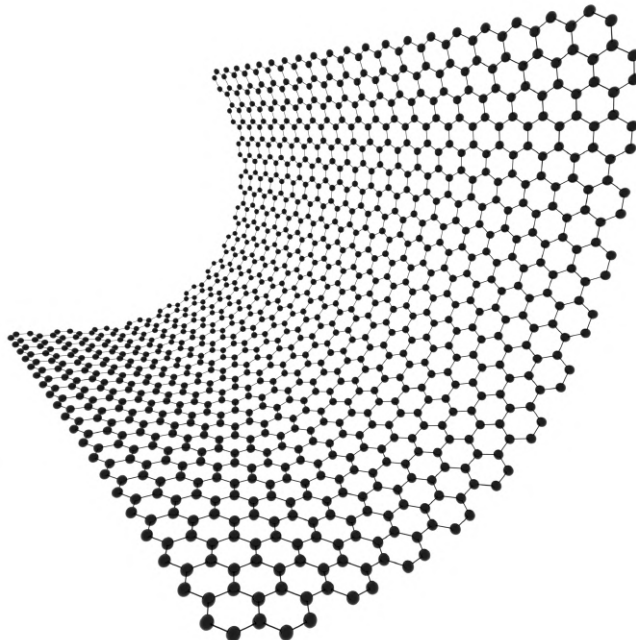


Figure 1.1: *Artistic rendering of a graphene sheet.*

Graphene is a two-dimensional (2D) material , which consists of a single layer of carbon atoms arranged in a hexagonal lattice (Figure 1.1). This crystal structure leads to many interesting properties, which have the potential to exceed the characteristics of more conventional materials. Graphene has no band gap, but since the carrier density can still be tuned like a semiconductor, it is therefore commonly referred to as a semi-metal. The electronic band structure at low Fermi energies has a linear dispersion relation, and is in principle charge neutral at zero Fermi energy (Dirac point). The linear dispersion relation leads to effectively massless charge carriers, which result in exceptionally high carrier mobilities being observed at room temperature [1]. Furthermore, due to the lack of band gap graphene absorbs light in a broad range of frequencies, and the absorption is proportional to the fine structure constant α [2], absorbing around 2.3 % of visible light despite being atomically thin. The thermal conductivity is also high, with reported values up to 3000 W/mK, comparable to even copper [3]. Last but not least, its mechanical properties include being both flexible and strong. Relative to its size, graphene is sometimes hailed as the strongest material in the world [4].

The list of advantages is long, and this intriguing material was theoretically studied

starting from 1947 by Wallace [5]. Interestingly, one of the earliest experimental signs of graphene occurred already in 1975 [6]. In that work, graphene, or monolayer graphite as it was called back then, was actually grown on hexagonal silicon carbide (SiC). This early discovery lay dormant for some time, until around 2004, when Geim and Novoselov exfoliated graphene from graphite using a scotch-tape method, and presented a more complete experimental verification of its exciting electronic properties [7, 8]. This work earned them the 2010 Nobel Prize in physics, and graphene has enthralled researchers all over the world ever since. This new 2D material has been envisioned to have endless applications within new technological innovations, with lofty goals to surpass current technologies in fields such as bio-medicine, composites, chemical sensors, energy harvesting and storage, just to name a few. However, even after roughly a decade after the start of the graphene revolution, efforts to outperform established technologies have been difficult to realize in practice. While graphene possesses many exceptional properties in theory, their manifestation in practice is often contingent on excellent material quality. This highlights the importance of the production of high-quality monolayer graphene on a large scale, which remains an active field of study to this day.

1.2 Epitaxial Graphene

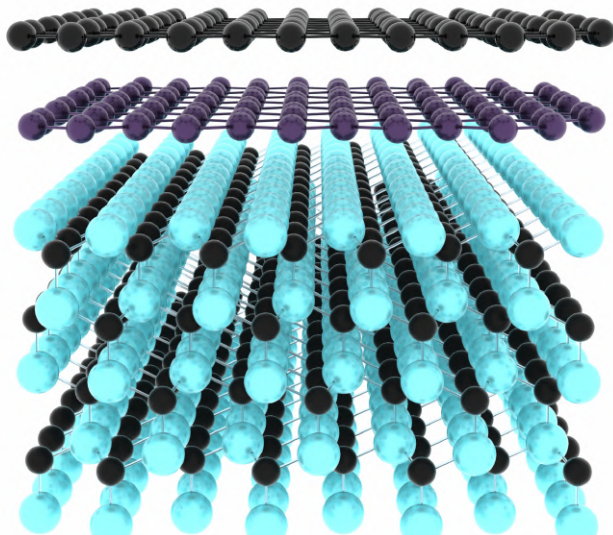


Figure 1.2: *Artistic rendering of epitaxial graphene (black), including the buffer layer (purple) and SiC substrate (Blue-black). Note that the buffer layer is depicted without covalent bonds to the substrate.*

Harking back to the forgotten roots of graphene, epitaxial graphene grown on silicon carbide (epigraphene) is the graphene of choice for this thesis. Epigraphene is in principle a very attractive choice for electronic applications of graphene which require scalability, reproducibility, and high electronic quality. This is because epigraphene is grown bottom-up, epitaxially on a silicon carbide crystal (SiC), which results in a high-quality monocrystalline graphene film across the entire substrate [9, 10]. Moreover, epigraphene can in principle be grown on a wafer-scale [11, 12], which is a prerequisite for real-world applications, where scalable production is paramount. Another benefit is that the insulating nature of the SiC substrate enables direct fabrication of electrical devices after epigraphene growth. This forgoes the need for further material transfer processes which are necessary for methods such as chemical vapor deposition (CVD) and mechanical exfoliation. The reduced complexity of fabrication ensures that the quality of epigraphene is preserved [13]. Finally, the unique combination of epigraphene with SiC results in a material that can withstand high operating temperatures, which is attractive for industrial applications such as magnetic sensing in automobiles.

In terms of real applications, epigraphene has already shown great promise in the field of quantum resistance metrology [14]. To date, this is perhaps the only electronic application which truly utilizes the unique electrical properties of graphene, and specifically epigraphene, to surpass conventional materials.

One of the main drawbacks which hinders widespread use of epigraphene, is the difficulty in tuning the charge carrier density n . Control over the carrier density is crucial not only because it gives epigraphene greater flexibility in potential applications, but also because it is the key which grants access to interesting physics phenomena near the charge neutrality point (Dirac point). Due to the nature of the growth process, there exists an interface layer of carbon known as the buffer layer (see Figure 1.2), which in conjunction with the SiC substrate influence the electronic properties of epigraphene. One consequence is high intrinsic n-doping ($n \approx 10^{13} \text{ cm}^{-2}$), and the other is Fermi energy pinning which effectively reduces the efficiency of gating [15]. These two problems work in tandem to provide a challenge to those who wish to tune the carrier density of epigraphene, especially across the Dirac point, and it is one of the core problems addressed in this thesis.

1.3 Initial Motivation

The starting point of the research presented in this thesis was to improve the application of epigraphene in quantum resistance metrology, where it fulfills a useful niche. Quantum resistance metrology deals with the definition and precise measurement of the unit of resistance Ohm (Ω), down to part-per-billion accuracy. Historically, it has relied on the quantum Hall effect (QHE) [16] in two-dimensional electron gases (2DEG) commonly based on gallium arsenide (GaAs). At sufficiently strong magnetic fields ($> 10 \text{ T}$) and low temperatures ($< 2 \text{ K}$), the measured transverse resistance (R_{XY}) takes on quantized values defined only by fundamental constants Planck's constant h and elementary charge e . The resistance is proportional to the aptly named von Klitzing constant $R_K = h/e^2$, the namesake of the discoverer of the QHE. Because the resistance is precisely defined solely by fundamental constants, it provides an excellent universal reference point for resistance

measurements. This universality ensures that in principle any graphene sample, regardless of device geometry, can be made into a primary resistance standard, eliminating the need for artifact standards which all have their own idiosyncrasies [17]. Due to the unique properties of epigraphene specifically, the QHE can be observed at lower magnetic fields, higher temperatures, and at higher bias currents than for conventional 2DEGs [14, 18, 19]. Additionally, the quantum Hall plateau corresponding to filling factor $\nu = 2$ is very robust in epigraphene, extending up to 50 T [20]. Owing to more relaxed measurement conditions, a graphene based quantum Hall resistance (QHR) standard would require neither high-end machinery, nor state-of-the-art laboratories to function. Work on developing a portable table-top cryogen-free version of a graphene QHR standard has already started in earnest [19]. QHR standards based on epigraphene are therefore not only the superior realization, but it also facilitates the dissemination of a primary standard closer to the end-user, thereby decreasing calibration uncertainty. In the beginning of this thesis, there existed unresolved issues regarding the fabrication process of epigraphene QHR standards which limited their performance and reliability. One of the main culprits was, as mentioned, charge carrier density control in epigraphene.

There are myriad reasons why charge carrier density control is important, and not only just for QHR applications, but for electronic devices in general. Carrier density control via gating or doping is after all the cornerstone of the modern digital society, which is entirely dependent on transistor logic. Regarding quantum resistance metrology, a high charge carrier density increases the minimum required magnetic field in order to reach quantizing conditions. A low carrier density is important in order to achieve relaxed operating conditions for an epigraphene QHR device. One also has to take into account allowed bias currents, which should be maximized in order to improve signal-to-noise-ratio and reduce the measurement uncertainty. For a specific combination of magnetic field and temperature, there is an optimum charge carrier density that maximizes critical current [19] and some fine-tuning of the carrier density is needed to find the sweet spot. Furthermore, the accuracy and robustness of resistance quantization can be sensitive to charge disorder [21, 22], which demands the use of high-quality epigraphene with spatially homogeneous doping. Finally, for real-world applications the method used to control the carrier density should ideally possess long-term stability, as this will extend the lifetime of epigraphene QHR standards.

1.4 Research Scope

This thesis summarizes and elaborates upon the works presented in **Paper A** through **Paper F**.

Paper A and **Paper B** deal with previous work related to the creation of a practical table-top epigraphene QHR system that needs to reliably operate at relaxed conditions of <5 T and 4.2 K. In order to achieve this feat, control over the carrier density of epigraphene is crucial. This conundrum provided one of the main motivating factors behind the pursuit of the development of a molecular dopant blend. The contributions from this thesis to these initial metrology projects are mainly sample fabrication and initial characterization.

The main result of this thesis is presented in **Paper C**. It pertains to the development of a novel molecular doping method, which utilizes an acceptor molecule¹ combined with a polymer² to form a dopant blend. This dopant blend can be applied onto epigraphene using simple spin-coating in ambient conditions, and the final doping level can be tuned using thermal annealing. Measurements demonstrated that it provides potent and homogeneous doping on a millimeter scale, with the ability to bring epigraphene very close to charge neutrality while maintaining high carrier mobilities. Chemical analysis of the deposited dopant blend revealed that the F4TCNQ molecules diffuse through the PMMA matrix and spontaneously assemble near the epigraphene surface, forming charge-transfer complexes between epigraphene and F4TCNQ molecules which results in a p-doping effect. Additionally, doped epigraphene showed exceptionally low charge disorder, comparable to state-of-the-art exfoliated graphene flakes encapsulated by hexagonal boron nitride (hBN) [23] or suspended graphene [24]. This work demonstrates that a F4TCNQ-based polymer dopant blend provides stable, potent, and tunable doping of epigraphene.

Armed with this effective molecular doping technique, the aforementioned problem of carrier density control in the realm of epigraphene quantum resistance metrology was tackled. **Paper D** marks the culmination of these efforts, wherein doped epigraphene QHR standards were compared to well-established conventional GaAs-based QHR standards. The tests were performed independently at two different national metrology institutes (NMI), and both verified that molecular doped epigraphene passes all the precision requirements for use in quantum resistance metrology. In addition, the samples showed a slow linear drift over the course of three years, with extrapolated device lifetimes potentially exceeding decades. This work reveals that molecular doping of epigraphene can be a solution for the real-world implementation of practical epigraphene-based QHR standards.

A natural extension to quantum Hall effect devices is to look at sensors based on the classical Hall effect. Instead of measuring the Hall voltage in the presence of an external magnetic field, epigraphene can perform the role of a magnetometer which measures the external field by detecting induced Hall voltage. In **Paper E**, doped epigraphene devices were leveraged as sensitive Hall elements. The parameter space and performance limits of devices under ambient conditions were studied using the molecular doping technique to tune the carrier density across the Dirac point. In the end, optimal points of operation for magnetic field sensing were identified, and it was shown that epigraphene doped close to neutrality can rival, and even surpass, the best graphene-based Hall sensors reported in literature thus far. Lastly, the doped Hall sensors showed respectable high temperature performance up to 150 °C, which is potentially very attractive for industrial applications such as in the automotive field. This work shows that epigraphene doped close to neutrality can be utilized as high-performance Hall sensors.

For the third tested application of doped epigraphene, the focus shifts from magneto-transport phenomena to light sensing. **Paper F** demonstrates that epigraphene, uniformly doped to charge neutrality, can work as a fast and sensitive bolometric mixer for radiation in the terahertz frequency (THz) range. In the regime of charge neutrality, electrical transport in epigraphene is dominated by quantum interference effects, which results in

¹2,3,5,6-Tetrafluoro-tetracyanoquinodimethane or F4TCNQ

²poly(methyl-methacrylate) or PMMA

a logarithmic temperature dependence of resistance. This enables highly sensitive and wide-band coherent detection of signals due to a bolometric response. The measurements demonstrated that epigraphene can perform favorably compared to conventional THz mixers in terms of mixing bandwidth and gain, but with a notable advantage in its record-low power consumption. It was found that the reported proof-of-concept performance was limited by the measurement setup, and under ideal conditions this approach could, for the first time, provide THz detector arrays with quantum limited detection spanning the full THz range. This work indicates that epigraphene doped close to neutrality can be used for state-of-the-art THz detectors. The contributions from this thesis are sample fabrication and DC characterization.

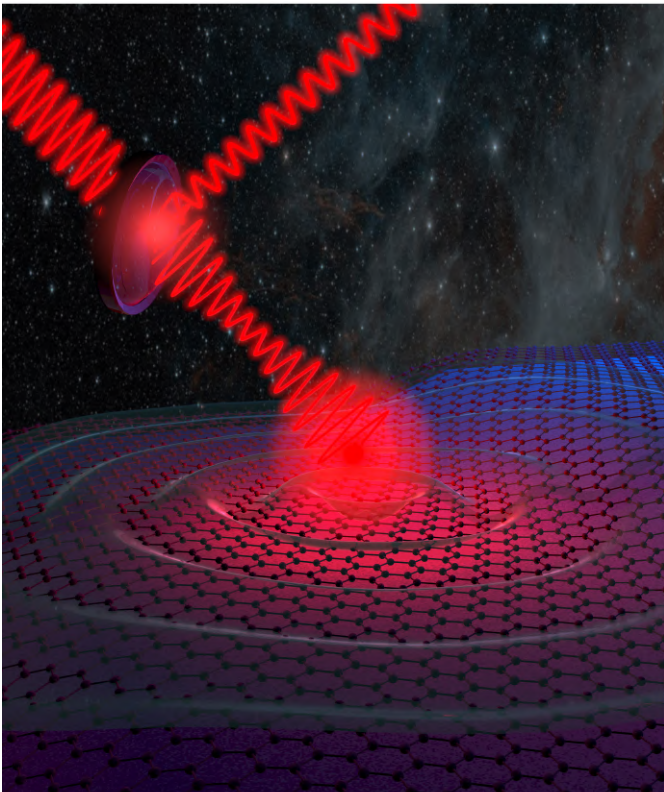


Figure 1.3: *Artistic rendering of an epigraphene THz detector. Incident THz radiation from the cosmos is combined with a reference signal, and directed to epigraphene. The light is absorbed and heats up the electronic system, which can be detected using resistance measurements.*

1.5 Thesis Outline

- Chapter 2 introduces concepts and theory regarding the electrical properties of graphene.
- Chapter 3 contains descriptions of various experimental methods needed to fabricate a working epigraphene device. The minute details of microfabrication recipes have been relegated to Appendix A.
- Chapter 4 begins with a brief introduction to previous work related to a table-top QHR standard (**Paper A**, **Paper B**) which serves as the starting point and driving force behind investigations into carrier density control of epigraphene. The subsequent sections contain the results of paper **Paper C**, and are dedicated to the intricacies of the molecular doping method.
- Chapter 5 presents the experimental results related to **Paper D**. The opening section provides some more insight into previous works (**Paper A**, **Paper B**), and their importance for metrology. The remaining sections deal with the metrological verification of doped epigraphene QHR standards, and how they compare to established conventional GaAs-based resistance standards.
- Chapter 6 presents the experimental results related to **Paper E**. The performance limits of doped epigraphene Hall sensors are explored in a wide parameter space spanning different carrier densities and temperatures.
- Chapter 7 presents the experimental results related to **Paper F**. The chapter starts with a short introductory background to the world of THz astronomy, before moving on the performance of a doped epigraphene THz detector.
- Chapter 8 is the final chapter and it provides a summary of the main results, alongside some concluding remarks, and future outlook.

2 Theory & Concepts

Graphene is an allotrope of carbon, with a crystal structure consisting of carbon atoms arranged in a 2D hexagonal lattice. The simple honeycomb structure results in interesting electrical properties which will be explored below. This chapter serves as a primer for the underlying theory and concepts behind the unique electrical properties of graphene in general, and epigraphene in particular. Graphene is introduced first, followed by the concepts required to grasp the peculiarities of epigraphene, and how they alter its properties. The latter sections start with a broad discussion on the classical Drude model and general magnetotransport phenomena in two dimensions (2D), followed by quantum transport phenomena. For a more in-depth look into general electron transport theory see references [25, 26]. For graphene specific theory see references [27–29].

2.1 Electrical Properties of Graphene

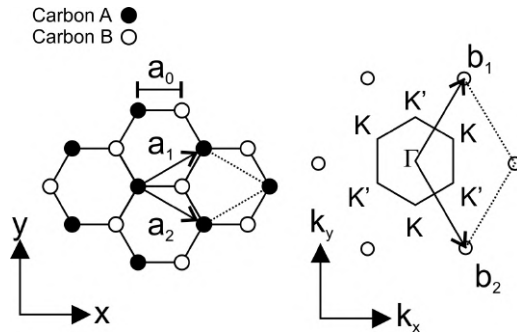


Figure 2.1: **Left:** Real space representation of the graphene crystal lattice. The lattice can be decomposed into two triangular sub-lattices A (Black atoms) and B (white atoms), shifted by the carbon-carbon distance a_0 . The lattice vectors \mathbf{a}_1 and \mathbf{a}_2 span the primitive cell. **Right:** Graphene in reciprocal space with reciprocal lattice vectors \mathbf{b}_1 and \mathbf{b}_2 . The 1st Brillouin zone is hexagonal with six points at its corners, but only two points \mathbf{K} and \mathbf{K}' are unique.

To grasp the origins of the electrical properties of graphene, and indeed any crystal, one must first study the underlying crystal structure. The graphene lattice in real and reciprocal (momentum) space can be seen in Figure 2.1. The real space unit cell can be described by lattice vectors:

$$\begin{aligned}\mathbf{a}_1 &= \frac{3a_0}{2}\hat{\mathbf{x}} + \frac{\sqrt{3}a_0}{2}\hat{\mathbf{y}} \\ \mathbf{a}_2 &= \frac{3a_0}{2}\hat{\mathbf{x}} - \frac{\sqrt{3}a_0}{2}\hat{\mathbf{y}}\end{aligned}\tag{2.1}$$

The distance between adjacent carbon atoms is $a_0 = 1.42 \text{ \AA}$, and the lattice constant $|\mathbf{a}_i| = a = \sqrt{3}a_0 = 2.46 \text{ \AA}$. The hexagonal lattice can be decomposed into a combination of

two identical triangular sub-lattices A and B. Each sub-lattice contributes one carbon atom respectively to the primitive cell. As will become evident later, the symmetry between the two sub-lattices permeates all of the electronic properties of graphene. Graphene owes its 2D planar structure to sp^2 hybridization of orbitals between carbon atoms. Three out of the four valence electrons in the carbon atom are occupied by covalent σ -bonds with adjacent atoms, resulting in strong in-plane stability of the lattice. The last valence electron joins its peers from other carbon atoms, and together they create an aromatic π -bond which spans the entire graphene sheet. This is the delocalized electron cloud which forms the valence and conduction bands in graphene.

The reciprocal lattice vectors \mathbf{b}_1 and \mathbf{b}_2 span the 1st Brillouin zone (BZ). They can be constructed by $\mathbf{b}_i \mathbf{a}_j = 2\pi\delta_{ij}$, where δ_{ij} is the Kronecker delta. In the corner of the hexagonal BZ there exist six points, but only two \mathbf{K} and \mathbf{K}' are nonequivalent points, and they are related to sub-lattices A and B. The four different reciprocal vectors are:

$$\begin{aligned}\mathbf{b}_1 &= \frac{2\pi}{3a_0} \hat{\mathbf{x}} + \frac{2\pi}{\sqrt{3}a_0} \hat{\mathbf{y}} \\ \mathbf{b}_2 &= \frac{2\pi}{3a_0} \hat{\mathbf{x}} - \frac{2\pi}{\sqrt{3}a_0} \hat{\mathbf{y}} \\ \mathbf{K} &= \frac{2\pi}{3a_0} \hat{\mathbf{x}} + \frac{2\pi}{\sqrt{33}a_0} \hat{\mathbf{y}} \\ \mathbf{K}' &= \frac{2\pi}{3a_0} \hat{\mathbf{x}} - \frac{2\pi}{\sqrt{33}a_0} \hat{\mathbf{y}}\end{aligned}\tag{2.2}$$

One simple way to derive the electronic band structure of graphene is to use a tight-binding approach. The idea behind the model is to only take into account interactions between nearest-neighbor carbon atoms. Assuming that the electrons are tightly bound to the nucleus, their wave functions can be expressed as a linear combination of atomic orbital functions. The full tight-binding derivation can be seen in Appendix B.2. The resulting tight-binding band structure is:

$$E_{\mathbf{k}} = \frac{\epsilon_0 \pm \gamma_0 |f(\mathbf{k})|}{1 \pm s_0 |f(\mathbf{k})|}\tag{2.3}$$

$$|f(\mathbf{k})| = \sqrt{3 + 2 \cos(\mathbf{k}\mathbf{a}_1) + 2 \cos(\mathbf{k}\mathbf{a}_2) + 2 \cos(\mathbf{k}\mathbf{a}_1 - \mathbf{k}\mathbf{a}_2)}.\tag{2.4}$$

The band structure equation contains the three tight-binding parameters ϵ_0 , γ_0 and s_0 . They can be determined by experimentally measuring the Fermi velocity or from ab initio calculations. When considering only strictly nearest-neighbor interactions, the self-energy is commonly set to zero $\epsilon_0 = 0$. This results in the valence and conduction bands crossing at the K point. The hopping energy is usually $\gamma_0 \approx -3$ eV based on fits to experimental data and first-principle calculations [30]. The overlap integral s_0 relates to the asymmetry between conduction and valence bands, and can be ignored at lower energies $s_0 = 0$. Finally, the low-energy band structure for graphene, as shown in Figure

2.2, is expressed as:

$$E_{\mathbf{k}} = \pm \gamma_0 |f(\mathbf{k})| = \sqrt{3 + 2 \cos(\mathbf{k}\mathbf{a}_1) + 2 \cos(\mathbf{k}\mathbf{a}_2) + 2 \cos(\mathbf{k}\mathbf{a}_1 - \mathbf{k}\mathbf{a}_2)} = \pm \gamma_0 \sqrt{3 + 2 \cos(\sqrt{3}a_0 k_y) + 4 \cos(\frac{3a_0}{2}k_x) \cos(\frac{\sqrt{3}a_0}{2}k_y)} \quad (2.5)$$

Where k_x and k_y are the $\hat{\mathbf{x}}$ and $\hat{\mathbf{y}}$ components of the wave vector respectively. The energy is zero only at \mathbf{K} or \mathbf{K}' , where the valence and conduction bands meet.

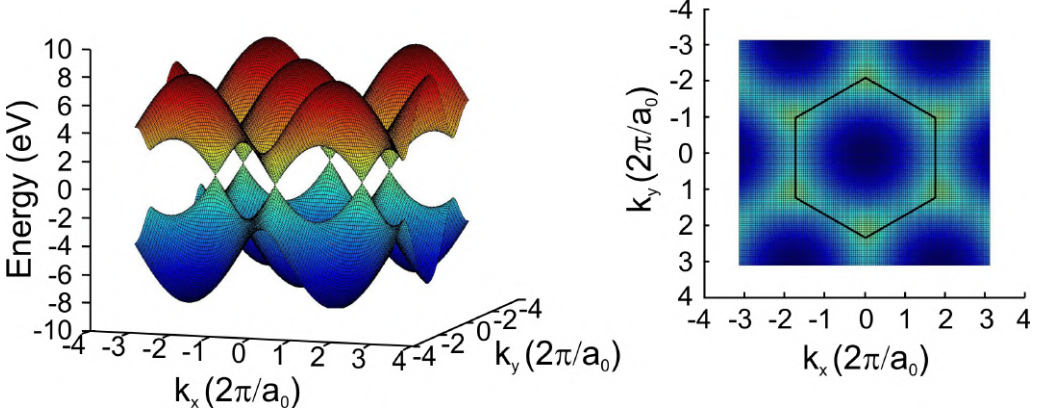


Figure 2.2: **Left:** Band structure of graphene calculated using the nearest-neighbor tight-binding model. Tight-binding parameters are set to $\epsilon_0 = s_0 = 0$ and $\gamma_0 = -3$ eV. The valence and conduction bands meet at six points in the reciprocal space and the dispersion relation is linear in the low energy regime $|E| < 3$ eV. **Right:** Top-down view of the band structure. Six points exist at zero energy (yellow/green color) and mark the corners of the 1st BZ.

To see the characteristic linear dispersion relation of graphene, Equation 2.5 can be transformed using Taylor expansion around the \mathbf{K} points by using $\mathbf{k} = \mathbf{K} + \mathbf{q}$ with $|\mathbf{q}| \ll |\mathbf{K}|$. Ignoring any higher order terms $\mathcal{O} = \mathbf{q}^2/\mathbf{K}^2$ leads to the linear dispersion:

$$E_{\mathbf{k}} = \hbar v_F |\mathbf{q}| \quad (2.6)$$

Here v_F is the Fermi velocity $v_F = \frac{1}{\hbar} \frac{\partial E}{\partial k} = 3\gamma_0 a_0 / 2$, which is approximately $v_f \approx 10^6$ m/s [8]. The resulting linear dispersion relation close to the \mathbf{K} point parallels the behavior of ultra-relativistic particles with zero rest mass, like photons for instance. The energy momentum relation $E^2 = |\mathbf{p}|^2 c^2 + m^2 c^4$ reduces to $E = c |\mathbf{p}| = \hbar c |\mathbf{k}|$ for massless particles, which is identical to that of graphene. For massless particles, the Schrodinger equation reduces to the 2D Dirac equation, which is used when dealing with massless Dirac fermions. This is the reason why the \mathbf{K} points are called Dirac points in graphene.

The linear dispersion forms a conical shape, or a Dirac cone, in the reciprocal space. The density of states (DOS) can be calculated by considering states living on an annulus

on the cone, with radius k and thickness dk . The area of the annulus, divided by the area of one state, is precisely the DOS. The area of the annulus is $2\pi k dk$ and the area of one state in reciprocal space is $(2\pi/L)^2$, where L is some unit length. Including a factor of 2 for spin degeneracy and a factor of 2 for the two Dirac cones for \mathbf{K} and \mathbf{K}' (valley degeneracy), the number of states is $N = 2kdkL^2/\pi$. The linear dispersion of graphene means that $dE/dk = \pm\hbar v_F$, and therefore $kdk = |E|dE(\hbar v_F)^2$. Finally the DOS per unit area L^2 is:

$$DOS(E) = \frac{2|E|}{\pi(\hbar v_F)^2} \quad (2.7)$$

The DOS is linear with energy and is zero at the Dirac point. In theory this means that graphene should have a large resistance at the Dirac point, because there are no available states for charge carriers to occupy. In practice, for real graphene samples there are factors such as spatial charge disorder which complicate this picture. There is always some residual charge carrier density, and experiments at the Dirac point always show finite resistance. The resistance values in literature can vary, and the maximum resistance of graphene at the Dirac point is still somewhat controversial, with different theories predicting different values [31]. Of note is that for epigraphene studied in this thesis the maximum resistivity is on the order of $\sim h/e^2$ at $T = 2$ K.

The relatively low DOS allows for the tuning of the carrier density in graphene, and the absence of a band gap allows for a transition between electron (n-type) and hole (p-type) dominated transport. Close to neutrality and at finite temperatures, both electrons and hole coexist and contribute to the transport (ambipolar transport).

The Fermi energy can be calculated from the expression of the DOS. Summing up all the occupied states, above zero energy, gives the carrier density n (number of carriers per area):

$$n = \int_0^\infty DOS(E)f(E)dE \quad (2.8)$$

For simplicity, the temperature can be assumed to be zero, in which case the Fermi distribution $f(E)$ turns into the Heaviside step function (=1 for energies below E_F , zero otherwise), and the upper energy limit of the integral becomes the Fermi energy E_F . The integration is now trivial and the carrier density is:

$$n = \frac{E_F^2}{\pi(\hbar v_F)^2} \quad (2.9)$$

In other words, the Fermi energy depends on the square root of carrier density:

$$E_F = \hbar v_F \sqrt{\pi n} \quad (2.10)$$

2.2 Epitaxial Graphene

The term epitaxy refers to crystal growth where new crystalline layers are formed in a well-defined manner with respect to the crystalline substrate. The etymology of the word epitaxy has roots in the Greek language where "epi" means "above" and "taxis"

means "an ordered manner". Epigraphene grows bottom-up from the SiC substrate, and it forms a monocrystalline layer with a well-defined orientation with respect to the SiC substrate. One defining feature is the presence of an insulating buffer layer, which grows before the first monolayer of epigraphene forms. Due to strong interactions with both the SiC substrate and buffer layer, the properties of epigraphene are altered. There are especially significant changes to the electrical properties, which are very relevant for device applications. This section begins with a brief introduction to the crystal structure of SiC and how epigraphene grows on top of it, and ends with a summary of the advantages and drawbacks of epigraphene in the context of electronic devices.

2.2.1 Growth on Silicon Carbide

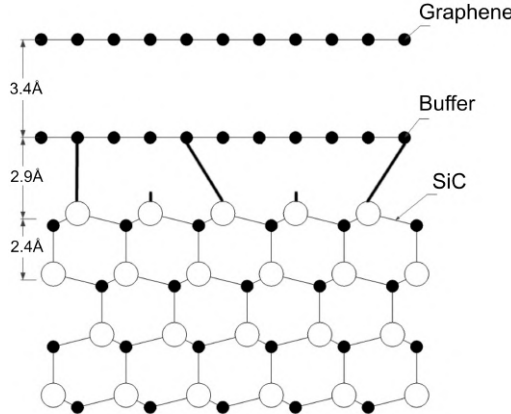


Figure 2.3: A side-view schematic representation (not to scale) of monolayer epigraphene grown on SiC, including the interface buffer layer [32]. The white circles and black circles represent Si and C atoms respectively. The approximate distance between the different surfaces are shown. The buffer layer interacts strongly with the substrate through covalent bonds, and is therefore insulating. The dangling bonds from the SiC substrate also affect the layers above. Note that the buffer layer and epigraphene obey A-B stacking.

As the name suggests, SiC is a crystal which consists entirely of Si and C atoms. The crystal structure of SiC can be imagined as consisting of layers of Si-C atoms bonded in a tetrahedral manner, as seen in Figure 2.3. There exist a plethora of polytypes of SiC, but the ones most commonly used for growth of epigraphene are the hexagonal polytypes 4H-SiC and 6H-SiC, shown in Figure 2.4. The first number describes the number of layers of Si-C pairs (also known as a Si-C bilayer) in the unit cell, and the letter H indicates that the crystal symmetry is hexagonal. Historically, the growth of epigraphene has been optimized primarily for the hexagonal polytypes 6H-SiC or 4H-SiC. These SiC substrates are electrically insulating at room temperature, with ~ 3 eV bandgap. While

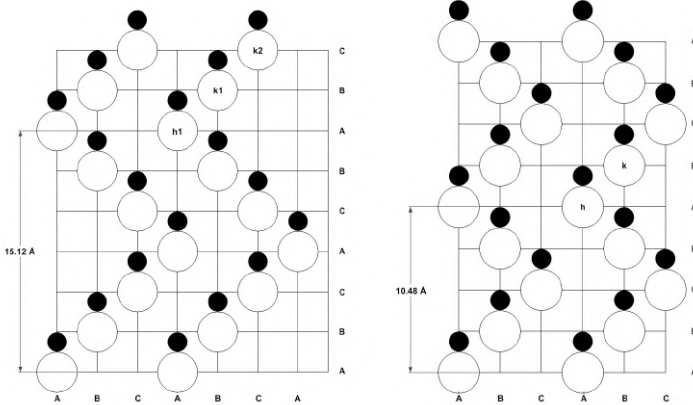


Figure 2.4: A two-dimensional schematic representation of the crystal structure of polytypes 6H-SiC (left) and 4H-SiC (right) [33]. The white circles represent Si atoms while the black circles represent C atoms. The layer stacking sequence is ABCACB and ABCB for 6H-SiC and 4H-SiC respectively. **Left:** For 6H-SiC, the letter h_1 represents the atom sites with hexagonal bonds, while k_1 and k_2 represent sites with two nonequivalent cubic bonds. This means that 6H-SiC has one third hexagonal bonds with the rest being cubic, but the crystal overall is still hexagonal. **Right:** For 4H-SiC, the letter h represents hexagonal bonds while k represent cubic bonds. 4H-SiC has equal parts hexagonal and cubic bonds.

the hexagonal crystal structure is relatively commensurate with the graphene lattice, the lattice mismatch of $\sim 20\%$ [34] is not insignificant. The resulting compressive strain on epigraphene can for instance be observed in Raman spectroscopy [35]. The reason behind the extensive use of hexagonal SiC is simply because high-quality single-crystal substrates are commercially available. High-quality large areas wafers are sold at a moderate price, which is still steadily decreasing as technology progresses. In fact, the cubic polytype 3C-SiC may prove to be a more suitable substrate for epigraphene, especially since epigraphene can be grown without buffer layer and lower strain [36]. However, cubic SiC is not industrially available and the growth process is not as well-understood. The work in this thesis focuses solely on 4H-SiC.

The polar SiC crystal has two types of surface terminations: Si atoms (Si-face) or C atoms (C-face). The Si-face is typically used for growth of monolayer graphene, due to the slower and more controlled growth kinetics [11, 37]. In contrast, the growth process on the C-face readily results in multi-layered patchy graphene films [38]. The Si-face is therefore preferred for applications which demand graphene of high electronic quality, like for QHR standards reliant on the QHE. The growth process of epigraphene utilizes thermal decomposition of the SiC substrate. When subjected to sufficiently high temperatures, the Si-atoms sublimate and leave behind a carbon rich surface layer, which upon further heating eventually forms into epigraphene. The first graphene-like layer which forms is electrically insulating and is referred to as buffer layer, 0-layer, or interface layer. The reason it is different from conductive epigraphene is that approximately 30 % of the carbon atoms form covalent bonds to the SiC substrate [39], thus destroying the conducting

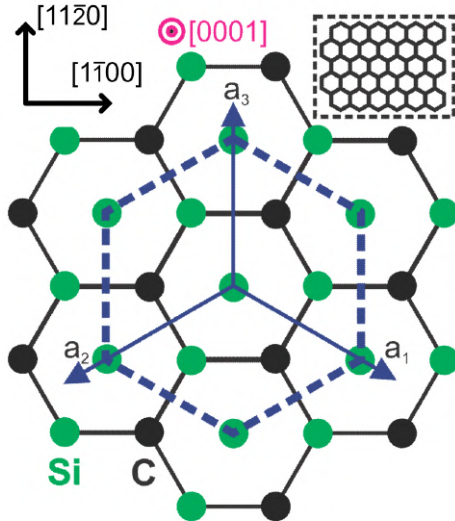


Figure 2.5: A schematic representation of the SiC crystal, including the three lattice vectors a_1 , a_2 , and a_3 . The image is drawn from the perspective of looking down on the Si-face, which has crystal plane (0001) in Miller-Bravais indices. The inset shows a sheet of epigraphene (not to scale) which has a 30° rotation with respect to the SiC crystal. The two perpendicular crystal directions of SiC point toward the armchair $[1\bar{1}00]$ or zigzag $[11\bar{2}0]$ edges of epigraphene.

π bands. Only starting from the second layer does an actual conducting monolayer of epigraphene appear (see Figure 2.3). Further growth of three or more layers is heavily suppressed once the buffer and first monolayer cover the SiC surface. This self-limiting effect makes uniform growth of bilayer epigraphene challenging.

Figure 2.5 shows the crystal structure of 4H-SiC and how it relates to epigraphene. Note that while the buffer layer grows similarly as epigraphene with 30° rotation w.r.t. SiC, it creates a large superstructure with $6\sqrt{3} \times 6\sqrt{3}$ reconstruction. Buffer, monolayer epigraphene, and subsequent epigraphene layers commonly obey Bernal stacking (A-B).

2.2.2 Carrier Density Control

While epigraphene retains most of its unique electrical properties, such as the Dirac spectrum, interactions with the substrate do influence some properties. Due to their proximity ($\sim 3 \text{ \AA}$), the epigraphene layer is heavily influenced by the buffer layer. For instance, the buffer layers acts as a high DOS charge donor and is responsible for the high intrinsic n-doping of epigraphene, which is observed to be on the order of $n \approx 10^{13} \text{ cm}^{-2}$. Additionally, the high density of states acts like charge traps and effectively pins the Fermi level of epigraphene in place, severely reducing the efficiency of charge carrier density tuning attempts [15]. The pinning is so strong that it can decrease the effective gate

capacitance of electrostatic gating by over 90 %. The SiC substrate also plays a crucial role in the aforementioned doping effects due to dangling bonds on its surface [40]. For both practical applications and theoretical studies, it is desirable to combat the influence of the substrate in order to be able to freely tune the carrier density of epigraphene. The practical realization of QHR standards, which desires to observe the QHE at moderate magnetic fields (< 5 T, 4 K) [19], is but one example of an application which requires doping control. The aforementioned problems make the plain electrostatic top-gate highly inefficient for epigraphene. A back-gate is even more impractical since the SiC substrate is too thick ($\sim 300 \mu\text{m}$) to be a dielectric.

There exist a few other methods which can be used to control the carrier density. One alternative is to use photo-chemical gating, which coats epigraphene with poly(methylstyrene-co-chloromethylacrylate), also known as ZEP520A, which is a common resist used for lithography. Upon exposure to UV light ZEP functions as an electron acceptor and causes epigraphene to become more p-doped. This method is stable and reliable, but lacks the potency to consistently bring epigraphene to charge neutrality. Another more potent method is corona discharge of ions [41]. A piezo-activated anti-static gun can be used to ionize air, which deposits charged ions on PMMA covered epigraphene. The method is potent, for both n and p-doping on epigraphene, but lacks stability at ambient conditions since the ions remain mobile. The molecular doping method based on acceptor molecules F4TCNQ presented later in this thesis aims to solve all of these problems.

While the aforementioned substrate interactions makes it difficult to access the Dirac point in epigraphene, the charge transfer processes comes with one advantage. In practice it has a positive side-effect on the robustness of the quantum Hall plateau, making it extended in a wide magnetic field range. In essence, the charge transfer process leads to a magnetic field dependent charge carrier density in graphene, which consequently prolongs the $R_{XY} = h/2e^2$ plateau, with experiments showing the plateau enduring up to 50 T [20]. One way to imagine this effect is that both the carrier density, and subsequently the Fermi energy, oscillates with magnetic field due to charge transfer [42]. For instance, when the Fermi energy is at a value where there is no resistance plateau, the carrier density decreases due to charge transfer to the substrate, effectively making the resistance plateau start at a lower magnetic field than normal. As the magnetic field increases further, the Fermi energy of graphene moves to a value which corresponds to a resistance plateau, and the carrier density then starts to increase due to substrate donors, effectively shifting the end of the resistance plateau to a higher magnetic field. The combination of both effects makes the resistance plateau extended in both low and high field directions.

2.3 Magnetotransport

The Drude model provides a simple classical model of the transport of electrons through a crystal. The electrons can be considered to be independent particles moving around like gas molecules. Electrostatic interactions with surrounding electrons and lattice ions can be simplified and bundled into an average effect, which can be encapsulated by replacing the mass of the electron with an effective mass m^* . An electron can then be considered

to move about like a free electron, but with an effective mass. It can travel freely across the crystal lattice until it encounters an obstacle, for example an ion, and the resulting collision leads to an instantaneous change of momentum and the electron is scattered. The average distance traveled before a collision is referred to as the mean free path ℓ . Scattering processes play a crucial role in determining the material properties, for instance it is through these collisions that electrons can reach thermal equilibrium with their surroundings.

Magnetic and electric fields can both affect the motion of electrons, and this interaction forms the basis for magnetotransport measurements. The resulting force due to external fields is called the Lorentz force, and can be expressed as Equation 2.11, where q is the charge ($-e$ for electrons, $+e$ for holes), \mathbf{E} is the electric field (vectors are bolded), \mathbf{B} is the magnetic field, and \mathbf{v}_I is the instantaneous velocity.

$$\mathbf{F} = q(\mathbf{E} + \mathbf{v}_I \times \mathbf{B}) \quad (2.11)$$

The equation states that the electric field accelerates electrons parallel to their travel path, while the magnetic field deflects the electrons perpendicular to both the field and the velocity direction. For an electron traveling in a 2D system, an external out-of-plane magnetic field will therefore bend the path of the electron into a circular trajectory. Under the influence of the Lorentz force (or any force), electrons also experience collisions at a rate of $1/\tau$, where $\tau = \ell/v$ is time between scattering events. For the electrons which suffer from a collision, the total effect of their individual scattering events can be approximated by adding a frictional damping force $F_{fric} = -m^*v/\tau$ to Equation 2.11. One way to understand this term is to look at how the average momentum of an electron $\mathbf{p}(t)$ changes after an infinitesimal increment in time dt . Out of the total electrons N , a fraction amounting to $N\frac{dt}{\tau}$ will have collided during this time. They acquire randomly distributed velocities due to random scattering, leading to zero average momentum. The remaining undisturbed electrons $N(1 - \frac{dt}{\tau})$ will have endured the Lorentz force $\mathbf{F}(t)$ in the meantime (dt) and changed their momentum accordingly. The average momentum of all electrons is then:

$$\begin{aligned} \mathbf{p}(t + dt) &\approx (1 - \frac{dt}{\tau})(\mathbf{p}(t) + \mathbf{F}(t)dt) \\ \frac{d\mathbf{p}(t)}{dt} &= -\frac{\mathbf{p}(t)}{\tau} + \mathbf{F}(t) \end{aligned} \quad (2.12)$$

In summary, the scattering process is treated as a damped movement of electrons in an external field. This scattering will eventually bring the system into thermal equilibrium, and the electrons will have acquired an average drift velocity \mathbf{v} . This is the net velocity resulting from the external influence of Lorentz and other forces. In contrast, electrons will normally move around in a random fashion at the Fermi velocity v_F . The drift velocity under the influence of Lorentz forces, with damping, follows from Newton's equation $\mathbf{F} = m\mathbf{a}$ as:

$$q(\mathbf{E} + \mathbf{v} \times \mathbf{B}) - m^* \frac{\mathbf{v}}{\tau} = m^* \left(\frac{d\mathbf{v}}{dt} \right) \quad (2.13)$$

For simplicity consider only the steady state situation where $dv/dt = 0$. Then the solutions in the 2D plane (x-y plane), with a perpendicular out-of-plane magnetic field (z-direction, see e.g. Figure 2.6), are given by solving:

$$\begin{aligned} 0 &= -eE_X - eBv_Y - m^* \frac{v_X}{\tau} \\ 0 &= -eE_Y + eBv_X - m^* \frac{v_Y}{\tau} \end{aligned} \quad (2.14)$$

The subscripts X and Y denote the direction along x or y-axis respectively. Because the current density \mathbf{J} is given by the drift velocity as $\mathbf{J} = qn\mathbf{v}$ were n is the carrier density, Equation 2.14 can be written:

$$\begin{aligned} \sigma_0 E_X &= \omega_c \tau J_Y + J_X \\ \sigma_0 E_Y &= -\omega_c \tau J_X + J_Y \end{aligned} \quad (2.15)$$

The factor $\sigma_0 = ne^2\tau/m^*$ corresponds to the DC Drude conductivity in the absence of magnetic fields. The cyclotron frequency $\omega_c = eB/m^*$ describes how quickly electrons complete one looped path (cyclotron orbit) due to an external magnetic field. Without the magnetic field dependent term, Equation 2.15 simply reduces to the familiar Ohm's Law $E = J/\sigma_0$. The conductivity can also be expressed as $\sigma_0 = en\mu$, where the carrier mobility $\mu = e\tau/m^*$ is a proportionality constant which describes how much an electrical field affects the drift velocity $\mathbf{v} = \mu\mathbf{E}$. A higher mobility figure is correlated with low scattering rate, which in general means that the material is of higher quality. For instance, a pristine material with fewer defects, i.e. fewer scattering centers, will yield a comparatively high mobility figure in contrast to a "dirty" material.

Equation 2.15 can be expressed in matrix form as:

$$\mathbf{E} = \rho \mathbf{J} = \begin{pmatrix} \rho_{XX} & \rho_{XY} \\ -\rho_{XY} & \rho_{YY} \end{pmatrix} \mathbf{J} = \sigma_0^{-1} \begin{pmatrix} 1 & \omega_c \tau \\ -\omega_c \tau & 1 \end{pmatrix} \mathbf{J} \quad (2.16)$$

The longitudinal resistance is defined as $R_{XX} = V_X/I_X$ (see Figure 2.6). It is typically more illuminating to consider the geometry independent sheet resistance or resistivity ρ , which in the longitudinal case is $\rho_{XX} = R_{XX}W/L$ where W is the width of the material and L the length. In the transverse case $\rho_{XY} = R_{XY} = V_Y/I_X$, the resistance and resistivity are one and the same. The conductivity tensor is the inverse of the resistivity tensor:

$$\sigma = \frac{\sigma_0}{1 + \omega_c^2 \tau^2} \begin{pmatrix} 1 & -\omega_c \tau \\ \omega_c \tau & 1 \end{pmatrix} \quad (2.17)$$

The conductivity, under the influence of a magnetic and an electric field, is then:

$$\begin{aligned} \sigma_{XX} &= \frac{\rho_{XX}}{\rho_{XX}^2 + \rho_{XY}^2} \\ \sigma_{XY} &= \frac{-\rho_{XY}}{\rho_{XX}^2 + \rho_{XY}^2} \end{aligned} \quad (2.18)$$

2.3.1 Single Band Hall Effect

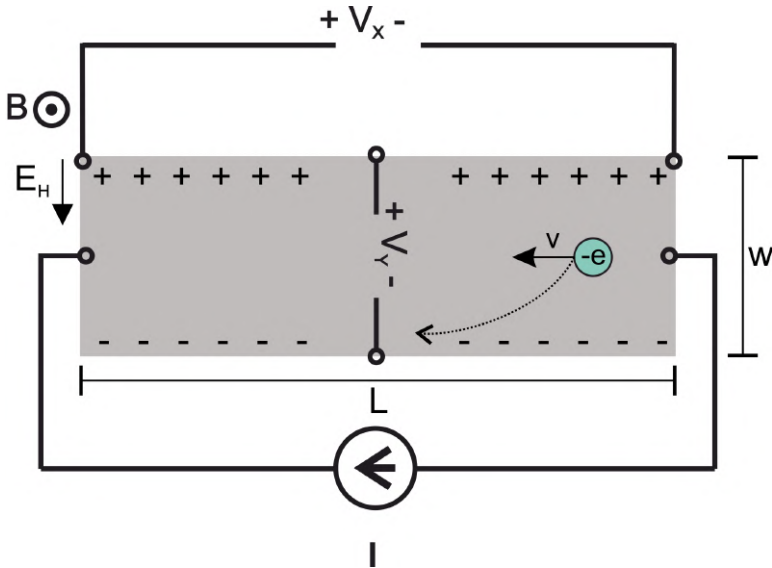


Figure 2.6: Schematic representation of a typical 2D sample geometry (Hall bar), with width W and length L , used to measure the Hall effect. As current passes from one end to the other, a longitudinal voltage V_x develops. If a magnetic field B is applied perpendicular to the plane, charges accumulate on one side of the Hall bar and an internal electric field \mathbf{E}_H appears. At equilibrium, the force from the electric field balances out the force from the magnetic field, and carriers are no longer deflected. The measured resulting transverse voltage V_y is the Hall voltage.

Figure 2.6 provides a schematic representation of an electron traveling along a rectangular 2D conductor (Hall bar) in the x -direction (longitudinal). When it is subjected to an external magnetic field B applied perpendicular to the plane, the electron is deflected to one side of the Hall bar due to the magnetic component of the Lorentz force. This eventually leads to separation of charges and a build-up of a net charge across the Hall bar width, which leads to the development of an internal electric field \mathbf{E}_H . This field gives rise to an counteracting electrical component of the Lorentz force, which at equilibrium exactly cancels the magnetic force, and no more electrons are deflected to the side. In this equilibrium state the resulting voltage V_y is then called the Hall voltage. To find out the expression for the Hall voltage, recall there is no longer any current in the y -direction (transverse) in equilibrium, which means $J_y = 0$ in Equation 2.15:

$$\begin{aligned} \sigma_0 E_y &= -\omega_c \tau J_x \\ E_y &= -\frac{\omega_c \tau}{\sigma} J_x = -\frac{1}{ne} J_x B \end{aligned} \tag{2.19}$$

Rewriting the above question in terms of the so called Hall coefficient $R_H = E_y / J_x B$

leads to:

$$R_H = -\frac{1}{ne} \quad (2.20)$$

In practice, the Hall coefficient is calculated from measurements as $R_H = dR_{XY}/dB$. Equation 2.20 is commonly used for low-field measurements, where R_{XY} is linear with magnetic field, in order to calculate the charge carrier density n of a certain material. Additionally, the sign of R_H also reveals if the electrical transport is dominated by electron or hole carriers, assuming that the direction of current and magnetic field is known. A Hall measurement can also determine the carrier mobility μ :

$$\mu = \frac{\sigma_0}{en} = \frac{|R_H|}{\rho} \quad (2.21)$$

2.3.2 Two Band Hall Effect

Since graphene is a zero band gap semi-metal, the absence of forbidden states in the band structure enables continuous tuning from hole to electron dominated transport [7]. It also means that there are in principle no forbidden excitations, and both electrons and hole can contribute to the current. This behavior is called ambipolar transport, and it is well-known for field-effect transistors used in the semiconductor industry. When graphene is very close to charge neutrality, ambipolar transport may occur either because of thermal excitations, which is present for any finite temperature due to zero band gap, or the presence of spatial charge disorder which creates regions of p-doping and n-doping (charge puddle regime) [43].

By taking into account both electrons and holes in the ambipolar regime, the Hall coefficient R_H becomes:

$$R_H = -\frac{1}{e} \frac{n_e \mu_e^2 - n_h \mu_h^2}{e(n_e \mu_e + n_h \mu_h)^2} \quad (2.22)$$

Where n_e, μ_e and n_h, μ_h denote contributions from electrons and holes respectively. The effective carrier density is:

$$n_{eff} = \frac{e(n_e \mu_e + n_h \mu_h)^2}{n_e \mu_e^2 - n_h \mu_h^2} \quad (2.23)$$

The longitudinal sheet resistance ρ_{XX} is:

$$\rho_{XX} = \frac{1}{e(n_e \mu_e + n_h \mu_h)} \quad (2.24)$$

When graphene is at charge neutrality and the Fermi energy is zero, the number of thermally excited electron and hole carriers is identical $n_e = n_h > 0$. The effective charge carrier density can then be reduced to $n_{eff} = \beta n_e$ with the coefficient dependent on the mobility ratio between carriers $\beta = (\frac{\mu_e}{\mu_h} + 1)/(\frac{\mu_e}{\mu_h} - 1)$. For electron-like behavior the ratio is positive $\beta > 0$ and vice versa for hole-like behavior $\beta < 0$.

Not only do thermal excitations give rise to excess carriers, but in a real sample there also exist spatial charge fluctuations due to disorder. In graphene these spatial variations are called charge-puddles. If the charge disorder is modeled by a Gaussian probability distribution in real space, then the charge carrier density for charge neutral graphene can be expressed as [31]:

$$n_e(T) = n_h(T) = \frac{2}{\pi(\hbar v_F)^2} \left[\frac{s^2}{4} + \frac{(\pi k_B T)^2}{12} \right] \quad (2.25)$$

Here the disorder strength is characterized by s (units of energy) [44]. Note that it is assumed that the disorder strength s and mobility ratio β are constant in the relevant temperature range. The above equation provides a way to experimentally estimate the disorder strength for charge neutral graphene.

Ambipolar transport is normally not necessary to take into account, especially at cryogenic temperatures and for highly doped graphene. At high doping levels, the large Fermi energy acts like a potential barrier which suppresses the excitation of minority carriers and the electrical transport behaves approximately the same as for the single band case. How high the carrier density needs to be is dependent on the sample temperature. For example, at very low doping levels of $n = 1 \times 10^{10} \text{ cm}^{-2}$, the corresponding energy according to Equation 2.10 is $E_F = 12 \text{ meV}$. In comparison, the thermal energy $k_B T$ at cryogenic temperatures of 2 K is only 0.2 meV. The Fermi-Dirac distribution $f(E) = 1/(e^{(E-E_F)/k_B T} + 1)$ states that the probability of finding an occupied state at 1 meV above the Fermi energy at 2 K is < 1 %, and $E_F = 13 \text{ meV}$ corresponds to only $n = 1.2 \times 10^{10} \text{ cm}^{-2}$.

2.3.3 Integer Quantum Hall Effect

According to Equation 2.16, the transverse resistance R_{XY} is always linear with magnetic field while the longitudinal resistance R_{XX} remains constant. However, in practical experiments with graphene this behavior can be different for high magnetic fields and low temperatures. In some 2D systems with high carrier mobility, low-temperature measurements at high magnetic fields lead to observations of quantum mechanical phenomena such as Shubnikov-De Haas oscillations and quantum Hall effect (QHE). Shubnikov-De Haas oscillations appear as oscillations in longitudinal resistance R_{XX} with a periodicity determined by $1/B$ [45]. The QHE on the other hand manifests itself as zero longitudinal resistance R_{XX} and quantized transverse resistance R_{XY} . The transverse resistance values are determined solely by two fundamental constants: the Planck constant h , and the elementary charge e . These quantized values of resistance are integer fraction of the von Klitzing constant $R_K = h/e^2$, and form plateaus of constant resistance at different magnetic fields. While R_{XY} is quantized, the longitudinal resistance vanishes $R_{XX} = 0$ (Figure 2.7).

Both of these phenomena share the same origin. At high enough magnetic fields the electron cyclotron orbits become quantized and the electronic DOS of 2D systems transform into Landau levels (LLs). The LLs are formally derived by solving the Schrodinger equation for free electrons in an external magnetic field. See Appendix B.1.1 for more details.

In essence, the quantum Hall Hamiltonian is almost identical to the quantum harmonic oscillator, and it is known that the eigenenergies for any quantum harmonic oscillator is:

$$E_n = \hbar\omega_c(N + \frac{1}{2}), \quad N \in \mathbb{N}^0 \quad (2.26)$$

This means that the energy spacing between two LLs is equidistant.

One difference is that the position of the energy minimum is shifted from the ideal quantum harmonic oscillator on the order of $l_B = \sqrt{\frac{\hbar}{eB}}$, where l_B is the magnetic length. It is the characteristic length scale for quantum interactions in a magnetic field, and it is closely related to the minimum radius of cyclotron orbits, limited by the Heisenberg uncertainty principle. The energy eigenfunctions are in fact localized on the order of the magnetic length l_B along the width of the Hall bar, while being completely extended along its length. This predicts the existence of elongated states along the length of the Hall bar, which turn out to be the edge states explored at the end of this section (Figure 2.8).

Since the eigenenergies are independent of momentum, the LLs are therefore highly degenerate and contain many states in each level. For a given carrier density n , the number of filled LLs is given by the filling factor $\nu = n/n_L$, where n_L the number of electrons required to completely fill one level. An upper bound of the degeneracy can be estimated by assuming that each localized electron in the LL encircles a single quanta of magnetic flux $\Phi_0 = h/e$, which is the minimum possible flux. Then the number of electrons in the LL, per unit area A , depends on the external flux density (magnetic field) as $n_L = B/\Phi_0$.

The degeneracy of LLs can be used to calculate the quantization of the transverse resistance R_{XY} . Recall that the Drude model and Equation 2.20 states the transverse resistance is dependent on the charge carrier density $R_{XY} = B/ne$. Simply inserting $n = \nu n_L = \nu B/\Phi_0$ yields:

$$R_{XY} = \frac{h}{\nu e^2}, \quad \nu \in \mathbb{Z} \quad (2.27)$$

In practice, for experimental observations of the QHE the charge carrier density can be kept constant while the magnetic field is changed, as seen in Figure 2.7. Alternatively, measurements can be performed at a fixed magnetic field, while the charge carrier density is tuned by an electrostatic gate for instance. In the case of constant carrier density, as the magnetic field is increased the energy spacing between LLs grow and the higher LLs are emptied. As each one is emptied the transverse resistance increases. The quantized value of resistance expressed in Equation 2.27 are in principle achieved only when exactly ν LLs are filled. However, it is experimentally observed that even when the Fermi energy lies between two LLs, resistance plateaus can still exist. These extended plateaus are attributed to broadening of the LLs due to disorder, which is omnipresent in real samples. If the disorder is small enough as to not cause overlap of LLs, the QHE plateaus can occur in between levels. For a pristine sample, the LLs are in theory represented by delta functions, i.e. sharp spikes, in the DOS and no plateaus exist. However, the presence of disorder broadens the LLs in energy, and this creates so-called localized and extended states inside each LL. The difference is that the localized states do not contribute to

electrical conduction, while the extended states do. The extended states live closer to the center of the LLs, while the localized states exist on either side. As the magnetic field is swept and the Fermi energy moves between one level to another, the localized states are affected (emptied/filled) first, and since they do not affect conduction, there is a constant resistance plateau in magnetic field.

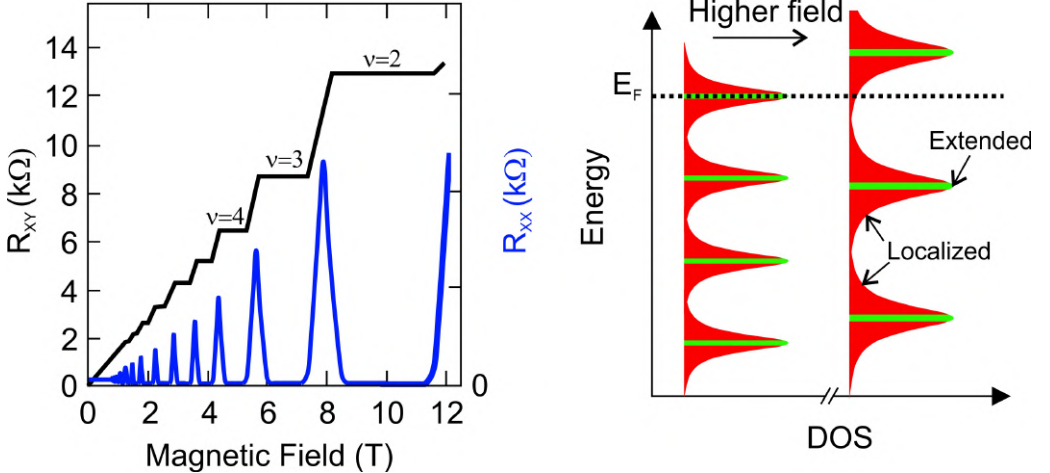


Figure 2.7: **Left:** Schematic representation of the evolution of transverse resistance R_{XY} and longitudinal resistance R_{XX} under the influence of a magnetic field B . At low B , classical Hall effects yields linear R_{XY} and constant R_{XX} . As B increases, R_{XY} develops resistance plateaus while R_{XX} decreases towards zero at each plateau. At small B , the quantization is imperfect because the energy overlap between LLs is still too large. For higher B the system enters fully into the regime of QHE, with exactly quantized plateaus and zero longitudinal resistance. As B is increased further, the lower energy LLs are successively emptied leading to further steps in R_{XY} and oscillating peaks in R_{XX} **Right:** Schematic representation of the LL DOS with broadening due to sample disorder. The red regions denote localized states and the green regions are the extended states. The energy spacing and degeneracy of the LLs increase as B does. Assuming fixed Fermi energy, the consequence is that more and more LLs are emptied with increasing B . The Fermi energy can be seen as sweeping through LLs as B is changing. The plateau in R_{XY} and zero resistance R_{XX} both occur when the Fermi energy sits somewhere in the localized states, between two extended states. The slope in R_{XY} and peak in R_{XX} both occur when the Fermi level passes through the extended states in the center of a LL.

The spatial location of localized and extended states are important to understand when trying to explain why $\rho_{XX} = 0$ in the QHE regime. The existence of edge states can be seen by considering a real Hall bar sample, which necessarily has finite dimensions and edges at the boundary, as depicted in Figure 2.8. For simplicity, consider only the spatial variation of the potential $V(x)$ in one dimension, across the width of the Hall bar. In the ideal case of no disorder, the energy of LLs lie flat in the bulk and rise steeply at the edges, similar to the confining walls of a potential well. It is this confinement potential

which gives rise to edge states. See Appendix B.1.2 for a more detailed derivation.

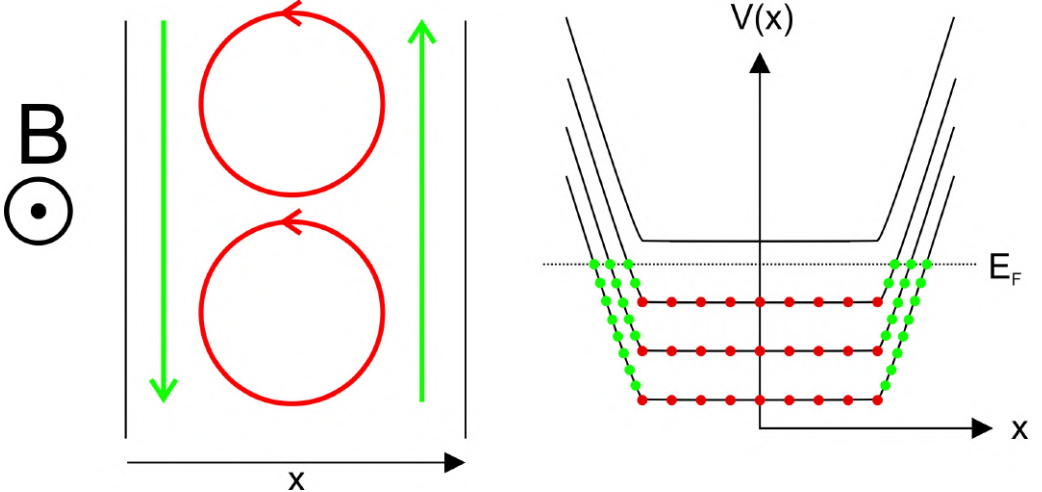


Figure 2.8: *Schematic representation of the conducting chiral edge states and insulating bulk states in QHE regime. Left:* Top-down view of a Hall bar with the directions of chiral edge currents (green) and localized bulk currents (red). *Right:* Spatial variation of the potential in QHE regime, where each line represents one LL. In the ideal case the potential lies flat inside the sample due to absence of disorder. The potential increases rapidly near the sample edges to model that the Hall bar confines the electrons. The location of the two edge states (green) and the localized bulk states (red) are determined by the drift velocity, which is related to the spatial derivative of the potential.

In short, the addition of a confinement potential alters the eigenenergies to become dependent on the momentum and lifting the degeneracy of LLs. Importantly, since the drift velocity is defined as $v_y = \frac{1}{\hbar} \frac{\partial E_n}{\partial k}$ there is also now a finite drift velocity. The drift velocity on opposite edges (x or $-x$) of the Hall bar point in opposite y -directions. In total, this means that there exist localized edge states with chiral edge currents parallel to the y -direction. They are chiral because the flow direction of the edge current is locked to the edge it propagates along, and the flow direction is reversed for the opposite edge. The chirality is flipped only if the magnetic field direction is flipped. Since the direction of travel is fixed for the edge states, back-scattering is suppressed and results in $\rho_{XX} = 0$ in QHE regime. The bulk on the other hand has zero drift velocity due to a constant potential, and can be thought of consisting of localized states which isolate the two edge channels from each other. Note that the general picture of edge states still holds true even if the potential in the bulk has spatial variations due to disorder, like in real samples. This is however only the case for small variations, which do not cause the energies of LLs to overlap. Furthermore, the general picture also holds for a wide range of edge confinement potentials, including a more realistic smooth potential [46, 47].

In the semi-classical picture, the formation of these edge states and bulk states can only occur if the electron can complete a few cyclotron orbits before being scattered.

This imposes practical restrictions on experimental observations of the aforementioned quantum phenomena. The necessary, but not sufficient, condition which must be met is $\omega_c \gg \tau^{-1}$ or equivalently $B \gg \mu^{-1}$. In other words, to experimentally observe QHE at reasonably low magnetic fields, the carrier mobility needs to be high enough. For reference, if the mobility exceeds $\mu = 10\,000\,\text{cm}^2/\text{Vs}$, the QHE can occur already at $B = 1\,\text{T}$, which is readily achievable with a strong rare-earth permanent magnet. This condition affects practical applications of epigraphene QHR standards in terms of demanding high sample quality, but also control over carrier density. Generally it is observed that the mobility increases as carrier density decreases, thus it is advantageous to be able to lower the carrier density, especially for epigraphene with its high intrinsic n-doping.

2.3.4 Half-integer Quantum Hall Effect

The physics of graphene near the Dirac points is described by the Dirac equations, and it is special due to the effectively massless Dirac fermions. These properties impact the physics behind the cyclotron motion of graphene carriers [8, 48] and the cyclotron orbit becomes:

$$\omega_c = \sqrt{2} \frac{v_F}{l_B} = v_F \frac{2eB}{h} \quad (2.28)$$

The LL spectrum of graphene can be obtained by solving the Dirac equation in the presence of a magnetic field [27–29]:

$$E = \pm \hbar \omega_c \sqrt{N} = v_F \sqrt{2\hbar eBN}, N = 0, 1, 2\dots \quad (2.29)$$

The LLs of graphene are very different from conventional 2D systems. For instance, the energy spacing is no longer equidistant and scales as $\Delta E \propto \sqrt{B}$ instead of linearly with B . Furthermore, an additional factor of 2 is added to the degeneracy of each LL due to the valley degeneracy (\mathbf{K} and \mathbf{K}'). Lastly, a new LL has appeared at zero energy, which is shared by the two valleys and is only spin degenerate. Consequently, the resistance plateaus in R_{XY} are altered. The number of electrons required to fill a single LL in the case of conventional 2D systems is B/Φ_0 per unit area. For instance, this is typically the case for conventional 2DEGs like GaAs, which do not commonly display spin degenerate LLs. Adding the spin and valley degeneracy, each filled LL in graphene instead contains $4B/\Phi_0$ electrons. The zero energy LL is the sole exception and only fits $2B/\Phi_0$ electrons. By summing the electrons from N completely filled LLs above zero energy, the charge carrier density for graphene is:

$$n = N \frac{4eB}{\hbar} + \frac{2eB}{\hbar} = \frac{4eB}{\hbar} (N + 1/2) \quad (2.30)$$

Note that $N = 0$ means that only the zero energy LL is filled. Inserting the above expression for into the equation for the transverse resistance:

$$R_{XY} = \frac{B}{en} = \frac{h}{4e^2(N + 1/2)} \quad (2.31)$$

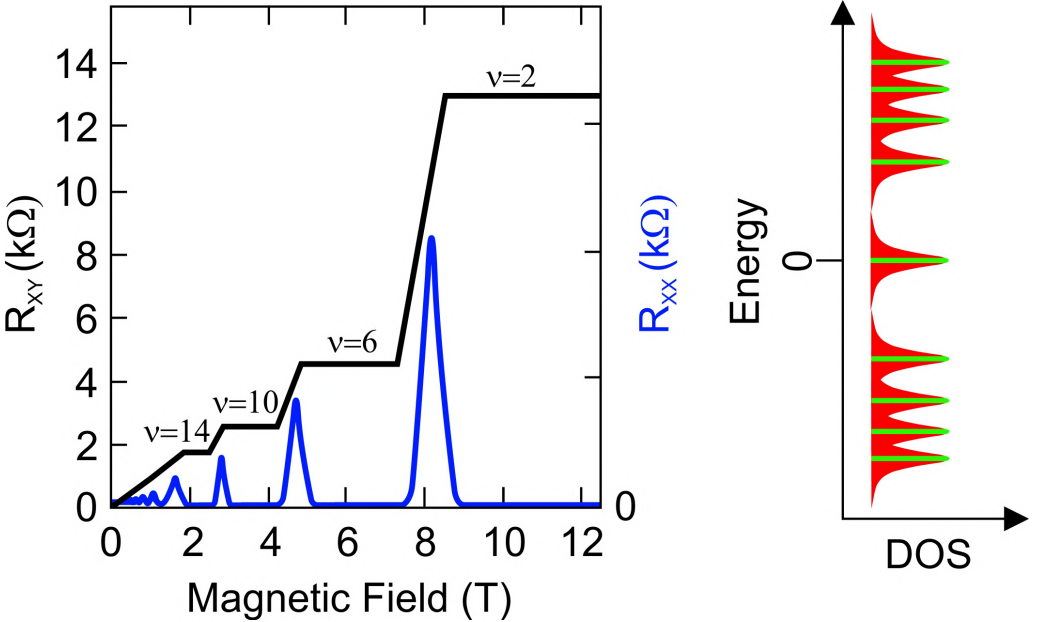


Figure 2.9: **Right:** Schematic representation of the transverse resistance R_{XY} and longitudinal resistance R_{XX} for graphene in QHE regime. The unique series of filling factors is a fingerprint of monolayer graphene and its Dirac nature. **Left:** Schematic representation of the LL energy spectrum for graphene. Graphene has a relatively large energy spacing between the 1st and 0th LL, and variable energy spacing between adjacent LLs.

The result is that instead of resistance plateaus appearing at integer multiples of h/e^2 , graphene has quantized values equal to half-integer multiples of $h/4e^2$. In terms of quantized resistance $h/\nu e^2$, graphene has the progression of filling factors $\nu = 2, 6, 10, 14\dots$ instead of the conventional $\nu = 1, 2, 3, 4\dots$. The half-integer QHE is an identifying fingerprint for graphene, and its Dirac nature. The experimental observation of these special filling factors is an unequivocal proof that the sample under study is indeed monolayer graphene. The LL energy spacing of graphene is not only theoretically interesting, but it is also advantageous for practical applications. One beneficial feature is the particularly pronounced energy spacing between the 0th LL and 1st LL. For QHE observations, this means that the plateau $\nu = 2$ and $R_{XY} = h/2e^2$ can be seen at lower fields and higher temperatures than in conventional 2DEGs such as GaAs. For comparison, at $B = 1$ T graphene LLs have over 20 times greater energy spacing between the 0th LL and 1st LL than in GaAs-based 2DEGs. This uniquely large energy spacing has enabled the observation of QHE in graphene even at room temperature [49].

2.3.5 Quantum Corrections to Classical Resistance

Continuing the trend of looking at quantum transport, there are some additional corrections to the classical Drude model which are relevant for this thesis. Each scattering process correspond to some relaxation rate $1/\tau$ in the Drude model, and different scattering processes sum together (Matthiessen's Rule) to affect the final resistance. The scattering rates increase with temperature (higher velocity and carrier density), and the Drude model therefore predicts a monotonously decreasing resistance with decreasing temperature.

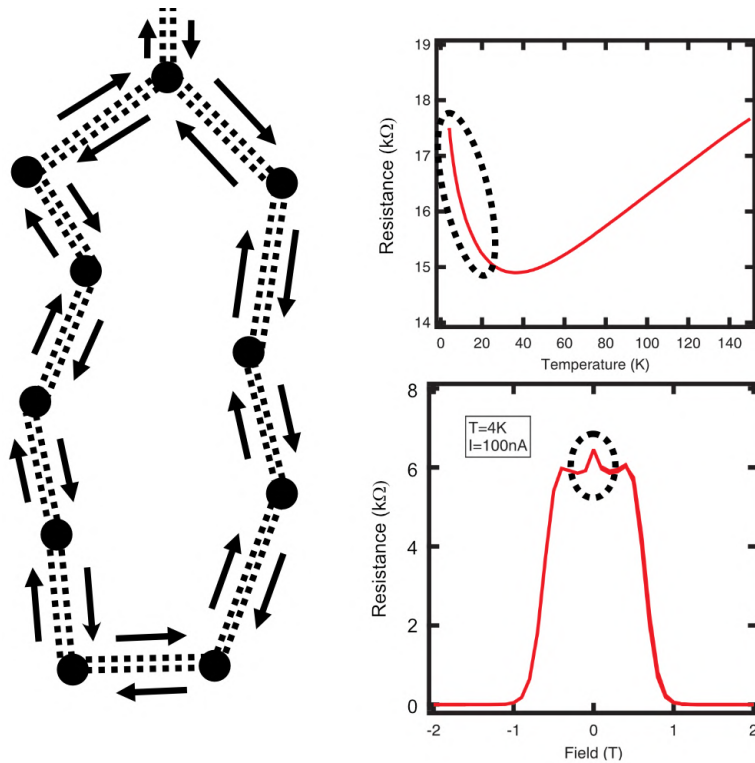


Figure 2.10: **Left:** A schematic representation of self-intersecting paths. The electrons scatter between the impurities (black dots) and can take either clockwise or counter-clockwise paths. Its wave-nature causes interference between the two time-reversal symmetric paths, and gives rise to weak-localization effects which increase resistance. **Right:** The influence of quantum interference in epigraphene is encircled by the black dotted lines. For temperature dependence of resistance, quantum interference is responsible for increased resistance at low temperature (logarithmic scaling). This can be due to both weak-localization and electron-electron interactions. For magnetotransport measured for a different sample, weak-localization manifests itself as a peak in resistance R_{XX} at zero field. It is suppressed by the presence of an external magnetic field, which breaks time-reversal symmetry.

For 2D materials like graphene experiments show an additional increase in resistance at low temperatures, which is unaccounted for in the Drude model. One of the most important corrections arises from the wave nature of electrons, which in reality causes coherent quantum interference effects.

In a real electronic device there exist defects which lead to excessive elastic scattering of electrons. The electrical conductance of a medium is related to the total probability of an electron propagating through it, scattering all over along the way. In the classical case, the total probability of propagation is simply the sum of the probabilities for each individual scattering path $|a_i^2|$ as $\sum_i P_i = \sum_i |a_i^2|$. However, in the quantum mechanical case one has to take the square of the sum of the quantum-mechanical amplitudes $A_i = a_i e^{i\Phi}$ of the paths instead [50]. The total transmission probability is:

$$P_T = \left| \sum_i A_i \right|^2 = \sum_i P_i + 2\text{Re} \sum_{ij} A_i^* A_j \quad (2.32)$$

The first term is the classical probability contribution, and the second term is the quantum mechanical interference term between two paths i and j . There is no special phase correlation for random paths, and the average effect of interference is zero due to averaging scattering events with random phases. However, for certain paths, such as self-crossing ones where $A_i = A_j$, the interference terms contributes to the final probability. Since these paths form closed loops and obey time-reversal symmetry, their phases are identical and the total probability becomes $P_T = \sum_i P_i + \sum_{ij} a_i a_j e^{\Phi_i - \Phi_j} = \sum_i P_i + \sum_{ij} a_i a_j$. The quantum interference leads to a positive contribution to the probability for self-crossing paths, which means enhanced back-scattering of electrons and therefore increased resistance. This phenomena is called weak-localization (WL) and is shown in Figure 2.10. Weak-localization manifests itself in both temperature dependence of resistance and in magnetotransport. In temperature dependence of resistance, WL is responsible for the logarithmic increase in resistance at low temperatures. Note the WL is not the sole source of this increasing resistance, but electron-electron interactions also play a role [51]. In magnetotransport measurement of the QHE, WL gives rise to a resistance peak around zero magnetic field. The WL dies out as the field strength is increased, because the magnetic field breaks the time-reversal symmetry which is required for quantum interference to survive. The relative amplitude of the quantum correction peak is related to carrier density, and at lower densities the effect is more pronounced (also true for lower temperatures). This is due to the relationship between carrier density and phase coherence length, which typically decreases as the number of carriers increases. The Coulomb screening also decreases with carrier density, which further favors quantum interference effects [51, 52]. On a related note, the shape of the peak versus magnetic field and temperature can reveal a great deal of information about the different scattering mechanism in the material [51, 53].

3 Experimental Methods

This chapter describes the fabrication and characterization techniques used to produce working epigraphene electronic devices. The first section focuses on epitaxial growth of epigraphene on SiC. It includes information on non-invasive methods which are used to assess the material quality, such as atomic force microscopy (AFM), optical microscopy, and Raman spectroscopy. The second section is devoted to microfabrication using lithographic techniques to pattern epigraphene devices. The third section presents how the acceptor molecule F4TCNQ can be used to dope epigraphene. The final section deals with DC electrical characterization techniques, including Hall measurements, van der Pauw, and precision measurements. Detailed descriptions of microfabrication recipes can be found in Appendix A.

3.1 Graphene Growth

Graphene can be produced in a multitude of ways, and each growth method has its strengths and weaknesses. The final properties of graphene depend greatly on the chosen method, and there is usually a trade-off between quantity and quality. For the creation of graphene with high electronic quality, the popular methods include: mechanical exfoliation, chemical vapor deposition (CVD), and epitaxial growth. Mechanical exfoliation of graphene by cleaving graphite produces in general the highest quality material, but due to manual labor requirements the throughput is low and the process is not suitable for real-world applications. CVD utilizes a carbon-rich precursor gas which reacts on a metallic catalyst substrate to grow graphene over a large scale. This technology is in principle scalable and the material quality can be high. However, one main drawback is that CVD graphene needs to be transferred to an insulating substrate before device fabrication. This is not a trivial process and inevitably results in contamination and degradation of the material [13]. The preferred method in this thesis is epitaxial growth of graphene, which utilizes thermal decomposition of an insulating SiC substrate to produce monocrystalline graphene over in principle an entire wafer [11]. It is advantageous for device fabrication since one can forgo graphene transfer and directly fabricate devices on pristine epigraphene fresh from the oven. All work in this thesis has been performed using epigraphene grown on the Si-face of the hexagonal SiC polytype 4H-SiC. A general outline of the epitaxial growth process is given below.

It is important to ensure that the surface of SiC is clean and free from defects before proceeding with growth, since any imperfections will nucleate rapid growth and result in inhomogeneous epigraphene. The first step is to acquire SiC wafers of the highest grade possible from commercial suppliers. For ease of handling, the 2-4 inch SiC wafers are diced into $7 \times 7 \text{ mm}^2$ square chips using a resin bound diamond blade mounted on a dicing saw. The SiC chips are then thoroughly cleaned using aggressive chemical agents. These chips undergo the RCA process (See A.2), a staple in the semiconductor industry. Organic contaminants are removed using ammonia and hydrogen peroxide, oxides are removed using hydrofluoric acid (HF), and metallic contaminants are removed using hydrochloric acid mixed with hydrogen peroxide. Immediately after the RCA process, the chips are

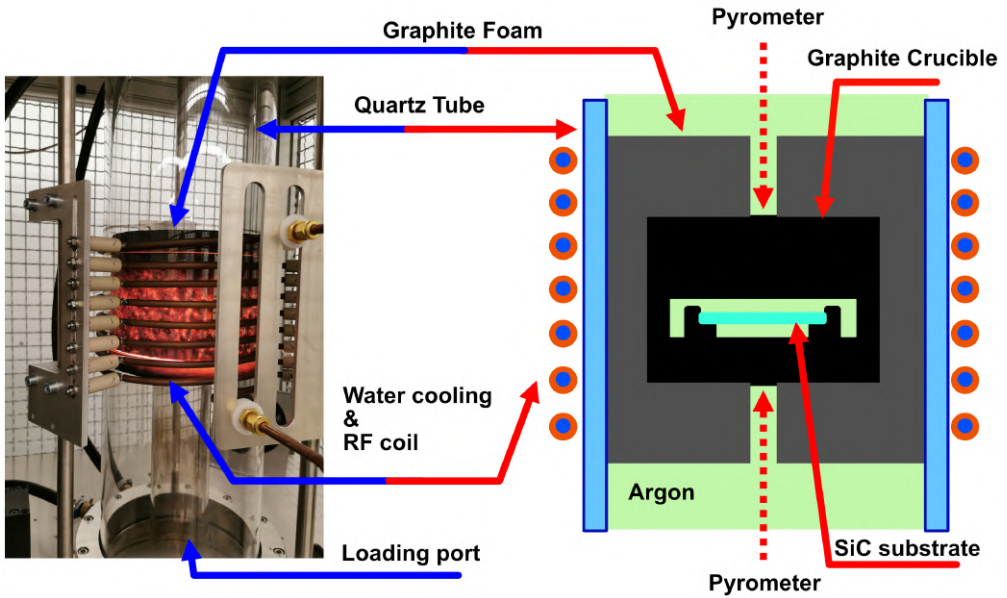


Figure 3.1: **Right:** Photograph of a furnace used for growth of epigraphene via thermal decomposition of SiC. The SiC substrate is placed inside a graphite crucible, enclosed in the graphite foam. **Left:** Schematic representation of a cross-section of the furnace, including the graphite crucible. The SiC is placed Si-face-down in the crucible, suspended on small graphite pillars. The crucible is heated using RF power in an inert argon atmosphere, and the temperature is monitored using two pyrometers.

thoroughly rinsed in a bath of high-purity deionized water. Before the growth process starts, the chips are usually dipped one last time in HF and kept submerged in water all the way to the growth furnace.

Figure 3.1 shows an example of how an epigraphene furnace looks like. In the center of the furnace rests a crucible carved from solid graphite. The chip is placed the center of the crucible with the Si-face pointing down, suspended on graphite pillars, and sealed inside by a solid graphite lid. In general, the confinement aids in suppressing growth rate in order to improve epigraphene quality. The crucible itself is enclosed in graphite foam, and the whole structure sits in a quartz tube which is surrounded by a heating coil and complementary water cooling system. For growth of monolayer graphene, the oven is set to approximately 1700 °C for a 4 inch crucible, and approximately 1900 °C for a 2 inch crucible. The graphite crucible is heated by induced eddy currents due to applied RF power. The entire quartz chamber is filled with an inert argon atmosphere of around 800 mbar. The furnace is heated up over the course of around 1 hour and kept at the desired temperature set-point for 5 minutes, after which the power is switched off. After waiting

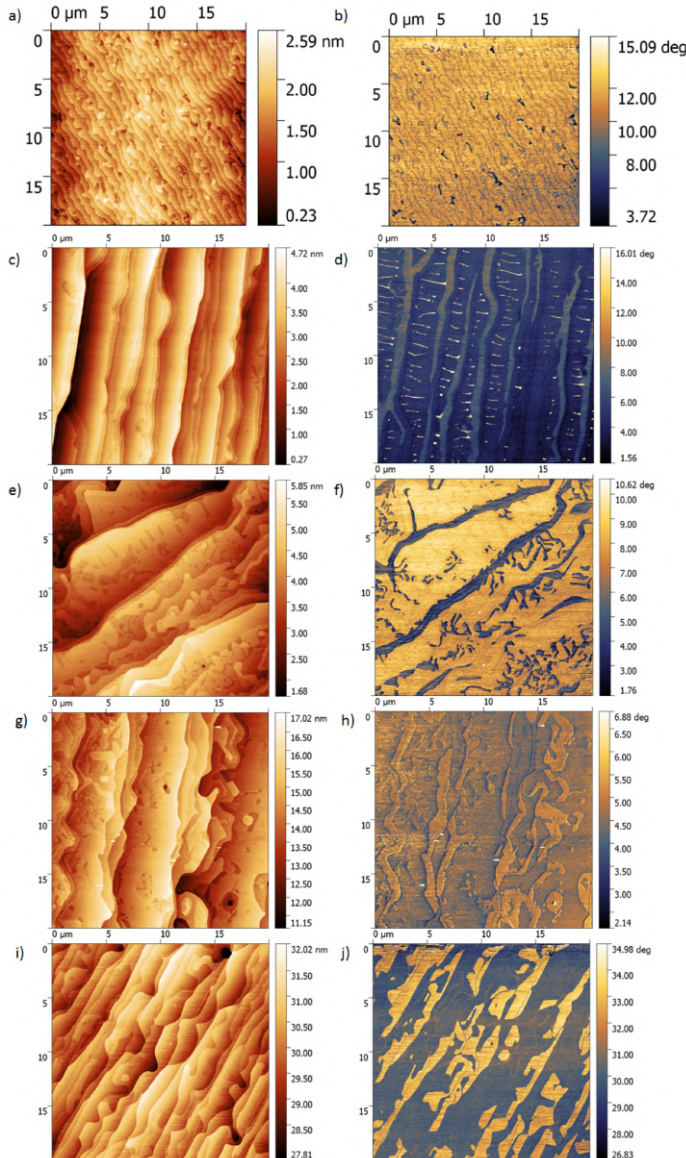


Figure 3.2: An overview of the growth optimization process. The AFM scans show the topography of epigraphene grown at different temperatures. The height scan images **a**, **c**, **e**, and **i** show how the SiC steps have reconstructed differently, while the phase images **b**, **d**, **f**, **h**, and **j** give an indication of the uniformity of growth. Epigraphene was grown at 1700 °C **a-b**, 1750 °C **c-d**, 1800 °C **e-f**, 1850 °C **g-h**, 1900 °C **i-j**. The phase images show that epigraphene is the most uniform for growth at 1700 °C.

more than 4 hours, the sample is usually sufficiently cold and can be removed from the oven. The growth quality, in terms of area coverage of monolayer epigraphene, can be quickly investigated using the non-invasive methods described in the coming sections.

The growth process is sensitive to temperature, pressure, and time, and it is difficult to predict in advance how uniformly epigraphene will grow. Optimization of the process implies varying these parameters, growing many samples, and investigating the quality. An example of this procedure can be seen in Figure 3.2, where the temperature for growth in a 4 inch crucible was changed between 1700-1900 °C, and the homogeneity was studied using non-destructive AFM techniques (Chapter 3.1.2).

3.1.1 Optical Microscopy

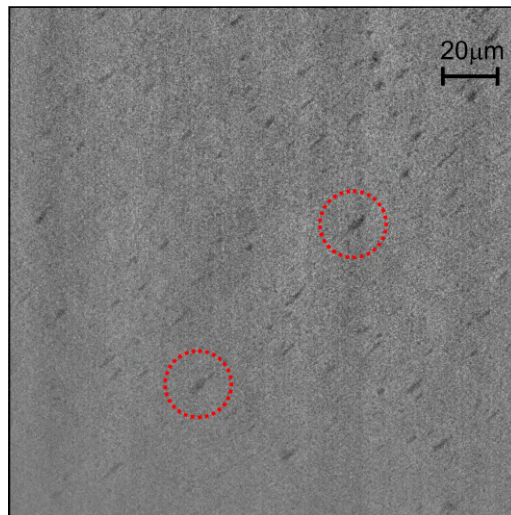


Figure 3.3: An optical micrograph of epigraphene taken using transmission mode optical microscopy. Imagine processing such as background subtraction, digital contrast enhancement, and gamma correction have been used to enhance the contrast between bilayer inclusions and monolayer. Since bilayer inclusion absorb more of the transmitted light, they appear as darker stripes (e.g. red dotted circles). Outside the bilayer, everything else is monolayer epigraphene and the area coverage of this particular sample area is approximately > 98 %.

Despite the fact that both the SiC substrate and epigraphene appear fully transparent to the naked eye, basic optical microscopy techniques in the visible spectrum can still provide valuable insight into the sample homogeneity after growth [54]. One such technique utilizes transmission mode microscopy, in combination with digital contrast enhancement, to differentiate between single and multi-layer epigraphene patches. This works because the light absorption increases by $\sim 1.3\%$ for each additional layer of epigraphene. Note that free-standing monolayer graphene absorbs $\sim 2.3\%$, but the SiC substrate decreases this contrast by a factor of 2. This method is useful because it allows for quick assessment

of the quality (i.e. homogeneity) of epigraphene over a large area and in real-time. Figure 3.3 shows an example of an image produced using this technique, where apparent bilayer inclusions can be clearly distinguished. Generally, this method can only reveal how many extra layers of graphene exist in one region compared to another. In order to determine the absolute layer count, a known reference such as region of bare SiC is needed. Monolayer epigraphene absorbs $\sim 2.4\%$ more than bare SiC, and the contrast is higher because epigraphene has the buffer layer underneath. It should be noted that the presence of monolayer epigraphene is in principle not verifiable from optical imaging alone. The use of optical microscopy simply serves to quickly determine whether a particular sample is homogeneous enough to be worthy of further processing.

3.1.2 Atomic Force Microscopy

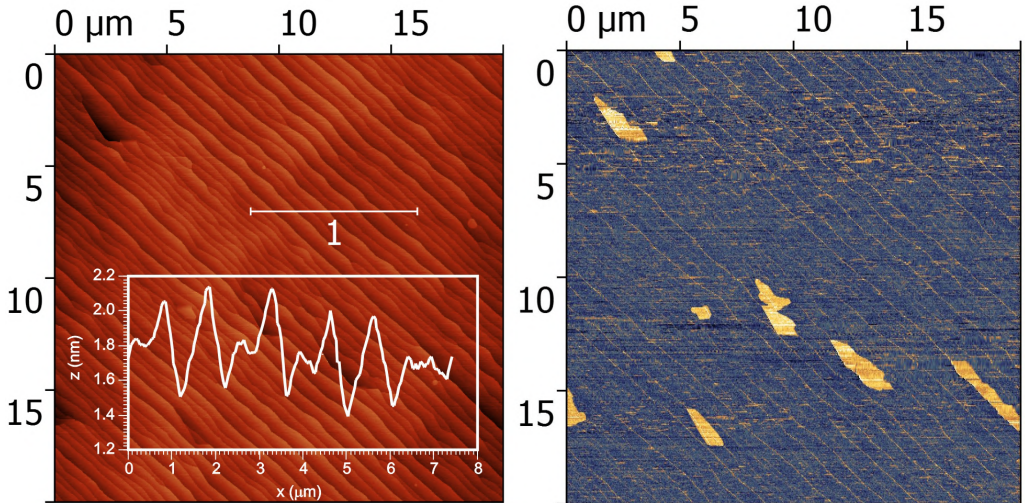


Figure 3.4: Epigraphene characterized by tapping mode AFM. **Left:** Height image shows the topography of epigraphene, after linear background subtraction. The most prominent features of epigraphene grown on SiC, are the myriad of steps formed on the surface of the SiC substrate during growth. The inset shows the cross sectional height profile taken along Line 1, which reveals that the steps are on the order of 1 nm high, on the order of unit cell height of 4H-SiC. The steps are separated by atomically flat SiC terraces 1–2 μm wide. The epigraphene, not directly visible, is draped like a carpet over the SiC steps. Certain regions have much larger SiC step size, and appear almost as holes in topography (black). These deeper regions hint at multilayer graphene growth, because more SiC needs to be consumed in order to supply enough carbon atoms. **Right:** The AFM phase image clearly reveals the presence of a different material (yellow), presumably bilayer inclusions, whose positions correspond well to the deep steps in topography.

While optical microscopy is an expedient method to image the material homogeneity, it lacks the necessary spatial resolution to detect the intricate features on the nanometer

scale. A scanning probe technique such as atomic Force Microscopy (AFM) is useful when high resolution is needed. It can provide atomic resolution in height, and can be used to image the topography of a sample as seen in Figure 3.4. The lateral resolution depends on the size of the AFM tip, and is typically on the order of 10 nm.

Tapping mode AFM is the most commonly used mode. All AFM-modes are based on the oscillation of a cantilever with a sharp tip, driven near its resonance frequency. In tapping mode, the tip is intermittently brought close to the sample and the change in oscillation amplitude due to interactions with the surface are used to determine the topography. In addition, changes in the mechanical properties and viscoelasticity of the surface can be detected from the phase signal, which is defined as the phase difference between the excitation signal of the cantilever and the measured output signal. This is in essence a measurement of the energy loss of the cantilever, and it is useful because it can distinguish between different graphene domains which can be hard to distinguish from topography alone. However, it ultimately only shows whether two regions have different graphene thickness, and not the exact layer count.

An electrical mode which complements regular mechanical tapping mode is the Kelvin probe microscopy (KPM) which can be used to image the work function of the surface. With a known reference point, such as gold, one can determine the work function of the underlying material and in principle estimate the number of graphene layers [55]. However, since the work function is dependent on carrier density, KPM measurements on graphene under ambient conditions can be difficult to interpret since bare graphene is sensitive to external doping.

3.1.3 Raman Spectroscopy

Raman spectroscopy is a popular technique to characterize graphene, as it can show a wealth of information regarding layer count, doping, and strain. The technique relies on detecting the inelastic scattering of monochromatic light, and probes the relaxation of the vibrational modes of a crystal, which reveal information about the underlying crystal structure. Graphene has many unique fingerprints which appear in a Raman spectra [56], but the main peaks which are the most studied are the 2D peak (breathing mode of six carbon atom rings), D peak (same fundamental origin as 2D peak, but requires disorder) and G peak (in-plane vibrational mode of carbon-carbon bonds). Figure 3.5 shows a typical spectra for epigraphene. A commonly accepted sign of high quality monolayer graphene is a sharp and intense 2D peak, combined with a small D peak. The Raman spectra have many subtleties, for instance the position, width, and intensity of the 2D and G peak depend both on strain and doping[35]. Furthermore, additional layers of graphene will result in a broadening and shift of the 2D peak [57]. In fact, the 2D peak will be a superposition of several peaks, depending on number of layers. However, due to the confounding influences of strain and doping, coupled with limited lateral resolution of a finite laser spot size, it is not always possible to clearly distinguish between mono and multilayer graphene domains, especially for epigraphene which contain small bilayer inclusions. Another unfortunate limitation of Raman spectroscopy on epigraphene is that the SiC substrate has strong Raman peaks which greatly overlap with the D and G peaks of graphene. Careful background subtraction can recover the buried peaks, but their

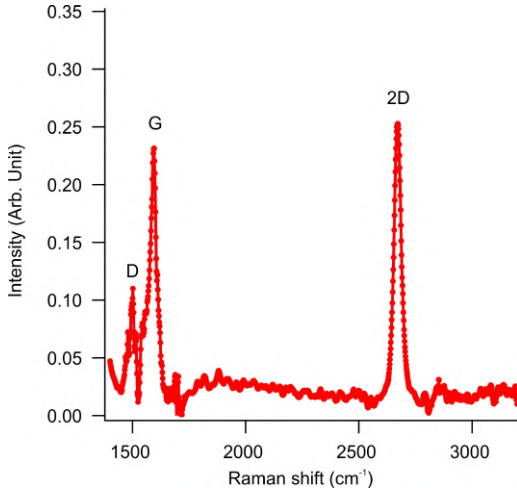


Figure 3.5: *Raman spectra of epigraphene, with the SiC background signal subtracted. A sharp 2D peak can be seen at a shift of 2670 cm^{-1} . The D (1500 cm^{-1}) and G (1590 cm^{-1}) peaks, while slightly distorted after background-subtraction, are also well-defined. The sharp ($\text{FWHM} = 40\text{ cm}^{-1}$) single Lorentzian 2D peak, combined with the relatively weak D peak, is a sign of high quality graphene.*

shapes can be distorted.

3.2 Electron Beam Lithography

This section describes the general lithography processes required to pattern epigraphene into an electronic device. The primary fabrication technique relies on electron beam lithography (EBL) to transfer device patterns to epigraphene. Photolithography is also a viable alternative, and commonly used in industry. It sees only limited use in this work because of the nature of the molecular doping method, which is only compatible with resists used in EBL.

Figure 3.6 shows a typical EBL process, which can be divided into three steps. In the first step, metallic cross-shaped markers are deposited to enable precise alignment of future layers. Metallic anchor pads are also created at the same time. These anchors ensure that the next layer of metallic contacts, which will connect to epigraphene itself, will adhere well to the chip. This precaution is necessary because the adhesion between metals and bare graphene is poor. The fabrication process begins by covering the surface of epigraphene with two layers of EBL compatible resist using spin-coating. The first is a poly(methyl-methacrylate) (PMMA) based copolymer, followed by a layer of A-RP 6200.13. The bottom layer can be replaced by normal PMMA if needed. These are all positive resists, which means that after exposure to the electron beam (ebeam) they become soluble in specific developers. The reason for using two types of resists, sensitive to different developers, is to enable control over the resist profile after development. The desired

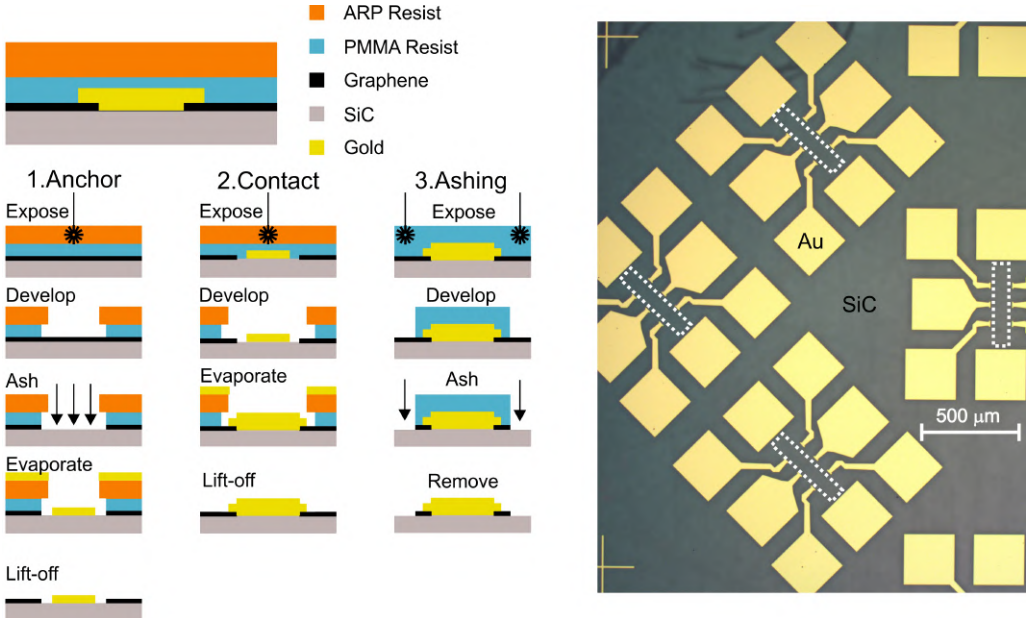


Figure 3.6: *Left: Schematic representation of the EBL process.* **1. Anchor:** In the first step Au anchors and markers are fabricated. Epigraphene is removed using oxygen plasma ashing and the metal layer is deposited directly on SiC. A thin adhesion layer of Ti is used before Au deposition. The anchors are important because they provide support and improve adhesion for future contact layers. **2. Contact:** The second EBL step uses the markers from the 1st step to align the Au contacts which connect to graphene itself. **3. Ashing:** In the final step, the device geometry is defined by removing excess graphene using ashing. *Right: Optical image of a finished epigraphene sample.* The sample contains arrays of Hall bars, each with eight electrical contacts made from Au. The white dotted lines mark the rectangular graphene regions. All graphene outside these regions have been removed, leaving behind only insulating SiC.

device pattern is transferred to the resists through exposure to an electron beam. The top and bottom layers are developed after the exposure in neat o-xylene and isopropanol (IPA) mixed with water, respectively. Their individual development times are adjusted so that the bottom layer develops more than the top layer, which effectively creates an undercut in the resist profile. After development is complete, the ebeam exposed regions of resist will reveal the underlying graphene. The entire sample is subjected to short oxygen plasma etching (ashing), laying bare the SiC substrate which will anchor the metal layers. Immediately after ashing, a thin adhesion layer of Ti followed by a thicker film of Au are evaporated over the entire chip. This is a physical vapor deposition (PVD) process in which the metals are evaporated by electron beam heating. Finally, the remaining resist along with the excess metal are removed using acetone in the lift-off process, which is greatly facilitated by the undercut in the resist profile.

Once the anchors are in place, the next metal layer will overlap the anchors and

connect to epigraphene itself. The second EBL step follows a similar procedure as the first one. The only difference is that oxygen plasma etching is omitted because the metal layer needs to connect to epigraphene, and not SiC. The metallic contact pads and leads are aligned to the anchors and graphene using the markers made in the first step. There are eight contacts in total for a typical graphene Hall bar, two reserved for source and drain, and the other six for voltage probes.

In the final EBL step the geometry of the epigraphene device (e.g. Hall bar) is defined. Before this point, the entire chip is still covered by epigraphene. In order ensure that the current takes a well-defined path within each individual device, and also to electrically isolate devices from each other, excess graphene is etched using oxygen plasma. This EBL step only requires one resist layer, and a simple PMMA resist mask can be used. Once again, the sample is exposed to the ebeam, developed using IPA mixed with water, and ultimately etched using oxygen plasma. The residual protective resist is dissolved using acetone. Immediately after fabrication, the epigraphene devices are encapsulated by a PMMA (or copolymer) layer in order to protect the graphene from unwanted exposure to dust particles, ambient dopants such as water, or other contaminants.

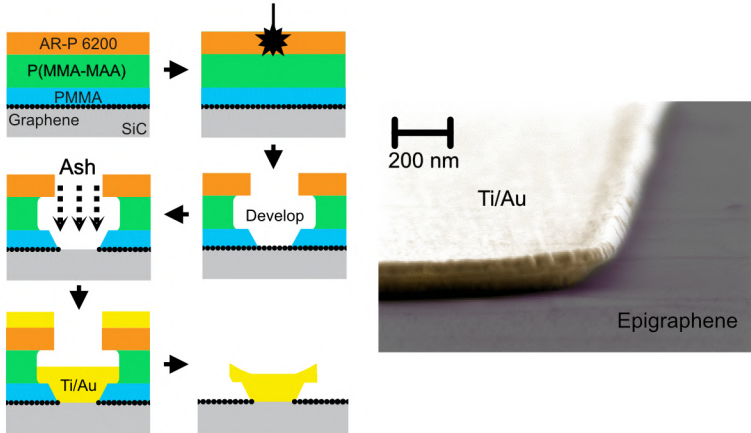


Figure 3.7: *Left:* Schematic representation of the lithography steps involved to fabricate pseudo-edge contacts to epigraphene. It mimics the regular EBL steps used to make anchor contacts, with the exception that three resist layers are used instead. The consequence is that the anchor metal forms an electrical contact to the edges of graphene. *Right:* False-color SEM image taken at an angle, showing the corner of a contact pad and the profile of the psuedo-edge contact.

As mentioned, metals do not adhere well to bare graphene. In fact, the strong sp^2 lattice of graphene tend to not form covalent bonds to any contact material. A normal contact placed on top of graphene will be bonded by van der Waals forces, which presents another barrier which injected electrons must overcome, thereby increasing the contact resistance

[58]. High contact resistance is rarely desirable because it induces additional heating and noise into measurements. State-of-the-art electrical contacts, with the lowest contact resistance, have circumvented this problem by fabricating one-dimensional contacts, or edge contacts, which only touch graphene at its sides [59]. This is commonly achieved in mechanically exfoliated graphene flakes encapsulated by hexagonal boron nitride (hBN). However, this process requires manual assembly of flakes and it is not suitable for real-world applications.

The idea of edge contacts is sound, but the process has to be altered for epigraphene, which is aiming for practical applications. The basic idea of edge contacts is to protect graphene, etch the sides and expose an edge of graphene, and finally deposit metal on the side edges. Instead of using tiny flakes of hBN ($\approx 10\mu m$), simple EBL resist can fulfill a similar role. This modified process is inspired by lithography of T-gate structures, which are electrostatic gates with narrow channel width, where three layers of resist are used in tandem to create a unique undercut profile. In order to lithographically create pseudo-edge contacts, a simple alteration of the anchor contact EBL recipe presented above is made. Figure 3.7 shows that a third layer consisting of PMMA is added below the two usual layers. The copolymer develops faster than the bottom PMMA layer, which creates an undercut in the middle layer and a protruding bottom layer. The ashing step removes graphene as usual, but the etched bottom PMMA layer leaves a protruding edge of graphene. When metal is evaporated on this structure, it drapes the edges of the bottom PMMA layer, coming into contact with graphene. The middle undercut is crucial because it makes sure that lift-off is still possible. The final result is a metallic pad with flared edges (see SEM picture), but still in electrical contact with graphene. This type of contact is useful not only because it eliminates one EBL lithography step, but it is observed that the resulting contact resistance are lower and more reproducible in general. One drawback is that the flared edges of the contacts can be problematic for closely-spaced structures, where they can cause shorts. This can be overcome with careful tuning of the recipe and development times. The development of this technique resulted in **Patent I**.

3.3 Molecular Doping Method

Exerting control over carrier density in epigraphene is one of the main challenges in the epigraphene research field. The solution found in this thesis to this long standing problem is to use a molecular doping method based on acceptor molecules F4TCNQ mixed with a polymer PMMA. This section will present how to prepare the dopant blend and how it can be used to dope epigraphene.

3.3.1 F4TCNQ Dopant Blend

The carrier density of epigraphene can be tuned from high n-doping to p-doping using strong acceptor molecules F4TCNQ mixed with PMMA, forming a dopant blend. This dopant blend can then be simply spin-coated onto the chip, or even large wafers.

The first step requires preparation of the dopant blend itself. Exact recipes, such as a mixing ratios, can be found in Appendix A.4. A dry powder of F4TCNQ molecules

is dissolved in anisole solvent, and the resulting solution is then mixed with PMMA resist, whose solvent is also anisole. The standard dopant blend used throughout this thesis consists of 7 wt.% F4TCNQ molecules in PMMA. Before the dopant blend is applied to epigraphene, a polymer layer of neat PMMA or copolymer PMMA is first deposited using spin-coating. This layer acts like a spacer layer and affects the diffusion of F4TCNQ dopants, and the doping recipe has been optimized with this spacer layer in mind. The dopant blend is then spin-coated directly onto the spacer layer. Lastly, and most importantly, the resist is annealed at elevated temperatures above the glass transition temperature of PMMA, around 160 °C. This step is common for EBL process to remove residual solvents from the resist. However, the main purpose here is to use the annealing process to tune the final carrier density of doped epigraphene. It is observed that thermal annealing at these temperatures irreversibly reduces the doping effect of F4TCNQ molecules, causing epigraphene to be more n-doped with increasing annealing time. In fact, using the standard dopant blend, samples can be either p-doped or n-doped depending on annealing time. For samples covered by a spacer layer and dopant layer on top, the optimal annealing time required to achieve charge neutral graphene is around 5 min.

For additional doping stability more polymer layers can be added. Typically five alternating layers like PMMA-dopant-PMMA-dopant-PMMA are used. Annealing is performed for 5 min at 160 °C after each polymer layer. In order to reach charge neutrality an additional 10-15 min of annealing is required.

3.3.2 Electrostatic Gating

For more advanced measurements which require tunable carrier density in real-time, an electrostatic top-gate can be deposited directly on top of the polymer layers. This process requires additional layers of spacer PMMA and dopant blend in order to preserve the carrier density level of the underlying epigraphene. In general, a total five layers are used, as described above. Caution is taken not to affect the dopants by wet chemistry by forgoing EBL, and instead using a shadow mask to evaporate the gate electrodes. The mask can be patterned using EBL and the Bosch etching process to create through-holes in a thin Si wafer. After deposition of the metal gate, the carrier density usually increases towards n-type by $\Delta n > 1 \times 10^{11} \text{ cm}^{-2}$ due to the strong attractive effects metals have on F4TCNQ (See Chapter 4.3).

An alternative to shadow mask deposition is to directly pattern a top-gate structure. This is desirable because it allows for greater flexibility in device design and reduces fabrication time. However, EBL cannot be used because the the dopant blend relies on ebeam sensitive resist. Photolithography is normally poorly suited for fabrication of epigraphene devices, since the residual resists disturb the homogeneity of the doping method (no such effect observed for PMMA-based residuals). However, once the sample is covered by PMMA polymers, photolithography can be performed on top to fabricate a top-gate, as shown in Figure 3.8. Photolithography is used because the chemicals involved adequately preserve the integrity of PMMA and the F4TCNQ dopants.

The first step involves deposition of the gate electrode layer. Initially, a thin layer of Al (40 nm) is used to cover the entire surface. It is evaporated using resistive evaporation,

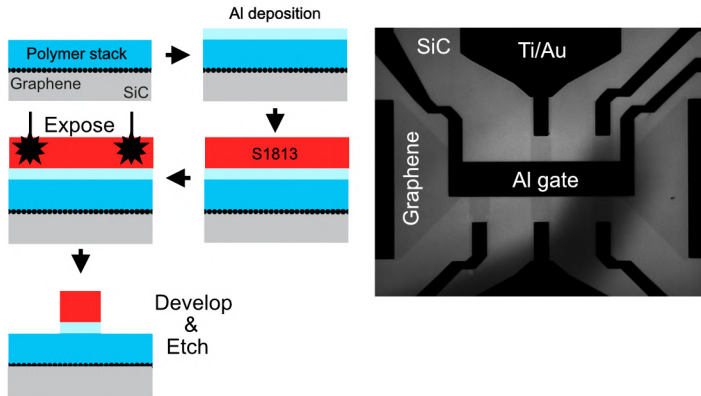


Figure 3.8: *Left:* Schematic representation of the photolithography steps involved in fabricating a top-gate on epigraphene. *Right:* Optical micrograph (transmission mode) of a top-gated epigraphene Hall bar.

since radiation from ebeam evaporation can weaken the polymer resist (PMMA is UV sensitive). A layer of positive photoresist (S1813) is then spin-coated directly on top of the Al, and a pattern is exposed using a direct-write laser system. The developer is MF-319, based on tetramethylammonium hydroxide (TMAH), which both removes the exposed resist and etches the underlying Al. While PMMA is resistant to short-term exposure to the developer, lengthy development times should be avoided. The sample is ready after the exposed Al has been removed, and the remaining S1813 resist is left on top of the gate electrodes for additional protection. This process also causes an increase of carrier density towards n-type by $\Delta n > 1 \times 10^{11} \text{ cm}^{-2}$ of doped devices.

3.4 Electrical Characterization

Electrical Characterization of epigraphene devices is the fundamental experimental technique in this thesis. This section explores different DC characterization techniques used to test the quality of grown epigraphene, the characteristics of fabricated devices, and homogeneity of molecular doping. It ends with a brief introduction to precision measurements.

3.4.1 Magnetotransport

The primary electrical characterization tool is Hall and quantum Hall effect (QHE) measurements. These magnetotransport measurements are used to extract important information such as the carrier density and carrier mobility. In order to observe quantum

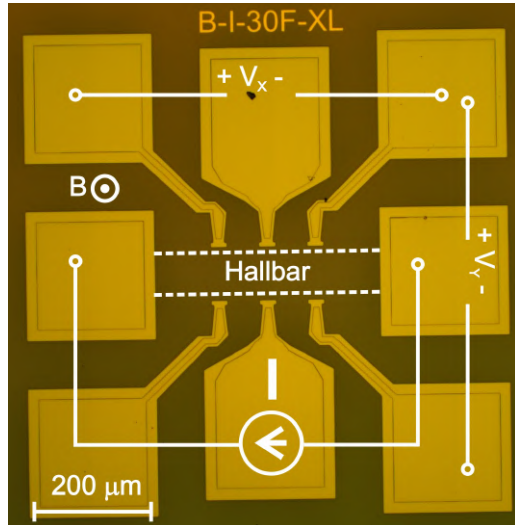


Figure 3.9: Optical micrograph of an epigraphene Hall bar device with eight Au contacts. This device is typically current biased and subjected to an out-of-plane perpendicular magnetic field B . The white overlays indicates the current direction with current I_X , the direction of magnetic field B , and where the longitudinal voltage V_X and transverse voltage V_Y are measured. The white dotted lines mark the boundaries of the epigraphene Hall bar.

transport phenomena, such as QHE, samples need to be cooled down to cryogenic temperatures and subjected to a perpendicular magnetic field. The cooling is achieved by inserting the sample into a helium gas-flow cryostat, in which liquid helium (${}^4\text{He}$) is used. By pumping on the helium in an enclosed sample volume, the temperature can be brought down to slightly below $T = 2\text{ K}$. The sample temperature is commonly monitored using a diode thermometer mounted next to the sample. The cryostat is equipped with a superconducting magnet which is capable of high magnetic fields from 9 T (Blue Oxford) or 14 T (Quantum Design PPMS).

The standard procedure for Hall measurements is to current bias the sample and measure voltage in four-probe configuration (Keithley 6221 DC and AC current source, Agilent 34420A nanovoltmeter). The appropriate current level depends on the doping level of epigraphene. The bias current is typically in the range of 100 nA for lowly doped samples, which prevents overheating and stays below the critical current limit of QHE. For higher doped samples, the current can be one or two orders of magnitude higher. The important consideration is that the current-voltage (IV) characteristics remain linear in the chosen current range, from room temperature down to cryogenic temperatures. Hall measurements can be performed at any temperature by applying a low magnetic field $|B| < 1\text{ T}$, and measuring the transverse Hall resistance R_{XY} . Assuming that R_{XY} is linear with field, the Hall coefficient can be extracted from a linear fit, after which the carrier density and carrier mobility can be determined. On the other hand, it is

only practically possible to observe the QHE at cryogenic temperatures. The maximum temperature depends on the available magnetic fields, and the carrier density level of epigraphene. QHE is typically measured at 2 K to be able to use as low magnetic fields as possible.

A fully quantized sample, meaning $R_{XX} = 0$ and $R_{XY} = h/2e^2$, indicates that the sample is of high electronic quality. All reported values of carrier mobility and carrier concentration in this work are extracted from four-probe Hall and quantum Hall measurements (single-band model), unless stated otherwise. Note that once the doping levels approach the Dirac point, the Hall voltage is no longer linear with magnetic field and this indicates that the sample has entered the charge-puddle regime, which is dominated by charge disorder. The data points inside this regime are intentionally omitted from carrier density and mobility plots.

3.4.2 Contact Resistance

A low contact resistance is desirable in general, due to reduced heating and noise in the device. This is especially important for applications in metrology, where a QHR standard should have contact resistances below 10Ω , but ideally much lower, in order to not influence the accuracy of quantization [60]. A common and simple method to estimate the contact resistance is to measure the length dependence of resistance, and analyze the data using the transfer length/transmission line model [61]. This method is useful because it works under any measurement conditions, but it is generally not suitable for Hall bar geometries. Instead, Hall bars exploit the fact that $R_{XX} = 0$ in QHE regime and use the so-called three-probe measurement [60] to directly measure the contact resistance. For instance, to achieve three-probe configuration the current is sent between source and drain contacts S and D on a Hall bar. The voltage is then measured between S-A, where A is one intermediate voltage probe. In the quantum Hall state, the edge state which travels from S to D, passing by A, is an equipotential line, and thus all of the potential drop occurs due to the contact resistance of contact S alone. This connection scheme can be repeated for all contacts. However, one has to be careful with the field and current directions when choosing where to measure the voltage. In the example device given in Figure 3.10, assuming n-doping and an out-of-plane magnetic field point towards the reader, a three probe contact resistance measurement for contact 1 could be achieved by passing current between contacts 1-3, and measuring the voltage between contacts 1-2.

3.4.3 Van der Pauw Method

In some samples the epigraphene device geometry is poorly defined, and normal Hall bar measurements are not ideal. In those cases, van der Pauw (vdP) measurements can be used to determine carrier density and mobility instead [62]. The general idea is that by utilizing a combination of measurements using four contact pads in different configurations, the Hall coefficient and sheet resistance of a device with arbitrary geometry can be determined. This technique is useful when characterizing Hall sensors for instance. The ideal sample should be flat and of uniform thickness, much thinner than the device width and length. Furthermore, the sample should be free from holes, homogeneous,

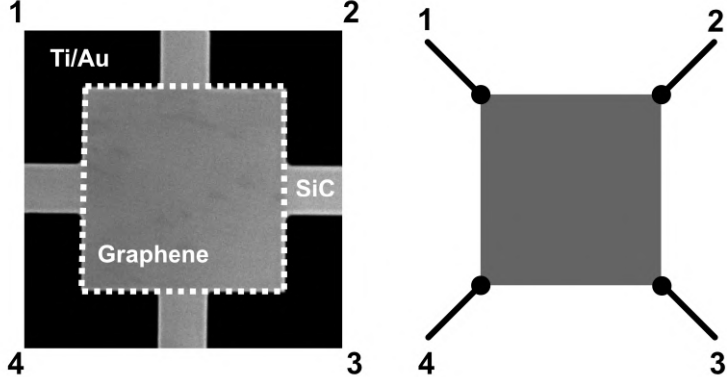


Figure 3.10: **Right:** Optical micrograph of an epigraphene device with van der Pauw geometry, including numbered contacts. The epigraphene area is marked by the dotted white line. **Left:** Schematic representation of a generic van der Pauw device with numbered contacts.

and isotropic. The electrical contacts should be ohmic, connected to the edges of the chip, and the contact area should be much smaller than the sample area. In practice, a real sample will deviate from this ideal situation, which leads to some inaccuracies in the vdP measurement. However, a well-designed uniformly doped epigraphene device does not deviate significantly from the ideal case. This can be tested by comparing the sheet resistance and carrier density calculated from vdP measurements with QHE measurements.

Figure 3.10 shows an example epigraphene device with vdP geometry, with contacts at the corners (pseudo-edge contacts to reduce contact area). Two resistances are needed for resistivity ρ measurements, one along a horizontal edge R_{hor} and one along a vertical edge R_{vert} . For example, if current is initially passed through the horizontal edge using contacts 1-2 and voltage is measured between 4-3, then the resistance is $R_{12,43} = V_{43}/I_{12}$. This is repeated for the polarity reversed case $R_{21,34}$ to remove offsets such as thermal voltages. Afterwards comes the reciprocal case $R_{43,12}$, before finally switching to the vertical edge and repeating the entire procedure. Eight measurements in total yield:

$$R_{hor} = \frac{R_{12,43} + R_{21,34} + R_{34,21} + R_{43,12}}{4} \quad (3.1)$$

$$R_{vert} = \frac{R_{14,23} + R_{41,32} + R_{32,41} + R_{23,14}}{4}$$

The sheet resistance ρ is then determined by solving the van der Pauw equation (typically numerically):

$$e^{-\frac{\pi R_{hor}}{\rho}} + e^{-\frac{\pi R_{vert}}{\rho}} = 1 \quad (3.2)$$

The Hall voltage is measured in a similar way by alternating between different configurations of contacts and switching the direction of the perpendicular magnetic field. The magnitude of the bias current and magnetic field is always fixed. One example vdP Hall measurement can be sending current between contacts 1-3, for a positive field $+B$, and measuring the voltage between 2-4, denoted as V_{2-4}^+ . This is again repeated with the polarity reversed, for the reciprocal case, and with reversed field. In total eight measurements yield the Hall voltage:

$$V_H = \frac{V_{2-4}^+ - V_{2-4}^- + V_{4-2}^+ - V_{4-2}^- + V_{1-3}^+ - V_{1-3}^- + V_{3-1}^+ - V_{3-1}^-}{8} \quad (3.3)$$

It is then straightforward to calculate the Hall coefficient $R_H = V_H/B$, the carrier density $n = 1/eR_H$, and carrier mobility $\mu = R_H/\rho$.

3.4.4 Electrostatic Gating

For measurements which require an electrostatic gate, the top-gate electrode is biased with voltages ranging from -100 to +200 V using a sourcemeter (Keithley 2400 series), which can monitor the current and voltage simultaneously. A $1\text{ M}\Omega$ resistor is placed in series with the gate connection, in order to prevent a current spike in the event of a dielectric breakdown. The gate voltage is stepped in small $< 10\text{ mV}$ steps per 200 ms in order to avoid capacitive current spikes.

The gate voltage is typically referenced to the sample drain contact, and a negative gate voltage therefore induces p-doping while a positive voltage induces n-doping. Very high voltages are necessary in practice due to the thick dielectric (polymer layers approach $1\text{ }\mu\text{m}$ thickness) and reduced gate efficiency owing to known substrate interactions. The measured gate leakage current is kept below $< 1\text{ nA}$, to ensure minimal effect on the current flowing through the device. It is observed that dielectric gate breakdown occurs earlier for negative gate voltages than positive, and this is attributed to an additional internal electric field due to charged F4TCNQ molecules.

3.4.5 Cryogenic Current Comparator

An eternal struggle in the art precision measurements is to decrease the measurement uncertainty. The pinnacle of this can be seen in quantum resistance metrology, where epigraphene QHR standards have provided measurements of the resistance quantum $h/2e^2$ with a precision of $0.086\text{ n}\Omega/\Omega$ (86 parts-per-trillion) [17]. This is no small feat, and it is made possible only by using the cryogenic current comparator (CCC) [63, 64]

The CCC is in essence a current comparator bridge which compares the value of two resistors. Figure 3.11 depicts a schematic of one type of CCC. The two resistors, called R_K and R_S , are compared by placing them in different current loops. In practice, R_S denotes a sample resistor which is to be calibrated against a QHR standard R_K , which has a fixed value of $h/2e^2$ (depending on the resistance plateau). The ratio between the coil windings N_p/N_s is adjusted to be as close as possible to the expected resistance ratio R_K/R_S . The goal is to ensure that the current flowing through both resistors is equal. When the current is balanced, the measured voltage ratio by the detector (nanovoltmeter)

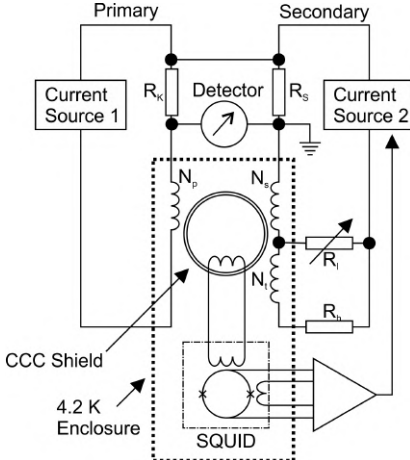


Figure 3.11: *Schematic representation of a CCC setup. The reference resistor R_K is usually a QHR standard, and it is used to calibrate another resistor R_s . The goal of the CCC is to ensure that the current flowing through both resistors is equal. When the circuit is balanced the voltage measured by the detector is exactly proportional to the resistance ratio. The ratio between coil windings N_p/N_s is set to be as close as possible to the expected resistance ratio R_K/R_s . The SQUID ensures that a precise balance is kept by measuring the net magnetic field in the superconducting CCC shield, induced by the current through the resistors. A feedback signal is sent to one of the current sources to change the current and null the magnetic field. An additional trim coil N_t , variable resistor R_l , and high resistance R_h are used to null the detector itself.*

is used in order to determine the resistance ratio. The wires which carry the current are passed through a superconducting tube which acts like a shield. Thanks to the Meissner effect, screening eddy currents form on the inside surface of the tube and exactly cancel the induced magnetic field inside the superconductor. These screening currents flow across the surface of the shield, and to the outer surface and induce another magnetic field. This weak magnetic field is measured by a superconducting quantum interference device (SQUID), which has the ultimate sensitivity to magnetic flux. The field is fed to the SQUID via the assistance of a pick-up coil placed close to the shield. The output signal of the SQUID is then sent back to one of the current sources, which changes the current in order to zero the net magnetic field in the CCC shield. In other words, it accurately adjusts the current ratio between the two resistors to match the coil winding ratio. When the CCC bridge is exactly balanced, the voltage reading on the detector is exactly proportional to the resistance ratio. Furthermore, the detector itself is usually balanced with the use of a third compensating circuit containing a trim coil N_t , a variable resistor R_l , and a fixed resistor R_h with a high resistance value. When all of the pieces

are in place, the measured resistance ratio is [63]:

$$\frac{R_K}{R_S} = \frac{N_p}{N_s} \frac{1}{(1+d)} \frac{1}{(1+V_M/V)}$$

$$d = \frac{N_t}{N_s} \frac{R_l}{(R_l + R_h)} \quad (3.4)$$

Here V_M is the voltage measured by the detector, which should be close to zero, and V is the voltage drop across the resistors under investigation. For reference, when comparing the quantized resistance of epigraphene $h/2e^2 \approx 12.9064\ldots \text{k}\Omega$ against a 100Ω standard resistor, the coil windings are set to $N_p = 2065$ and $N_s = 16$, with ratio $N_p/N_s = 129.0625$. This is already very close to the nominal true ratio, but not accurate on the level of $\text{n}\Omega/\Omega$.

4 Molecular Doping

Epigraphene is in principle well-suited for electronic applications that require scalability, reproducibility, and high electronic quality. The nature of the epitaxial growth process produces a high quality monocrystalline epigraphene film across the entire insulating substrate [9, 10], which allows for direct fabrication of devices without disturbing the electronic and structural integrity of epigraphene [13]. However, the difficulty in tuning the charge carrier density n of epigraphene remains one of its major flaws [15]. Control over the carrier density is crucial because it is the key that unlocks the possibility to alter the properties of epigraphene, and to tailor them to different needs. Not only does it allow for fundamental studies of physics (e.g. near the Dirac point), but it also grants greater flexibility in potential applications. The usefulness of carrier density control, for instance via molecular doping, extends beyond graphene, as it is a pervasive technology in modern society, and the pillar upon which the semiconductor industry rests on. New doping methods which work for epigraphene may also have wide-reaching implications for other materials.

The study of carrier density control and doping of epigraphene was originally motivated by the fact that epigraphene devices play a role in one of the few real applications of graphene electronics. Starting from a decade ago, epigraphene has found a useful niche in the field of quantum resistance metrology [14, 19, 65, 66], which deals with the definition and precise measurement of the unit of resistance Ohm (Ω) using the QHE (see Chapter 2.3.3). The use of epigraphene as a QHR standard is an especially interesting application, because it truly utilizes the unique electrical properties of epigraphene in order to surpass previous technologies. Due to the characteristics of epigraphene specifically, the QHE can be observed at lower magnetic fields, higher temperatures, using higher bias currents, and with a more robust quantized resistance plateau [14, 18–20] compared to conventional 2DEGs like GaAs. In order to exploit these possibilities, the development of a portable and cryogen-free table-top version of an epigraphene QHR standard is already underway (**Paper A**, **Paper B**), with the goal of facilitating the dissemination of a primary resistance standard closer to the end-user, and thereby decreasing calibration uncertainties.

However, exerting control over the carrier density in epigraphene is a challenge, and this fact hinders practical implementations of epigraphene quantum Hall resistance standards (QHR), which places several requirements on the carrier density level [19]. Firstly, in order to operate under relaxed operating conditions (QHE at 4.2 K and below 5 T), the carrier density cannot be too high. Secondly, the carrier density needs to be tuned in order to optimize the critical current. Thirdly, the charge disorder should be low (i.e. homogeneous doping) to ensure an accurate quantization of resistance [21, 22]. Finally, for real-world applications the device carrier density should possess long-term stability, as this directly impacts the lifetime of epigraphene QHR standards. In literature there exist several reported doping techniques such as photo-chemical gating [67], corona discharge of ions [41], electrostatic gating [68], and direct molecular doping [69, 70]. However, none are able to meet all requirements since they either lack potency, stability, or tunability.

The approach to carrier density control used in this thesis was inspired by the previous uses of F4TCNQ molecular dopants directly deposited on graphene [69, 70]. This technique

resulted in potent doping, but suffered from degradation under ambient conditions. The key difference in this work is the addition of a PMMA polymer as a host matrix in order to stabilize the dopant molecules. As will be explored in the following sections, this combination results in the spontaneously accumulation of dopants on the surface of epigraphene. This changes the carrier density of epigraphene and leads to an air-stable, potent, tunable, and reliable doping scheme, with the ability to homogeneously dope epigraphene over large areas. This chapter covers the results presented in **Paper C** and **Patent II**.

4.1 Towards Charge Neutrality

Before moving on to molecular doping, this section presents initial gating attempts using hexagonal boron nitride (hBN) as a gate dielectric in order to demonstrate the practical difficulties in gating epigraphene. Thin flakes of hBN are widely used as both a substrate and encapsulation layer for state-of-the-art graphene devices [23, 59, 71]. In graphene research, thin flakes of hBN are commonly utilized as a powerful gate dielectric [72], capable of high dielectric strengths around 4 MV/cm [73], or in ideal cases even above 10 MV/cm [74]. To test this method on epigraphene, a chip was patterned into an array of metallic markers and epigraphene Hall bars using ebeam lithography. Mechanical exfoliation via tape was used to produce hBN flakes from hBN powder. The flakes were transferred to epigraphene using a dry PDMS stamping technique [75]. The hBN-encapsulated epigraphene device was then annealed in an argon atmosphere at 1150 °C to clean the interface. Since the flakes are spread randomly, optical microscopy was used to locate devices which were fully encapsulated by a hBN flake. Devices were patterned using ebeam lithography, including a top-gate for the Hall bar channel.

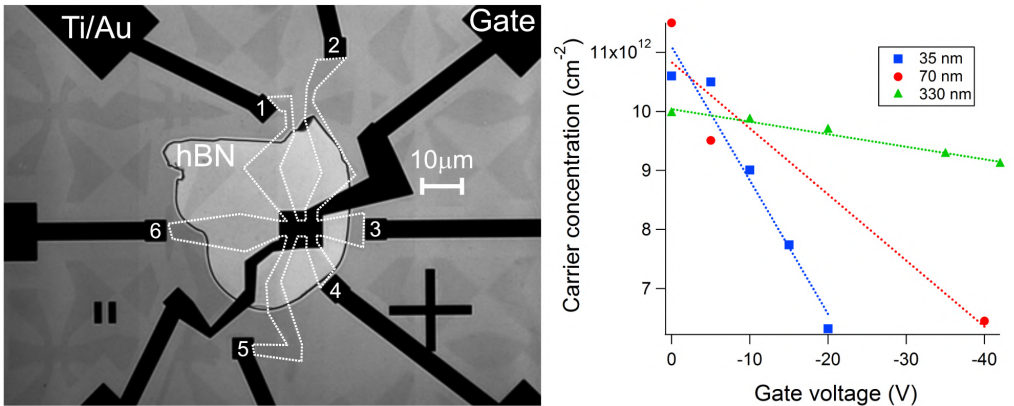


Figure 4.1: **Left:** Optical micrograph of a hBN-encapsulated epigraphene Hall bar device. The white dotted line outlines the epigraphene area under the hBN flake. There are six contacts (1-6) connected to the Hall bar, with one top-gate. **Right:** Carrier density versus gate voltage for devices with different hBN thickness, measured at 2 K. The gate voltage was limited by dielectric breakdown of hBN. The dotted lines are linear fits to data.

Figure 4.1 shows an example of a hBN-encapsulated epigraphene Hall bar. The thickness of the hBN flakes were investigated using AFM before fabrication of electrical contacts. The gating attempts demonstrate that even when pushing the limits of gate voltages to where dielectric breakdown of hBN occurs, the carrier density only changes from high n-doping $n \approx 10^{13} \text{ cm}^{-2}$ to $n \approx 6 \times 10^{12} \text{ cm}^{-2}$ at most. This limitation is not due to poor quality hBN, as the dielectric strength for 35 nm and 70 nm thick flakes are both around 5.7 MV/cm. Even the best hBN flakes would be hard pressed to withstand the electric fields required to pass through the Dirac point, especially since the effective gate capacitance is reduced even further near neutrality [76]. In the end, it appears that hBN is inadequate when it comes to carrier density tuning, and cannot be used to bring epigraphene close to charge neutrality. However, one benefit of hBN is that it preserves the intrinsic quality of epigraphene and protects it from external contamination and doping. For instance, these devices have a relatively high carrier mobility figure $> 2000 \text{ cm}^2/\text{Vs}$ at 2 K, despite the very high n-doping $n \approx 10^{13} \text{ cm}^{-2}$.

4.2 Molecular Doping Schemes

After exhausting other familiar options, the acceptor molecule F4TCNQ was explored as a novel solution to the problem of carrier density control in epigraphene. Different schemes were tested in order to explore the possibilities of F4TCNQ doping of epigraphene. Figure 4.2 shows three initially tested approaches to molecular doping, and their influence on the charge carrier density and mobility of epigraphene. The doped samples were all cooled down in a cryostat and the evolution of carrier density and mobility was monitored as the temperature decreased. The mixture of F4TCNQ acceptor molecules and PMMA polymer (henceforth referred to as dopant blend), combined with a PMMA (or copolymer PMMA) spacer layer, has a strong p-doping effect on epigraphene, capable of bringing the carrier density very close to the charge neutrality point ($n \approx 10^{10} \text{ cm}^{-2}$) at cryogenic temperatures of 2 K. The low doping level gives rise to a strong temperature dependence of carrier density due to thermal excitation above the Fermi energy, which at such low doping is only $E_F \approx 11 \text{ meV}$. The carrier mobility increases as temperature decreases, reaching a maximum value of $50\,000 \text{ cm}^2/\text{Vs}$ for this particular sample. The observed downturn in mobility at the lowest temperatures is due to the onset of quantum corrections to resistance, such as weak-localization and electron-electron interactions. As a reference, pristine epigraphene was prepared through hBN-encapsulation of epigraphene and it reveals that the intrinsic n-doping of epigraphene is on the order of $n \approx 10^{13} \text{ cm}^{-2}$. The decrease in carrier density due to F4TCNQ, compared to the pristine case, is three orders of magnitude. The surface coverage of F4TCNQ is then comparable to the estimates from literature values, with an estimated packing of 2-4 molecules per nm^2 , or equivalently a coverage of $2-4 \times 10^{14} \text{ cm}^{-2}$.

In the absence of the spacer PMMA layer, the dopant blend deposited directly on epigraphene acts only as a moderate p-dopant. It is also observed that neat PMMA itself acts as a weak p-dopant. The optimal doping which results in charge neutral epigraphene is achieved only in the case when the dopant layer and spacer PMMA layer operate in tandem, and only then was charge neutrality and high carrier mobility obtained.

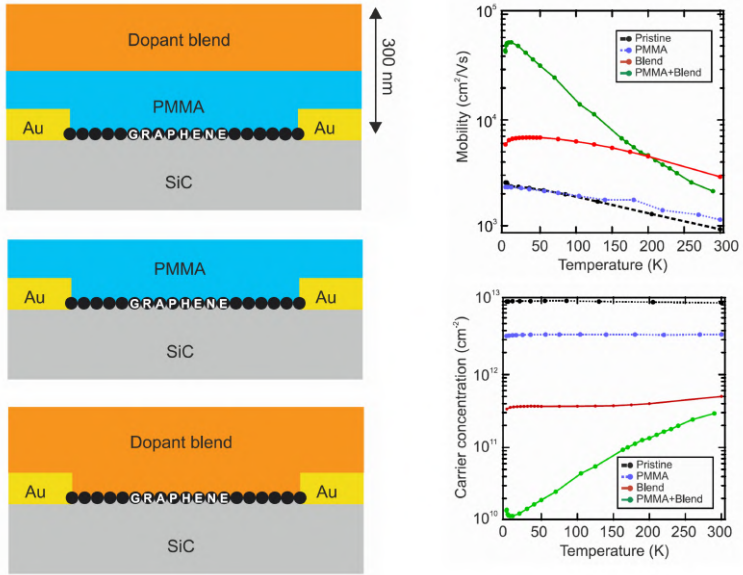


Figure 4.2: **Left:** Schematic representation of three variants of molecular doping schemes of epigraphene using polymer layers. The dopant blend consists of F4TCNQ molecules mixed with PMMA polymer. **Right:** Carrier density and mobility extracted from Hall measurements reveal that when the dopant blend and a PMMA spacer are used in combination, the carrier density of epigraphene decreases by three orders of magnitude compared to pristine epigraphene, reaching a low doping level of $n \approx 10^{10} \text{ cm}^{-2}$ at 2 K. The carrier mobility is very high, reaching 50 000 cm^2/Vs at cryogenic temperatures. The two other tested methods, using only PMMA and only dopant blend, act only as weak to moderate p-dopants.

The thickness of the spacer PMMA layer was varied between 100-400 nm without any appreciable change in doping effect. This suggests that there is a minimum spacer layer thickness needed to achieve charge neutral graphene. Therefore, the standard molecular doping technique used in this work utilizes the combination of PMMA spacer and dopant blend, described in Appendix A.4. Note that these findings are valid for the specific choice of dopant blend set by the ratio of F4TCNQ and PMMA, polymer thickness, annealing temperature, and annealing time described in the section 3.3. It is clear from brief tests that changing any of these parameters can result in widely different doping levels of epigraphene, and the interplay between different factors is not fully understood yet. For instance, thinning down the polymer layers results in lowered thermal stability of doping, and samples become much more n-doped after heating. This could in part explain the higher n-doping observed for the cases using only the dopant blend, compared to using both spacer and blend (effectively thicker layer). As will be clear in later sections, using multiple polymer layers results in samples with very stable carrier densities.

For Hall measurements performed at cryogenic temperatures, the simpler single band

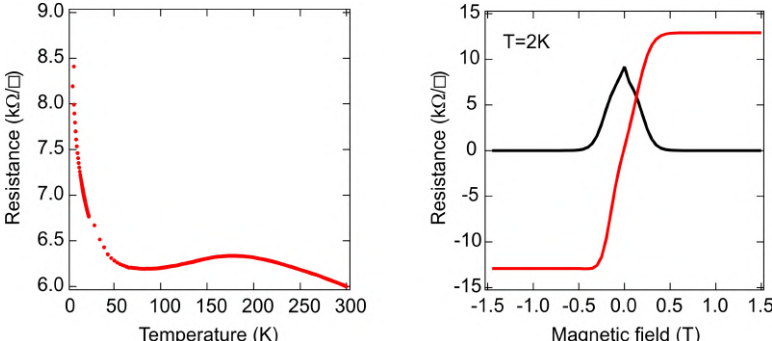


Figure 4.3: **Left:** Typical temperature dependence of ρ_{XX} , measured for epigraphene with a low carrier density. The initial increase of resistance as the temperature decreases from room temperature is due to the freezing of thermally excited carriers. After passing the hump around 175 K, the resistance decreases linearly as is expected for the suppression of phonon scattering in metals. At even lower temperatures, around 70 K, quantum corrections to resistance give rise to a logarithmic increase of resistance. **Right:** Quantum Hall measurements performed at 2 K. The red plot is ρ_{XY} and the black is ρ_{XX} . The sample shows well-developed QHE below 1.5 T, with $n \approx 1.5 \times 10^{10} \text{ cm}^{-2}$.

Hall model is sufficient to calculate the carrier density and mobility. Figure 4.3 shows the typical temperature dependence of ρ_{XX} for epigraphene with a low carrier density. From 300 K to around 175 K there is an unusual increase in resistance as the temperature drops, and this non-metallic behavior is due to the suppression of thermally excited carriers. In fact, the temperature at which the maximum of the hump in resistance occurs, around 175 K in this case, is closely related to the final doping level observed at cryogenic temperatures. At 175 K the thermal energy scale is $k_B T \approx 15 \text{ meV}$, and when this energy is well below the Fermi energy of graphene the thermal excitations can be considered suppressed. A Fermi energy of 15 meV corresponds to a carrier density of $n \approx 1.7 \times 10^{10} \text{ cm}^{-2}$ in epigraphene. The quantum Hall measurements performed at 2 K show that the charge carrier density is $n \approx 1.5 \times 10^{10} \text{ cm}^{-2}$, which is in excellent agreement with the above estimate. At temperatures below 175 K, normal metallic behavior dominates again, and the resistance decreases linearly with temperature due to suppression of scattering from acoustic phonons. At the Bloch-Gruneisen temperature of around 70 K quantum corrections such as weak-localization and electron-electron interactions become noticeable and lead to a logarithmic temperature dependence of resistance.

4.3 Spontaneous Assembly

In order to better understand the mechanism behind F4TCNQ doping of epigraphene, secondary-ion mass spectroscopy (SIMS) can be used to provide a chemical profile of the entire polymer stack, from the top surface all the way down to epigraphene, and even beyond into SiC. More specifically, this technique is called time-of-flight (ToF) SIMS. The

basic idea is that a primary ion beam sputters away material as it drills deeper down into a sample. The secondary ions ejected during this process are all accelerated to the same velocity by an externally applied electric field. Neglecting any small differences in the initial velocities, a detector measures their ToF and obtains information on their masses. The high mass-resolution of ToF-SIMS allows for the identification of which specific ions were ejected. Since SIMS is a surface sensitive technique, the analyzed particles are ejected only from the first few monolayers, and the measured ion intensity is ideally related to surface concentration of a particular species. In practice, finite surface roughness and varying sputter rates due to different binding energies and materials often lead to a broadening of signals.

The unique fingerprints of the F4TCNQ molecule are tracked during the measurements. Some signals of interest can for instance be fluorine ions (F^-) and cyano-group (CN^-) ions. Any signal from silicon (Si) ions indicates that the SiC substrate has been reached. To prevent excessive surface damage, a gentler pulsed primary ion beam (Bi^{3++} , 0.34 pA at 50 keV) is used during the ToF analysis. The more aggressive sputtering step is performed using a powerful $C60^{++}$ beam at 20 keV with a current of 0.2 nA. The measurement alternates between the two beams, with 1 second of analysis, followed by 1 seconds of sputtering, and finally 1 second of pause for each measurement cycle.

Figure 4.4 shows the SIMS data for a sample covered by a PMMA spacer layer, dopant blend layer, and an additional PMMA encapsulation layer. The SIMS measurement probed three distinct underlying regions: epigraphene surface, Au surface, and SiC surface. These aim was to provide a picture of the spatial distribution of F4TCNQ molecules, from the top of the PMMA surface down to each unique surface type.

The first measurement was taken on the polymer stack above the surface of epigraphene. The intense peaks in F^- and CN^- signals, which occur after 250 seconds of sputtering, coincide with the appearance of the Si signal. This signifies that there is spontaneous accumulation of F4TCNQ molecules near the surface of epigraphene. It appears that the molecules have diffused to the epigraphene surface from the original dopant blend layer. The full resist thickness is approximately 475 nm, and assuming that the sputtering rate is constant, then the full-width-at-half-maximum (FWHM) of the CN^- peak corresponds to a 10 nm thick accumulation layer. This is a rough estimate, since the spatial resolution of SIMS is limited due to inhomogeneous sputtering and surface roughness. The measured signal intensity can be taken as an approximation of the surface density, and the resulting surface density of F4TCNQ near epigraphene is over 50 % greater than inside the partially depleted dopant blend layer. The F^- and CN^- signals also reveal that molecules diffuse not only towards epigraphene, but also into the upper PMMA encapsulation layer. This is not surprising since F4TCNQ molecules are known to be mobile in polymers like PMMA, with their diffusion being dependent on material properties like polarity and glass transition temperature [77, 78]. After spin-coating of the dopant blend, the samples are typically baked for some time at 160 °C, which lies above the glass transition temperature of PMMA ($T_G \approx 100$ °C). The lowest heating temperature where permanent (but weak) doping change has been observed is 80 °C. The accumulation of molecules near graphene is attributed to the formation of a charge-transfer complex between the molecule and epigraphene. The F4TCNQ molecules remain neutrally charged inside the PMMA [79], but when they encounter a charge donor, like epigraphene, the formation of a charge-

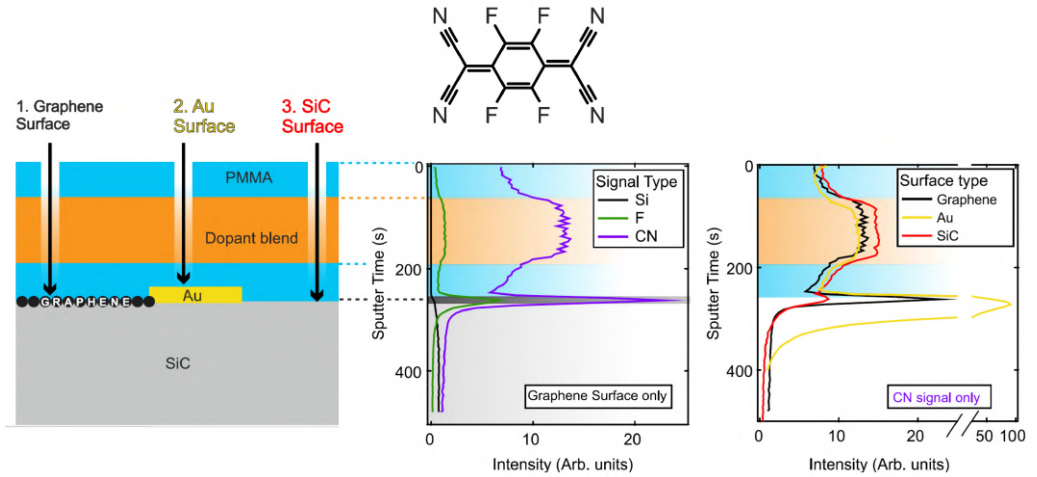


Figure 4.4: **Left:** Schematic representation of epigraphene prepared with a PMMA spacer layer, dopant blend layer, and a PMMA encapsulation layer. The arrows indicate three distinct regions probed using ToF-SIMS. **Center:** Data measured on the polymer layers above the surface of epigraphene. As the sputtering time increases, the measurement probes deeper into the polymer stack. The plot focuses on three signals: F and CN, which are fingerprints of F₄TCNQ (molecular structure shown on top), and Si which indicates when the SiC substrate has been reached. The sharp peaks in the F and C intensity signals indicate that there is a significant accumulation of F₄TCNQ molecules near the surface of graphene. The diffusion of molecules from the dopant blend layer also occurs towards the upper PMMA surface. **Right:** Focusing solely on the CN signal, there is a clear difference in the spatial distribution of F₄TCNQ molecules above the three distinct regions. Accumulation of F₄TCNQ molecules occurs only on conductive surfaces, such as epigraphene and Au, but not on the insulating SiC substrate.

transfer complex causes them to be bound and stabilized by the Coulomb interaction [80].

The same accumulation behavior can also be observed for the second measurement above the surface of Au. The CN signal is three times greater than for epigraphene, which points to a much stronger accumulation effect of molecules on Au, possibly due to differences in material characteristics such as carrier density and work function. The relative width and area of the accumulation peak compared to the dopant blend region is much larger, meaning that a large portion of the F₄TNCQ molecules have diffused from the dopant blend to the surface of Au and formed a thick accumulation layer.

The third and final measurement was a reference taken above bare insulating SiC, where epigraphene was removed using oxygen plasma ashing. The data shows a relatively tiny peak, which means that barely any accumulation of F₄TCNQ occurred on SiC. This result is consistent with the idea that the formation of a charge-transfer complex, between F₄TCNQ and a donor, is required in order to trap the molecules.

Since the intensity of the SIMS signal is related to surface density, the data in Figure

4.4 can therefore be used to provide another estimate for the surface coverage of F4TCNQ molecules. The sputter time can be approximately translated to distance, by comparing it to the nominal resist thickness of 475 nm, and assuming constant sputtering rate. By taking the area under the entire SIMS intensity curve, for example for the CN signal, the total amount of F4TCNQ molecules can be calculated (arbitrary intensity units per unit area). The same can be done for the area under the accumulation peak near epigraphene. From experimental data, the ratio between the two areas is around 15 %. This means that 15 % of the total amount of F4TCNQ molecules inside the dopant blend layer has reached the surface of graphene. What remains is to estimate the total amount of molecules in the original dopant blend. The mixing ratio between F4TCNQ and PMMA is known to be 7 wt.% F4TCNQ in PMMA, the density of F4TCNQ is $P_{F4TCNQ} = 1.4 \text{ g/cm}^3$, with molar mass $M_{F4TCNQ} = 276 \text{ g/mol}$. On the other hand PMMA has density $P_{PMMA} = 1.18 \text{ g/cm}^3$, and molar mass $M_{PMMA} = 950 \text{ g/mol}$. Assuming that the dopant layer consists of a slab of PMMA and F4TCNQ (7 mm x 7 mm x 175 nm), the total number of F4TCNQ molecules is 1.3×10^{15} . If 15 % of them reach epigraphene, the surface density of F4TCNQ is then $4 \times 10^{14} \text{ cm}^{-2}$ for a monolayer, or around 4 molecules per nm^2 . This is comparable to what was estimated from electrical transport measurements (2-4 molecules per nm^2).

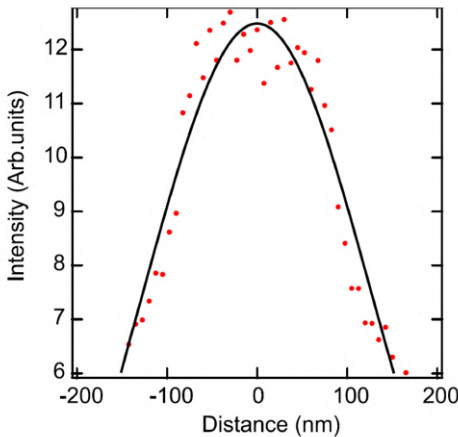


Figure 4.5: The red dots show the CN signal intensities extracted from SIMS. The x-axis is the distance, estimated from sputtering time and total polymer thickness. The intensity on the y-axis is related to the surface concentration at a certain distance. The maximum peak is centered in the middle of the 175 nm wide dopant layer. After 600 seconds of annealing at 160 °C, there are clear signs of diffusion of F4TCNQ from the dopant blend into the surrounding PMMA layers. The black solid line is a fit, modeling the surface concentration due to diffusion from an instantaneous extended source using Fick's law. The diffusion coefficient is estimated to be $D \approx 10^{-13} \text{ cm}^2/\text{s}$, in PMMA at 160 °C.

The diffusion coefficient of F4TCNQ through PMMA, at 160 °C can be estimated from the CN signal. This estimate assumes that the SIMS signal intensity is an accurate

representation of the relative surface concentration of F4TCNQ, and that sputter seconds corresponds well to distance. Applying Fick's laws of diffusion in order to model the diffusion from an instantaneous extended limited source (i.e. dopant blend) yields the following equation [81]:

$$\frac{c(x,t)}{C_0} = \frac{1}{2} \left(\operatorname{erf} \left(\frac{h-x}{2\sqrt{Dt}} \right) + \operatorname{erf} \left(\frac{h-x}{2\sqrt{Dt}} \right) \right) \quad (4.1)$$

Here $\operatorname{erf}(x)$ is the error function $\operatorname{erf}(x) = \frac{1}{\sqrt{\pi}} \int_{-x}^x e^{-t^2} dt$, $c(x,t)$ is the surface concentration at position x with the origin located in the center of the source, t time, C_0 the initial surface concentration, $2h$ is the width of the extended source, and D is the diffusion coefficient. Figure 4.5 shows data on the CN signal measured over the surface of epigraphene. For simplicity sake, the focus has been put on the dopant blend layer (limiting the x-axis), which includes the extended source, and its immediate surroundings limited to roughly halfway inside the top and bottom PMMA layer. By fitting Equation 4.1 using a 175 nm wide source and 600 seconds (5 min baking for dopant layer, 5 min for top PMMA layer) the diffusion coefficient was determined to be $D \approx 10^{-13} \text{ cm}^2/\text{s}$ (in PMMA at 160 °C). Note that this simple model assumes that the total number of F4TCNQ molecules remains constant in the region of interest, which is not true partly because of accumulation at graphene but also because of the possibility of molecules leaving the polymer entirely. For instance, neat F4TCNQ is known to sublime already at 80 °C [77], and while it may be more stable inside a polymer, extended annealing may reduce the total amount of F4TCNQ. Another erroneous assumption is that the source is instantaneous, while in reality the dopant blend was annealed without the top PMMA layer for the first 5 minutes.

Using the estimate for the diffusion coefficient, the flux of F4TCNQ molecules to the epigraphene surface is given by $j = D \frac{\Delta c}{\Delta d} = 1.4 \times 10^{-12} \text{ mol/cm}^2\text{s}$, where $\Delta c = 2.6 \times 10^{-4} \text{ mol/cm}^3$ is the initial concentration gradient and $\Delta d = 185 \text{ nm}$ the distance between the center of the source and epigraphene surface, of which 100 nm is PMMA spacer. This means that a concentration of $4.6 \times 10^{14} \text{ cm}^{-2}$ of F4TCNQ molecules can reach epigraphene within 600 seconds, which corresponds well with the experimental value obtained from samples with 600 seconds baking time. This provides only a rough estimate of the diffusion time scales because both the accumulation at the epigraphene surface, and the diffusion into the upper PMMA layer have been ignored.

4.4 Tuning Carrier Density via Annealing

One experimental observation is that the p-doping effects of F4TCNQ molecules appears more pronounced for shorter annealing times. This fact shows that the simple analysis in the previous chapter is flawed. Figure 4.6 presents the charge carrier density versus total annealing time at 160 °C for epigraphene covered by a PMMA spacer and dopant blend. At shorter annealing times the sample is in fact p-doped, and as the annealing time is successively increased the sample irreversibly becomes increasingly n-doped. From the ρ_{XX} versus carrier density data, a clear shape of the Dirac peak can be seen, and charge neutrality is reached after a total of 4 min of annealing. In the span of 12 minutes,

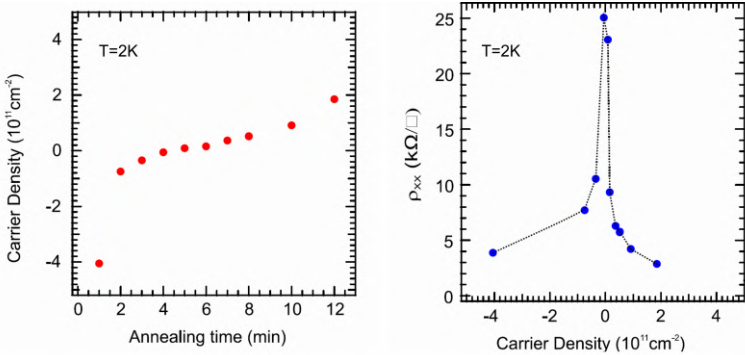


Figure 4.6: *Annealing of a epigraphene Hall bar sample prepared with PMMA spacer and dopant blend. The dopant blend has been annealed at 160°C in steps, starting from 1 min to a total of 12 min of accumulated annealing.* **Left:** Carrier density versus annealing time shows that epigraphene becomes more *n*-doped as the total annealing time increases. Charge neutrality is crossed after approximately 4 min of annealing. **Right:** Sheet resistance ρ_{xx} versus carrier density show the typical Dirac peak shape, where the maximum resistance is reached near charge neutrality, with a value close to h/e^2 .

the charge carrier density changes almost by $\Delta n \approx 10^{12} \text{ cm}^{-2}$, which is 10 % of the total doping strength of $\sim 10^{13} \text{ cm}^{-2}$. This therefore a relatively small change in doping. Note that the carrier density change slows down dramatically near charge neutrality, and this is related to the charge transfer between substrate and epigraphene [76]. The change in carrier density with annealing can be speculated the be due to the molecules changing conformation, which affects charge-transfer [82]. Molecules could also be leaving the epigraphene surface and diffusing away to metallic surfaces nearby (e.g. contacts), or even completely leaving the sample [77, 80]. Quantum Hall measurements were performed for each annealing time and the general trend is that quantization is not perfect at the extreme lower end of annealing times. Samples usually require a few minutes of annealing before they exhibit well-developed QHE at low doping levels. This is a hint that there is a time scale for F4TCNQ to rearrange near graphene and to provide homogeneous doping. It is also observed that in the extreme case of lengthy annealing for hours, the sample will return to a *n*-doping level similar to what is observed for pure PMMA on epigraphene (Figure 4.2), which means that the doping effect of molecules eventually disappear with annealing, possibly due to a complete removal of F4TCNQ dopants.

As mentioned briefly in Chapter 4.2, the diffusion of F4TCNQ molecules appear insensitive to thickness variations of the PMMA spacer layer between 100 – 400 nm. All samples showed similarly low doping levels after 5 min of annealing. This hints at that the initial diffusion of F4TCNQ is very fast and lead to high *p*-doping initially, which is then gradually changed towards *n*-type by subsequent annealing.

To test the limit of how thin the resist can be, a sample prepared with spacer PMMA layer and dopant blend, annealed for 5 min, was ashed using oxygen plasma. The ashing removed the residual partially depleted dopant layer and thinned down the PMMA spacer, with the final thickness being only 50 nm. Note that the doping effect of epigraphene was

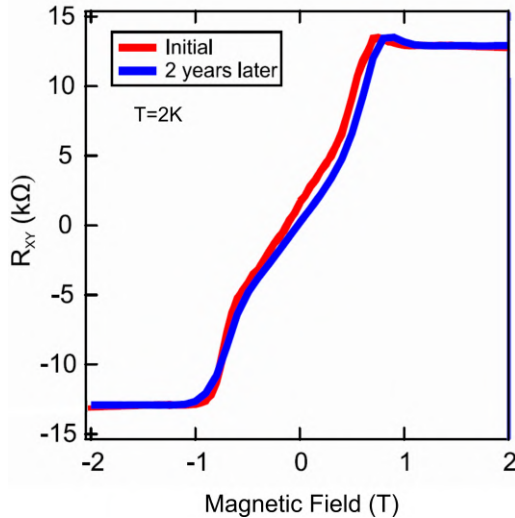


Figure 4.7: Long-term stability investigation of a doped epigraphene Hall bar measured approximately two years apart. For additional protection the sample was covered with extra polymer layers, with a final structure of PMMA-Dopant-PMMA-Dopant-PMMA. This sample was kept primarily at ambient conditions inside a simple nitrogen ventilated box, taken out only for measurements. During a two-year period the carrier density changed from $n = 5.3 \times 10^{10} \text{ cm}^{-2}$ to $n = 6.2 \times 10^{10} \text{ cm}^{-2}$.

overall preserved, owing to the still intact accumulation layer of F4TCNQ near epigraphene. In fact, the samples treated this way become slightly more p-doped. This could be due to increased sensitivity to ambient dopants, which normally p-dope epigraphene. With this extremely thin resist layer, the increase of n-doping with annealing time is also greatly sped up. After only 1 min of baking the carrier density changed on the order of $4 \times 10^{11} \text{ cm}^{-2}$ away from charge neutrality. This is an order of magnitude faster than what is observed in Figure 4.6. This is another clear sign that additional polymer thickness slows down the diffusion of F4TCNQ away from epigraphene.

While it appears that the initial process of accumulation of dopants is fast and relatively insensitive to polymer thickness, the subsequent doping change due to annealing is slower and strongly dependent on polymer thickness. From the experimental data, a plausible scenario could be that the initial doping process is very fast because there is a strong concentration gradient due to the dopant blend layer. As molecules diffuse and spread out, the concentration gradient decreases and the diffusion slows down overall. During continuous thermal annealing the dopants start to leave the polymer entirely, primarily from the top PMMA surface, and the resulting drop in concentration forms a gradient which pulls more dopants from the accumulation layer, leading to the loss of p-doping effect on epigraphene. This desorption process is naturally dependent on resist thickness, occurring faster for thinner resists. Note that this is all speculative, and the exact kinetics of F4TCNQ diffusion to and from the accumulation layer near epigraphene remains unexplored.

Since thermal annealing is required to activate diffusion, the doping effect can be significantly stable under ambient conditions. Additionally, as shown in Figure 4.6, multiple measurements performed on the same sample shows resilience to thermal cycling. Furthermore, a sample kept in a simple nitrogen closet at room temperature retained its low doping level for more than two years as demonstrated in Figure 4.7. The most stable samples were covered by five layers of polymers: PMMA-Dopant-PMMA-Dopant-PMMA. Over the course of two years the total doping strength degraded by $< 0.2\%$, because the increase in n-doping was $\Delta n < 2 \times 10^{10} \text{ cm}^{-2}$. However, even samples fabricated with just the standard PMMA spacer and dopant blend were found to be significantly stable, and kept their low doping level $n \approx 10^{10} \text{ cm}^{-2}$ for at least six months, with little sign of degradation.

The effect of ambient doping can definitely be felt for samples covered by only a standard PMMA spacer and dopant blend. Ambient doping can change the carrier density towards p-side faster than $\Delta n \approx 10^{11} \text{ cm}^{-2}$ per year. A controlled nitrogen environment (or equivalent) is therefore preferred for long-term storage. The effect of ambient doping on thicker polymer stacks PMMA-Dopant-PMMA-Dopant-PMMA remains untested, but it is likely significantly reduced. Since ambient doping changes carrier density towards p-type, but the doped samples drift towards more n-doping in nitrogen, the ideal environment could perhaps be a mixture of both nitrogen and air.

4.5 Macroscopic Homogeneity

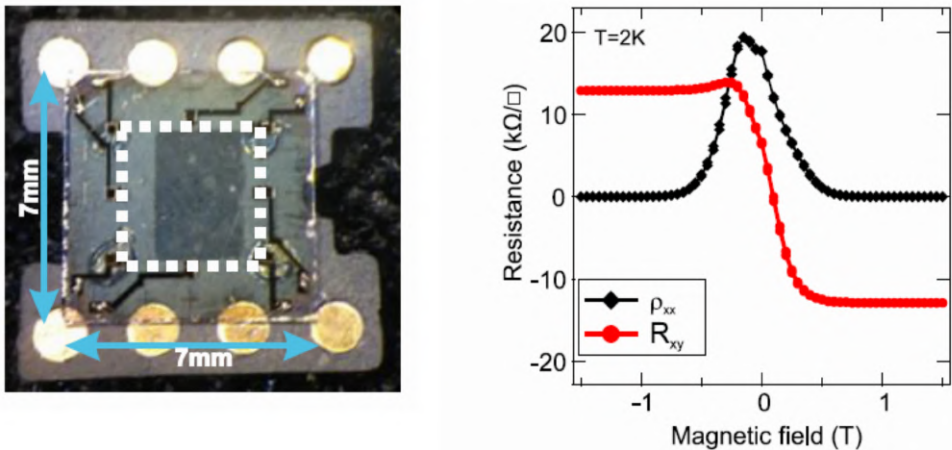


Figure 4.8: **Left:** Optical micrograph of a macroscopic epigraphene Hall bar device with dimensions $W = 5 \text{ mm} \times L = 5 \text{ mm}$. The white dotted line indicates extent of the epigraphene area, which connects to eight Au contact pads. **Left:** Magnetotransport measurement show that QHE occurs at 2 K and below 2 T. The charge carrier density is hole-type $p = 9 \times 10^9 \text{ cm}^{-2}$, and carrier mobility is $\mu = 39\,000 \text{ cm}^2/\text{Vs}$.

The measurements presented in Chapter 4.2 were performed on microscopic Hall bars with $W = 2 - 100 \mu\text{m} \times L = 10 - 300 \mu\text{m}$. In order to test the large area homogeneity of the molecular doping, macroscopic hall bars $W = 5 \text{ mm} \times L = 5 \text{ mm}$ were also investigated. Figure 4.8 shows quantum Hall measurements at 2 K on a macroscopic epigraphene Hall bar device covered by standard PMMA spacer and dopant blend. The linear low-field R_{XY} [22, 83–85] and the fully developed QHE below 2 T, with $\rho_{XX} = 0$ and $R_{XY} = h/2e^2$, indicate that the device acts like a system with a single band, and a spatially homogeneous carrier density distribution [21, 86]. The carrier density for this device is very low p-type, with $p = 9 \times 10^9 \text{ cm}^{-2}$ and mobility is $\mu = 39\,000 \text{ cm}^2/\text{Vs}$. The combination of low macroscopic charge disorder and high carrier mobility demonstrates that the F4TCNQ doping technique is promising for wafer-scale electronic applications. Note that the slight asymmetries visible in the data, especially around zero magnetic field for ρ_{XX} , can be attributed to the presence of steps in the SiC substrate, bilayer graphene inclusions, and other material defects. These effects can be mitigated for microscopic hall bars by careful placement of the device, but impossible to avoid for devices which span the entire chip.

The molecular doping method is not only useful for homogeneous doping of a single chip, but it is also reproducible across multiple devices. However, despite being doped using nominally the same annealing time and temperature, there can still exist a slight difference in the final carrier density between different devices (example in Chapter 4.2). Due to natural sample variations and ambient doping effects, samples doped in nominally the same way can be expected to differ in carrier density. However, the aspect which has the greatest impact on reproducibility is the freshness of the dopant blend, since a new mixture remains useful ~ 6 months before it becomes too degraded. Table 4.1 contains a collection of magnetotransport data on doped samples from various chips, with various device geometries. The final doping level of epigraphene devices, using a single PMMA spacer layer and dopant blend, baked at 160°C for 5 minutes, is on average $n_{avg} = 3 \times 10^{10} \pm 2.5 \times 10^{10} \text{ cm}^{-2}$. The variations in carrier density are typically lower for doped devices measured on the same chip.

Table 4.1: The table below shows the reproducibility of F4TCNQ doping. It lists a summary of carrier densities n and mobilities μ extracted from quantum Hall measurements performed on various devices doped in nominally the same way.

Dev. No.	Area (μm^2)	$ n $ (cm^{-2})	μ (cm^2/Vs)
1	30×180	8.10×10^9	5.10×10^4
2	30×180	9.60×10^9	4.50×10^4
3	30×180	8.90×10^9	4.90×10^4
4	18×90	9.10×10^9	4.50×10^4
5	18×90	6.00×10^9	8.20×10^4
6	18×90	6.50×10^9	7.60×10^4
7	36×144	9.60×10^9	6.30×10^4
8	36×144	8.60×10^9	5.80×10^4
9	36×144	9.10×10^9	5.50×10^4
10	5000×5000	9.10×10^{10}	6.70×10^4
11	10×10	5.50×10^{10}	3.80×10^4

Continued on next page

Table 4.1 – *Continued from previous page*

Dev. No.	Area (μm^2)	$ n (\text{cm}^{-2})$	$\mu(\text{cm}^2/\text{Vs})$
12	10×10	5.20×10^{10}	4.00×10^4
13	30×180	5.80×10^{10}	2.00×10^4
14	30×180	7.90×10^{10}	1.40×10^4
15	30×180	2.00×10^{10}	3.80×10^4
16	30×180	2.70×10^{10}	2.90×10^4
17	30×180	4.70×10^{10}	2.30×10^4
18	30×180	7.10×10^{10}	1.50×10^4
19	36×144	1.50×10^{10}	4.80×10^4
20	36×144	2.40×10^{10}	3.00×10^4
21	36×144	1.40×10^{10}	4.30×10^4
22	36×144	1.80×10^{10}	4.60×10^4
23	36×144	6.40×10^{10}	2.30×10^4
24	2×4	4.00×10^{10}	2.00×10^4
25	36×144	5.00×10^{10}	2.70×10^4
26	36×144	9.00×10^{10}	1.50×10^4
27	5000×5000	1.87×10^{10}	2.10×10^4
28	36×144	1.50×10^{10}	4.50×10^4
29	100×180	1.50×10^{10}	3.00×10^4
30	100×180	2.80×10^{10}	2.50×10^4
31	100×180	7.00×10^{10}	1.40×10^4
32	100×180	1.50×10^{10}	4.10×10^4

4.6 Microscopic Homogeneity

An electrostatic gate was deposited directly on the polymer stack in order to further study the electron transport properties of doped epigraphene. While the charge carrier density can be tuned using annealing during fabrication, it is much more convenient to use an electrostatic gate since it can be controlled in real-time. Furthermore, the gate also allows for fine-tuning of the carrier density close to the charge neutrality point. However, due to the reduced gate efficiency inherent to epigraphene, and the thick polymer dielectric, the gate can only change the carrier density on the order of $\Delta n = 10^{11} \text{ cm}^2$ before dielectric breakdown occurs. This is still sufficient to be able to bring the carrier density of epigraphene across the Dirac point, provided that epigraphene has already been doped close to neutrality by F4TCNQ. Gate experiments have been tested in the range of $V_G = -150 \text{ V}$ to $+200 \text{ V}$, and the polarity is such that negative V_G induces more p-doping and vice versa. Figure 4.9 shows the typical shape of ρ_{XX} as a function of applied gate voltage V_G . The resistance is maximal at the Dirac point, which in this case is reached at around $V_G = -40 \text{ V}$. The maximum allowed V_G before dielectric breakdown occurs is asymmetric around the Dirac point, and this is likely due to the presence of the induced electric field from F4TCNQ dopants effectively acting as additional applied negative gate

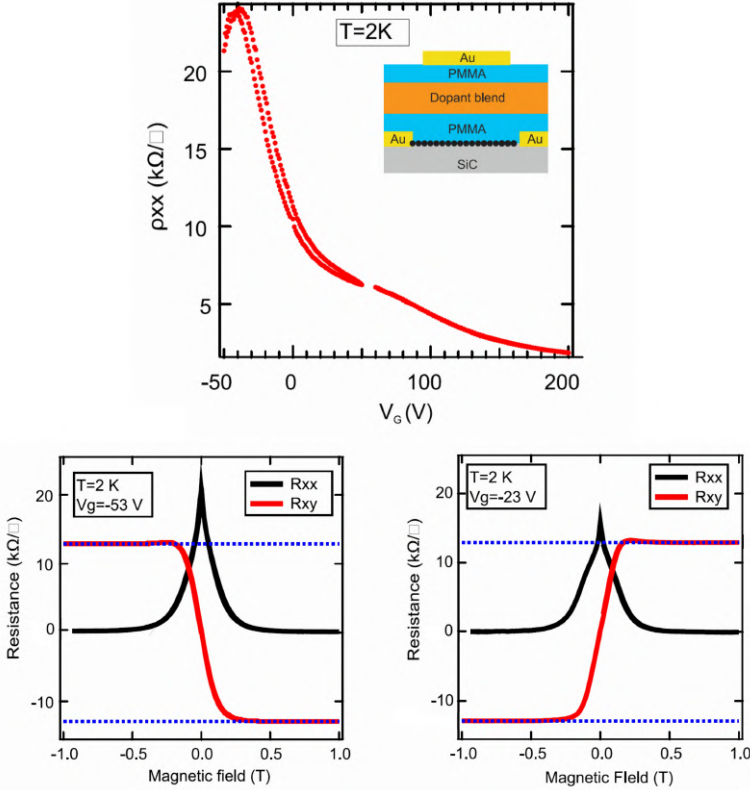


Figure 4.9: **Top:** The inset shows a schematic representation of the epigraphene device. The data shows zero-field ρ_{XX} as a function of applied gate voltage V_G at 2 K. The maximum resistance (Dirac point) is reached at $V_G = -40$ V. For each data point V_G , a full quantum Hall measurement was performed. **Bottom:** Fully developed QHE for low charge carrier densities near the Dirac point. The blue dotted lines mark the resistance quantum of $\pm h/2e^2$. At $V_G = -53$ V, the sample shows p-type behavior with $p = 5.6 \times 10^9 \text{ cm}^{-2}$ and mobility $\mu = 52\,000 \text{ cm}^2/\text{Vs}$. At $V_G = -23$ V, the sample shows n-type behavior with $n = 6.4 \times 10^9 \text{ cm}^{-2}$ and mobility $\mu = 61\,000 \text{ cm}^2/\text{Vs}$. The disordered charge puddle regime lies in between these gate voltages, and in that regime the single-band charge carrier density and mobility are poorly defined due to non-linear low-field R_{XY} and imperfect quantization.

voltage. A full quantum Hall measurement was performed for each step in V_G , in order to investigate the charge disorder. Figure 4.9 shows two examples of QHE measured very close to neutrality, one at $V_G = -53$ V which has p-type behavior with $p = 5.6 \times 10^9 \text{ cm}^{-2}$ and mobility $\mu = 52\,000 \text{ cm}^2/\text{Vs}$, and one at $V_G = -23$ V which has n-type behavior with $n = 6.4 \times 10^9 \text{ cm}^{-2}$ and mobility $\mu = 61\,000 \text{ cm}^2/\text{Vs}$. The QHE is well-developed in both of these cases, which means that the sample has yet to enter into the disordered charge

puddle regime, despite the low carrier densities. The QHE show signs of inhomogeneous charge distribution for carrier densities even closer to the Dirac point, where R_{XY} is no longer linear at low magnetic fields. There is also no R_{XY} resistance plateau at $h/2e^2$, and no vanishing ρ_{XX} at high magnetic fields. The single-band charge carrier density and mobility is therefore poorly defined in the puddle regime, and omitted from future plots.

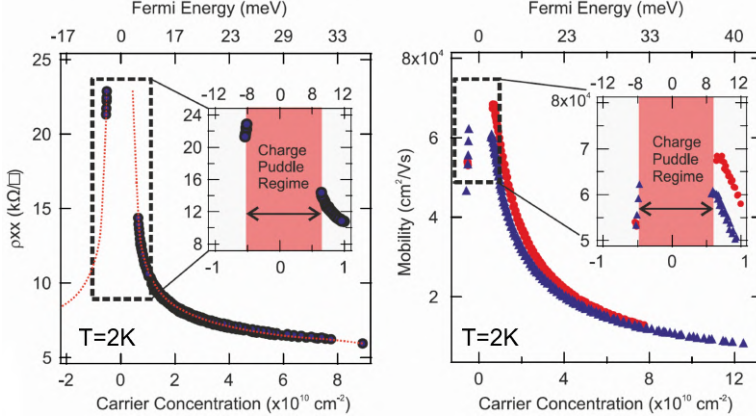


Figure 4.10: **Left:** Zero-field ρ_{XX} versus charge carrier density, extracted from QHE measurements performed at different gate voltages. The red dotted lines are a guide to the eye to highlight the shape of the Dirac cone. The omitted data points near neutrality mark the extent of the charge puddle region, which extends ± 9 meV around the Dirac point. **Right:** Two set of carrier mobility versus carrier density data, measured at two places on the same chip. The mobility approaches a value of $70\,000\,\text{cm}^2/\text{Vs}$ close to the Dirac point.

Figure 4.10 shows the extracted carrier density and mobility for the gate sweep in Figure 4.9. As mentioned, the missing data near neutrality marks the extent of the charge puddle region. The plot of resistivity versus carrier density reproduces the typical conical shape. The peak is very sharp, i.e. the charge puddle regime is narrow in terms of energy, which means that charge disorder is low. The minimum charge carrier densities which still has well-developed QHE marks the boundaries of the charge puddle regime, and the strength of charge puddle fluctuations is related to the puddle width of $\approx \pm 9$ meV. At the lowest doping level the maximum carrier mobility approaches a value of $70\,000\,\text{cm}^2/\text{Vs}$.

The two-band model of disorder-induced temperature dependent transport (see Chapter 2.3.2) is used to provide another way to estimate the charge disorder strength [31, 44]. It is achieved by studying Hall measurements at varying temperatures, and fitting the temperature dependence of effective charge carrier density using Equation 2.25. The fit yields the disorder strength s , which is a parameter that corresponds to the average strength of spatially distributed charge disorder, i.e. charge puddles. Figure 4.11 shows an example of fitted measurement data, which displays good agreement between theory and experiment. Four different samples were investigated this way, and the average disorder strength is calculated to be $s = 7.7 \pm 1.2$ meV, with an error of two standard deviations. This is in excellent agreement with the electrostatic gating experiments, in which the

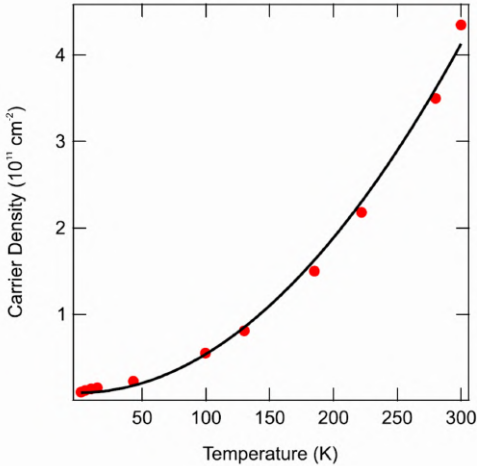


Figure 4.11: The data (red dots) shows the temperature dependence of effective carrier density n_e . A fit to the two-band model of disorder-induced temperature dependent transport (black line) is made in order to extract the disorder strength s . The average result of fits to four different measurement sets is $s = 7.7 \pm 1.2$ meV, where the error denotes two standard deviations. The same fit also yields the carrier mobility ratio $u_e/u_h = 1.5$, with electrons having 50 % higher carrier mobility compared to holes.

puddle strength is estimated to be ~ 9 meV. The two-band model also provides a mobility ratio between electron and holes, which show that electrons have $\sim 50\%$ higher carrier mobility. This explains the observed asymmetry seen in Figure 4.10, where electrons have a higher mobility compared to holes at a given carrier density.

The flexibility of an electrostatic gate allows for the investigation of temperature dependence of resistivity very close to charge neutrality. Figure 4.12 shows a comparison measurement between a non-gated device versus a gated one, plotted in logarithmic temperature scale. The non-gated device shows similar non-monotonous behavior similar to Figure 4.3, but with the difference that this particular sample has higher n-doping which makes the initial resistance hump, due to carrier excitations, occur at higher temperatures of around 300 K. The quantum corrections to resistance are also less pronounced. For the gated sample, the resistivity shows a simple monotonous increase as temperature decreases, similar to disorder activated transport (variable range hopping etc.). This is a signature of very low doping levels, and corresponding Hall measurements confirmed that the sample was indeed in the disordered charge puddle regime. The temperature dependence of resistivity in this regime is approximately logarithmic at low temperatures, a feature which is exploited in later chapters on THz detection.

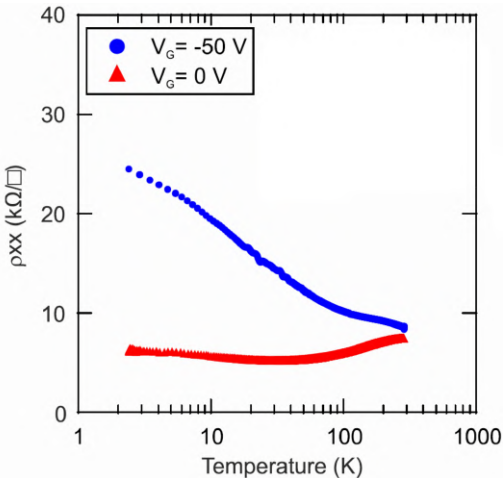


Figure 4.12: Temperature dependence of zero-field resistivity ρ_{XX} measured for two different samples, with and without an applied gate voltage. The gate voltage is applied starting from 300 K and kept constant down to 2 K. At high applied gate voltages the sample is lowly doped and in the charge puddle regime, where the resistivity increases monotonously with temperature. Without a gate voltage, the temperature dependence has the normal non-monotonic behavior for highly doped epigraphene. See also Figure 4.3.

4.7 Grazing-incidence Wide-angle X-ray Scattering

Grazing-incidence wide-angle x-ray scattering (GIWAXs) is a useful technique to investigate the structure of the F4TCNQ molecules inside the PMMA matrix. Similar to traditional x-ray diffraction, this technique relies on Bragg's law of reflection to determine the spacing between atomic planes. The grazing-incidence part refers to the shallow incident angle of the beam, which is suitable for probing thin films due to the efficient surface reflection. The wide-angle part refers to the detection of wide-angle scattered intensity, which corresponds to a large momentum transfer in the reciprocal space, and thus small distances in real space. This technique is commonly used to analyze samples which have length-scales on the order of nanometers. Reflected signals are weak for thin films because the beam passes through only a small amount of material, as opposed to bulk samples. The measurements are therefore performed using a powerful synchrotron source. The GIWAXs data in this thesis were obtained at the D1-beam line at the Cornell High Energy Synchrotron Source (CHESS) at Cornell University.

Epigraphene was doped using the standard recipe of spacer PMMA layer and dopant blend. The samples were investigated using GIWAXs at room temperature and under ambient conditions. Figure 4.13 shows the 2D spectra collected at 0.15° incident beam angle. Incident angles between 0.1°-0.25° were also tested but no significant change in features were observed. Starting from 0.125° angle, the attenuation length of the x-ray beam (0.1162 nm wavelength) in PMMA is already 500 nm. This means that the distance at which beam intensity drops to 1/e of the original intensity is long enough to penetrate

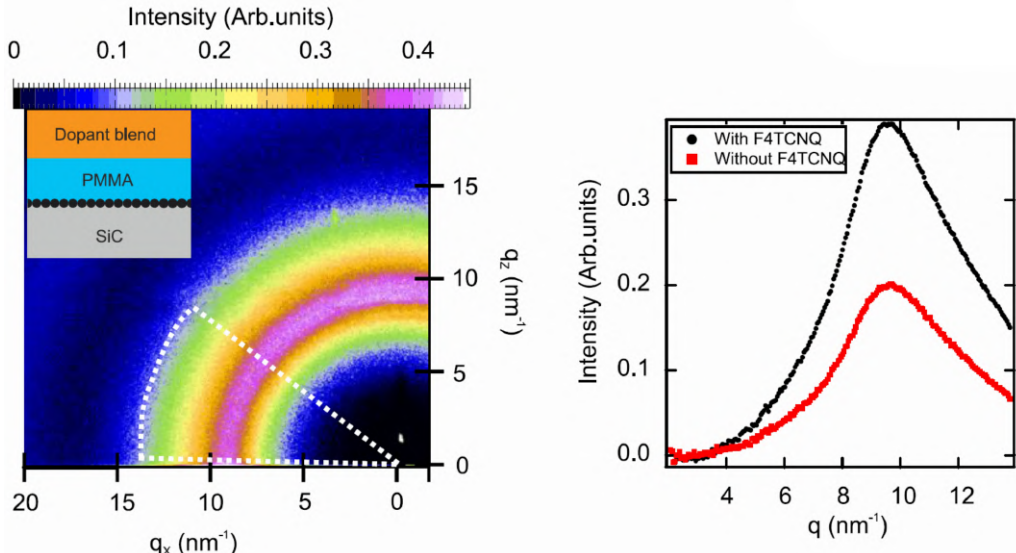


Figure 4.13: **Left:** 2D plot of GIWAXs intensity measured at room temperature and ambient conditions. The inset shows a schematic of the investigated epigraphene sample, doped using PMMA spacer and dopant blend. The incident beam angle was 0.15 degrees. A diffuse background has been subtracted from the raw data. There is a clear halo of peak intensity with radius $q = 9.6 \text{ nm}^{-1}$. The white dotted line indicates a region where the data was integrated over azimuthal angles to produce an intensity profile. **Right:** Intensity profile shows a broad diffraction peak at $q = 9.6 \text{ nm}^{-1}$ for doped epigraphene. The red curve shows a reference measurement taken on a sample prepared using only neat PMMA. The intensity peak is present even in the reference sample, which means that it originates from PMMA itself. However, the addition of F4TCNQ appears to enhance the signal twofold.

the entire polymer stack. Note that since long exposures to high intensity radiation bleach the resist surface, the samples were usually not exposed for more than 20 seconds. After subtracting the background signal due to diffuse scattering, the only remaining feature is a broad amorphous intensity halo with a diffraction peak centered at $q = 9.6 \text{ nm}^{-1}$. The origin of this peak appears to be from PMMA itself, as verified by a reference measurement using a sample with only PMMA (PMMA spacer with neat PMMA on top). The addition of F4TCNQ molecules enhances the signal by a factor of two, but creates no additional diffraction spots.

The enhancement of the original PMMA signal due to F4TCNQ molecules implies that the dopant either stabilizes the polymer backbone, follows the packing of PMMA itself, or possibly both. The characteristic length-scale of the mixed PMMA-F4TCNQ system is $2\pi/q = 6.6 \text{ \AA}$. Assuming that F4TCNQ obeys this packing even down to the accumulation layer near epigraphene, the surface coverage is then 2-3 F4TCNQ molecules per nm^2 , which corresponds surprisingly well to estimates from both SIMS

and electrical transport of 2-4 molecules per nm². At these high packing densities, the conformation of molecules is likely non-planar due to their size, and they stand up on the surface of epigraphene [69].

The absence of distinct diffraction spots in GIWAXs intensity suggests that F4TCNQ molecules are well-dispersed in the PMMA matrix, and do not form significant crystal aggregates. The size of potential crystallites can be estimated using Scherrer analysis. The Scherrer equation states that $\tau_c = \frac{\kappa\lambda}{\beta\cos\theta}$, where τ_c is the mean size of crystal domains, κ a dimensionless shape factor (for spherical particle = 0.9), λ the x-ray wavelength, θ the Bragg angle, and β the FWHM of the diffraction peak. The resulting average coherence length of F4TCNQ crystallites is $\tau_c \approx 2 - 3$ nm, which is only a few molecules in size.

The charge homogeneity of F4TCNQ doped epigraphene is clearly excellent as evidenced by magnetotransport data, and one might except that this charge order is related to crystalline order of F4TCNQ. However, the GIWAXs measurements reveal that there is no long range crystalline order, at least at room temperature. Due to the thick polymer stack, it is also likely that any interesting signal from the buried accumulation layer near epigraphene could be drowned out by the strong signal from the bulk dopant blend layer. Additionally, the signal could also be smeared out by thermal fluctuations. Future GIWAXs measurements would need to be performed at cryogenic temperatures to mimic the conditions of QHE measurements where excellent charge order is observed. Ideally, the samples should also make use of thinned-down polymer layers.

Naively, the presence of adsorbates on graphene should normally decrease the electronic quality due to increased scattering, and is actively avoided in the case for encapsulated graphene. However, the presence of certain molecules can actually enhance carrier mobility [87]. There are in principle other physical mechanisms which can explain the high charge order in molecular doped epigraphene, without requiring crystalline order of F4TCNQ itself. For instance, the combination of low carrier density and increasing impurity density, achieved through the addition of densely packed F4TCNQ molecules, can actually suppress charge scattering in epigraphene if there is enough spatial correlation between impurities [88, 89]. This is plausible in the case of F4TCNQ-PMMA, because the GIWAXs measurements points to the possibility of PMMA acting as a template for the packing of F4TCNQ, with a characteristic length scale of 6.6 Å. Another contributing phenomena which can create low charge disorder, is thermally induced redistribution of charges in the dopant accumulating layer, which when subjected to external electric field can potentially screen charge inhomogeneity in doped epigraphene [90]. Indeed, the next section will reveal that F4TCNQ molecules remain mobile in PMMA even below room temperature.

4.8 Redistribution of Dopants

In order to investigate the movement and redistribution of F4TCNQ molecules throughout the PMMA matrix, a positive gate voltage was applied to a doped sample starting from room temperature and kept on all the way down to 2 K, mimicking the measurement in Figure 4.12. The effect of a positive V_G is an increase in the n-doping level, which leads to a decrease in the resistance. Once the sample was cooled down to 2 K, the gate was abruptly turned off and consequently there was an immediate increase in resistance.

However, it appears that some F4TCNQ molecules were frozen in place at cryogenic temperatures, effectively retaining some of the initial external electrical field, because the resistance did return fully to its true non-gated value. Figure 4.14 shows an example of the temperature dependence of resistance immediately after the gate has been turned off. The resistance value started at point A and 2 K. The sample was first heated up to point B, and then cooled down back to the temperature of 2 K. Any hysteresis in resistance, a sign that F4TCNQ molecules are mobile, was monitored during this time. The process was then repeated for progressively higher temperatures. Only once the sample reached 250 K, did a clear hysteresis in resistance appear, with the new resistance value at 2 K being point F. This higher resistance value implies that some of the trapped field has been released due to charge redistribution. The sample was completely recovered to its initial, non-gated state, by keeping it at 300 K for an extended period of time. This is the first hint that F4TCNQ molecules are mobile in PMMA, far below the standard annealing temperature of 160 °C. In fact, a much closer look at the data reveals that there are signs of hysteresis at much lower temperatures, starting already from around 100 K.

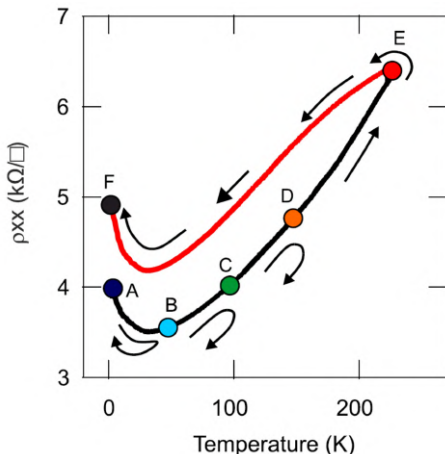


Figure 4.14: An initial field of $V_G = +50$ V is applied at 300 K and kept on during cool down. Once the temperature is at 2 K, the gate is turned off and the resistance takes the value at point A. Starting from point A at 2 K, sequential temperature sweeps, trace and retrace, are performed to successively higher temperatures and then back to 2 K. The sweeps are performed to point B at 50 K, point C at 100 K, and point D at 150 K, but no strong hysteresis occurs. Clear hysteresis in resistance can be seen starting only from 250 K, point E, after which the behavior in temperature is irreversibly switched from the black curve to the red one, ending up in point F.

A more thorough measurement of the charge redistribution of F4TCNQ molecules was performed by switching the gate voltage abruptly, while monitoring the transients in resistance as F4TCNQ responded to the applied field. Figure 4.15 shows an experiment where the gate voltage was abruptly set to $V_G = -5$ V (the response is symmetric for

positive gates) and the time evolution of zero-field resistivity ρ_{XX} was continuously monitored. The negative V_G reduces n-doping and increases the resistance for an initially lowly n-doped epigraphene sample. The initial response to the gate was fast (< 2 s), and includes the gate response of epigraphene itself, and other RC-constants etc. After the first signal spike and the fast transients die out, a much slower transient emerges, which was monitored for 200 s. ΔR is the change in resistance of the transient signal, w.r.t. the initial value after the fast transients have passed. This slower transient is attributed to the slower movements of F4TCNQ molecules. The measurement was repeated for several different temperatures, from 200 K down to 100 K. As the temperature decreases the time constant for the transient signal increases, which is consistent with the freezing of F4TCNQ motions. At 113 K the molecules appear to be almost completely frozen, at least on the time scale of 200 s. The typical time dependence was logarithmic for all tested temperatures. According to literature, a logarithmic time dependence of charge redistribution is typical for glass type (non-crystalline) disorder [91], which is expected for polymer based dopant blends. Note that this type of measurement setup is sensitive to time drift due to the small induced relative change in resistance ($< 5\%$), compared to the large initial change immediately following the activation of the gate source. All curves also have a slightly decreasing slope in resistance due to temperature drift in the system, which is most noticeable for the $\times 10$ zoomed in curve at 113 K. The thermal energy scale for the earliest activation of F4TCNQ movement is $k_B T \approx 10$ meV, and is in notable coincidence with the measured charge disorder ± 9 meV from magnetotransport at 2 K. This could possibly indicate that F4TCNQ is capable of screening charge disorder, but only as long as they are still mobile. Below 113 K the F4TCNQ molecule freeze out, and 10 meV worth of thermally activated charge disorder remains unscreened.

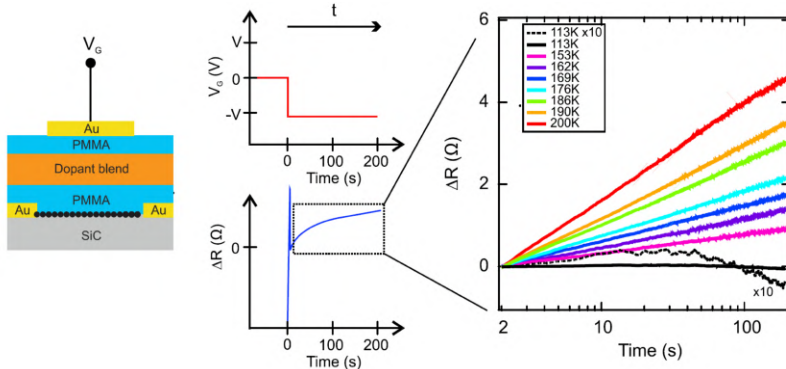


Figure 4.15: **Left:** Schematic representation of doped epigraphene device with an electrostatic top gate. **Center:** Schematic representation of the gate-switching measurement process. When gate voltage is switched to a negative voltage there is a spike in resistance. After initial fast transients have settled down (< 2 s), a much slower and long-lived transient appears. **Right:** Real measurement data show how the slower transient evolves over 200 s. Note that the signal is weak and the relative change in resistance ΔR during this time is $< 5\%$ of the total change immediately after the gate is switched on. The transient shows logarithmic time dependence, and appears to freeze out at 113 K.

4.9 Conclusions

In conclusion, F4TCNQ mixed with PMMA creates an effective dopant blend which can be used to control the carrier density of epigraphene. The dopant blend can be applied over large areas using simple spin-coating, and the final carrier density can be tuned via thermal annealing. Chemical analysis using ToF-SIMS show that the dopants diffuse through PMMA and spontaneously accumulate near epigraphene and form of charge-transfer complexes, resulting in a p-doping effect. Molecular doping is capable of tuning the carrier density towards p-type on the order of $\sim 10^{13} \text{ cm}^{-2}$. Furthermore, the doping is homogeneous with low charge disorder $n \approx 6 \times 10^9 \text{ cm}^{-2}$ or equivalently $\sim 9 \text{ meV}$, and high mobility $\mu \approx 80\,000 \text{ cm}^{-2} \text{ s}^{-1}$ at 2 K.

There are still many open questions regarding the details behind the doping methods and observed charge homogeneity. While room temperature GIWAXs measurements provide a hint about the packing density of F4TCNQ molecules, exact information regarding their conformation and potential crystallinity is still lacking, especially at low temperatures. For instance, it remains unconfirmed if F4TCNQ molecules can form a crystalline layer when cooled down. Future experiments which could elucidate this possibility could include cryogenic GIWAXs and cryogenic Raman spectroscopy [92]. No matter which technique is employed, isolation of the buried accumulation layer from the rest of the polymers layers above is crucial in order to extract the relevant signals. If the buried accumulation could be physically exposed, then it would even be possible to utilize scanning probe techniques with atomic resolution to directly probe the F4TCNQ layer. Such experiments may prove impractical due to the volatile nature of exposed F4TCNQ, and would probably require in-situ removal of the top polymer layers under vacuum or an inert atmosphere. Another option is to look at a cross-sectional cut of epigraphene, including all polymer layers, using high resolution transmission mode microscopy (HR-TEM).

Beyond further experiments which complement this current work, the method of introducing molecules to epigraphene through spontaneous accumulation has interesting implications by itself. This type of method is in principle applicable to any combination of suitable host polymers and molecules, as long as diffusion is allowed. Introducing certain adatoms and molecules to graphene can have profound effects on its properties, opening up avenues to explore magnetic order, spin-orbit-coupling, and topological insulators [93]. Moving past graphene-based substrates, this method could be used to expand the properties of 2D materials in general. One can fantasize about the creation and investigation of new two-dimensional systems of ordered molecular arrays templated by 2D crystalline substrates [94, 95]. The possible combinations of polymers, molecules, and substrates is nearly endless, which makes for an interesting, if not daunting, task for future research.

5 Quantum Resistance Standard

The field of metrology deals with the science of measurements, and it includes important tasks such as the definition and realization of the international system of units (SI). The primary standards of meter, second, ampere etc. are all kept and maintained in national metrology institutes (NMI), and they serve as the primary reference which all instrument calibrations can be traced back to. Calibration is important because it ensures that a measurement is reliable, trustworthy, accurate, and consistent with other measurements.

For the typical end-user, their instrument will not be directly calibrated against a primary standard, and they must make do with a less accurate working standard. The primary standard is by definition the most accurate, after which comes the secondary standard which is calibrated directly against the primary standard. Finally, the working standard is produced by calibrating against the secondary standard. For each step in the calibration chain, the standard accrues more measurement uncertainties. It is therefore of practical importance to find ways to bring the primary standard closer to the end-user, thereby decreasing the traceability chain and reducing calibration uncertainties. For resistance metrology, this means that a practical QHR standard should be able to operate without utilizing complicated and bulky laboratory equipment like those employed by NMIs. Furthermore, the operation of such a system should in the ideal case be as simple as pressing a single button. All of this would enable the user to directly calibrate their instruments against a primary standard. The first steps towards realizing this goal was made with the advent of QHR standards based on epigraphene, a project which started a decade ago [14]. Epigraphene has the potential to fulfill this goal, because it can endure larger bias currents, in combination with displaying QHE at higher temperatures and lower magnetic fields compared to conventional materials [18, 19]. This can be considered as the first, and to this day perhaps the only, real electronic application which utilizes the unique properties of epigraphene to surpass conventional technologies.

Significant progress towards a working prototype epigraphene-based QHR system has been made in recent years. A portable table-top cryogen-free cryostat system has already been constructed, with an epigraphene QHR standard at its core. The fabrication of the epigraphene chip is described in **Paper A**. In **Paper B**, the table-system demonstrated QHE with metrological accuracy while operating at relatively relaxed conditions of 4.2 K and magnetic fields below 5 T [19]. In this first incarnation, there was still a need for an externally connected CCC, so all necessary components were not fully integrated. More work is required to combine all components into one complete package, and this development is still ongoing. At the time, another problem was that the carrier density of the epigraphene chip had to be tuned by corona discharge gating [41], which is unstable at ambient conditions. As a consequence, every time the system was heated up, the charge carrier density of the QHR standard needed to be adjusted anew to reach QHE at the desired operating conditions. Tuning of the carrier density is not only required for quantization at relaxed conditions of 4.2 K and 5 T, but is also crucial to optimize the critical current to boost signal-to-noise ratio [19]. The added layer of complexity in manual carrier density control may be acceptable for research purposes, but it is not feasible in practice. This was the inspiration behind the search for novel techniques, which are more stable and more reliable, to gain control over the carrier density of epigraphene.

This endeavor eventually lead to the development of the molecular doping method which utilizes F4TCNQ molecules mixed with PMMA presented in Chapter 4.

Armed with a potent molecular doping method, it was finally time to tackle the initially proposed challenge of achieving a practical QHR standard based on epigraphene. In order to truly test the metrological viability of the F4TCNQ doping method, the quantized value of $R_{XY} = h/2e^2$ for doped epigraphene was compared to a conventional well-established GaAs based QHR standard. One potential concern is that the accumulation layer of F4TCNQ molecules can cause a resistive leakage in parallel with epigraphene, which would spoil the accuracy of quantization. To be able to meet the strict requirements for a viable QHR standard, these measurements required a CCC (Chapter 3.4.5) in order to achieve precision measurements with uncertainty on the order of $n\Omega/\Omega$ (part-per-billion).

This section discusses the metrological trials using two doped epigraphene QHR standards, tested independently at two separate NMIs. It covers the results presented in **Paper D**, including sample preparation, initial characterization, comparison with GaAs standards, and long-term stability of doping.

5.1 Sample Preparation

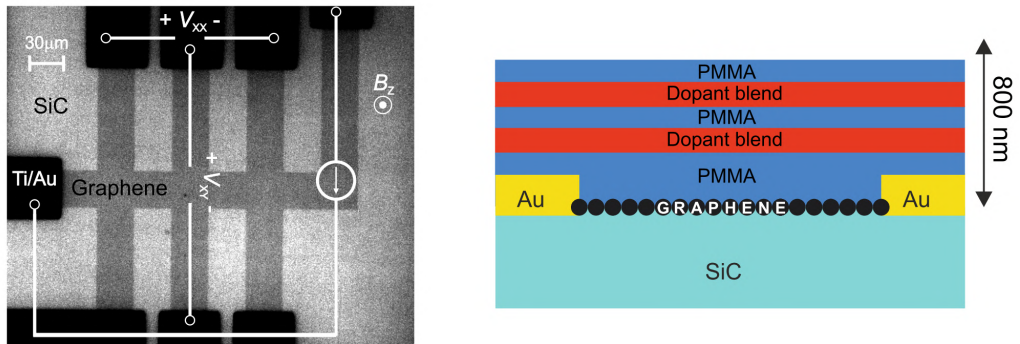


Figure 5.1: **Left:** Optical micrograph of a graphene QHR device, showing the connection setup for QHE measurements and magnetic field B_z direction. **Right:** Schematic representation of doped epigraphene, which uses five polymer layers for higher device stability.

For real-world metrological applications of epigraphene QHR standards, the optimal carrier density is on the order of $n \approx 2 \times 10^{11} \text{ cm}^{-2}$. The reason is that this level of carrier density will ensure that the critical current I_C is maximized for relaxed operating conditions of 4.2 K and 5 T [19]. All of the samples in this current section were prepared using a full five polymer layers, PMMA-Dopant-PMMA-Dopant-PMMA, for added long-term stability and device lifetime (see Figure 5.1). Each polymer layer requires 5 min of annealing at 160 °C by default, and in order to reach optimal carrier density an additional 15-20 min of annealing is added on top. If the carrier density is not satisfactory, the

doping level can always be fine-tuned by annealing at 160 °C in smaller time increments 2 – 5 minutes and performing a Hall measurement, repeating until the desired carrier density has been reached. The fabrication process is reproducible enough that it typically takes two QHE measurements at cryogenic temperatures to reach the optimal carrier density. The variance in annealing time comes mainly from the degradation of the dopant blend mixture, which loses potency over time.

Two separate devices were prepared in nominally the same way with device geometries like Figure 5.1, intended for precision measurements at two different NMIs. The first sample is called G-RISE, and it was tested at the Research Institutes of Sweden (RISE), measured in a standard liquid helium cryostat, with base temperature 1.9 K and equipped with an 11 T superconducting magnet. The second sample is called G-NPL, and it was tested at the National Physical Laboratory (NPL) using the small table-top mechanical cryostat, with a base temperature of 4 K and a magnetic field up to 5 T [19]. The carrier density for G-RISE was initially tuned to $n = 1.3 \times 10^{11} \text{ cm}^{-2}$, while G-NPL was tuned to $n = 1.6 \times 10^{11} \text{ cm}^{-2}$.

5.2 Initial Characterization

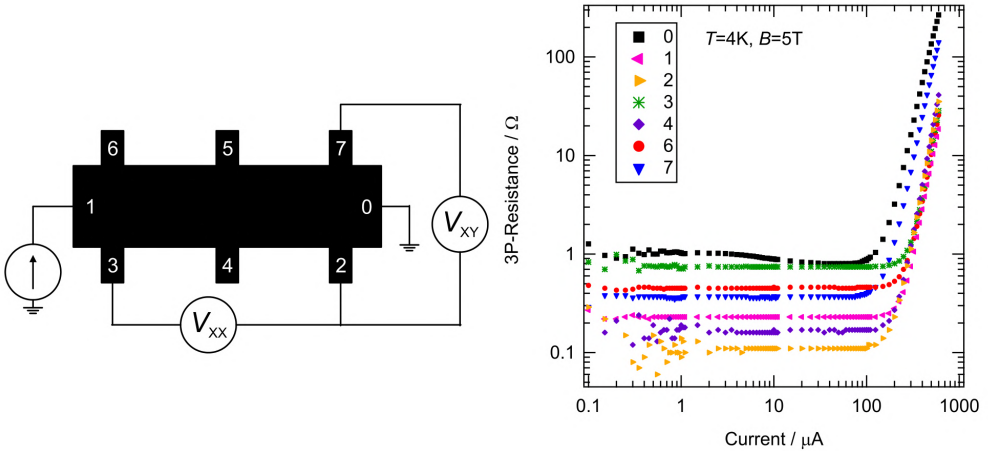


Figure 5.2: **Left:** Schematic of an epigraphene Hall bar with numbered contacts. The voltage connection scheme shows a standard QHE configuration. **Right:** Measured contact resistances for each contact (except pad 5). The measurements were performed using three-probe configuration in the QHE regime. All contacts resistances are below 1 Ω for bias currents below 100 μA .

Before the samples were sent to the two NMIs, they were tested at Chalmers to confirm that the QHE is well-developed. Although the measurement setup at Chalmers is not as suited for precision measurements, it is relatively easy to verify that $R_{XY} = h/2e^2$ and $R_{XX} = 0$, within an uncertainty of $\mu\Omega/\Omega$, or part-per-million accuracy. The serious metrological trials were then performed at the NMIs, following well-established guidelines

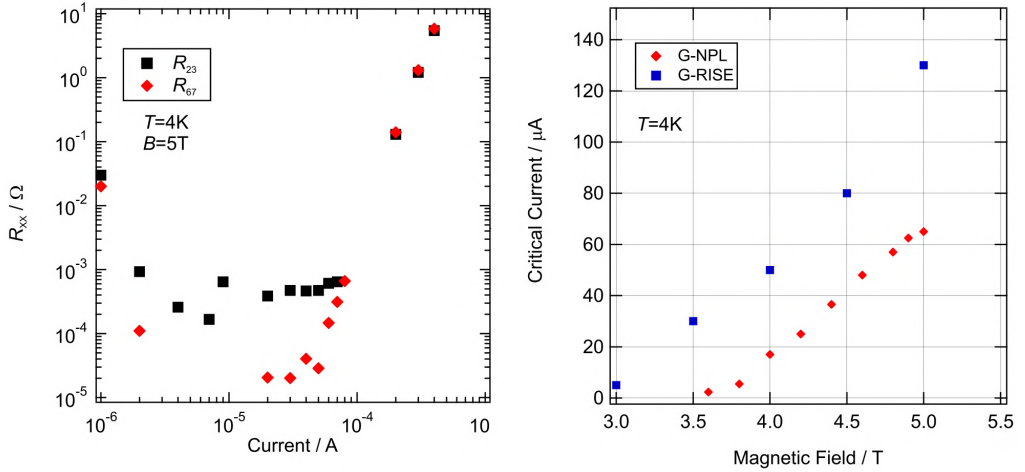


Figure 5.3: **Left:** Longitudinal resistance R_{XX} versus bias current in quantum Hall state. The red and black dots correspond to different sides of the Hall bar. **Right:** Critical current I_C extracted from measurements at different magnetic fields for G-NPL and G-RISE samples.

for DC quantum resistance metrology [60]. The samples were brought into the quantum Hall regime, and first tested for faulty contacts using a three-probe configuration as shown in Figure 5.2. Note that while the displayed data is only for G-NPL, G-RISE showed comparable performance. All measured contact resistances for both samples were around 1Ω or below, which is below the recommended maximum value of 10Ω , needed to achieve metrological accuracy of QHE. The contact resistance is typically measured as a function of bias current, and at some critical bias current I_C the measured resistance starts to increase above its constant value, which is a sign of breakdown of QHE due to overheating of the electron system. However, the finite contact resistance masks the true onset of the breakdown, and I_C is better measured using R_{XX} .

A precision measurement of R_{XX} in quantizing conditions is always performed in parallel with the contact resistance measurements, and serves as another check of the quality on the QHE and a more accurate way to measure I_C . The data in Figure 5.3 shows a measurement of R_{XX} performed on both sides of the same G-NPL Hall bar. The red dots show that the measured resistance disappears into the noise level, below 10 nV , at a critical current level of $I_C \approx 60 \mu\text{A}$. The black dots show an apparent residual resistance of $1 \text{ m}\Omega$, but this was due to ground leakage currents [60], and it disappeared when Contact 1 was grounded instead of Contact 0. The critical currents were extracted for both samples at different magnetic fields, and they are well-above the metrologically useful currents of $10 \mu\text{A}$ starting from 3-4 T, depending on the sample. The discrepancies between samples is attributed to differences in charge disorder and carrier density.

5.3 Measurements at National Physical Laboratory

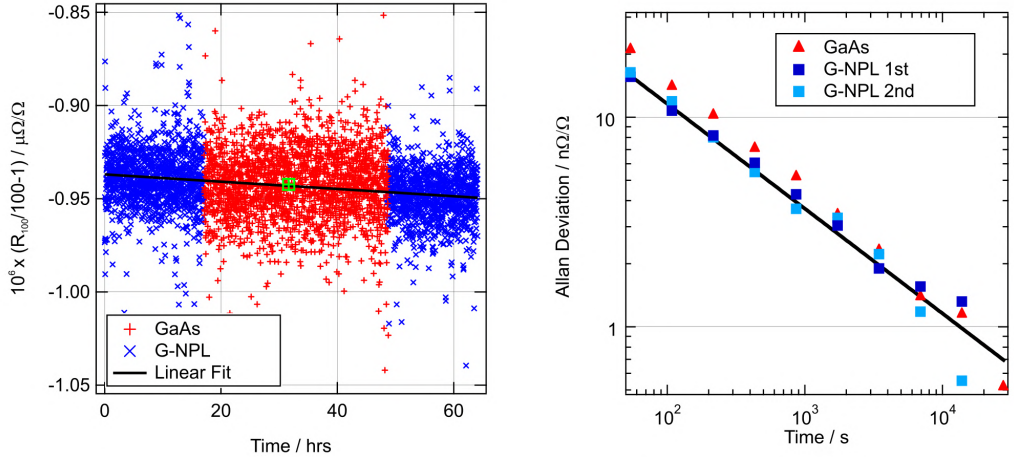


Figure 5.4: Comparison measurements between GaAs and G-NPL, via a $100\ \Omega$ standard. **Left:** The data shows a A-B-A type measurement where the linear drift of the measurement is compensated for by switching between G-NPL and GaAs QHR standards. The y-axis plots the relative deviation of the $100\ \Omega$ standard from its nominal value as compared to the QHR standard. The black line is a linear fit to G-NPL data and the green square is the mean value of GaAs deviation at mean measurement time. GaAs was measured at $< 0.3\text{ K}$, with a magnetic field at 9.4 T . G-NPL was measured at 4 K and a magnetic field of 4.9 T . The bias current was $23\ \mu\text{A}$ for both samples. **Right:** Allan deviation measurement for the three data blocks, GaAs and two G-NPL. The solid black line shows that the Allan deviation decreases with time $\propto 1/\sqrt{t}$, indicating that white noise dominates.

The initial characterization in the previous section confirms that samples pass the recommended criteria for reliable QHR measurements. In order to further probe the accuracy of the quantization of doped epigraphene QHR standard, a high precision measurement using CCC (Section 3.4.5) is needed. Of special interest is whether the presence of the dopant accumulation layer can spoil the accuracy of quantization, for instance by providing a parallel conducting channel to epigraphene. This kind of leakage can be detected in 2DEGs like GaAs, by comparing the $\nu = 2$ and $\nu = 4$ quantized R_{XY} plateaus, but this is not possible in epigraphene since only the robust $\nu = 2$ is typically observed. Instead, epigraphene was indirectly compared to a well-tested GaAs sample (in use for 20 years), by comparing the two in quantized conditions to a $100\ \Omega$ standard (Tinsley Evanohm).

Measurements at NPL used two dedicated systems, one cryostat for GaAs QHR standard and one table-top cryostat for doped epigraphene QHR standard. This allowed for quick alternating CCC measurements between G-NPL and the $100\ \Omega$ standard, GaAs

and the $100\ \Omega$ standard, and then back to G-NPL again. This type of A-B-A measurement allows for the elimination of temperature drift and short term drift of the $100\ \Omega$ standard, which is kept in a thermostated enclosure with a temperature stability of mK over days. However, one drawback is that any potential leakage in cryogenic wiring can be different between the two cryostats, and may impact the comparison measurements. Fortunately, the leakage in the GaAs system has previously been measured to contribute only $10\ p\Omega/\Omega$ relative uncertainty to a QHR comparison measurement, while the table-top system has been shown to contribute only $0.1\ n\Omega/\Omega$ relative uncertainty.

Both QHR standard were brought into the quantum Hall state, with $\nu = 2$, $R_{XY} = h/2e^2$. GaAs was measured at temperatures $< 0.3\ K$ and a magnetic field of $9.4\ T$, while G-NPL was measured at $4\ K$ and $4.9\ T$. The CCC bias current was $23\ \mu A$ for both samples. Figure 5.4 shows the results of the lengthy comparison measurement. The y-axis plots the measured relative deviation of the $100\ \Omega$ standard from its nominal value of $100\ \Omega$, as compared to the QHR standard which is assumed to have a resistance of exactly $h/2e^2$. Each data point consists of $54\ s$ of CCC data averaging, and the data series shows a clear linear drift in time. This data set is used to calculate the mean difference between G-NPL and GaAs comparison measurements, i.e. how well they agree with each other. A linear fit to G-NPL is calculated from the two blocks of data, and the value of this fit at the mean measurement time of the GaAs data (x-value at green square) is compared to the mean value of the GaAs data (y-value at green square), thus eliminating the linear drift contribution. The final mean difference, including the expanded uncertainty containing the measurement error for GaAs and error in fitting to G-NPL data, is $\Delta_{Gr-GaAs} = 1.02 \pm 1.42\ n\Omega/\Omega$, including two standard errors of the mean. The quantization of G-NPL agrees well with GaAs, which demonstrates the viability of F4TCNQ doped epigraphene in quantum resistance metrology.

The previous calculations of the final mean difference between GaAs and G-NPL QHR standards assumes that the measurement uncertainty comes from uncorrelated white noise. This assumption is tested in Figure 5.4, which shows the calculated Allan deviation [96] for each of the three CCC data sets (1st G-NPL, GaAs, then 2nd G-NPL measurements). The fit shows that the Allan deviation decreases with time $\propto t^{-0.5}$, which signifies that uncorrelated white noise is the dominating source of measurement uncertainty. This means that the uncertainty can in principle be decreased through additional averaging. The noise level is then ideally limited only by resistive noise of the resistors, which in the case for a QHR standard at $2\ K$ and $100\ \Omega$ resistor at room temperature is around $2\ nV/\sqrt{Hz}$. This corresponds to a relative uncertainty contribution of $1\ n\Omega/\Omega$ for a $100\ s$ long measurement at $23\ \mu A$. The measured Allan deviation shows a noise level almost an order of magnitude higher, which can be attributed to excess electromagnetic interference from ambient noise sources present inside the laboratory. For a longer measurement periods above 6 hours, the final uncertainty reaches $< 1\ n\Omega/\Omega$, which is a sufficient demonstration of the accuracy of doped epigraphene QHR standard, which meets all requirements for use in resistance metrology.

5.4 Measurements at Research Institutes of Sweden

In contrast to NPL, G-RISE was compared to a well-known GaAs QHR standard (20 years of service) sequentially using the same cryostat. The advantage of this approach is that any leakage in the measurement wiring will be ideally canceled out when comparing the two different samples. The drawback is that the samples have to be swapped out which takes a considerable amount of time, and increases the effect of time drift. The CCC measurement was performed using a $100\ \Omega$ resistor (Tinsley), stored in an oil bath of 25°C and $\sim 1\text{ mK}$ long-term drift. The short-term instability can be either be taken into account by adding an estimated uncertainty of $3\text{ n}\Omega/\Omega$, or performing an A-B-A type measurement.

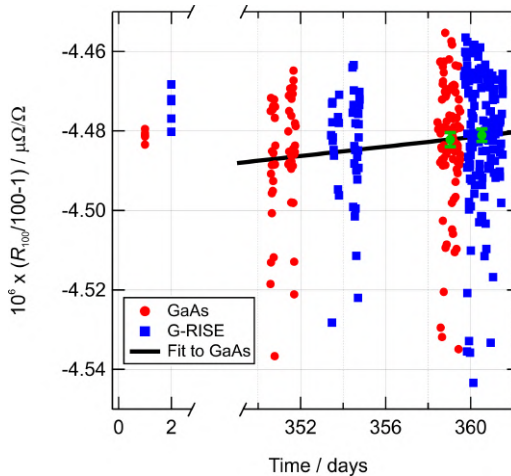


Figure 5.5: *Comparison measurements between GaAs and G-RISE, via a $100\ \Omega$ standard. The data shows a comparison measurement spanning one year, showing that both long term and short term drift are low. The y-axis plots the relative deviation of the $100\ \Omega$ standard from its nominal value as compared to the QHR standard. The black line is a linear fit to two G-RISE data blocks, used to eliminate short-term linear drift. The two green circles are the mean value of GaAs and G-RISE deviation at mean measurement time for each data block, with error bars representing two standard error of the mean. GaAs was measured at $< 2\text{ K}$, with a magnetic field at $9.65\text{--}9.95\text{ T}$. G-RISE was measured at 4.2 K and a magnetic field $< 5\text{ T}$. The bias current was $23\ \mu\text{A}$ for both samples.*

Figure 5.5 shows two measurement sequences, performed one year apart. Each data point represents one full, current reversed, CCC measurement cycle. The initial two day measurements yield a rough mean relative deviation of G-RISE compared to GaAs on the levels of $\Delta_{Gr-GaAs} = 7.2 \pm 7.4\text{ n}\Omega/\Omega$, including two standard errors of the mean. The expanded uncertainty includes the measurement error, and the added uncertainty from the estimated instability of the $100\ \Omega$ standard. The second set of measurements were performed one year later, and used the A-B-A-B type scheme in order to eliminate short term linear drift. Since there was only one cryostat available, the samples had to be

switched out and measured in sequence over a period of 10 days. Fortunately, the drift of the $100\ \Omega$ standard appeared to be linear within this time span. Due to the lengthy time between measurement blocks, the analysis is slightly different compared to G-NPL. Only the last two measurement blocks for GaAs and G-RISE are considered, since they were measured closest in time and this reduces the error introduced by linear fitting. Additionally, over 70% of the data point are located in these last blocks, which give them more weight when considering the mean deviation. Although the short-term drift was estimated only for the last two data blocks, the fitted line still passes relatively close to the mean of the other two data blocks. The final mean difference between GaAs and G-RISE, including the expanded uncertainty consisting of measurement error of GaAs and error from fitting to G-RISE data, is $\Delta_{Gr-GaAs} = 0.19 \pm 4.81\text{ n}\Omega/\Omega$, including two standard errors of the mean. This is another, independently verified, demonstration of the viability of doped epigraphene as a QHR standard.

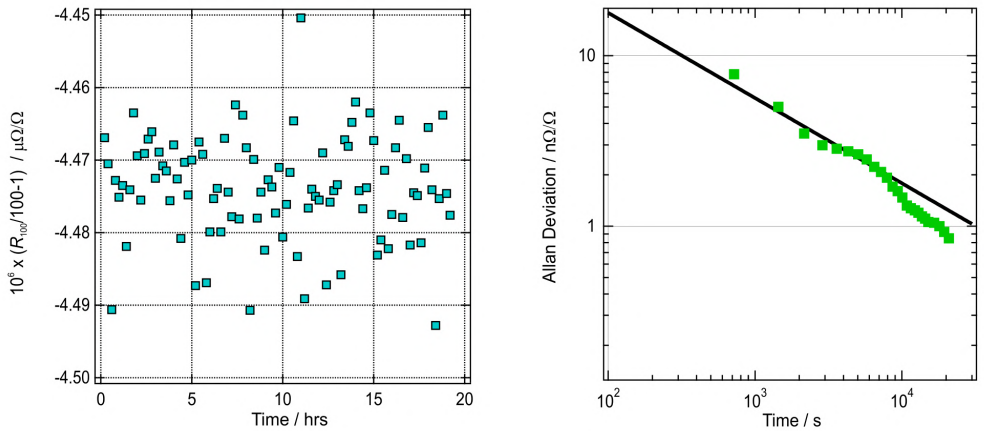


Figure 5.6: **Left:** Extended measurement series for G-RISE performed over 20 hours. Each data point represents a measurement period of 12 min. **Right:** Allan deviation calculated from the G-RISE data. The solid black line shows that the Allan deviation decreases with time $\propto 1/\sqrt{t}$, indicating that white noise dominates.

Analogous to G-NPL, the G-RISE sample also underwent noise characterization to determine the Allan deviation and the dominant noise source. Figure 5.6 shows an extended CCC measurement series for over 20 hours. The resulting Allan deviation reveals once again that uncorrelated white noise is dominant, and that after 6 hours the final uncertainty reaches $< 1\text{ n}\Omega/\Omega$, which is a suitable device accuracy for QHR standards.

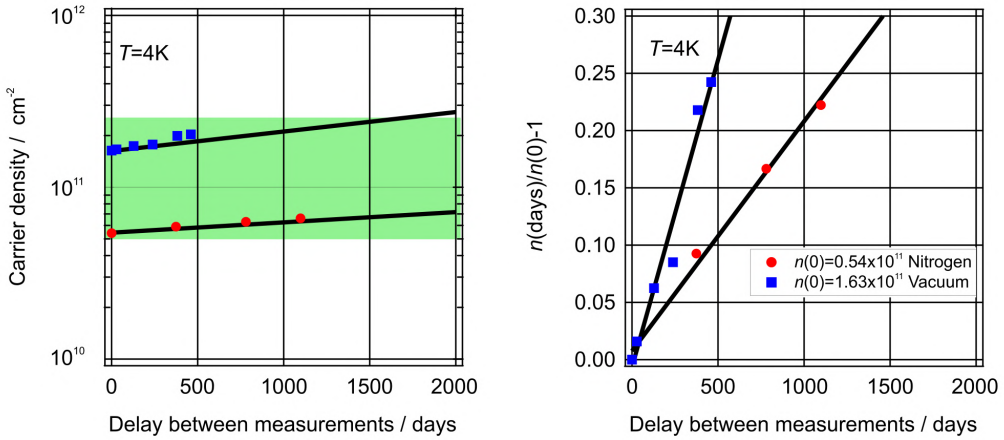


Figure 5.7: **Left:** Time evolution of carrier density monitored for two doped epigraphene QHR devices. The blue and red data represent devices kept primarily in vacuum or nitrogen respectively. The black lines are linear fits to the doping drift in time. The green zone marks the metrological useful carrier densities, which ultimately limits device lifetime. **Right:** Relative change in carrier density versus time. The blue and red data respectively show a relative change of 0.05 % and 0.02 % from initial carrier density per day.

5.5 Long-term Stability

The two previous section demonstrate that doped epigraphene is suitable for QHR from an accuracy point of view. For real-world applications, it is also desirable that the samples have a long life time. For example, the two tested GaAs chips have both been used for decades. Doped epigraphene has already shown potential, and Figure 4.7 shows that long-term doping stability is possible. Furthermore, the G-RISE sample retained metrological accuracy for over a year and counting. To further investigate the ultimate device lifetime, two other samples were kept in different environments and their the carrier densities was periodically monitored over three years. Figure 5.7 shows data for one sample kept in vacuum (blue) and one kept in nitrogen gas at room temperature (red), with samples occasionally brought out into ambient only for QHE measurements. The nitrogen sample was initially doped to $n = 5.4 \times 10^{10} \text{ cm}^{-2}$ and has a relative drift in carrier density of 0.02 % per day. The vacuum sample was initially doped to $n = 1.63 \times 10^{11} \text{ cm}^{-2}$ and has a relative drift in carrier density of 0.05 % per day. The device lifetime is set by its metrological usefulness, and from critical current considerations the carrier density needs to be high enough that a current of $> 10 \mu\text{A}$ can be used, and low enough that QHE can develop at least 4 K and 5 T. This puts constraints on the range of allowable carrier densities [19], which is illustrated using the marked green region in the plot. With the current linear drift, the nitrogen sample has an expected life time of 20 years and the vacuum sample 4 years. The life time is however highly dependent on the initial carrier density, and it appears that lower carrier density, despite not being optimal for

maximum critical current, may be used as a compromise to extend lifetime. The nature of the observed drift towards higher n-doping is not entirely known, but it is likely due to slow degradation of F4TCNQ dopants. It is observed that samples covered with a thinner polymer layer (two layers instead of five) are less stable. Additionally, samples kept outside in ambient conditions and exposed to air become slowly more p-doped, consistent with what is observed for ambient doping of pristine epigraphene [55].

5.6 Conclusions

In conclusion, the F4TCNQ dopant blend method was used to fabricate epigraphene QHR standards. The results of two independently performed metrological trials, prove that doped epigraphene is viable for quantum resistance metrology with part-per-billion accuracy of quantization. There was no observed significant adverse effect due to the F4TCNQ accumulation layer. The molecular doping method allows for reliable carrier density control, which enables epigraphene QHR standards to operate at relaxed conditions of 4 K and below 5 T. Finally, the doping level appears to be stable over three years and counting, with projected device lifetimes potentially exceeding decades.

The two tested samples are currently kept at the respective NMI, to undergo continuous tests in a metrological environment. The samples have started to be used for real-life resistance calibrations, and calibration of certain industrial instruments can already be traced back to an epigraphene QHR standard. What remains to be seen is whether the doping levels remains stable over the long run, and how its linear drift will change over the years, especially after repeated use and thermal cycling. There was a noticeable difference in the doping drift depending on the storage environment, and this is something that can be investigated further in order to find the optimal storage conditions.

Regarding new developments, work has started on developing new methods to increase the long-term stability of F4TCNQ dopants. While doped epigraphene has yet to approach the lifetimes of established GaAs based 2DEGs, the potential is there. The room temperature ambient stability can be improved even further by hermetic sealing of the devices, and researching different encapsulation layers. Since F4TCNQ can diffuse through PMMA it is not surprising that samples drift in time. However, there are other materials which are impermeable to diffusion of F4TCNQ. One example which has already been experimentally confirmed is PMGI (polydimethylglutarimide) based LOR-resist. Whether this, or other encapsulation methods such as metals, will truly improve doping stability and device lifetime remains to be explored.

Another practical improvement is to scale the process up to large array of epigraphene QHR standards. This is useful in order to facilitate resistance calibrations over a broad range of resistance values [97, 98]. Arrays of QHR standards will test the limits of reproducibility of fabrication methods, and the large-scale homogeneity of molecular doping.

6 Epigraphene Hall Sensors

Hall sensors are magnetometers which detect magnetic fields via the classical Hall effect (see Chapter 2.3.1). These types of sensors are ubiquitous in modern society and are commonly used for precise position detection. They see extensive use in major markets such as the automotive industry, marine industry, and consumer electronics. One common application of Hall sensors is for instance in the navigation systems used in vehicles and smartphones. The most widely used Hall sensor are based on silicon (Si), and they have a widespread appeal due to well-established and low-cost production methods [99–101]. Sensors made from Si are however limited in terms of device sensitivity, and for increased performance III-V materials such as InSb or GaAs are used instead [102]. These Hall sensors have much higher sensitivities, but one drawback is that their performance often decreases rapidly at elevated temperatures beyond the common automotive and military operating range $> 125^\circ\text{C}$ [102–105]. There is a need for sensitive Hall elements which are more resilient to harsh conditions and high temperatures, and this demands the exploration of other materials. For a more in-depth look at Hall sensors see reference [102].

Hall sensors detect magnetic fields by measuring the Hall voltage V_H induced by an external field B . High device sensitivity is important because it leads to a large magnitude of the V_H response to an external field, relative to some bias current I_B or voltage V_B . There exist three important material-related sensor metrics which quantify the performance of a Hall sensor. The first is the current-related sensitivity $S_I = |\frac{V_H}{B I_B}|$ (units V/AT), which is essentially determined by the Hall coefficient R_H (units Ω/T). The second is the voltage-related sensitivity $S_V = |\frac{V_H}{B V_B}|$ (units V/VT), which is ultimately limited by the carrier mobility $\mu = R_H / \rho$ (units m^2/Vs). The third and final one is the magnetic field detection limit $B_{MIN} = \frac{V_N}{I_B R_H}$ (units T/ $\sqrt{\text{Hz}}$), where V_N is the voltage spectral density (units V/ $\sqrt{\text{Hz}}$).

Epigraphene posses many qualities which make it a natural candidate for high-performance Hall sensors, especially when combined with the molecular doping method presented in Chapter 4. The carrier density n can be now be tuned, and if it is brought close to the charge neutrality point the Hall coefficient increases as $R_H = 1/ne$, which leads to an increase in sensitivity S_I . In real graphene samples there is charge disorder (charge puddles) which limits how close one can come to charge neutrality point [43], but the molecular doping method is known to produce homogeneously doped samples rivaling even the best graphene samples in literature [106]. Epigraphene also has a relatively high carrier mobility, which is optimal for sensitivity S_V . Moreover, since the mobility is inversely proportional to carrier density, doping graphene close to neutrality is beneficial for both S_I and S_V . However, decreasing n will also lead to an increased sheet resistance ρ , which contributes to increased device noise V_N due to e.g. Johnson-Nyquist noise, and this may negatively impact the magnetic field detection limit B_{MIN} . Finally, epigraphene is known to be compatible with high-temperature operations [107], but this might degrade the doping method.

The balance between carrier density and resistance, alongside the interplay between high temperature operation and stability of molecular doping, are all explored in this

chapter. The following sections provide a thorough investigation of the behavior of doped epigraphene Hall sensors for different carrier densities, under both ambient conditions and elevated temperatures. It reveals the merits of doped epigraphene Hall sensors, and how they can perform as sensitive Hall elements with a record-low magnetic field detection limit compared to any graphene-based sensor. Furthermore, the Hall sensors show promise for operation at elevated temperatures, with stable operation tested up to least 150 °C, while maintaining a respectable sensor performance. This work is based on the results presented in **Paper F**.

6.1 Sample Preparation

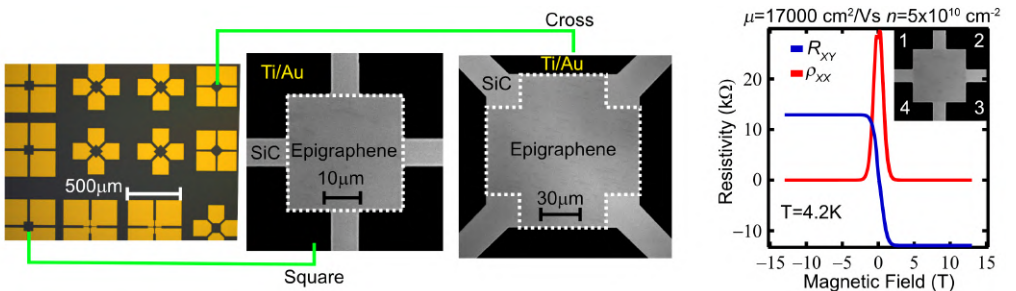


Figure 6.1: **Left:** Optical micrograph of a sample containing multiple epigraphene Hall sensor devices. The grayscale transmission mode micrographs show the two different device geometries: square or cross. **Right:** The QHE is used to verify the electronic quality of doped epigraphene Hall sensors. The inset shows four numbered contact pads used for van der Pauw (vdP) measurements. For quantum Hall measurements, R_{XY} can be measured by using 1-3 for current biasing, and 2-4 for voltage measurements. For measurements of ρ_{XX} , one can use 2-3 for current bias, and 1-4 for voltage measurements.

In total, seven different epigraphene Hall sensors were studied, spread across four separate chips. The Hall sensors were designed using symmetric square or cross shapes device geometries, which is optimal for maximal S_V [108, 109]. Figure 6.1 shows two examples for epigraphene Hall sensors. Each Hall sensor was equipped with four electrical contacts, and van der Pauw (vdP) measurements were used to extract carrier density n and sheet resistance ρ . QHE was measured at cryogenic temperatures to ensure that the doped Hall sensor was of high electronic quality, with uniform doping.

6.2 Carrier Density Tuning

The samples were doped using five polymer layers for maximal stability, and their final carrier densities were tuned to a wide range of values in order to cover performance over a broad spectrum. Figure 6.2 shows the the range of attained carrier density, and the respective values for R_H and ρ . The performance of doped epigraphene Hall sensors

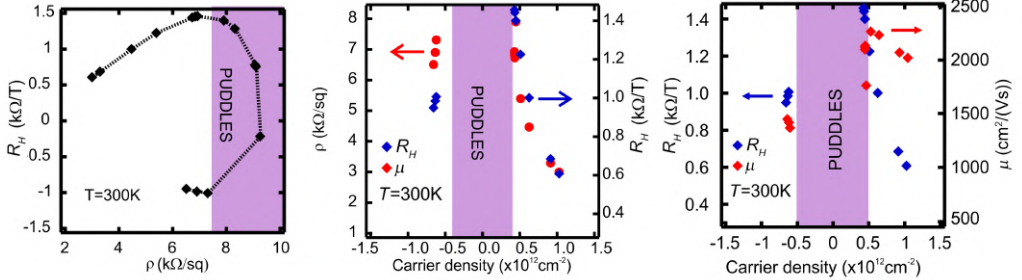


Figure 6.2: *Carrier density tuning of doped epigraphene Hall sensors at room temperate.* **Left:** The evolution of R_H versus ρ as the carrier density of epigraphene passes through the Dirac point. The purple region denote the disordered puddle regime. **Middle:** R_H and μ versus carrier density, showing that both have the same dependence on carrier density $\propto 1/n$. The data points inside the puddle region have been omitted. **Right:** R_H and μ versus carrier density. Carrier mobility shows a downturn starting even before the carrier density enters into the puddle regime.

were considered for doping levels ranging from $n = 5 \times 10^{11} - 2 \times 10^{12} \text{ cm}^{-2}$. The lowest doping level marks the size of the charge puddle regime, which is $|n| < 5 \times 10^{11} \text{ cm}^{-2}$, and is limited by the room temperature disorder. Inside the puddle regime, the singe-band carrier density is poorly defined and is therefore omitted from the plot. In order to avoid this problem, future data are plotted against R_H instead if possible.

6.3 Device Linearity

For practical applications of Hall sensors, the sensor output should ideally be linear with the input bias current and magnetic field. Operating in the linear regime makes data analysis significantly easier, and it is important in order to achieve high sensor accuracy without the need for complicated electronics.

Figure 6.3 shows the linearity of the transverse resistance R_{XY} , which is the same as V_H/I_B , measured versus magnetic field. There is a clear onset of non-linear response of R_{XY} as the magnetic field B increases. To quantify the non-linearity, the measure linearity error Δ_{LIN} is used. It is defined as the relative deviation of the raw data $R_{XY}(B)$ from the linear fit $F(B)$, normalized by the fit itself as $\Delta_{LIN} = |(R_{XY}(B) - F(B))/F(B)|$. An alternate measure uses the full scale fit value in the denominator instead $\Delta_{LIN} = |(R_{XY}(B) - F(B))/F(B_{MAX})|$, which eliminates potential low-field singularities due to $F(B) = 0$. In the low field range of $|B| < 0.5 \text{ T}$ the linearity error is $\ll 1\%$ for all carrier densities. For low doping ($R_H = 1284 \Omega/\text{T}$) the linearity error remains within 5% in a range of magnetic fields $B = \pm 1.2 \text{ T}$. For high doping ($R_H = 949 \Omega/\text{T}$) the linearity error remains within 5% in a range of magnetic fields $B = \pm 6 \text{ T}$. The non-linearity helps define the operating regime, whose operating magnetic field range is ultimately dependent on the sensing requirements. Typically for regular commercial sensors a linearity of error of 5% is acceptable, while precision sensors can have a linearity error $< 1\%$ (e.g. Honeywell).

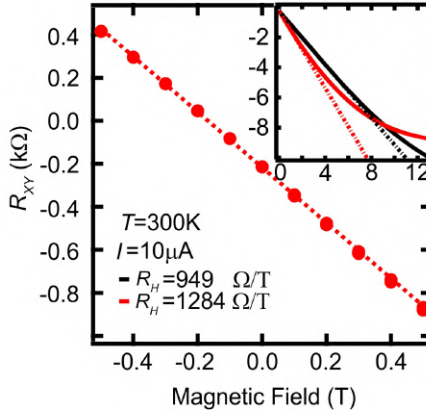


Figure 6.3: *Hall measurements showing the (non)linearity of R_{XY} versus applied magnetic field. In the low-field regime $|B| < 0.5$ T the response is highly linear, as demonstrated by the dotted line linear fit. The inset shows the behavior up to 13 T for two different doping levels. the non-linearity grows at higher magnetic fields, and it also grows as the carrier density decreases. All carrier densities and mobilities are extracted from low-field linear fits only.*

The non-linearity of R_{XY} manifests itself as approximately $R_{XY} \propto B^2$, and this is a known effect arising from geometrical and material correction effects [102].

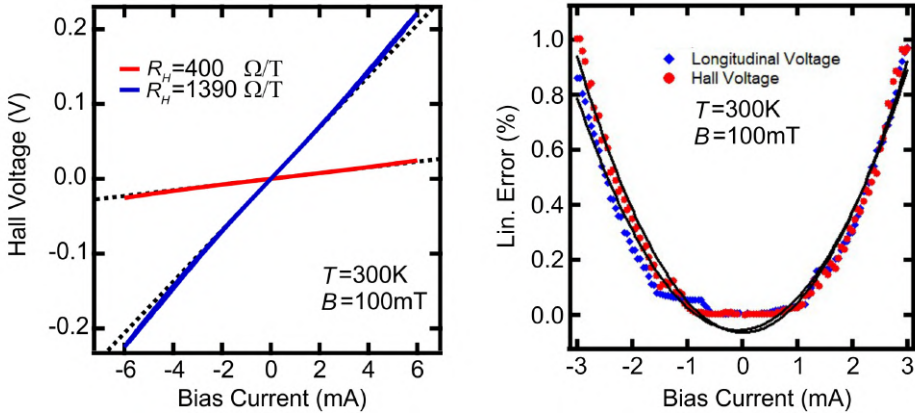


Figure 6.4: **Left:** Hall voltage versus bias current for high and low doping, at fixed magnetic field. The dotted black lines are linear fits to low current data $|I_B| < 0.5$ mA. The non-linearity increases as doping decreases. **Right:** Linearity error calculated for both longitudinal voltage and Hall voltage versus bias current. The black curves are parabolic fits which show that both scale $\propto I_B^2$.

In addition to linearity in magnetic field, the linearity of V_H with bias current was also investigated. Figure 6.4 shows current-voltage (I-V) characteristics for Hall voltage

V_H . Similar to high magnetic field, at high bias currents there is a clear non-linearity in Hall voltage, which also increases as the carrier density decreases. The linearity error is below 5% for $I_B < 2.5$ mA for the whole range of tested carrier densities. For most measurements, the current was limited to < 1.5 mA in order to ensure a linearity error $< 2\%$. The origin of this non linearity can be attributed mainly to the influence of a longitudinal voltage component, which has a current dependence due to Joule heating, added to the Hall voltage. Figure 6.4 shows the linearity error (scaled to full range value of the fit) for simultaneous measurements of Hall voltage and longitudinal voltage ($R_H = 900 \Omega/T$). Their dependence on bias current is the same $\propto I_B^2$, i.e. linear in applied power, which points to Joule heating.

6.4 Device Offset

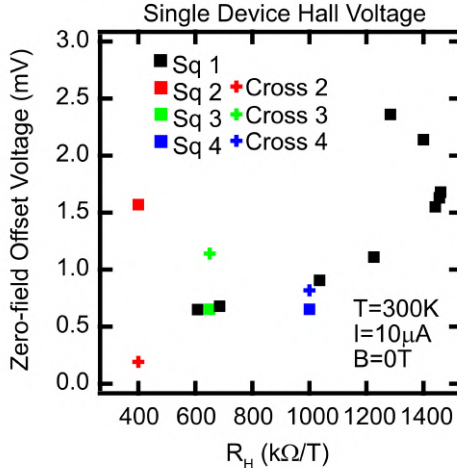


Figure 6.5: *Offset voltage for V_{OFF} measured at zero magnetic field. The data was collected across a total of seven devices with either square (sq) or cross (cr) geometries.*

In both of the above measurements of Hall voltage V_H , there exists an offset voltage at zero magnetic field and current. This is problematic for practical applications because it may dominate a weak measurement signal and saturate amplifiers in external circuitry.

The offset at zero current is commonly due to thermal electromotive force (EMF) due to the Seebeck effect, which can be eliminated by current reversal techniques. Thermal EMF is present in all systems, for instance due to various wire interconnects, and it is not necessarily intrinsic to the epigraphene devices. The measured offset at zero bias in the above I-V data is $\sim 10 \mu V$, which is on the same order with what is observed for commonly paired metals $\sim 1 - 10 \mu V/\text{°C}$ (Fluke thermocouple).

The most significant offset for Hall sensors is the zero-field offset voltage V_{OFF} , which arises due to geometrical correction effects and material inhomogeneity. Figure 6.5 shows

the measured V_{OFF} for many different devices and geometries. While there is no clear trend between cross or square shape geometries, the carrier density does play a role, with the offset increasing with decreasing carrier density in general (black data points). This is a consequence of the relationship between carrier density and resistivity. On average, the offset voltage is ~ 1 mV across a wide range of carrier densities. Note that these measurement were performed inside a depowered coil magnet with nominally zero field. However, a remnant magnetization on the order of 1 mT could still be detected, which skews the data somewhat towards higher offset voltages by ~ 100 μ V. Many practical applications utilize various offset compensation schemes to combat the influence of V_{OFF} . When the doped epigraphene Hall sensors was measured using Van der Pauw averaging, in combination with orthogonal coupling of two identical Hall sensors (requires uniform doping) [102], the final offset was readily reduced to < 1 μ V. Furthermore, current spinning techniques is commonly used to eliminate offset entirely for practical applications [102].

6.5 Noise Characterization

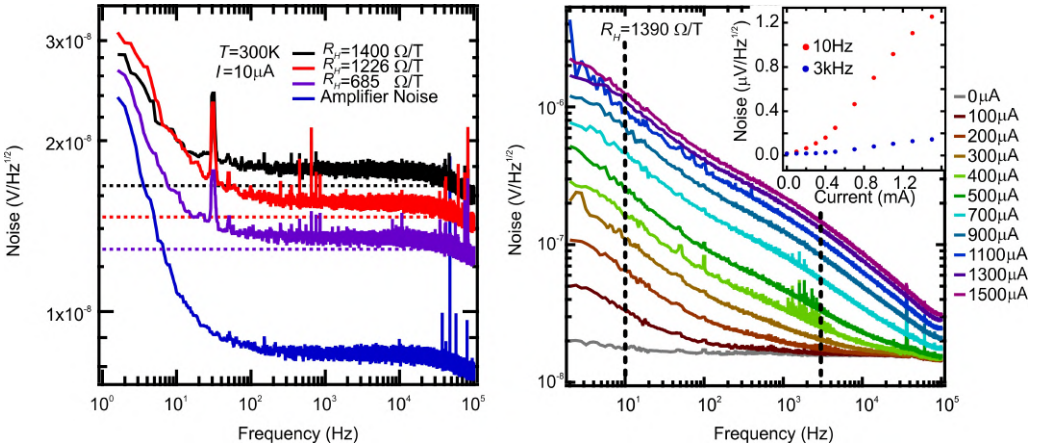


Figure 6.6: **Left:** Noise spectral density V_N versus frequency measured at fixed current, but with different doping levels. The blue curve is the measured base line noise of the amplifier. The dotted lines are calculated noise levels assuming purely thermal noise of a resistor (including amplifier noise). The corner frequency for $1/f$ -type noise for low current bias is below 100 Hz. Note that noise peaks related to power lines (50 Hz etc.) have been partially filtered out digitally. **Right:** Noise spectral density versus frequency for the lowest doping level at different bias currents. The dotted vertical lines indicate two frequency cuts (10 Hz and 30 kHz) where the noise spectral density is plotted versus bias current (inset).

The noise performance of a sensor has a large impact on the detection limit. For Hall sensors, the minimum detectable magnetic field is $B_{MIN} = \frac{V_N}{I_B R_H}$ where V_N is the voltage

spectral density. Figure 6.6 shows the noise characteristics for epigraphene Hall sensors. The noise was measured by biasing the Hall sensor using a battery source and sampling the zero-field Hall voltage (basically V_{OFF}) at 200 kHz. The frequency is limited by the 100 kHz bandwidth of the amplifier (DLPVA-100-F-D from Femto Messtechnik GmbH), which has a measured input noise of $9 \text{ nV}/\sqrt{\text{Hz}}$. The first plot shows the measured device noise as a function of three different doping levels, using a low current bias of $10 \mu\text{A}$. The corner frequency of the $1/f$ -noise is below 100 Hz, with the noise quickly saturating at higher frequencies. The noise dip towards 100 kHz occurs because the frequency approaches the bandwidth limit of the amplifier. The noise base level increases as the carrier density decreases (resistance increases), which points to thermal noise of resistor being the dominant noise source. This is further confirmed because the calculated thermal noise derived from measurements of the input resistance of the Hall sensor matches the direct noise measurements, including amplifier noise (dotted lines). There is a slight discrepancy between the theoretical value and the measurement data, but this is likely due to other noise sources stemming from the measurement setup itself.

Figure 6.6 also shows that the noise amplitude scales with bias current. Hooge's empirical noise relation [110] states that for noise stemming purely from resistance (carrier density) fluctuations, the noise voltage spectral density scales linearly with bias current as $V_N \propto I_B$. The full equation is $(\frac{V_N}{I_B R})^2 = \frac{\alpha_H}{N_f}$, where R is the device input resistance, N the total number of available carriers, f frequency, and α_H the Hooge parameter, which is a measure of the noisiness of a system. The plot in the inset shows that the noise amplitude scales roughly linearly with bias current, especially at higher frequencies. The deviation from ideal linear behavior can be attributed to joule heating [111] and carrier density excitations [112], both which are not taken into account in Hooge's model. The Hooge parameter can be estimated by taking a linear fit to V_N versus I_B , and using the corresponding input resistances ($3500 - 7000 \Omega$), carrier densities ($4.4 \times 10^{11} - 1.38 \times 10^{12} \text{ cm}^{-2}$), device area ($100 \times 100 \mu\text{m}^2$), and frequency (3 kHz). The resulting Hooge parameter is in the range of $\alpha_H \approx 10^{-5} - 10^{-4}$, depending on doping level. For comparison, this is lower than reported values for even suspended graphene samples[113], and comparable to GaAs [114], which means that the noise level for doped epigraphene Hall devices is excellent.

6.6 Figures of Merit

The aforementioned measurements investigated the carrier density, mobility, and noise, and they all culminate in the calculation of the three important figures of merit for Hall sensors: S_I , S_V , and B_{MIN} . Figure 6.7 show the collection of figures of merits obtained from all seven tested epigraphene Hall sensors, at various doping levels.

Since S_I is essentially the same as R_H , the data set (orange region) fall on a straight line with unity slope. S_I is maximized at the lowest doping possible, same as where R_H is maximized. The best value of $S_I \approx 1440 \text{ V/AT}$ is limited by the observed charge disorder at room temperature, which sets the minimum attainable carrier density to $|n| < 5 \times 10^{11} \text{ cm}^{-2}$. S_V is related to the carrier mobility, and makes an arc shape (purple region) as a function of R_H . The shape is a direct consequence of how sheet resistance

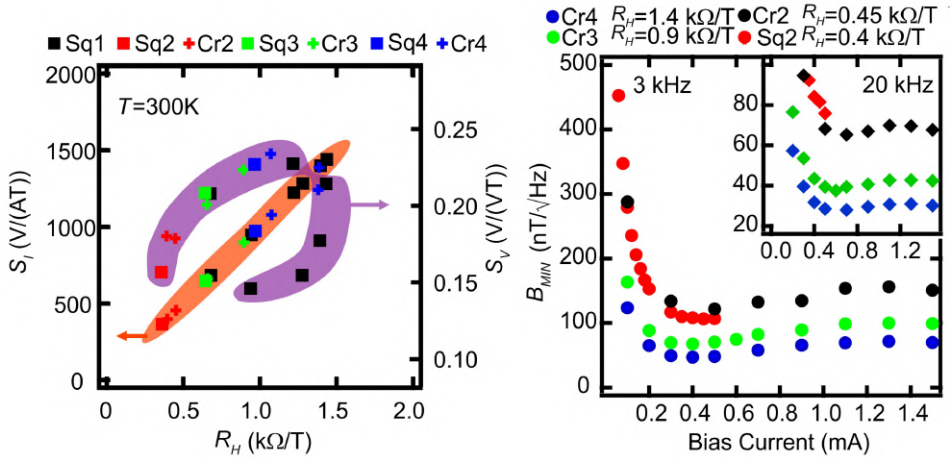


Figure 6.7: **Left:** Figures of merit S_I and S_V versus R_H , collected from seven Hall devices with various doping levels. **Right:** Minimum field detection limit B_{MIN} versus bias current at 3 and 20 kHz. The observed local minimum at around 0.5 mA is due to the non-linear evolution of voltage spectral density with bias current. The best value is $B_{MIN} = 27 \text{nT}\sqrt{\text{Hz}}$, for $R_H = 1400 \Omega/\text{T}$ at 20 kHz.

depends on doping (Figure 6.2). S_V is maximized when mobility is the highest, which occurs just outside the puddle regime. At $R_H \approx 1000 \Omega/\text{T}$, the highest value is $S_V = 0.23$, which in terms of mobility is $\mu = 2300 \text{cm}^2/\text{Vs}$.

B_{MIN} is calculated directly from noise characteristics like those shown in the inset of Figure 6.6, which means that it also includes external noise sources from the measurement setup. The detection limit is a measure of the minimum detectable magnetic field limited by device noise, and is therefore the practical detection limit for a Hall sensor. B_{MIN} is in general lower (i.e. the best performance) for lower doping levels, and higher frequencies. The sensor frequency of 3 kHz is used for fair comparison with other graphene-based Hall sensors, but there is no practical reason for that limit, and performance is even better at 20 kHz and onward. B_{MIN} also depends on the bias current, with an observed local minimum point around 0.5 mA for the studied samples. The appearance of a local minimum is due to the experimentally observed non-linearity of voltage spectral density. In the ideal case of perfectly linear voltage spectral density versus bias (Hooge type), B_{MIN} should theoretically change monotonously as $1/I_B$.

Table 6.1: A comparison table over figures of merit for room temperature Hall sensor performance. The entries in the last two rows show examples of doped epigraphene Hall sensor performance taken from this work.

Type	S_I (V/AT)	S_V (V/VT)	B_{MIN} (nT/√Hz)	Freq (kHz)
$\text{Si}^{[102, 115]}$	100	0.1	50 – 500	0.1-100

Continued on next page

Table 6.1 – *Continued from previous page*

Type	S_I (V/AT)	S_V (V/VT)	B_{MIN} (nT/ $\sqrt{\text{Hz}}$)	Freq (kHz)
InSb ^[102–105]	140 – 700	1 – 7.2	1 – 60	0–50
GaAs ^[102–105]	30 – 3200	0.6 – 1	10 – 6000	0–50
hBN-G ^[116]	4100	2.6	50	3
CVD ^[112]	2093	0.35	100	3
CVD ^[117]	1200	N/A	300000	3
CVD ^[118]	97	0.03	400000	1
Epigraphene ^[119]	1021	0.3	2000	3
Doped Epi	1080	0.23	60, 40	3, 20
Doped Epi	1442	0.21	47, 27	3, 20

Table 6.1 shows a collection of Hall sensor figures of merits. The two entries which represent doped epigraphene Hall sensors are chosen to either maximize S_V or S_I . Compared to other reported graphene Hall sensors, doped epigraphene compares very favorably, especially in terms of B_{MIN} . The minimum detectable magnetic field B_{MIN} is in essence what will limit the sensitivity of a practical sensor, since it takes into account the device noise. Of special note is that epigraphene can match, and even exceed, the detection limit of hBN-encapsulated graphene flakes, which is typically the graphene with the highest electronic quality. The value of $B_{MIN} = 27 \text{ nT}\sqrt{\text{Hz}}$, for $R_H = 1400 \Omega/\text{T}$ at 20 kHz is the best reported value in literature for graphene thus far. Epigraphene also compares favorably to common commercial Hall sensors like Si. However, ultra-sensitive InSb and GaAs Hall sensors can still be superior when it comes to detection limit, at least at room temperature.

6.7 Thermal Stability

Another important aspect of a Hall sensor is its performance at elevated temperatures. All Hall sensors degrade in performance as the temperature is increased, due to a combination of factors such as reduced Hall voltage and increased thermal noise. For commercial sensors, this degradation is usually expressed as a temperature coefficient Δ_T , which is defined as the percentage change in Hall voltage (or resistance) relative to its room temperature value per Celsius.

For doped epigraphene Hall sensors, the measurement of the temperature coefficient is not as straightforward, especially at elevated temperatures. This is because annealing can induce a permanent doping change, which is normally intentionally exploited to tune the initial device carrier density. However, this is problematic for a sensor since the performance will at some point suffer from hysteresis in temperature. The temperature coefficient should ideally be defined only for temperature regimes where there is no permanent doping change during thermal cycling.

The heating of doped epigraphene Hall sensors was investigated using in-situ sample heating by a ceramic heater. The temperature was tracked using an on-chip diode

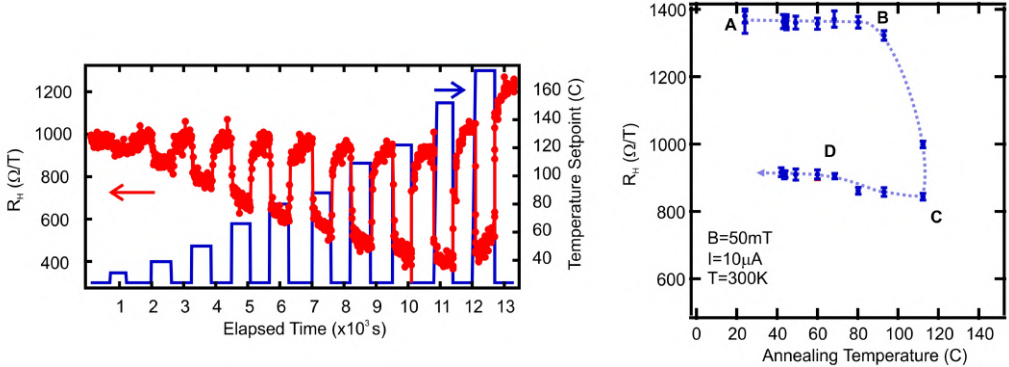


Figure 6.8: *Left:* Example of Hall measurement with *in-situ* heating for an initially *p*-doped sample $R_H \approx 1000 \Omega/\text{T}$. The heating occurs in steps, with the sample being heated at elevated temperatures for 10–15 min before it is allowed to cool down to room temperature. The Hall voltage is monitored in real time using a fast sweeping coil magnet. The doping changes as the temperature does, but returns to its room temperature value upon cool down. Clear permanent change towards more *n*-doping occurs only after 100°C . The dip in R_H indicates that the doping passed through Dirac point, from *p*-type to *n*-type. *Right:* An *n*-doped sample $R_H \approx 1400 \Omega/\text{T}$ is heated using *in-situ* heat sweeps. The data shows the measured room temperature Hall coefficient after the sample has cooled down, versus annealing temperature. The data has been averaged over 5–10 min of measurements, and error bars represent two standard deviations. A clear permanent doping change occurs after heating above 80°C . After the initial change, no further permanent change of doping occurs for annealing below 80°C .

thermometer, and the magnetic field was supplied by a coil magnet which performed fast sweeps < 1 min of magnetic fields up to $10 - 50$ mT. This setup allowed for real-time measurements of the Hall voltage and resistance as the sample was heated. Figure 6.8 shows an example of a temperature sweep in the first plot. The heating occurred in steps, and the sample (red points) was kept at each elevated temperature set-point (blue curve) for 10–15 min, and then allowed to cooled down back to room temperature for 10–15 min. Note that the first sweep shows an apparent dip in R_H because the sample was *p*-doped and passed through Dirac point after heating above 100°C . Nonetheless, there is a clear permanent change in doping level after some point during the annealing process. To investigate this further, similar kinds of sweeps were used to construct the second plot, which shows the room temperature Hall coefficient after annealing up to a certain max temperature. Each point is the average of the R_H values after temperature has stabilized at the set-point, and the error bars represent two standard deviations. The sample started initially as *n*-doped with $R_H \approx 1400 \Omega/\text{T}$ (Point A). No significant change occurred in doping until the maximum temperature passed 80°C , after which the room temperature *n*-doping significantly increased (Point C). After the sample has undergone annealing at higher temperatures for an extended amount of time (~ 1.5 hours total), annealing below 80°C induces no further permanent change in doping. This reveals that

the lowest annealing temperature which can tune the doping level appears to be 80 °C. Furthermore, it hints at that the doped samples can be "cured" after prolonged heating at some temperature and for some time, after which the sample becomes robust against thermal cycling. Note however that the carrier density may still undergo change with temperature, but it is reversible change below the curing temperature.

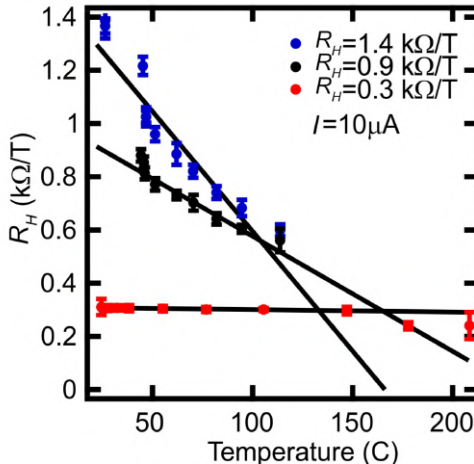


Figure 6.9: *Hall coefficient versus sample temperature for three different doping levels. The error bars represent two standard deviations for R_H averaged over 5 – 10 min of measurements, when temperature was stable. The solid black lines are linear fits to the lower temperature regime, with no permanent doping change. The blue and black data represent normal doped epigraphene Hall sensors, without any curing step. They undergo permanent doping change after passing 80 °C. The red data represent a cured sample which has been annealed for ~ 4 hours at 160 °C, and is resistant against thermal cycling up to at least 150 °C.*

In order to further test the curing, a sample was annealed at 160 °C for ~ 4 hours. After this lengthy curing procedure, the carrier density saturated at a high n-doping level $n = 2.1 \times 10^{12} \text{ cm}^{-2}$ and $R_H = 300 \Omega/\text{T}$. The observed doping level is very close to the resulting doping from neat PMMA deposited on epigraphene ($n \approx 3 \times 10^{12} \text{ cm}^{-2}$), and indicates that the doping effect of F4TCNQ is almost gone, possibly due to complete desorption of dopants. Figure 6.9 show the measurements of R_H versus sample temperature, which can be used to extract the temperature coefficient Δ_T through linear fitting. The fits are only performed for data measured at low enough temperatures where no permanent change in doping occurs. For the lowest two doping levels $R_H = 1400 \Omega/\text{T}$ and $R_H = 900 \Omega/\text{T}$, the temperature coefficient is $\Delta_T = -0.6\%/\text{°C}$ and $\Delta_T = -0.5\%/\text{°C}$ respectively. Since these sample were not cured, they underwent permanent doping change after 80 °C. On the other hand, the highest n-doped sample $R_H = 300 \Omega/\text{T}$ was cured, and has a low temperature coefficient of $\Delta_T = -0.03\%/\text{°C}$ up to at least 150 °C. When passing the curing temperature of 160 °C, the doping level undergoes permanent change yet again. It is expected that curing at even higher temperatures will increase the thermal stability

further. The highest n-doping is possibly limited by PMMA doping of epigraphene to $n \approx 3 \times 10^{12} \text{ cm}^{-2}$.

The thermal stability, i.e. temperature coefficient, of R_H is influenced by the thermal excitation of carriers in epigraphene. This process is dependent on doping since the Fermi energy acts as an energy barrier, and defines the intrinsic temperature coefficient of epigraphene itself. Furthermore, the F4TCNQ dopants also likely play a role, since their diffusion is temperature dependent. The low temperature coefficient of the cured sample $\Delta_T = 0.03\%/\text{ }^\circ\text{C}$ is achieved through a combination of higher n-doping as a result of annealing, and a decrease in active dopant molecules, and it is therefore closer to the intrinsic stability of epigraphene itself. The cured sample compares very favorably to industrial Hall sensors [102–105] in terms of stability and operating temperature range. Additionally, the epigraphene Hall sensor maintains a respectable device performance even at $150\text{ }^\circ\text{C}$ with $S_V \approx 0.12 \text{ V/VT}$, $S_I \approx 300 \text{ V/AT}$, and $B_{MIN} \approx 100 \text{ nT}/\sqrt{\text{Hz}}$. Here S_V and S_I are measured values, while B_{MIN} is estimated from the noise voltage spectral density, whose temperature scaling is assumed to be the same as for thermal noise of a resistor. While doped epigraphene Hall sensors does not outperform ultra-sensitive III-V based sensors (e.g. GaAs) at room temperature, there is potential to outperform them at higher temperatures, in the industrial automotive and military ranges. These prospects are promising because the intrinsic temperature coefficient of epigraphene appears to be low, and the main issue is to develop an improved and more temperature-resistant doping scheme.

6.8 Conclusions

In conclusion, F4TCNQ doping method was used to investigate the performance limits of epigraphene Hall sensors. This method allows for reproducible fabrication of high-quality low-noise sensors with a wide range of carrier densities. It was found that doped epigraphene Hall sensors with low carrier densities can have respectable room temperature performance with sensitivities $S_I = 1442 \text{ V/AT}$, $S_V = 0.23 \text{ V/VT}$, and record-low detection limit $B_{MIN} = 27 \text{ nT}/\sqrt{\text{Hz}}$ at 20 kHz. The doped Hall sensors were also tested at elevated temperatures, and it was found that using thermal curing, the doped Hall sensors can be thermally stable with temperature coefficient $\Delta_T = 0.03\%/\text{ }^\circ\text{C}$ up to $150\text{ }^\circ\text{C}$, while maintaining a good sensor performance at $150\text{ }^\circ\text{C}$ with $S_I \approx 300 \text{ V/AT}$, $S_V \approx 0.12 \text{ V/VT}$, and a detection limit $B_{MIN} \approx 100 \text{ nT}/\sqrt{\text{Hz}}$.

The doped epigraphene Hall sensors have the lowest detection limits compared to other graphene-based sensors in literature, and they also posses very low device noise levels. The fabrication techniques are demonstrably reliable, with excellent contact resistances and homogeneous doping. In combination with the fact that epigraphene can be grown over large area, it is entirely feasible to create sensitive epigraphene Hall sensors arrays. A single standard epigraphene chip $7 \times 7 \text{ mm}^2$ could for instance fit hundreds of Hall sensors or more.

The conventional III-V type sensors still reign supreme at room temperature in terms of detection limit. However, their weakness is high temperature performance, where most of them quickly lose their capabilities. The thermally cured epigraphene chip shows

promise in this regard, with the demonstrated performance at 150 °C already outpacing many commercially available sensors [102–105]. The main weakness lies in the current doping method, which is poorly suited to high temperatures. Future prospects rely on the development of either a new doping scheme, a new encapsulation scheme, or both. The goal is to find a way to keep the carrier density of doped epigraphene Hall sensors low, and stable, even at elevated temperatures.

7 Coherent THz Detection

The terahertz (THz) portion of the radiated energy originating from the cosmos is of special interest because it contains spectroscopic fingerprints of a myriad of chemical compounds, including the building blocks of life such as water, oxygen, and carbon. These molecules, and many others, have spectroscopic fingerprints in the THz frequency range loosely defined as $f \approx 0.1 - 10 \text{ THz}$ and $\lambda \approx 300 - 30 \mu\text{m}$. Astronomers therefore utilize THz signals to monitor the chemical compositions of remote areas of space. Furthermore, THz waves have a relatively large wave length and do not interact much with the smaller grains of interstellar dust which permeates all of space [120]. This makes THz signals a powerful probe which can pierce through the interstellar medium and allow for unclouded studies of astronomical events like the birth and death of stars.

The first type of detector which was used for THz astronomy was the bolometer, and they are still central to astronomy to this day. Bolometers belong to the family of *incoherent* detectors, which are sensitive to the power of incoming radiation, but not the phase of the incident photons. This detection scheme relies on the absorbed photons heating the bolometer, which leads to a measurable change in resistance. Bolometers are commonly used for broadband observations (e.g. interstellar dust), where they provide a superior signal-to-noise per integration cycle [120].

In order to retain the phase information of the photon, coherent detection technique are required. This can be achieved by using a local oscillator (LO) to effectively stamp the phase of the incoming photons [120]. The basic coherent receiver uses heterodyning, or mixing, of an input signal with the LO in order to detect weak signals, down-convert THz signals to a more tractable frequency range, and to deal with measurements which require high spectral resolution (e.g. star forming nebulae). This technique relies on non-linear elements to achieve mixing.

The current challenge for modern THz astronomy is to advance from coherent detection reliant on a few devices (pixels), to large scale imaging using sensitive arrays with over 1000 pixels, operating in the whole THz range. Arrays are practically important because they allow for much faster data acquisition rates and higher sensitivities [121, 122]. For applications in space-borne missions, it is also crucial that the arrays are light-weight, compact, and power efficient. Due to these stringent requirements, no coherent large array detectors have been realized thus far. Established THz detectors are held back by intrinsic material properties, which either limit detection to frequencies to below 1 THz, or have prohibitively large power consumption requirements. There is a need for new materials, and this is where epigraphene enters the picture.

In this chapter molecular doped charge neutral epigraphene is explored as a sensitive bolometric mixer for coherent detection in the THz regime, with potential for low-power quantum-limited heterodyne detection for applications in astronomy. This chapter covers the results presented in **Paper F**, in which the contributions from this thesis are mainly related to sample preparation and DC characterization. For more detailed description of THz astronomy in general see [120].

7.1 Heterodyne Detection

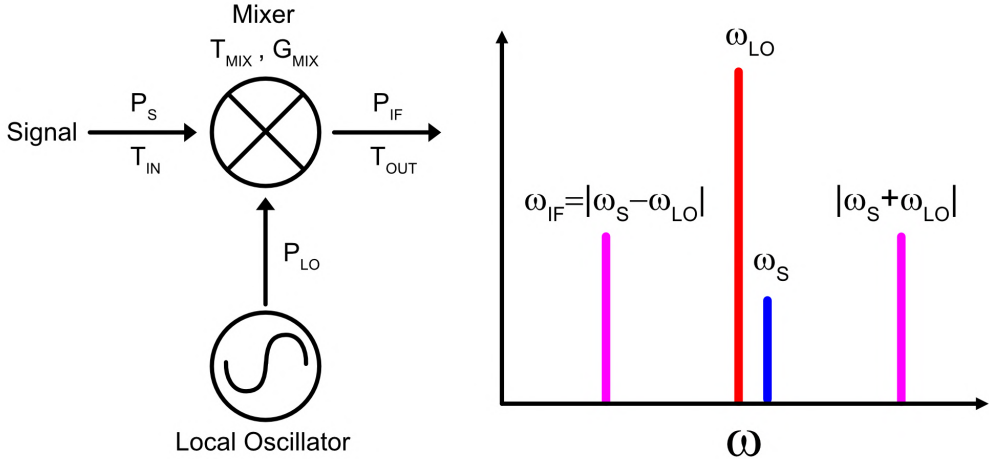


Figure 7.1: **Left:** Schematic representation of a heterodyne receiver system. The input signal P_S is mixed with a local oscillator signal P_{LO} , resulting in the intermediate frequency signal P_{IF} . The mixer has a gain G_{mix} and T_S , T_{mix} , and T_{out} are the noise temperatures at each stage. **Left:** Schematic representation of mixing in the frequency domain, showing both lower (ω_{IF}) and upper sidebands.

Heterodyne detection techniques work by mixing a signal of interest at power P_S , with an intense monochromatic light emitted by a local oscillator (LO) at power P_{LO} (Figure 7.1). The input signal and LO lie close to each other in frequency, with angular frequencies denoted ω_S and ω_{LO} respectively. The mixing is performed by some non-linear element, and results in a new mixed signal $F(t)$ with two components:

$$F(t) \propto \sin(\omega_{LO}t)\sin(\omega_S t) = \frac{1}{2}\cos((\omega_{LO} - \omega_S)t) - \frac{1}{2}\cos((\omega_{LO} + \omega_S)t) \quad (7.1)$$

The higher frequency component can be filtered out, making this a single sideband (SSB) mode. The remaining lower frequency component, henceforth referred to as intermediate frequency f_{IF} , is determined by the frequency difference between the two input signals, as $f_{IF} = |\omega_{LO} - \omega_S|/2\pi$. This is also how heterodyning allows for down-conversion from the more practically challenging THz range to the easier microwave range, where more developed detection capabilities like low-noise amplifiers exist.

An important figure of merit for a heterodyne mixer is the noise temperature T_{mix} , because it is what ultimately limits the device sensitivity. The noise temperature is related to the noise contribution of a component expressed in terms of temperature, related to the power spectral density of Johnson-Nyquist noise for a resistor at the same physical temperature. This parameter is crucial for heterodyne mixers used beyond the

atmosphere, because for space-borne missions it is mainly the mixer noise temperature which limits the performance of THz receivers [120].

A mixer component (see Figure 7.1) has a noise temperature of $T_{mix} = \frac{P}{\Delta f k_B G_{mix}}$, where P is mixer noise power, Δf bandwidth, k_B Boltzmann constant, and G_{mix} the mixing gain [120]. The noise temperature can also be expressed as $T_{mix} = T_S/G_{mix}$, where T_S is the noise equivalent temperature of the mixer. The relationship between these two temperatures is that T_{mix} is equivalent to the noise power at the input of the mixer that would be amplified by an ideal amplifier with gain G_{mix} , in order to cause an equivalent signal power T_S at the output. If the mixer uses both upper and lower frequency bands (Figure 7.1) it is considered to be in double sideband (DSB) mode, and the noise temperature changes by a factor of 2 compared to the single sideband case $T_{SSB} = 2T_{DSB}$. In practice, there will also be noise contributions from other electrical components placed after the mixer like low-noise amplifiers etc.

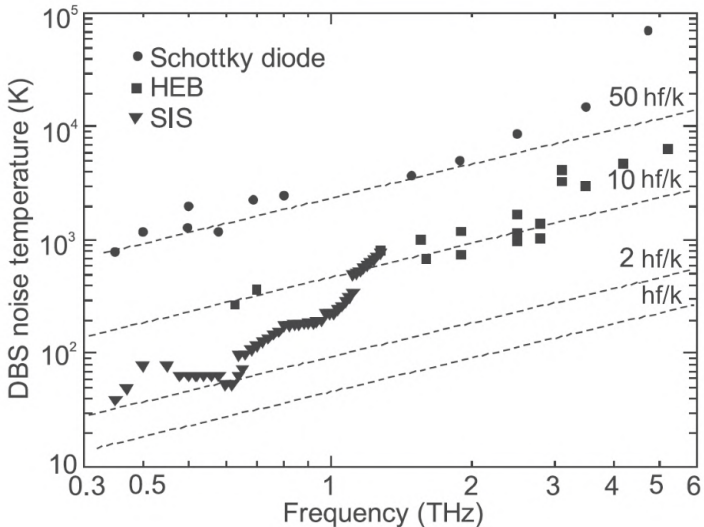


Figure 7.2: Comparison of noise temperature for common types of mixers. The dotted lines represent comparisons to quantum limited performance, where the ultimate limit is hf/k , where h is Planck constant, f operating frequency, and k Boltzmann constant. Taken from [123].

The mixer can in principle be constructed from any nonlinear device. Commonly used components in THz astronomy, which have non-linear I-V characteristics, are Schottky diodes, superconductor-insulator-superconductor (SIS) junctions, and hot electron bolometers (HEB). Their noise temperatures are shown for comparison in Figure 7.2. The most sensitive mixers are based on superconductors, but they are limited in frequency to below 1 THz. In the > 1 THz range, the mixers typically operate with a noise level an order of magnitude above the quantum limit.

This work focuses solely on HEB mixers, which play a crucial role in modern astronomy in the 1 THz range and beyond. The working principle is that a non-linear I-V response

is used to generate the mixed signal with an intermediate frequency. The incident THz signal and LO cause temperature oscillations in the material, with a corresponding modulation of electrical resistance R at f_{IF} . This is predicated on the assumption that the temperature change can keep up with the signal modulation, which puts constraints on the thermal properties of the mixer material. The maximum attainable f_{IF} is limited by how quickly heat can be transferred out from the mixer. For the commonly used superconducting HEB mixers, the limiting processes are either phonon cooling determined by the electron-phonon coupling, or diffusion cooling of hot electrons through the electrical contacts determined by the diffusion constant and device size [124, 125]. In practice, the performance of common NbN-based superconducting HEB mixers has a limited gain bandwidth of $f_0 = 4 - 5$ GHz [126]. Other superconductors can increase the bandwidth, but at the expense of increasing LO power requirements [127], which is problematic for heterodyne arrays.

7.2 DC Characterization of Epigraphene HEB

Graphene is an attractive material for HEB applications due to its low heat capacity, which is conducive to a fast device response [128]. However, it is known to have a weak to non-existent temperature dependence of resistance [126, 127, 129]. As discussed in Chapter 4.2, molecular doping of epigraphene close to the charge neutrality results in a sizable temperature dependence of resistance. In that regime, the electron transport phenomena becomes dominated by quantum effects like weak-localization and electron-electron interactions, and this leads to a logarithmic temperature dependence of conductance $\sigma(T)$:

$$\sigma(T) = \sigma_0 + \sigma_1 \ln(T) \quad (7.2)$$

Here T is the temperature in Kelvin normalized by $T = 1$ K. The temperature dependent term is related to quantum corrections and its strength is on the order of one conductance quantum $\sigma_1 \approx e^2/h \approx 3.9 \times 10^{-5}$ S. The emergence of quantum interference effects is desirable because it gives epigraphene a significant temperature dependence of resistance at low temperatures, enabling its use as a thermometer. As mentioned in Chapter 2.3.5, and seen in Figure 4.12, the quantum interference effect grows as carrier density decreases, which makes charge neutral epigraphene attractive as a resistance thermometer. However, care must be taken near the vicinity of the Dirac point due to the presence of the disordered charge puddle regime. Excess charge disorder can effectively decrease the contribution from quantum transport phenomena and lead to a saturation of the low-temperature resistance [7, 8]. On the other hand, low charge disorder will allow for the monotonous increase of resistance to persist at much lower temperatures [90, 130].

Two devices were fabricated on the same chip, one Hall bar and one interdigitated bolometric mixer. The Hall bar geometry allowed for four probe measurements and was used for material characterization. The Hall measurements were used to gain information about carrier density n , mobility μ , mean free path $\ell = \hbar\mu\sqrt{n\pi}/e$ [8], and diffusion coefficient $D = v_F l/2$ [131], where $v_F \approx 1 \times 10^6$ m/s [7]. Additionally, the Hall bar was used as a reference for the the temperature dependence of 2-probe resistance of the mixer, to verify that the mixer retained the same properties as large-area doped epigraphene.

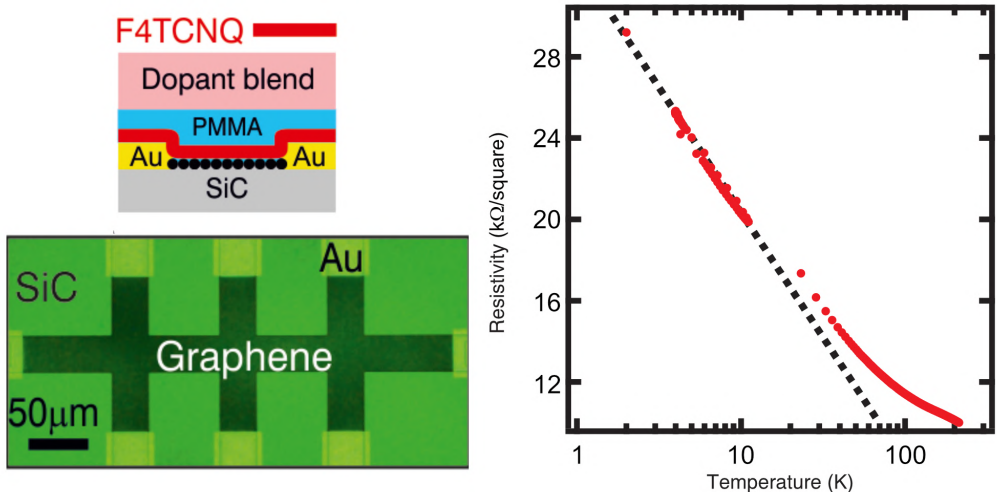


Figure 7.3: **Left:** Optical micrograph showing the dimensions of the doped epigraphene Hall bar. The inset shows a schematic representation of the doping scheme. **Right:** Temperature dependence of longitudinal resistivity. The dotted fit to low-temperature data shows a logarithmic temperature scaling $\rho \propto \ln(T)$, which persists down to 2 K.

Figure 7.3 shows measurements for a doped Hall bar using the standard PMMA spacer and dopant blend layer, with carrier density tuned close to charge neutrality. The Hall bar device was fabricated using dimensions $L = 180\text{ }\mu\text{m}$ and $W = 30\text{ }\mu\text{m}$. The sample was measured in a liquid helium cryostat, and a logarithmic temperature dependence of resistance was observed at lower temperatures $< 20\text{ K}$, as described in Equation 7.2, with a slope of $\sigma_1 \approx 0.3e^2/h$. Note that there is a temperature offset between high ($> 30\text{ K}$) and low temperature ($< 20\text{ K}$) data, which arises from thermal lag due to rapid cooling. The sample was cooled down to 2 K and then slowly warmed up to measure the low temperature data set.

The Hall bar was also studied at cryogenic temperatures using magnetotransport to ascertain the doping level and to confirm the nature of the observed quantum correction phenomena. Figure 7.4 shows the quantum Hall measurements performed at 4 K. The imperfect quantization points to the fact that the sample is in the disordered puddle regime, and the carrier density is therefore estimated to be on the order of the charge disorder (see Chapter 4.6) of doped epigraphene $n \approx 1 \times 10^{10}\text{ cm}^{-2}$, resulting in an estimated mean free path $\ell \approx 25\text{ nm}$ and diffusion coefficient $D \approx 125\text{ cm}^2/\text{s}$. Note that the disorder, i.e. minimum carrier density, can be even lower for lower temperatures. Figure 7.4 also demonstrates that the quantum corrections to resistance can be suppressed using a perpendicular magnetic field $< 1\text{ T}$, which indicates that they originate mostly due to quantum interference effects. The quantum corrections for this particular device also disappear above 30 K.

Once the logarithmic temperature dependence due to quantum corrections was established, the experiments proceeded to the epigraphene THz mixer device. The epigraphene

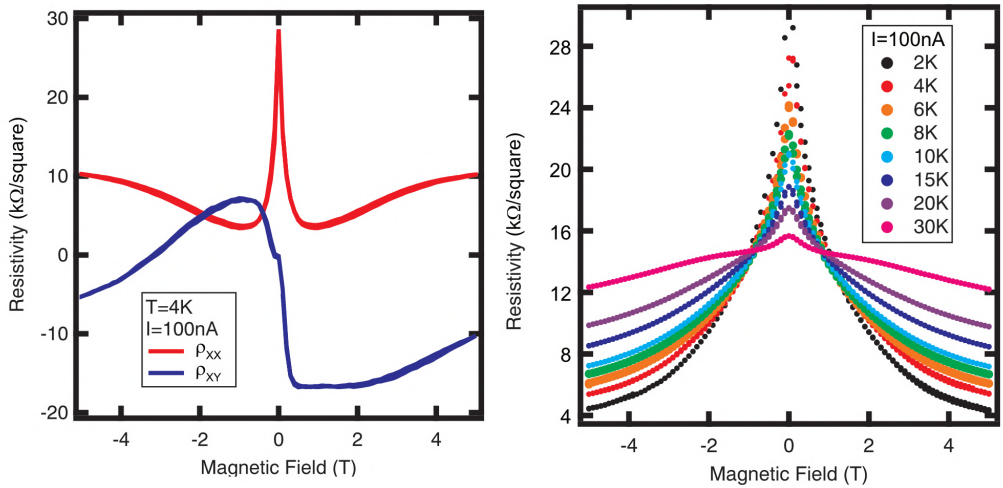


Figure 7.4: **Left:** Quantum Hall effect measurements reveal that the sample is in the disordered charge puddle regime. **Right:** Temperature dependence of quantum corrections to resistance, which gets suppressed with both increasing magnetic field and temperature. The quantum interference effects vanish above 30 K.

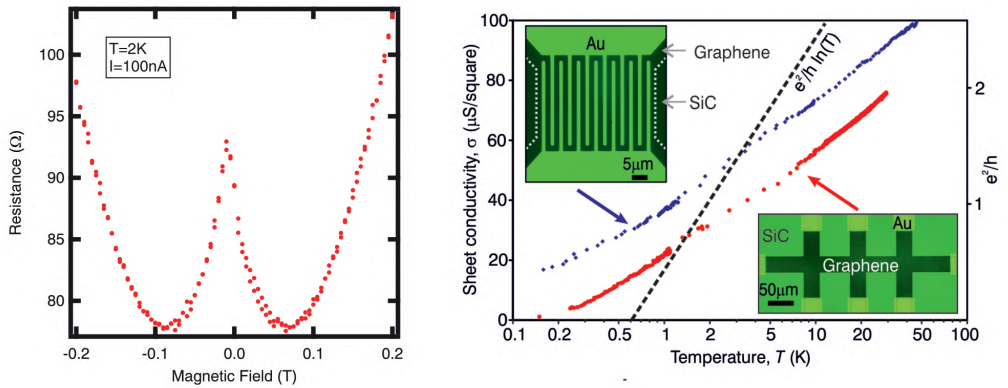


Figure 7.5: **Left:** Two-probe magnetotransport data for epigraphene HEB shows that a perpendicular magnetic field can suppress corrections to longitudinal resistance, which signifies that they originate from quantum interference effects. **Right:** Temperature dependence of conductivity, measured for an interdigitated THz mixer device and a Hall bar on the same chip. The logarithmic temperature dependence remains down to 0.2 K for both devices. The dotted line has a slope of one conductance quantum for comparison.

THz mixer device is a two-terminal device and was designed to be closely matched to the impedance of the on-chip antenna and readout electronics (see Figure 7.10). The device

was therefore fabricated using interdigitated electrodes, with an effective epigraphene channel length of $L = 1.5 \mu\text{m}$ and width of $W = 345 \mu\text{m}$, resulting in a parallel connection of approximately 230 squares of epigraphene, with a room temperature resistance of 35Ω and 92Ω at 2 K. Figure 7.5 shows the low-temperature measurements for the epigraphene THz mixer compared to the Hall bar. Two-probe magnetotransport data on the THz mixer show that the low-temperature corrections to resistance arise primarily from quantum interference effects, same as for the Hall bar. The temperature dependence of conductance shows the zero-bias differential conductivity $\sigma(T) = dI/dV|_{V=0}$ measured in a optically shielded cryostat for two different devices. Figure 7.5 shows that both devices display the same logarithmic temperature dependence of resistance, which persists down to at least 0.2 K. The offset in conductance between the two devices is attributed to the presence of bilayer patches, which shunt the epigraphene THz mixer due to the narrow gap between interdigitated electrodes.

7.3 Diffusion Cooling

Initially it was unclear from a theoretical standpoint how quantum interference and strong electron-electron interactions in charge neutral epigraphene could affect the performance of a bolometric mixer device. The logarithmic temperature dependence demonstrated above implies a diverging sensitivity for resistive measurements at low temperature since $dR/dT \propto 1/T \ln^2(T)$. However, the divergence of the electron-phonon cooling time $\tau_{e-ph} \propto 1/T^2 \sqrt{n}$ near charge neutrality, and at low temperatures, limits performance because the device cools down too slowly [132, 133]. This called for direct experimental investigations of the THz mixer, shown below. In the end, it was found that due to the small scale of the device geometry ($\sim \mu\text{m}$), the electronic properties of epigraphene led to diffusion cooling of carriers.

Figure 7.6 shows the differential resistance dV/dI , which makes any non-linearity in the I-V appear more prominent. The measurements were taken at different temperatures and bias currents I_{DC} , for the epigraphene HEB using zero incident THz power. At zero bias current, the resistance is maximal, but at higher bias the resistance decreases due to heating. The inset shows the zero bias conductance extracted from the same data set, which deviates from the ideal logarithmic behavior, suggesting that the sample is being overheated. In order to explain the experimentally observed temperature dependence of the I-V, a thermal model was formulated based on the diffusion cooling of electrons, called the Diffusion Cooling Model (DCM). For more detailed derivations see **Paper F**.

The model considers the situation in Figure 7.7, which shows a schematic representation of an epigraphene device with effective width W and length L , connected to two large metallic leads and biased with a DC current. The incident radiation $I_{ac} \cos(\omega t)$ heats the epigraphene and induces an AC current $I(t) = \sqrt{2} I_{ac} \cos(\omega t)$ which causes time-varying Joule heating. The heating is balanced by a combination of diffusive cooling where charge carriers dissipate heat into the two adjacent metallic leads, and electron-phonon cooling. Ab-initio calculations of the heat-balance equation were solved numerically for three cases: pure phonon cooling, pure diffusion cooling, and the combination of them both [134]. Figure 7.7 shows the measured effective temperature epigraphene T , extracted from $R(T)$

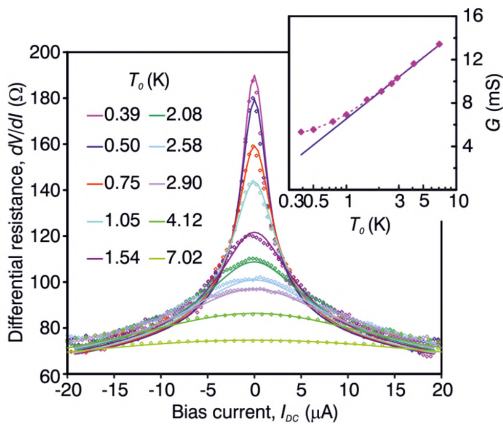


Figure 7.6: Differential resistance of an epigraphene bolometer versus bias current, in the absence of THz radiation. The resistance decreases due to heating, which is dependent on the base temperature. The dots represent real data and the solid lines are fits to the DCM model. The inset shows the temperature dependence of zero-bias conductivity for the same device. Deviation from ideal logarithmic dependence at low temperatures is due to a remnant background radiation P_{Bkg} .

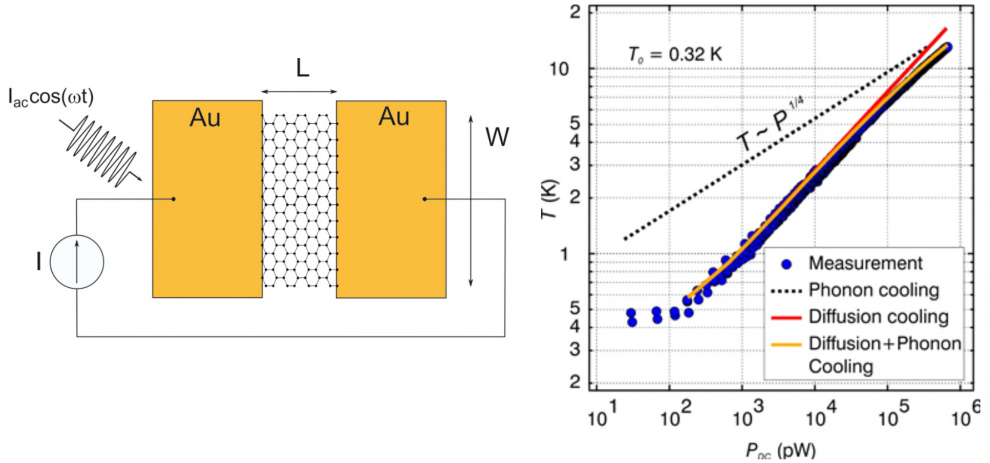


Figure 7.7: **Left:** Schematic view of the epigraphene sample device considered in the DCM. **Right:** Sample effective temperature T versus dissipated power $P_{DC} = IV$, measured at a base temperature $T_0 = 0.32$ K (blue circles). The data is compared to ab-initio calculations for three different cooling models.

experiments and corroborated using noise thermometry, plotted against dissipated power $P_{DC} = IV$, all measured at a base temperature of $T_0 = 0.32$ K. The theoretical calculation which takes into account both phonon and diffusion cooling matches the experimental data in the entire tested temperature range. However, pure diffusion cooling can explain the data below 6 K, meaning that the influence of phonon cooling is not significant at lower temperatures.

At the low temperatures relevant for THz operation (< 6 K), diffusion cooling is the only pathway considered in the DCM. The DCM model also assumes that the Wiedemann-Franz law holds $\kappa/\sigma = L_W T$. It states that the thermal conductivity κ contributes to conductance σ proportional to epigraphene temperature T according to the Lorentz number $L_W = (\pi k_B)^2/3e^2 = 2.44 \times 10^{-8}$ WΩ/K². Furthermore, the model uses the experimental fact that charge neutral epigraphene has a logarithmic temperature dependence of conductivity $G(T) = G_0 + G_1 \ln(T)$, like Equation 7.2. The maximum temperature for diffusion cooled epigraphene according to the DCM:

$$T_{max} = \sqrt{T_0^2 + \frac{I^2 + I_{ac}^2}{I^2} \frac{V^2}{4L_W}} \quad (7.3)$$

It also leads to the following equation for I-V:

$$\begin{aligned} I(V) &= G(T_0)V + G_1 V \left(\frac{\sqrt{1+u^2}}{u} (\sqrt{1+u^2} + u) - 1 \right) \\ u &= \frac{1}{V_T} \sqrt{V^2 + \frac{V}{I} P_{ac}} \end{aligned} \quad (7.4)$$

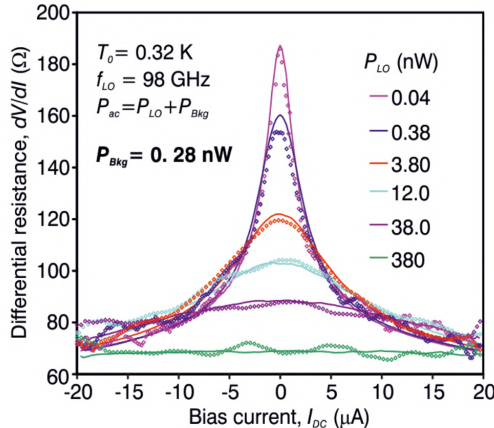


Figure 7.8: The differential resistance measured at constant base temperature $T_0 = 0.32$ K. There is a decrease in resistance under illumination of THz radiation due to heating, which scales with incident power P_{LO} . The solid lines are not fits, but predicted behavior based on the DCM.

Here T_0 is the base temperature of the metallic leads which is constant (cryostat temperature). $G(T_0) = \sigma(T_0)W/L$ is zero bias differential conductivity and $G_1 = \sigma_1 W/L$. The dimensionless parameter u depends on the optical power coupled to epigraphene P_{ac} . The thermal voltage is $V_T = T_0\sqrt{L_W}$. The DCM model Equation 7.4 can be used to produce the fits (solid lines) in Figure 7.6, using fit parameters P_{ac} and L_W . The resulting non-zero power P_{ac} from the fit must come from the remnant background power $P_{Bkg} = 0.28$ nW due to heat leakage, since the external THz source was turned off. This also explains the observed deviation from logarithmic temperature behavior of conductivity shown in the inset, which disappeared for measurements in a optically filtered dark cryostat. The fit also gives a value for the Lorentz number $L_{fit} = 3.1 \times 10^{-8}$ WΩ/K², which agrees well with theoretical predictions.

To further test the predictive power of the DCM, a second measurement was performed at a constant base temperature of $T_0 = 0.32$ K, with varying incident THz power using the setup in Figure 7.9. The data shown in Figure 7.8 plots the differential resistance of the epigraphene HEB measured at constant base temperature, heated by illumination of THz radiation with different power. Using the extracted values of P_{Bkg} and L_W , Equation 7.4 can be used to predict (solid lines) the experimental I-V curves (dots) to a very accurate degree, which further verifies the validity of the DCM model.

7.4 THz Mixer

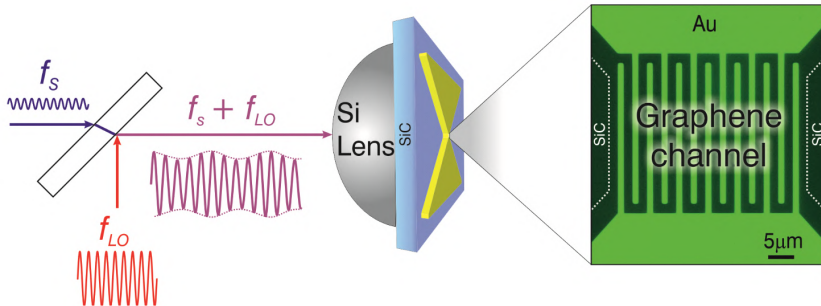


Figure 7.9: Schematic representation of a heterodyne THz setup using a doped epigraphene bolometric mixer. A THz signal at frequency f_s is combined with the local oscillator at a nearby frequency f_{LO} , and both signals pass through a silicon lens and are fed into epigraphene via an integrated antenna. Epigraphene then produces a mixed signal at the intermediate frequency, which can be measured using spectrum analyzers.

THz mixing experiments were performed to study both the response time and frequency mixer sensitivity. Figure 7.9 shows a schematic overview of the mixing experiment. A THz signal with frequency f_s was combined with a monochromatic light emitted by a local oscillator with frequency f_{LO} , and both were directed through a silicon lens towards an integrated bow-tie antenna connected to the interdigitated epigraphene device. The

output signal is then amplified and finally measured using a spectrum analyzer. The setup allowed for simultaneous measurements of DC, THz response, and noise thermometry at temperatures down $T = 0.32$ K. For gain bandwidth measurements, one THz source was kept at constant frequency acting as the local oscillator, while the other source had variable frequency. The resulting THz signal going into the epigraphene device causes an amplitude modulated output signal with an intermediate frequency $f_{IF} = |f_{LO} - f_S|$.

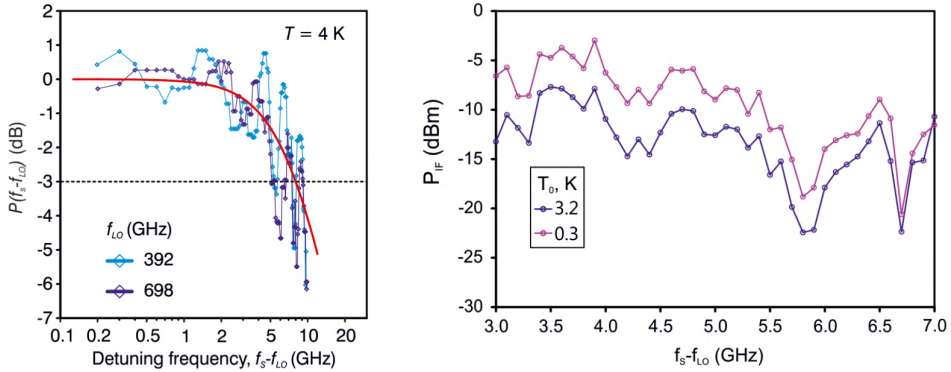


Figure 7.10: **Left:** Measured power at the intermediate frequency P_{IF} versus frequency f_{IF} at 4 K. The horizontal dotted line marks the cutoff $P_{IF} = -3$ dB. The solid line is a fit to $P(f_{IF}) = 1/(1 + (f_{IF}/f_0)^2)$ and yields a gain bandwidth of $f_0 = 8$ GHz. The ripples in the data are due unwanted interference in the measurement setup. **Right:** Gain bandwidth measured at lower temperatures $T_0 = 0.3$ K and $T_0 = 3$ K show that the bandwidth remains high.

Figure 7.10 shows a central result of the THz experiments, where the measured power P_{IF} is plotted against the intermediate frequency f_{IF} . The fitting curve follows $P(f_{IF}) = 1/(1 + (f_{IF}/f_0)^2)$ and leads to a gain bandwidth of $f_0 = 8$ GHz, corresponding to a time constant of $1/2\pi f_0 = 20$ ps for the epigraphene mixer. For comparison, the commonly used NbN-based HEBs have $f_0 < 5.5$ GHz [126, 135]. Figure 7.10 also shows the temperature dependence of the gain bandwidth measured at $T_0 = 0.3$ K compared to $T_0 = 3$ K, and it does not change much with temperature. The intermediate frequency response is similar within a bandwidth of 3 – 7 GHz, limited by the cryogenic low-noise amplifier (LNA) used for 0.3 K measurements. The fast response is due to the high Fermi velocity v_F of carriers in epigraphene combined with highly transparent contacts [59], which leads to quick dissipation of heat via diffusion of hot electrons through metallic contacts. The time scale of 20 ps extracted from grain bandwidth experiments is in good agreement with the estimated time scale from the diffusion constant D determined from DC Hall bar measurements. Using this diffusion coefficient, the time scale for diffusion is limited by channel length $L = 1.5 \mu\text{m}$, and is approximately $\tau_D = L^2/\pi^2 D \approx 18$ ps.

Figure 7.11 shows the mixing gain. Similar to the gain bandwidth, the mixing gain was investigated by simultaneously sending two THz waves, one from the LO and one from another THz source S, to epigraphene. The gain ratio $G_{mix} = P_{IF}/P_S$

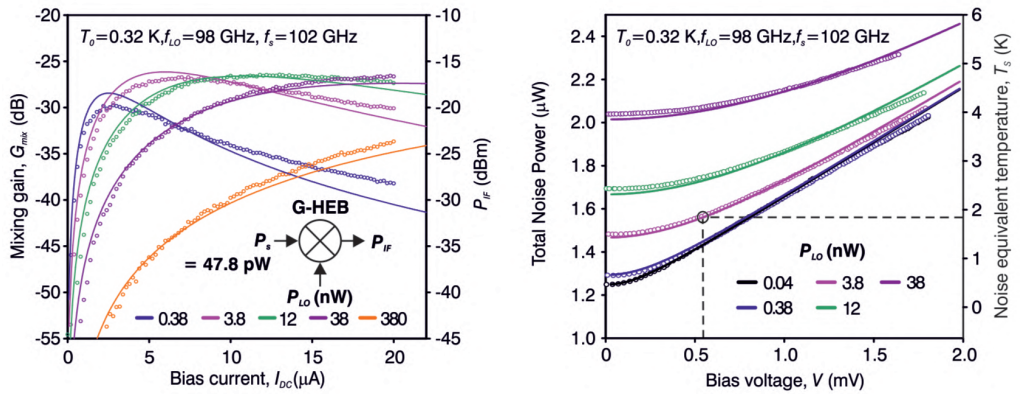


Figure 7.11: *Mixing performance for an epigraphene HEB.* **Left:** Mixing gain G_{mix} at $f_{IF} = 3.5$ GHz versus different LO power P_{LO} . The right y-axis represents measured P_{IF} . Dots correspond to measurements while solid lines are fits to the classical bolometric mixer equation [136]. **Right:** Thermal noise power versus different LO power P_{LO} for $f_{IF} = 4$ GHz. The right y-axis shows the calculated noise equivalent temperatures of epigraphene using DCM and solid lines are fits to the DCM. The dotted lines marks the optimal mixing point, where epigraphene has $T_S \approx 1.9$ K.

describes the relationship between the output power P_{IF} after mixing, and the input signal P_S . The classical bolometric mixer equation [136] fits the data well, and can also be derived using the DCM [134]. The maximum observed mixer gain is $G_{mix} = -27$ dB for $P_{IF}/P_S = 0.2\%$, which was obtained at the optimal mixing gain conditions of $P_{LO} = 3.8$ nW and $I_{DC} = 5$ μA.

Noise thermometry measurements were used to measure the noise equivalent temperature of epigraphene in Figure 7.11. The sample has an effective noise equivalent temperature of $T_S \approx 1.9$ K at the optimal mixing point. Deviation from base temperature T_0 is due to overheating from DC bias and incident radiation P_{ac} . The noise equivalent temperature for epigraphene was also calculated using the DCM, and it matches well with the noise thermometry data [134].

Combining the mixing gain and noise equivalent temperature, the figure of merit for the epigraphene HEB is the mixer noise temperature of $T_{mix} = T_S/2G_{mix} = 475$ K. From the quantum mechanical limit of noise temperature $T_{mix} = 2hf/k_B$ [120], the measured noise temperature is equivalent to quantum limited performance at frequency of $f = 5$ THz and above. The noise temperature ultimately limits the sensitivity of the mixer, however the experimental value is limited by the measurement setup which causes overheating. This is problematic because the sensitivity, and therefore performance, increases at lower temperatures as mentioned.

The validity of the DCM has been cemented by its successful explanation of both the observed DC transport, and the direct and mixing THz response. It therefore justified to use it to predicting future device performance, under more ideal conditions.

7.5 Future Prospects

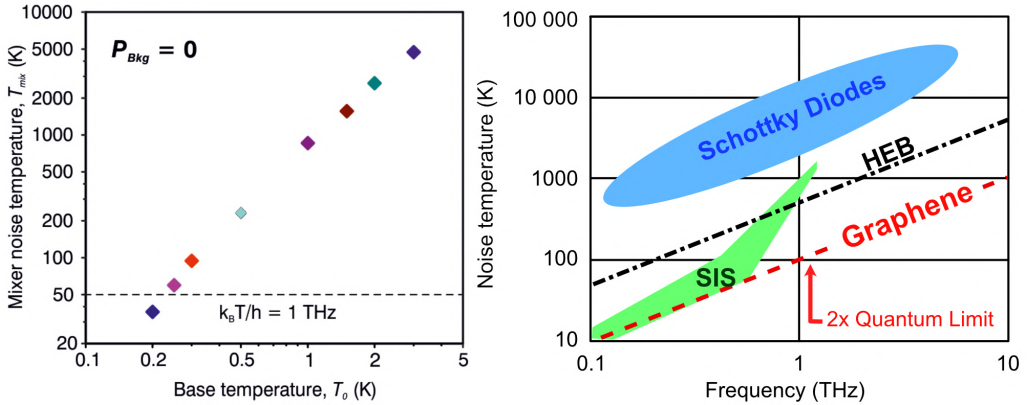


Figure 7.12: **Left:** Extrapolated noise temperature $T_{mix} = T_S/2G_{mix}$ versus base temperature T_0 for zero background radiation. The dotted line marks the noise temperature quantum limit for 1 THz. **Right:** Noise temperature comparison between modern THz mixers and epigraphene. The projected ideal performance of epigraphene-based technology (dashed red line) is closer to the ultimate quantum limit over a wide frequency range. Based on [137].

The aforementioned results demonstrate that epigraphene doped to neutrality could be an interesting technology for future coherent THz detectors. Crucially, the projected power requirements are very low, even reaching $P_{LO} = 0.04 \text{ nW}$ at $T_0 = 0.2 \text{ K}$ (Figure 7.12), which is several orders of magnitude better than current technologies (usually $P_{LO} > 100 \text{ nW}$) [120]. This could enable, for the first time, the development of large arrays of epigraphene HEBs with realistic power consumption requirements for future space missions.

Since the current proof-of-concept iteration was limited by overheating due to the measurement setup, the performance can actually be improved further. For instance, the DCM theoretically predicts that for zero background radiation the mixer noise temperature can be as low as $T_{mix} = 36 \text{ K}$ at $T_0 = 0.2 \text{ K}$ (see Figure 7.12). This means that the doped epigraphene bolometric mixer can in principle operate at quantum limited regime above 0.75 THz. Furthermore, the measured gain bandwidth of $f_0 = 8 \text{ GHz}$ was for a device with $L = 1.5 \mu\text{m}$. If the DCM holds, it is expected that a smaller device $L = 0.8 \mu\text{m}$ can increase the bandwidth to $f_0 = 20 \text{ GHz}$, which is well within reach of current lithographic techniques. Additionally, the achievable mixing gain scales as $G_{mix} \propto (G_1 V/I)^2$, and is limited by the strength of quantum interference effects, which is $\sigma_1 \approx 0.3 e^2/h$ in the current work. This can for instance be changed by playing with the scattering mechanisms via different doping methods. The noise temperature of epigraphene is estimated to be as low as $T_S = 0.4 \text{ K}$ (measured $T_S = 1.9 \text{ K}$), which means that other instruments like amplifiers (best available $T_{amp} \approx 1 \text{ K}$) will limit performance instead. Figure 7.12 shows the ideal projected performance of a doped epigraphene bolometric mixer, and it

illustrates that epigraphene can in principle operate closer to the quantum limit over a wider frequency range compared to modern THz mixers.

7.6 Conclusions

In conclusion, epigraphene doped to charge neutrality using the F4TCNQ dopant blend gives rise to a logarithmic temperature dependence, which was exploited to create a proof-of-concept epigraphene bolometric mixer for coherent THz detection. The epigraphene HEB demonstrated fast device response with mixing bandwidth $f_0 = 8$ GHz, mixing gain $G_{mix} = -27$ dB, and a mixer noise temperature of $T_{mix} = 475$ K, all the while requiring low power $P_{LO} < 1$ nW. The measured device performance, which is already respectable compared to conventional superconductors like NbN, was limited by the measurement setup causing sample overheating, and is not indicative of the intrinsic performance of epigraphene HEBs.

A model based on diffusion cooling of carrier was developed which explained all the experimental observations, including overheating. The model was shown to have predictive powers, and can be used to extrapolate mixer performance under more ideal conditions. The projected performance for doped epigraphene bolometric mixers under realistic space-borne conditions, combined with new advances in instrumentation [138], could lead, for the first time, to the development of large arrays of quantum limited THz detectors, operating across the entire THz regime.

8 Summary & Outlook

This thesis focuses on epigraphene, the study of its properties, and potential applications. The starting point of this PhD research project was marked by the pursuit of a more practical realization of QHR standards based of epigraphene. The unique properties of epigraphene make it attractive for applications in quantum resistance metrology, but historically it was held back by its high intrinsic n-doping and difficulty in controlling its carrier density. There was a need for a stable, potent, reliable, and tunable doping method to gain control over the carrier density. It was desired not only for the sake of metrology, but also to unlock the potential of epigraphene in general.

The linchpin of this thesis is the development of a dopant blend using F4TCNQ stabilized in a polymer matrix. After much study, this combination was found to result in a novel spontaneous assembly of molecules near the surface of epigraphene. Extensive experimental tests show that this reliably leads to large-area, potent, homogeneous doping of epigraphene. Outside improving existing technologies, more interesting future prospects involve taking the essence of the doping scheme, which is spontaneous accumulation templated by 2D materials, and exploring new combinations of polymers, molecules, and 2D systems. The possibilities here are practically endless.

Molecular doping was successfully implemented to solve the initially stated problem of creating practical epigraphene QHR standards. Precision measurements prove that F4TCNQ has no discernible adverse effect on device performance, and it is now possible to create epigraphene devices which can consistently operate as resistance standards. This technology is already being tested in industry, with epigraphene QHR products being commercialized by the Swedish company Graphensic. The product can be further improved by the development of large epigraphene QHR arrays, in order to allow for more flexibility in resistance calibrations.

The potential to dope epigraphene through the charge neutrality point made it possible to study of the performance limits of Hall sensors. The in-depth test of the magnetic field detection capabilities, in a wide range of operating conditions, establish that doped epigraphene Hall sensors can outperform other graphene Hall sensors in terms of magnetic field detection limits. Furthermore, the sensors also show potential for future applications in higher industrial temperature ranges. The development of an alternate doping scheme, which can push the high temperature performance even further, will be the key to the future success of epigraphene Hall sensors.

Finally, epigraphene doped to the neutrality point develops a logarithmic temperature dependence of resistance which opens up its use in THz detection. The experiments demonstrate that an epigraphene HEB mixer can operate as a sensitive and fast mixer for coherent detection of THz radiation with low power consumption. The projected future performance, under more ideal conditions, could enable the creation of large THz detector arrays with quantum limited performance across the entire THz range, a possibility which has been out of reach for conventional (superconductor) materials. Future developments involve taking the proof-of-concept epigraphene HEB mixer to the next level and fabricating an array detector, and if possible testing its ultimate performance under space-borne conditions.

In summary, the developments in epigraphene technology have solved one of its core

issues of carrier density control, and opened up new avenues for real-world applications. This thesis demonstrates three possible applications of doped epigraphene, with a common goal to prove that there is potential for epigraphene electronics to surpass conventional technologies in certain niches. All proof-of-concept devices were fabricated while keeping in mind the scalability of the process, and aiming for eventual use in industry. This thesis has laid the groundwork for many promising applications of epigraphene, with various technology readiness levels, and future research will hopefully build upon these results to one day create a tangible product which will leave a lasting impression. One of the driving factors behind graphene research since the very beginning has been to utilize its remarkable properties to revolutionize various technologies. While that vision has yet to be realized, the work presented in this thesis on epigraphene is a stepping stone on the path which will take graphene from the research laboratory into the forefront of industrial applications.

There are a plethora of other activities that were explored in these PhD studies, which have fallen outside the scope of this thesis. Some of these works have been published, while others are ongoing projects that have yet to reach the publication stage. For example, significant efforts have been devoted to understanding if the molecules assembled on the surface of epigraphene posses long-range crystalline order. The record-high carrier mobilities measured in epigraphene doped with molecules suggests this possibility, but it has been challenging to probe the epigraphene-molecule interface by using conventional surface science tools. Future studies are needed to understand if spontaneous assembly can lead to epitaxy of molecular crystals on 2D materials. Another interesting research direction is the formation of one-atom thin platinum layers on the buffer layer (see “list of papers not included in this thesis”). The formation of atomically thin metals on buffer is the first step towards intercalation of atoms at the SiC-buffer interface, which can produce a quasi-free-standing monolayer epigraphene decoupled from the influence of the substrate. Moreover, the intercalated atoms can even order and form a crystal underneath epigraphene. This is an alternative way to modify the electronic properties of epigraphene, but instead of creating molecular crystals on top of epigraphene, intercalation promotes the formation of a crystal underneath epigraphene. This process has been recently dubbed confinement heteroepitaxy, and more effort is required in order to understand if intercalated epigraphene will display exciting properties like those achieved by molecular doping, or even exceed them.

A Recipes

A.1 Growth

An outline of the general growth procedure is given below. The final temperature, time, and pressure for monolayer growth are approximate and have to be optimized for each growth environment through repeated experiments.

- Load SiC chip into the 4 inch graphite crucible. The Si-face is face-down, towards to crucible bottom. The chip rests on graphite pillars, leaving around 1 mm space.
- Close chamber and use a roughing pump to reduce pressure to below 2 mbar.
- Use a turbo pump to reduce pressure to below 5×10^{-7} mbar.
- Optimal extra annealing step. Manually heat the sample for 10 min, until temperature is above 300 °C, while pumping.
- Using the RF heater, ramp temperature to 1150 °C at a rate of 40 °C/min.
- Start ramping temperature to 1700 °C at 20 °C/min.
- Whilte heating, stop pumping and fill the chamber with argon gas, stop when pressure is 800 mbar.
- When temperature reaches 1700 °C, hold for 5 min.
- Turn off heater and wait for natural cool down (4 hours).

A.2 RCA cleaning

Required cleaning step of SiC chips before growth of epigraphene.

- Mix 200 mL deionized water, 40 mL ammonia water (NH_3 30 wt. %) and 40 mL aqueous hydrogen peroxide (H_2O_2 30 wt. %) . This mixture is referred to as SC1.
- Heat to 80 °C on a hotplate.
- Submerge SiC chips in the heated solution for 10 min.
- Rinse in deionized water bath.
- Submerge chip for 30 s in 1:50 aqueous solution of hydrofluoric acid (HF) kept at 25 °C.
- Mix 200 mL deionized water, 40 mL hydrochloric acid (HCl_3 37 wt. %) and 40 mL aqueous hydrogen peroxide (H_2O_2 30 wt. %) . This mixture is referred to as SC2.
- Heat to 80 °C on a hotplate.

- Submerge SiC chips in the heated solution for 10 min.
- Rinse in deionized water bath.
- Dry using nitrogen gas.

A.3 Electron Beam Lithography

A.3.1 Anchors

A metallic anchoring layer provides improved adhesion of future metallic contact layers.

- Spin coat P(MMA-MAA 8.5 %), 6 wt. % in ethyl lactate solvent (COPEL6). At 6000 rpm for 1 min, the resulting thickness is ~ 100 nm.
- Bake for 5 min at 170 °C
- Spin coat A-RP 6200.13 dissolved 2:1 in anisole. At 6000 rpm for 1 min, the resulting thickness is ~ 175 nm.
- Bake for 5 min at 170 °C
- Expose to e-beam. For large features ($> 1 \mu\text{m}$) use 35 nA beam current and dose of 600 $\mu\text{C}/\text{cm}^2$. For small features ($< 1 \mu\text{m}$) use 2 nA beam current and dose of 700 $\mu\text{C}/\text{cm}^2$.
- Develop the top resist layer A-RP using o-xylene developer for 30 s.
- Develop the bottom resist layer COPEL6 using o-xylene developer for 40 s.
- Remove exposed graphene using 1 min of oxygen plasma ashing. 50 W, 250 mT chamber pressure and 10 sccm flow of oxygen.
- Deposit metal using PVD by e-beam evaporation of Ti (5 nm) followed by Au (80 nm).
- Lift-off using acetone.
- Rinse with isopropanol.
- Dry using nitrogen gas

A.3.2 Normal Contacts

This recipe is used in combination with Anchors to fabricate contacts to epigraphene.

- Spin coat P(MMA-MAA 8.5 %), 6 wt. % in ethyl lactate solvent (COPEL6). At 6000 rpm for 1 min, the resulting thickness is ~ 100 nm.
- Bake for 5 min at 160 °C (lower temperature because of no ashing step).

- Spin coat A-RP 6200.13 dissolved 2:1 in anisole. At 6000 rpm for 1 min, the resulting thickness is \sim 175 nm.
- Bake for 5 min at 160 °C.
- Expose to e-beam. For large features ($> 1 \mu\text{m}$) use 35 nA beam current and dose of 600 $\mu\text{C}/\text{cm}^2$. For small features ($< 1 \mu\text{m}$) use 2 nA beam current and dose of 700 $\mu\text{C}/\text{cm}^2$.
- Develop the top resist layer A-RP using o-xylene developer for 30 s.
- Develop the bottom resist layer COPEL6 using o-xylene developer for 40 s.
- Deposit metal using PVD by e-beam evaporation of Ti (5 nm) followed by Au (80 nm).
- Lift-off using acetone.
- Rinse with isopropanol.
- Dry using nitrogen gas.

A.3.3 Pseudo-Edge Contacts

This recipe forgoes the need for an anchoring layer and directly fabricates pseudo-edge contacts to epigraphene.

- Spin coat 950K PMMA, 4 wt. % in anisole (PMMA A4). At 6000 rpm for 1 min, the resulting thickness is \sim 150 nm.
- Bake for 5 min at 170 °C.
- Spin coat P(MMA-MAA 8.5 %), 10 wt. % in ethyl lactate solvent (COPEL10). At 6000 rpm for 1 min, the resulting thickness is \sim 270 nm.
- Bake for 5 min at 170 °C.
- Spin coat A-RP 6200.13 dissolved 2:1 in anisole. At 6000 rpm for 1 min, the resulting thickness is \sim 175 nm.
- Bake for 5 min at 170 °C.
- Expose to e-beam. For large features ($> 1 \mu\text{m}$) use 35 nA beam current and dose of 600 $\mu\text{C}/\text{cm}^2$. For small features ($< 1 \mu\text{m}$) use 2 nA beam current and dose of 700 $\mu\text{C}/\text{cm}^2$.
- Develop the top resist layer A-RP using o-xylene developer for 30 s.
- Develop the bottom resist layer COPEL6 using o-xylene developer for 40 s.
- Remove exposed graphene using 1 min of oxygen plasma ashing. 50 W, 250 mT chamber pressure and 10 sccm flow of oxygen.

- Deposit metal using PVD by e-beam evaporation of Ti (5 nm) followed by Au (80 nm).
- Lift-off using acetone.
- Rinse with isopropanol.
- Dry using nitrogen gas.

A.3.4 Ashing

This recipe is used to etch away epigraphene.

- Spin coat 950K PMMA, 6 wt. % in anisole (PMMA A6). At 6000 rpm for 1 min, the resulting thickness is ~ 375 nm.
- Bake for 5 min at 170 °C.
- Expose to e-beam. For large features ($> 1 \mu\text{m}$) use 35 nA beam current and dose of $600 \mu\text{C}/\text{cm}^2$. For small features ($< 1 \mu\text{m}$) use 2 nA beam current and dose of $700 \mu\text{C}/\text{cm}^2$.
- Develop the top resist layer A-RP using o-xylene developer for 30 s.
- Develop the bottom resist layer COPEL6 using o-xylene developer for 40 s.
- Remove exposed graphene using 1.5 min of oxygen plasma ashing. 50 W, 250 mT chamber pressure and 10 sccm flow of oxygen.
- Remove remaining resist using acetone.
- Rinse with isopropanol.
- Dry using nitrogen gas.

A.4 Chemical Doping

A.4.1 Dopant blend

The standard dopant blend consisting of F4TCNQ molecules mixed with PMMA is made using the following recipe:

- 25 mg of dry F4TCNQ powder is mixed with 3 mL of anisole. This solution is referred to as ‘X’.
- 0.5 mL of X is mixed with 1 mL of PMMA A6 (PMMA, 6 wt. % in anisole), yielding the final dopant blend.

A.4.2 Two polymer layers

This recipe is intended for charge neutral epigraphene. Baking time is related to final doping level, and can be changed as needed.

- Spin coat P(MMA-MAA 8.5 %), 6 wt. % in ethyl lactate solvent (COPEL6). At 6000 rpm for 1 min, the resulting thickness is \sim 100 nm. This is the spacer layer
- Bake for 5 min at 160 °C.
- Spin coat dopant blend. At 6000 rpm for 1 min, the resulting thickness is \sim 150 nm.
- Bake for 5 min at 160 °C.

A.4.3 Five polymer layers

This recipe is intended for charge neutral epigraphene with higher doping stability. Baking time is related to final doping level, and can be changed as needed.

- Spin coat P(MMA-MAA 8.5 %), 6 wt. % in ethyl lactate solvent (COPEL6). At 6000 rpm for 1 min, the resulting thickness is \sim 100 nm.
- Bake for 5 min at 160 °C.
- Spin coat dopant blend. At 6000 rpm for 1 min, the resulting thickness is \sim 150 nm.
- Bake for 5 min at 160 °C.
- Spin coat P(MMA-MAA 8.5 %), 6 wt. % in ethyl lactate solvent (COPEL6). At 6000 rpm for 1 min, the resulting thickness is \sim 100 nm.
- Bake for 5 min at 160 °C.
- Spin coat dopant blend. At 6000 rpm for 1 min, the resulting thickness is \sim 150 nm.
- Bake for 5 min at 160 °C.
- Spin coat P(MMA-MAA 8.5 %), 6 wt. % in ethyl lactate solvent (COPEL6). At 6000 rpm for 1 min, the resulting thickness is \sim 100 nm.
- Bake for 15 min at 160 °C.

A.5 Electrostatic Gating

This is a recipe to fabricate an electrostatic top gate using direct-write photolithography on top of PMMA. Note that molecular doping is affected by this process, and some fine tuning of the initial doping level by changing the final annealing time for the dopant layer.

- Follow previous EBL recipes to produce an epigraphene Hall bar.

- Spin coat the full five polymer layers to dope epigraphene. Note that the final 15 min annealing step can be reduced.
- Deposit metal using PVD by resistive evaporation of 40 nm Al over the entire chip.
- Spin coat S1813. At 6000 rpm for 1 min, the resulting thickness is $\sim 1 \mu\text{m}$.
- Bake for 2 min at 90 °C.
- Expose in laser writer system Heidelberg Instruments DWL 2000, 405 nm diode laser and 4 mm write head.
- Use Focus offset 25 %, Intensity 55 %, and Transmission 100 %.
- Develop the resist layer and etch Al using MF-319 for 3-4 min, or until the Al looks completely gone.
- Rinse with deionized water.
- Dry using nitrogen gas.

B Derivations

B.1 Integer Quantum Hall Effect

B.1.1 Landau Levels

This section provides some background calculations behind the derivation of the quantum Hall effect, discussed in Chapter 2.3.3.

The quantum Hamiltonian which describes the quantum Hall effect in a 2D system is:

$$H = \frac{1}{2m}(\mathbf{p} + e\mathbf{A})^2 \quad (\text{B.1})$$

The magnetic field is represented here by the vector potential \mathbf{A} . If the 2D systems is assumed to exist in the x-y plane, then an out-of-plane perpendicular field in the z-direction leads to $\nabla\mathbf{A} = B\hat{\mathbf{z}}$. There is always the freedom to choose a gauge, and the aptly named Landau gauge is used $\mathbf{A} = xB\hat{\mathbf{y}}$ to simplify calculations. The Hamiltonian now reads:

$$H = \frac{1}{2m}(p_x^2 + (p_y + eBx)^2) \quad (\text{B.2})$$

The specific choice of the Landau gauge means that the y-direction is invariant under translation, but not x. The energy eigenstates, which also are eigenstates of p_y , are plane waves in the y-direction. As a guess for the wavefunction take the separation of variables ansatz $\Psi_k(x, y) = e^{iky}f_k(x)$ (k is restricted to y-direction). This means that the operator $p_y = -i\hbar\frac{\partial}{\partial y}$ effectively is replaced by the eigenvalue $\hbar k$ in the Schrödinger equation:

$$H\Psi_k(x, y) = \frac{1}{2m}(p_x^2 + (\hbar k + eBx)^2)\Psi_k(x, y) \quad (\text{B.3})$$

The resulting Hamiltonian can be simplified and rewritten as:

$$H = \frac{1}{2m}p_x^2 + \frac{m\omega_c^2}{2}(x + kl_B^2)^2 \quad (\text{B.4})$$

The terms in this Hamiltonian looks identical to the quantum harmonic oscillator, with a small difference that the energy minimum is shifted by $-kl_B^2$ where $l_B = \sqrt{\frac{\hbar}{eB}}$. l_B is called the magnetic length. This is the characteristic length scale for quantum interactions in a magnetic field, and is closely related to the minimum radius of cyclotron orbits, limited by the Heisenberg uncertainty principle.

It is known that the eigenenergies for any quantum harmonic oscillator is $E_n = \hbar\omega_c(N + \frac{1}{2})$, $N \in \mathbb{N}^0$ and this means that the energy spacing between LLs is equidistant. The energy eigenfunctions are the product of a plane wave and the known 1D harmonic oscillator eigenfunctions (H_n are Hermite polynomials):

$$\Phi_{n,k} \approx e^{iky}H_n(x + kl_B^2)e^{-(x + kl_B^2)^2/(2l_B^2)} \quad (\text{B.5})$$

This expression contains a Gaussian term $e^{-(x+kl_B^2)^2}$ which describes the localization of the eigenfunctions around $x_0 = -kl_B^2$, on the order of magnetic length. Note that the states are completely extended in y-direction however. This predicts the existence of elongated states along the length of the Hall bar, which later turns out to be the edge states.

B.1.2 Edge states

This section provides some background calculations behind the emergence of edge states in the QHE, discussed in Chapter 2.3.3.

Consider a real Hall bar sample, which necessarily has finite dimensions and edges at the boundary, as depicted in Figure 2.8. Now consider the spatial variation of the potential $V(x)$ in one dimension, across the width of the Hall bar. In the ideal case of no disorder, the energy of LLs lie flat in the bulk and rise steeply at the edges, similar to the confining walls of a potential well. In the regime of QHE the Fermi energy lies in between two LLs.

The Hamiltonian from Equation B.4 changes to:

$$H = \frac{1}{2m}p_x^2 + \frac{m\omega_c^2}{2}(x + kl_B^2)^2 + V(x) \quad (\text{B.6})$$

The potential $V(x)$, to first approximation, is linear and assuming that it is smooth on the order of magnetic length, can be expressed by the Taylor expansion around each state's position X as $V(x) \approx V(X) + (\frac{\partial V}{\partial x})(x - X) \dots \approx \frac{\partial V}{\partial x}x$. Here all the constant terms have been dropped, since they will not affect the final result. The Hamiltonian with this linear scalar potential can be solved using the same ansatz as before $\Psi_k(x, y) = e^{iky}f_k(x)$. The task is yet again to rewrite the new Hamiltonian as a shifted quantum harmonic oscillator by completing the square:

$$H = \frac{p_x^2}{2m} + \frac{1}{2}m\omega_c^2 \left(\left(kl_B^2 + \frac{\partial V}{\partial x} \frac{1}{m\omega_c^2} \right) + x \right)^2 - \frac{1}{2m\omega_c^2} \left(\frac{\partial V}{\partial x} \right)^2 - kl_B^2 \frac{\partial V}{\partial x} \quad (\text{B.7})$$

Two extra terms are introduced when completing the square, but since they are constant in $\hbar k$ -subspace they enter directly into the expression for the shifted eigenenergies:

$$E_n(k) = \hbar\omega_c(N + \frac{1}{2}) - \frac{1}{2m\omega_c^2} \left(\frac{\partial V}{\partial x} \right)^2 - kl_B^2 \frac{\partial V}{\partial x} \quad (\text{B.8})$$

The eigenenergies are now dependent on momentum and the degeneracy of LLs is lifted. In addition, there is also now a finite drift velocity. The drift velocity is defined as $v_y = \frac{1}{\hbar} \frac{\partial E_n}{\partial k} = -\frac{1}{eB} \frac{\partial V}{\partial x}$. Importantly this means that the drift velocity on opposite edges (x or $-x$) of the Hall bar point in opposite y-directions. The eigenfunctions are similar to the bulk case, so there is still localization in x-direction. In total this means that there exist localized edge states with chiral edge currents along the y-direction.

B.2 Tight-binding Graphene

The following tight-bindng calculation is an extension of the discussion in Chapter 2.1. The tight-binding wave function for the two-atom unit cell of graphene is:

$$\Psi_{\mathbf{k}}^{\lambda}(\mathbf{r}) = C_{\mathbf{k},A}^{\lambda}(\mathbf{r})\Phi_{\mathbf{k},A}^{\lambda}(\mathbf{r}) + C_{\mathbf{k},B}^{\lambda}(\mathbf{r})\Phi_{\mathbf{k},B}^{\lambda}(\mathbf{r}) \quad (\text{B.9})$$

where A, B represent the two atoms in the graphene unit cell stemming from the two sub-lattices, \mathbf{k} is the momentum vector, λ is the band index, and $\Phi_{\lambda\mathbf{k}}(\mathbf{r}) = \frac{1}{\sqrt{N}} \sum_{\mathbf{R}_N} e^{i\mathbf{k}\mathbf{R}_N} \phi_{\lambda}(\mathbf{r} - \mathbf{R}_i)$ is the tight-binding wave function where $\phi_{\lambda}(\mathbf{r} - \mathbf{R}_i)$ represent $2p_z$ -orbital wave functions. The solution to the Schrödinger equation $H\Psi_{\mathbf{k}}^{\lambda} = E_{\mathbf{k}}^{\lambda}\Psi_{\mathbf{k}}^{\lambda}$ are found by first multiplying with $\Phi_{\mathbf{k},A}^{\lambda*}$ and integrating over all space, and then doing the same for $\Phi_{\mathbf{k},B}^{\lambda*}$. The resulting two equations are combined into the matrix:

$$\begin{pmatrix} H_{AA} - E_{\mathbf{k}}^{\lambda}S_{AA} & H_{AB} - E_{\mathbf{k}}^{\lambda}S_{AB} \\ H_{BA} - E_{\mathbf{k}}^{\lambda}S_{BA} & H_{BB} - E_{\mathbf{k}}^{\lambda}S_{BB} \end{pmatrix} \begin{pmatrix} C_{\mathbf{k},A}^{\lambda} \\ C_{\mathbf{k},B}^{\lambda} \end{pmatrix} = \begin{pmatrix} 0 \\ 0 \end{pmatrix} \quad (\text{B.10})$$

Here $H_{ij} = \int \Phi_{\mathbf{k},i}^{\lambda*} H \Phi_{\mathbf{k},j}^{\lambda} d\mathbf{r}$ and $S_{ij} = \int \Phi_{\mathbf{k},i}^{\lambda*} \Phi_{\mathbf{k},j}^{\lambda} d\mathbf{r}$. The equivalence between A and B atoms lead to $S_{AB} = S_{BA}^*$, $H_{AA} = H_{BB}$, $H_{AB} = H_{BA}^*$. The transfer matrix element H_{AB} and overlap integrals S_{AB} are simplified using the nearest-neighbor approximation:

$$\begin{aligned} H_{AB} &= \frac{1}{N} \sum_A^N \sum_B^N e^{i\mathbf{k}(\mathbf{R}_B - \mathbf{R}_A)} \langle \phi(\mathbf{r} - \mathbf{R}_A) | H | \phi(\mathbf{r} - \mathbf{R}_B) \rangle = \\ &= \frac{1}{N} \sum_A^N \sum_{B_{nn}}^3 e^{i\mathbf{k}(\mathbf{R}_B - \mathbf{R}_A)} \langle \phi(\mathbf{r} - \mathbf{R}_A) | H | \phi(\mathbf{r} - \mathbf{R}_B) \rangle = \\ &= \frac{1}{N} N \sum_{\delta_i}^3 e^{i\mathbf{k}\delta_i} \langle \phi(\mathbf{r} - \mathbf{R}_A) | H | \phi(\mathbf{r} - \mathbf{R}_A - \delta_i) \rangle = \\ &= \gamma_0 (e^{i\mathbf{k}\delta_1} + e^{i\mathbf{k}\delta_2} + e^{i\mathbf{k}\delta_3}) \end{aligned} \quad (\text{B.11})$$

Here δ_i represent the vectors to the three nearest carbon atoms and are expressed in terms of graphene lattice vectors $\delta_1 = \frac{1}{3}(a_1 + a_2)$, $\delta_2 = \frac{1}{3}(a_2 - 2a_1)$ and $\delta_3 = \frac{1}{3}(a_1 - 2a_2)$. This results in:

$$\begin{aligned} H_{AB} &= \gamma_0 e^{i\frac{1}{3}\mathbf{k}(\mathbf{a}_1 + \mathbf{a}_2)} (1 + e^{-i\mathbf{k}\mathbf{a}_1} + e^{-i\mathbf{k}\mathbf{a}_2}) = \\ &= \gamma_0 e^{i\frac{1}{3}\mathbf{k}(\mathbf{a}_1 + \mathbf{a}_2)} f(\mathbf{k}) \\ S_{AB} &= s_0 e^{i\frac{1}{3}\mathbf{k}(\mathbf{a}_1 + \mathbf{a}_2)} f(\mathbf{k}) \end{aligned} \quad (\text{B.12})$$

γ_0 and s_0 are real-valued and are related to the hopping and orbital overlap integral respectively. The energy eigenvalues $E_{\mathbf{k}}^{\lambda}$ of graphene are then found from the determinant of Equation B.10. The solution can be simplified by fixing the value of some matrix elements. $H_{AA} = H_{BB} = \epsilon_0$ is the self/site energy of the atomic orbitals. $S_{AA} = S_{BB} = 1$

due to the normalized atomic orbital wave functions. The determinant now can be solved to yield an expression for the band structure:

$$E_{\mathbf{k}} = \frac{\epsilon_0 \pm \gamma_0 |f(\mathbf{k})|}{1 \pm s_0 |f(\mathbf{k})|} \quad (\text{B.13})$$

Note that the band index has been omitted. Recall that $f(\mathbf{k}) = (1 + e^{-i\mathbf{k}\mathbf{a}_1} + e^{-i\mathbf{k}\mathbf{a}_2})$ which leads to the norm $|f(\mathbf{k})| = ((1 + e^{-i\mathbf{k}\mathbf{a}_1} + e^{-i\mathbf{k}\mathbf{a}_2})(1 + e^{i\mathbf{k}\mathbf{a}_1} + e^{i\mathbf{k}\mathbf{a}_2}))^{\frac{1}{2}}$. The simplified form is:

The simplified form is:

$$|f(\mathbf{k})| = \sqrt{3 + 2 \cos(\mathbf{k}\mathbf{a}_1) + 2 \cos(\mathbf{k}\mathbf{a}_2) + 2 \cos(\mathbf{k}\mathbf{a}_1 - \mathbf{k}\mathbf{a}_2)}. \quad (\text{B.14})$$

What remains is to determine the three tight-binding parameters ϵ_0 , γ_0 and s_0 . They can be determined by, for instance, experimentally measuring the Fermi velocity, or from ab initio calculations. When considering only strictly nearest-neighbor interactions the self-energy is commonly set to zero $\epsilon_0 = 0$. This results in the valence and conduction bands crossing at the K point in accordance with experimental observations. The hopping energy is usually set to $\gamma_0 \approx -3 \text{ eV}$ [30]. The overlap integral s_0 relates to the asymmetry between conduction and valence bands and can be ignored at lower energies $s_0 = 0$. Finally, the low-energy band structure for graphene, as shown in Figure 2.2, is:

$$\begin{aligned} E_{\mathbf{k}} = \pm \gamma_0 |f(\mathbf{k})| &= \sqrt{3 + 2 \cos(\mathbf{k}\mathbf{a}_1) + 2 \cos(\mathbf{k}\mathbf{a}_2) + 2 \cos(\mathbf{k}\mathbf{a}_1 - \mathbf{k}\mathbf{a}_2)} = \\ &\pm \gamma_0 \sqrt{3 + 2 \cos(\sqrt{3}a_0 k_y) + 4 \cos\left(\frac{3a_0}{2}k_x\right) \cos\left(\frac{\sqrt{3}a_0}{2}k_y\right)} \end{aligned} \quad (\text{B.15})$$

k_x and k_y are the $\hat{\mathbf{x}}$ and $\hat{\mathbf{y}}$ components of the wave vector respectively. The energy is zero only at \mathbf{K} or \mathbf{K}' , the so called Dirac points. Since the valence and conduction bands meet at the Dirac points, graphene is referred to as a zero gap semi-metal.

References

- [1] A. S. Mayorov et al. Micrometer-Scale Ballistic Transport in Encapsulated Graphene at Room Temperature. *Nano Letters* **11**.6 (2011), 2396–2399.
- [2] R. R. Nair et al. Fine structure constant defines visual transparency of graphene. *Science (New York, N.Y.)* **320**.5881 (2008), 1308.
- [3] A. A. Balandin. Thermal properties of graphene and nanostructured carbon materials. *Nature Materials* **10**.8 (2011), 569–581.
- [4] C. Lee et al. Measurement of the elastic properties and intrinsic strength of monolayer graphene. *Science (New York, N.Y.)* **321**.5887 (2008), 385–8.
- [5] P. R. Wallace. The band theory of graphite. *Physical Review* **71**.9 (1947), 622–634.
- [6] A. J. Van Bommel et al. LEED and Auger electron observations of the SiC(0001) surface. *Surface Science* **48**.2 (1975), 463–472.
- [7] K. S. K. S. Novoselov et al. Electric field effect in atomically thin carbon films. *Science* **306**.5696 (2004), 666–669.
- [8] K. S. Novoselov et al. Two-dimensional gas of massless Dirac fermions in graphene. *Nature* **438**.7065 (2005), 197–200.
- [9] C. Berger et al. Ultrathin epitaxial graphite: 2D electron gas properties and a route toward graphene-based nanoelectronics. *Journal of Physical Chemistry B* **108**.52 (2004), 19912–19916.
- [10] K. V. Emtsev et al. Towards wafer-size graphene layers by atmospheric pressure graphitization of silicon carbide. *Nature materials* **8**.3 (2009), 203–207.
- [11] C. Virojanadara et al. Homogeneous large-area graphene layer growth on 6H-SiC(0001). *Physical Review B* **78**.24 (2008), 245403.
- [12] W. A. De Heer et al. Large area and structured epitaxial graphene produced by confinement controlled sublimation of silicon carbide. *Proceedings of the National Academy of Sciences of the United States of America* **108**.41 (2011), 16900–16905.
- [13] J. Chan et al. Reducing extrinsic performance-limiting factors in graphene grown by chemical vapor deposition. *ACS Nano* **6**.4 (2012), 3224–3229.
- [14] A. Tzalenchuk et al. Towards a quantum resistance standard based on epitaxial graphene. *Nature nanotechnology* **5**.3 (2010), 186–9.
- [15] S. Kopylov et al. Charge transfer between epitaxial graphene and silicon carbide. *Applied Physics Letters* **97**.11 (2010).
- [16] K. v. Klitzing et al. New Method for High-Accuracy Determination of the Fine-Structure Constant Based on Quantized Hall Resistance. *Physical Review Letters* **45**.6 (1980), 494–497.
- [17] T. J. B M Janssen et al. Graphene, universality of the quantum Hall effect and redefinition of the SI system universality of the quantum Hall effect and redefinition of the SI system New Journal of Physics Graphene, universality of the quantum Hall effect and redefinition of the SI system. *New Journal of Physics* **9**.13 (2011), 93026–93026.
- [18] R. Ribeiro-Palau et al. Quantum Hall resistance standard in graphene devices under relaxed experimental conditions. *Nature Nanotechnology* **10**.September (2015), 1–18.

- [19] T. J. B. M. Janssen et al. Operation of graphene quantum Hall resistance standard in a cryogen-free table-top system. *2D Materials* **2**.3 (2015), 035015.
- [20] J. A. Alexander-Webber et al. Giant quantum Hall plateaus generated by charge transfer in epitaxial graphene. *Scientific Reports* **6**.May (2016), 30296.
- [21] M Yang et al. Puddle-Induced Resistance Oscillations in the Breakdown of the Graphene Quantum Hall Effect. *Physical Review Letters* **117**.23 (2016).
- [22] S. Cho et al. Charge transport and inhomogeneity near the minimum conductivity point in graphene. *Physical Review B - Condensed Matter and Materials Physics* **77**.8 (2008).
- [23] J. Xue et al. Scanning tunnelling microscopy and spectroscopy of ultra-flat graphene on hexagonal boron nitride. *Nature Materials* **10** (2011).
- [24] A. S. Mayorov et al. How Close Can One Approach the Dirac Point in Graphene Experimentally? *Nano Letters* **12**.9 (2012), 4629–4634.
- [25] S. Datta et al. *Quantum Transport: Atom to Transistor*. Cambridge University Press, 2005.
- [26] S. Datta. *Electronic Transport in Mesoscopic Systems*. Cambridge Studies in Semiconductor Physi. Cambridge University Press, 1997.
- [27] M. Katsnelson et al. *Graphene: Carbon in Two Dimensions*. Cambridge University Press, 2012.
- [28] H. Aoki et al. *Physics of Graphene*. NanoScience and Technology. Springer International Publishing, 2013.
- [29] E. Malic et al. *Graphene and Carbon Nanotubes: Ultrafast Optics and Relaxation Dynamics*. Wiley, 2013.
- [30] R. Kundu. Tight-binding parameters for graphene. *Modern Physics Letters B* **25**.03 (2011), 163–173.
- [31] J. Huang et al. Disorder induced Dirac-point physics in epitaxial graphene from temperature-dependent magneto-transport measurements. *Physical Review B* **075407** (2015), 6.
- [32] C. Riedl et al. Quasi-Free-Standing Epitaxial Graphene on SiC Obtained by Hydrogen Intercalation. *Physical Review Letters* **103**.24 (2009), 246804.
- [33] H. Morkoc et al. Large-band-gap SiC, III-V nitride, and II-VI ZnSe-based semiconductor device technologies. *Journal of Applied Physics* **76** (3 1994), 1363.
- [34] J. Hass et al. The interface structure of epitaxial graphene grown on 4H-SiC(0001) (0001 Aug. 2008), 1–23.
- [35] Z. H. Ni et al. Raman spectroscopy of epitaxial graphene on a SiC substrate. *Physical Review B - Condensed Matter and Materials Physics* **77** (11 Mar. 2008).
- [36] P. Hens et al. Large area buffer-free graphene on non-polar (001) cubic silicon carbide. *Carbon* **80**.1 (2014), 823–829.
- [37] G. R. Yazdi et al. Epitaxial graphene on SiC: A review of growth and characterization. *Crystals* **6** (5 May 2016).
- [38] W. A. D. Heer et al. Large area and structured epitaxial graphene produced by confinement controlled sublimation of silicon carbide (2011).
- [39] S. Goler et al. Revealing the atomic structure of the buffer layer between SiC(0001) and epitaxial graphene. *Carbon* **51** (2013), 249 –254.

- [40] J. Ristein et al. Origin of Doping in Quasi-Free-Standing Graphene on Silicon Carbide. *Phys. Rev. Lett.* **108** (24 2012), 246104.
- [41] A. Lartsev et al. Tuning carrier density across Dirac point in epitaxial graphene on SiC by corona discharge. *Applied Physics Letters* **105**.6 (2014), 063106.
- [42] T. J. Janssen et al. Anomalously strong pinning of the filling factor $\nu=2$ in epitaxial graphene. *Physical Review B - Condensed Matter and Materials Physics* **83**.23 (2011), 3–6.
- [43] Y. Zhang et al. Origin of spatial charge inhomogeneity in graphene. *Nature Physics* **6**.1 (2010), 74–74.
- [44] Q. Li et al. Disorder-induced temperature-dependent transport in graphene: Puddles, impurities, activation, and diffusion. *Physical Review B - Condensed Matter and Materials Physics* **84**.11 (2011).
- [45] E. M. Lifshits et al. Theory of the Shubnikov-de Haas effect. *Journal of Physics and Chemistry of Solids* **4**.1-2 (1958), 1–10.
- [46] C. d. C. Chamon et al. Sharp and smooth boundaries of quantum Hall liquids. *Phys. Rev. B* **49** (12 1994), 8227–8241.
- [47] T. Karzig et al. Relaxation and edge reconstruction in integer quantum Hall systems. *New Journal of Physics* **14**.10 (2012), 105009.
- [48] I. A. LuKYanchuk et al. Phase analysis of quantum oscillations in graphite. *Physical Review Letters* **93**.16 (2004).
- [49] K. S. Novoselov et al. Room-temperature quantum hall effect in graphene. *Science* **315**.5817 (2007), 1379.
- [50] G. Bergmann. Physical interpretation of weak localization: A time-of-flight experiment with conduction electrons. *Phys. Rev. B* **28** (6 1983), 2914–2920.
- [51] S. Lara-Avila et al. Disordered Fermi Liquid in Epitaxial Graphene from Quantum Transport Measurements. *Phys. Rev. Lett.* **107** (16 2011), 166602.
- [52] I. L. Aleiner et al. Effect of Disorder on Transport in Graphene. *Phys. Rev. Lett.* **97** (23 2006), 236801.
- [53] E. McCann et al. Weak-Localization Magnetoresistance and Valley Symmetry in Graphene. *Phys. Rev. Lett.* **97** (14 2006), 146805.
- [54] T. Yager et al. Express optical analysis of epitaxial graphene on SiC: Impact of morphology on quantum transport. *Nano Letters* **13**.9 (2013), 4217–4223.
- [55] V. Panchal et al. Standardization of surface potential measurements of graphene domains. *Scientific reports* **3**.2 (2013), 2597.
- [56] A. C. Ferrari et al. Raman spectroscopy as a versatile tool for studying the properties of graphene. *Nature Nanotechnology* **8**.4 (2013), 235–246.
- [57] J. Rohrl et al. Raman spectra of epitaxial graphene on SiC(0001). *Applied Physics Letters* **92**.20 (2008), 201918.
- [58] A. Allain et al. Electrical contacts to two-dimensional semiconductors. *Nature Materials* **14**.12 (2015), 1195–1205.
- [59] L Wang et al. One-Dimensional Electrical Contact to a Two-Dimensional Material. *Science* **342**.November (2013), 614–617.
- [60] F. Delahaye. Technical guidelines for reliable measurements of the quantized hall resistance. *Metrologia* **26**.1 (1989), 63–68.

- [61] G. K. Reeves et al. Obtaining the specific contact resistance from transmission line model measurements. *IEEE Electron Device Letters* **3**.5 (1982), 111–113.
- [62] L. J. van der Pauw. A Method of Measuring Specific Resistivity and Hall Effect of Discs of Arbitrary Shape. *Philips Research Reports* **13** (1958), 1–9.
- [63] B Jeckelmann et al. The quantum Hall effect as an electrical resistance standard. *Rep. Prog. Phys* **64** (2001), 1603–1655.
- [64] J. M. Williams et al. An automated cryogenic current comparator resistance ratio bridge for routine resistance measurements. *Metrologia* **47**.3 (2010), 167–174.
- [65] M. Kruskopf et al. Comeback of epitaxial graphene for electronics: large-area growth of bilayer-free graphene on SiC. *2D Materials* **3**.4 (2016), 041002.
- [66] t. He et al. Polymer-encapsulated molecular doped epigraphene for quantum resistance metrology. *Metrologia* **56**.4 (2019), 045004.
- [67] S. Lara-Avila et al. Non-volatile photochemical gating of an epitaxial graphene/polymer heterostructure. *Advanced Materials* **23**.7 (2011), 878–882.
- [68] D. Waldmann et al. Bottom-gated epitaxial graphene. *Nature Materials* **10**.5 (2011), 357–360.
- [69] C Coletti et al. Charge neutrality and band-gap tuning of epitaxial graphene on SiC by molecular doping. *Physical Review B - Condensed Matter and Materials Physics* **81**.23 (2010).
- [70] W. Chen et al. Surface Transfer p-Type Doping of Epitaxial Graphene. *Journal of the American Chemical Society* **129**.34 (2007), 10418–10422.
- [71] K. S. Novoselov et al. 2D materials and van der Waals heterostructures. *Science* **353**.6298 (2016).
- [72] L. H. Li et al. Dielectric Screening in Atomically Thin Boron Nitride Nanosheets. *Nano Letters* **15**.1 (2015), 218–223.
- [73] J. Li et al. Dielectric strength, optical absorption, and deep ultraviolet detectors of hexagonal boron nitride epilayers. *Applied Physics Letters* **101**.17 (2012), 171112.
- [74] Y. Hattori et al. Layer-by-Layer Dielectric Breakdown of Hexagonal Boron Nitride. *ACS Nano* **9**.1 (2015), 916–921.
- [75] R. Frisenda et al. Recent progress in the assembly of nanodevices and van der Waals heterostructures by deterministic placement of 2D materials. *Chemical Society Reviews* **47** (Nov. 2017).
- [76] K. Takase et al. Impact of graphene quantum capacitance on transport spectroscopy. *Physical Review B - Condensed Matter and Materials Physics* **86** (16 2012), 1–8.
- [77] J. Li et al. Measurement of Small Molecular Dopant F4TCNQ and C60F36 Diffusion in Organic Bilayer Architectures. *ACS Applied Materials and Interfaces* **7**.51 (2015), 28420–28428.
- [78] I. E. Jacobs et al. *Controlling Molecular Doping in Organic Semiconductors*. 2017.
- [79] P Pingel et al. Comprehensive picture of p-type doping of P3HT with the molecular acceptor F 4 TCNQ. *PHYSICAL REVIEW B* **87**.73 (2013).
- [80] J. Li et al. Quantitative Measurements of the Temperature-Dependent Microscopic and Macroscopic Dynamics of a Molecular Dopant in a Conjugated Polymer. *Macromolecules* **50**.14 (2017), 5476–5489.
- [81] J. Crank et al. *The Mathematics of Diffusion*. Oxford science publications. Clarendon Press, 1979.

- [82] A. Kumar et al. Charge-Transfer-Driven Nonplanar Adsorption of F₄ TCNQ Molecules on Epitaxial Graphene. *ACS Nano* **11**.5 (2017), acsnano.7b01599.
- [83] M. Knap et al. Transport in two-dimensional disordered semimetals. *Physical Review Letters* **113**.18 (2014), 1–5.
- [84] J. Ping et al. Disorder-induced magnetoresistance in a two-dimensional electron system. *Physical Review Letters* **113**.4 (2014), 1–5.
- [85] R. P. Tiwari et al. Model for the magnetoresistance and Hall coefficient of inhomogeneous graphene. *Physical Review B - Condensed Matter and Materials Physics* **79**.16 (2009), 1–7.
- [86] J. M. Poumirol et al. Electron-hole coexistence in disordered graphene probed by high-field magneto-transport. *New Journal of Physics* **12**.8 (2010), 083006.
- [87] C. Li et al. Signature of gate-tunable magnetism in graphene grafted with Pt-porphyrins. *Phys. Rev. B* **93** (4 2016), 045403.
- [88] J. Yan et al. Correlated charged impurity scattering in graphene. *Physical Review Letters* **107**.20 (2011).
- [89] Q. Li et al. Theory of 2D transport in graphene for correlated disorder. *Physical Review Letters* **107**.15 (2011).
- [90] L. A. Ponomarenko et al. Tunable metal-insulator transition in double-layer graphene heterostructures. *Nature Physics* **7** (2011).
- [91] H. Ishiwara et al. *Ferroelectric Random Access Memories: Fundamentals and Applications*. Topics in Applied Physics. Springer, 2004.
- [92] X. Ling et al. Can Graphene be used as a Substrate for Raman Enhancement? *Nano Letters* **10**.2 (2010), 553–561.
- [93] C. Li et al. “Quantum Transport in Graphene: Impurity Scattering as a Probe of the Dirac Spectrum”. *Dirac Matter*. Ed. by B. Duplantier et al. Cham: Springer International Publishing, 2017, pp. 55–73.
- [94] C. Cervetti et al. The classical and quantum dynamics of molecular spins on graphene. *Nature Materials* **15**.2 (2016), 164–168.
- [95] M. Garnica et al. Long-range magnetic order in a purely organic 2D layer adsorbed on epitaxial graphene. *Nature Physics* **9**.6 (2013), 368–374.
- [96] D. W. Allan. Should the Classical Variance Be Used As a Basic Measure in Standards Metrology? *IEEE Transactions on Instrumentation and Measurement* **IM-36**.2 (1987), 646–654.
- [97] A. Lartsev et al. A prototype of RK/200 quantum Hall array resistance standard on epitaxial graphene. *Journal of Applied Physics* **118**.4 (2015), 044506.
- [98] M. Kruskopf et al. Two-Terminal and Multi-Terminal Designs for Next-Generation Quantized Hall Resistance Standards: Contact Material and Geometry. *IEEE Transactions on Electron Devices* **66**.9 (2019), 3973–3977.
- [99] J Heremans. Solid state magnetic field sensors and applications. *Journal of Physics D: Applied Physics* **26** (8 Aug. 1993), 1149–1168.
- [100] G. Boero et al. Micro-Hall devices: performance, technologies and applications. *Sensors and Actuators A: Physical* **106** (1-3 Sept. 2003), 314–320.
- [101] P. Kejik et al. An integrated micro-Hall probe for scanning magnetic microscopy. *Sensors and Actuators A: Physical* **129** (1-2 May 2006), 212–215.

- [102] R. S. Popovic. Hall Effect Devices , Second Edition (Series in Sensors). *CRC Press* (2 2003), 420.
- [103] Y. Sugiyama et al. S/N study of micro-hall sensors made of single crystal InSb and GaAs. *Sensors and Actuators* **8** (1 Sept. 1985), 29–38.
- [104] F. Bell. F.W. Bell Hall generator catalog. *Bell Technologies Inc., a SYPRIS company* ().
- [105] AKM. AKM Hall Sensor Catalog. *Akahi Kasei Microdevices* (2020).
- [106] H. He et al. Uniform doping of graphene close to the Dirac point by polymer-assisted assembly of molecular dopants. *Nature Communications* **9**.1 (2018), 3–9.
- [107] T. Ciuk et al. High-Temperature Hall Effect Sensor Based on Epitaxial Graphene on High-Purity Semiconducting 4H-SiC. *IEEE Transactions on Electron Devices* **66** (7 2019), 3134–3138.
- [108] M. Cornils et al. The magnetic calibration and optimization of symmetric hall plates may be accomplished even in the absence of a magnetic field. *Proceedings of the IEEE International Conference on Micro Electro Mechanical Systems (MEMS)* (2008), 940–943.
- [109] M. Cornils. Sheet Resistance and Hall Mobility Determination Beyond Van Der Pauw (2009), 196.
- [110] F. N. Hooge. 1/F Noise. *Physica B+C* **83** (1 1976), 14–23.
- [111] T. G. M. Kleinpenning. DESIGN OF AN A.C. MICRO-GAUSS SENSOR*. *Sensors and Actuators* **4** (1983), 3–9.
- [112] L. Huang et al. Ultra-sensitive graphene Hall elements. *Applied Physics Letters* **104** (18 2014).
- [113] Y. Zhang et al. Mobility-dependent low-frequency noise in graphene field-effect transistors. *ACS Nano* **5** (10 Oct. 2011), 8124–8130.
- [114] S. Kim et al. Dependence of Hooge Parameter of Compound Semiconductors on Temperature. *Japanese Journal of Applied Physics* **31** (2011).
- [115] K. Vervaeke et al. Size dependence of microscopic Hall sensor detection limits. *Review of Scientific Instruments* **80** (7 2009).
- [116] J. Dauber et al. Ultra-sensitive Hall sensors based on graphene encapsulated in hexagonal boron nitride. *Applied Physics Letters* **106** (19 May 2015), 193501.
- [117] C.-C. Tang et al. Characteristics of a sensitive micro-Hall probe fabricated on chemical vapor deposited graphene over the temperature range from liquid-helium to room temperature. *Applied Physics Letters* **99** (11 Sept. 2011), 112107.
- [118] A. Dankert et al. Hall sensors batch-fabricated on all-CVD h-BN/graphene/h-BN heterostructures. *Scientific Reports* **7** (1 Dec. 2017), 15231.
- [119] V. Panchal et al. Small epitaxial graphene devices for magnetosensing applications. *Journal of Applied Physics* **111** (7 2012), 8–11.
- [120] C. Walker. *Terahertz Astronomy*. Taylor and Francis, 2015.
- [121] C. Battersby et al. The Origins Space Telescope. *Nature Astronomy* **2**.8 (2018), 596–599.
- [122] A. W. Blain et al. Submillimeter galaxies. *Physics Reports* **369**.2 (2002), 111 –176.
- [123] H.-W. Hubers. Terahertz Heterodyne Receivers. *IEEE Journal of Selected Topics in Quantum Electronics* **14** (Apr. 2008), 378–391.

- [124] T. M. Klapwijk et al. Engineering Physics of Superconducting Hot-Electron Bolometer Mixers. *IEEE Transactions on Terahertz Science and Technology* **7**.6 (2017), 627–648.
- [125] D. E. Prober. Superconducting terahertz mixer using a transition-edge microbolometer. *Applied Physics Letters* **62**.17 (1993), 2119–2121.
- [126] de Graauw, Th. et al. The Herschel-Heterodyne Instrument for the Far-Infrared (HIFI)*. *Astronomy and Astrophysics* **518** (2010), L6.
- [127] E. Novoselov et al. Low noise terahertz MgB₂ hot-electron bolometer mixers with an 11 GHz bandwidth. *Applied Physics Letters* **110**.3 (2017), 032601.
- [128] A. A. Balandin. Thermal properties of graphene and nanostructured carbon materials. *Nature Materials* **10**.8 (2011), 569–581.
- [129] A. El Fatimy et al. Epitaxial graphene quantum dots for high-performance terahertz bolometers. *Nature Nanotechnology* **11**.4 (2016), 335–338.
- [130] D. K. Efetov et al. Fast thermal relaxation in cavity-coupled graphene bolometers with a Johnson noise read-out. *Nature Nanotechnology* **13**.9 (2018), 797–801.
- [131] S. Das Sarma et al. Electronic transport in two-dimensional graphene. *Rev. Mod. Phys.* **83** (2 2011), 407–470.
- [132] S. S. Kubakaddi. Interaction of massless Dirac electrons with acoustic phonons in graphene at low temperatures. *Phys. Rev. B* **79** (7 2009), 075417.
- [133] A. M. R. Baker et al. Energy loss rates of hot Dirac fermions in epitaxial, exfoliated, and CVD graphene. *Phys. Rev. B* **87** (4 2013), 045414.
- [134] S. Lara-Avila et al. Towards quantum-limited coherent detection of terahertz waves in charge-neutral graphene. *Nature Astronomy* **3**.November (2019).
- [135] S. Krause et al. Noise and IF Gain Bandwidth of a Balanced Waveguide NbN/GaN Hot Electron Bolometer Mixer Operating at 1.3 THz. *IEEE Transactions on Terahertz Science and Technology* **8**.3 (2018), 365–371.
- [136] H. Ekstrom et al. Conversion gain and noise of niobium superconducting hot-electron-mixers. *IEEE Transactions on Microwave Theory and Techniques* **43**.4 (1995), 938–947.
- [137] N. Wang et al. Room-temperature heterodyne terahertz detection with quantum-level sensitivity. *Nature Astronomy* **3**.11 (2019), 977–982.
- [138] B. Ho Eom et al. A wideband, low-noise superconducting amplifier with high dynamic range. *Nature Physics* **8**.8 (2012), 623–627.
- [139] H. He et al. Fabrication of graphene quantum hall resistance standard in a cryogen-free table-top system. *2016 Conference on Precision Electromagnetic Measurements (CPEM 2016)* (2016), 1–2.
- [140] H. He et al. The performance limits of Epigraphene Hall sensors doped across the Dirac point. *Submitted to Applied Physics Letters* (2020).

Part I

Appended Papers

Paper A

Operation of graphene quantum Hall resistance standard in a cryogen-free table-top system

Operation of graphene quantum Hall resistance standard in a cryogen-free table-top system

This content has been downloaded from IOPscience. Please scroll down to see the full text.

2015 2D Mater. 2 035015

(<http://iopscience.iop.org/2053-1583/2/3/035015>)

View [the table of contents for this issue](#), or go to the [journal homepage](#) for more

Download details:

IP Address: 129.16.137.182

This content was downloaded on 16/11/2015 at 16:58

Please note that [terms and conditions apply](#).

2D Materials



PAPER

RECEIVED
16 July 2015ACCEPTED FOR PUBLICATION
21 July 2015PUBLISHED
19 August 2015

Operation of graphene quantum Hall resistance standard in a cryogen-free table-top system

T J B M Janssen¹, S Rozhko¹, I Antonov², A Tzalenchuk^{1,2}, J M Williams¹, Z Melhem³, H He⁴, S Lara-Avila⁴, S Kubatkin⁴ and R Yakimova⁵

¹ National Physical Laboratory, Hampton Road, Teddington TW11 0LW, UK

² Royal Holloway, University of London, Egham TW20 0EX, UK

³ Oxford Instruments Nanoscience, Tubney Woods, Abingdon OX13 5QX, UK

⁴ Department of Microtechnology and Nanoscience, Chalmers University of Technology, S-41296 Göteborg, Sweden

⁵ Department of Physics, Chemistry and Biology (IFM), Linköping University, S-58183 Linköping, Sweden

E-mail: jt.janssen@npl.co.uk

Keywords: graphene, quantum Hall effect, metrology

Abstract

We demonstrate quantum Hall resistance measurements with metrological accuracy in a small cryogen-free system operating at a temperature of around 3.8 K and magnetic fields below 5 T. Operating this system requires little experimental knowledge or laboratory infrastructure, thereby greatly advancing the proliferation of primary quantum standards for precision electrical metrology. This significant advance in technology has come about as a result of the unique properties of epitaxial graphene on SiC.

1. Introduction

One of the goals of the modern-day metrology is to provide quantum standards at the fingertips of the end-users, shortening the calibration chain from primary standards to the final product. A shorter calibration chain will result in a higher accuracy for end-users which can be exploited to develop more advanced test and measurement equipment and subsequently lead to societal benefits where measurement is an issue.

Resistance metrology is one of the cornerstones of electrical metrology with most national measurement laboratories around the world providing an extensive range of calibration services across many decades of resistance value [1]. The primary standard for resistance is based on the quantum Hall effect (QHE) [2] which is presently realized by a lot fewer laboratories [3]. This is because the infrastructure needed to create the QHE in conventional semiconductor systems is quite elaborate and expensive as it requires temperatures of 1 K or below and magnetic fields around 10 T. Another important barrier is the expertise needed to run a quantum Hall system and verify the correct operation and quantization parameters. Finally, liquid Helium is becoming a scarce resource, significantly increasing in price year on year, and not readily available in every country.

A simpler, cryogen-free, system is needed if more laboratories are to realize the primary standard directly and this has recently become possible with the advent of graphene. One of the first properties observed in graphene was the QHE and it was immediately realized that it is ideal for metrology by virtue of its unique band structure [4–7]. The Landau level quantization in graphene is a lot stronger than in traditional semiconductor systems which implies that both a lower magnetic field can be used and that the low temperature constraint is more relaxed [6]. Following the original demonstration of high-accuracy quantum Hall resistance measurements in epitaxial graphene grown on SiC [8] and proof of the universality of the QHE between graphene and GaAs [9], recently these results have been very nicely reproduced by a number of different research groups [10–12]. Particularly, a recent publication by the Laboratoire national de métrologie et d'essais (LNE) group has demonstrated that high accuracy can be achieved over a large experimental parameter range [12]. These results also demonstrate that devices which show extraordinary good QHE at high magnetic field and low temperature are not necessarily optimum for low magnetic field and high temperature measurements.

Measurements of the QHE at low magnetic field are complicated by the fact that the carrier density

needs to be reduced to a level well below the as-grown density of epitaxial graphene on SiC [13] (SiC/G). Unlike exfoliated graphene on SiO_2 , gating of graphene on SiC is not straightforward [14–16]. Recently, a novel technique was demonstrated which creates a static top-gate by depositing ions via corona discharge [17]. This technique allows for a systematic control of the carrier density and both n and p-type densities can be achieved on both sides of the Dirac point. Importantly this method is fully reversible and can be applied repeatedly. Another issue with low carrier density graphene is the homogeneity. Under these conditions it is well known that electron–hole puddles form [18] induced by charged impurities, however, in epitaxial graphene the disorder strength can be of order 10 meV, comparable to flakes on boron-nitride [19].

Here we demonstrate for the first time measurements of the QHE with part-per-billion (ppb)-accuracy in a small table-top cryogen-free pulse-tube system. Both the longitudinal resistivity R_{xx} and the contact resistance R_c were well within the limits set by the guidelines for primary resistive metrology [20]. Using corona gating the carrier density was controlled such that the maximum breakdown current occurred just below the maximum magnetic field of our system. The noise sources in the system were reduced to a level such that the overall standard deviation of the measurements was comparable to those achieved for a conventional liquid $^4\text{He}/^3\text{He}$ system. The system is extremely easy to operate (it has only one button) and can run unattended for months on end, providing a stable and primary resistance reference whenever and wherever it is needed.

2. Device design and fabrication

Graphene was grown on the Si-face of SiC at $T = 2000\text{ }^\circ\text{C}$ and $P = 1\text{ atm Ar}$ (Graphenics AB) [21]. In total 20 Hall bars (see figure 1) of different dimensions (30 and 100 μm wide channels) and voltage probe types were patterned on the SiC/G using standard electron-beam lithography, lift-off, and oxygen plasma etching, as reported elsewhere [22]. The Hall bars are oriented parallel or perpendicular with respect to the predominant step edge direction of the SiC substrate. The sample was spin-coated with a thin, 100 nm, layer of poly(methyl methacrylate-co-methacrylate acid), henceforth P(MMA-MAA) (MicroChem Corp., PMMA copolymer resist solids 6% in ethyl lactate).

All results presented in this paper are measured on a Hall bar with a 30 μm wide and 180 μm long channel. A comprehensive study of all devices on this chip will be presented at a later date.

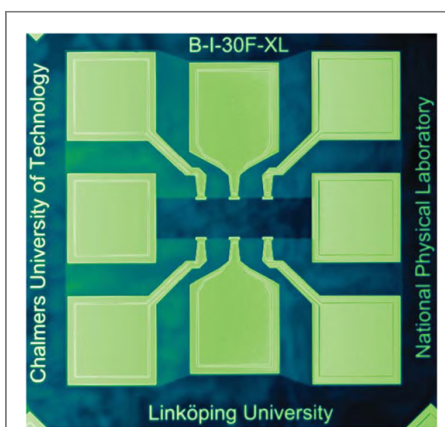


Figure 1. Optical microscope image of a typical device used in our experiments (not the one used for the actual experiments). The channel width is 100 μm , dark area is graphene channel, light area is SiC substrate and gold are the metallic contact.

3. The measurement system

The measurement system for primary resistance consists of two parts, the quantum Hall system and the measurement bridge.

3.1. Table-top cryogen-free QHR cryostat

Today, cryogen-free superconducting magnet systems have become omnipresent in low temperature physics laboratories because of their ease-of-use and reduced operational cost. In particular, for low magnet fields, $\leq 5\text{ T}$, these systems can very small and simple. The 5 T superconducting magnet in our system is only 7.5 cm tall with an outer diameter of 6 cm. The inductance is 0.5 H and is small enough to be cooled by a 0.25 W pulse-tube cooler (see figure 2). The bore of this magnet is 3 cm in diameter which large enough to take a standard TO8 header used in QHR metrology. The system has high- T_C current leads for the magnet which requires $\sim 60\text{ A}$ for full field. After evacuation the system cools down in approximately 5 h from room temperature to $\sim 3.8\text{ K}$.

In a cryogen-free system there are a number of noise sources not normally present in a traditional wet system. There is the compressor which produces the high-pressure helium gas and the rotating valve and stepper motor on top of the cryostat. These sources of noise need to be controlled and reduced as much as possible so as to not compromise the sensitivity of the measurement system. The noise of the compressor can simply be reduced by either placing an acoustic box around it or locating it in an adjoining space on the other side of a separating wall. Recently, a new type of high pressure hose was developed which significantly reduces the high-pitched hiss. These so-

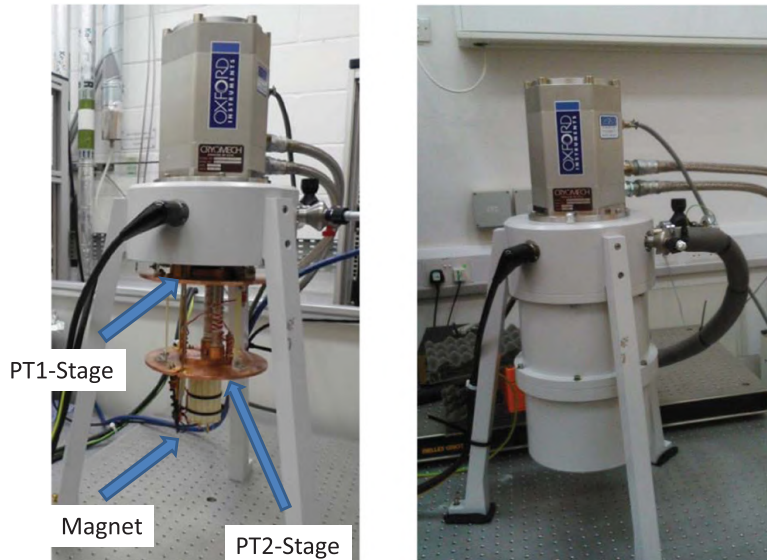


Figure 2. (a) Inside of the cryostat cooler showing the small superconducting magnet, mounted at the bottom of the PT2 Stage. (b) The system with vacuum can mounted. The overall height of the system is around 80 cm.

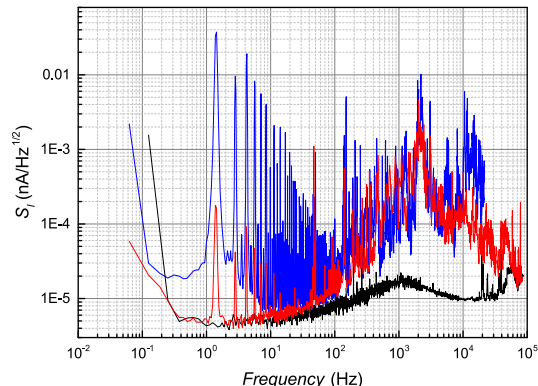


Figure 3. Current noise measurement traces before (blue) and after (red) modification of the pulse-tube cryostat. The black trace was measured with the pulse-tube compressor switched off. Current noise was measured on the sample wires without a sample present.

called quiet hoses have two beneficial effects, firstly it significantly reduces the vibrations in the cryostat system and secondly it is much more pleasant for the operator. Another improvement has been to replace the standard pulsed drive unit for the stepper motor with a low noise linear drive system. A number of other modifications are, plastic isolators on the high pressure lines to galvanically isolate the compressor from the cryostat and filters on the magnet current leads. Inside the cryostat care has to be taken that the experimental wiring is as tightly fixed as possible to

reduce the effect of vibrations. Also the measurement wiring requires good heat sinking because these are relatively short compared to traditional wet systems.

The corollary of these improvements can be seen in the noise traces in figure 3. The traces are measured on the sample wires with a spectrum analyser before and after the modifications. A reference trace with the compressor switched off is also shown. We can see that the low frequency noise peaks are reduced by more than two orders of magnitude and noise floor is equal

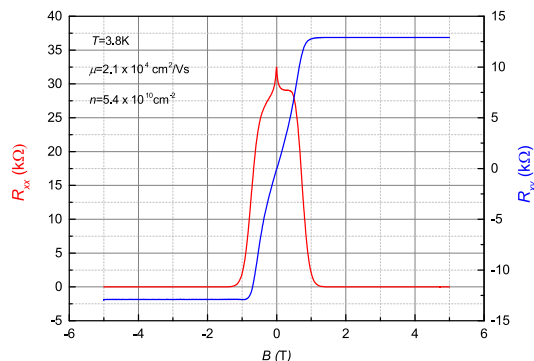


Figure 4. R_{xx} (red) and R_{xy} (blue) on an epitaxial graphene Hall bar device at 3.8 K in the cryogen-free cryostat, measured with a source-drain current of $I_{sd} = 100$ nA.

to that measured with the compressor switched off. The higher frequency noise is largely unaffected by the modifications but this noise is outside the measurement bandwidth and is not critical.

3.2. The cryogenic current comparator (CCC) bridge

High accuracy measurements of resistance ratios are generally made using a so-called CCC bridge. The fully automated CCC bridge used in our experiments has been described in great detail before [23, 24]. In a CCC bridge, currents are locked in the inverse ratio of the resistances being compared. A CCC establishes the current ratio by passing the currents along wires through a superconducting tube and measuring the residual screening current on the outside of the tube with a superconducting quantum interference device (SQUID). The difference between the voltages developed across the resistors is measured using a sensitive voltmeter and allows one resistor to be determined with respect to the other. In primary resistance metrology one of the resistors is a quantum Hall device with a resistance value exactly equal of $R_H = R_K/i$ where $R_K = h/e^2$, e is the elementary charge, h is the Planck constant and i is an integer and generally $i = 2$ or 4 is used for semiconductor devices. In graphene, owing to the bandstructure, only $i = 2$ is available. The maximum achievable sensitivity of the bridge depends for a large part on the signal-to-noise ratio in the voltmeter and therefore on the maximum current used to drive the resistors (the Johnson noise in the resistors is the other limiting factor) [23]. Under optimum conditions measurement accuracies in access of 1 part in 10^{10} can be achieved [9, 25]. However, for routine resistance metrology a few parts in 10^9 in a reasonable measurement time (~ 15 min) is perfectly adequate. In the present system the cryogenic environment needed for the superconducting tube and SQUID is provided by a traditional liquid helium cryostat.

4. Characterization

Figure 4 shows an example measurement of R_{xx} and R_{xy} made at the base-temperature of 3.8 K in the cryogen-free system described in the previous section. The curves display the familiar shape characteristic for epitaxial graphene on SiC which has been observed many times before [8, 10, 12, 14, 26–28]. The carrier density was reduced to $5.4 \times 10^{10} \text{ cm}^{-2}$ by corona-gating from the as grown density of $n \approx 10^{12} \text{ cm}^{-2}$. A wide plateau in R_{xy} is observed whilst R_{xx} is zero. The width of the plateau is much larger than would be expected from the low field carrier density. This behaviour is explained in terms of a magnetic field driven charge transfer from the interface layer to the graphene layer which results in an increase in carrier density as the magnetic field increases and effectively pins the Fermi level at exact filling of $\nu = 2$ [13, 28].

When attempting to make accurate quantum Hall resistance measurements the first step is to properly characterize the sample according to guidelines set out for primary resistance metrology [20]. Key parameters are the longitudinal resistance (R_{xx}) and contact resistance (R_c) at the desired measurement current. The longitudinal resistance needs to be as low as possible and preferably below a few tens of $\mu\Omega$ and checked on both sides of the device. Often these measurements are limited by the resolution of the nanovoltmeter and other methods can be employed to verify accurate quantization [20]. The contact resistance can be accurately determined using a three terminal measurement technique in the quantized Hall state. This method determines $R_c + R_l$ where R_c is the contact resistance and $R_l = 6.4 \Omega$ is the lead resistance in the cryostat in our system. For our device we find R_c between 0.1 and 1 Ω for all contacts measured with a current of 10 μA .

The optimum conditions for QHR measurements are easiest to obtain when the breakdown current is maximum and significantly larger than the source-drain measurement current, I_{sd} . Here the breakdown

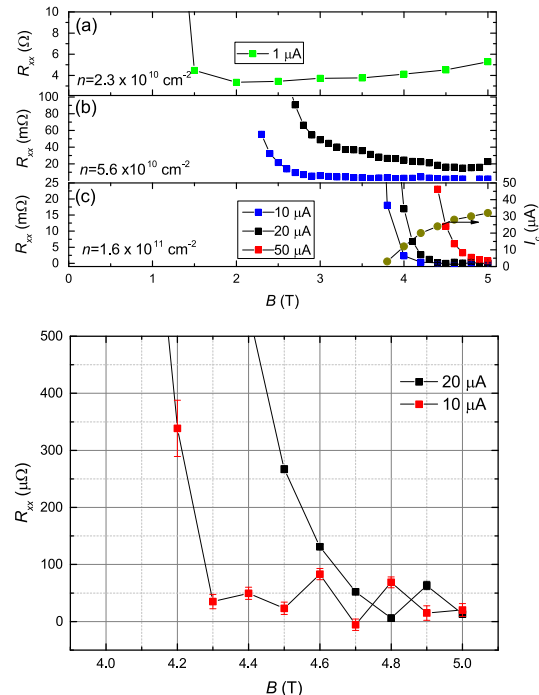


Figure 5. Top graph: R_{xx} as a function of magnetic field for different charge carrier densities. Temperature is ≈ 3.8 K. Plot (c) also shows the breakdown current I_C as a function of magnetic field. Bottom graph: high-resolution measurement of R_{xx} in a 1 T magnetic field range for $n = 1.6 \times 10^{11} \text{ cm}^{-2}$. This resolution was obtained by repeated measurements (typically 50 to 100) of V_{xx} with positive and negative I_{sd} .

current is defined as the maximum source-drain current the device can sustain before a measurable longitudinal resistance appears. We typically use a limit of 10 nV for V_{xx} which for $I_{sd} = 10 \mu\text{A}$ would imply $R_{xx} = 1 \text{ m}\Omega$. For higher carrier density devices, the breakdown current tends to be higher because the $\nu = 2$ state occurs at a higher magnetic field [29] which is simply related to the fact that at higher magnetic field, the Landau levels are further apart and hence the quantization is stronger [29]. For epitaxial graphene I_{sd} was shown to follow a $\propto B^{3/2}$ behaviour similar to that observed in semiconductor systems [30].

This effect poses a particular problem for optimizing the carrier density for accurate QHR measurements at the low magnetic fields available in our small cryogen-free system. If the carrier density is too low the maximum in the breakdown current will occur at a very low magnetic field and its value will be also low. Figure 5 (a) shows a measurement of R_{xx} at a $n = 2.3 \times 10^{10} \text{ cm}^{-2}$ very close to the Dirac point. For a $I_{sd} = 1 \mu\text{A}$ we find that the longitudinal resistance is always larger than a few Ohms and consequently the device is not properly quantized. Figure 5 (b) shows R_{xx} at a $n = 5.6 \times 10^{10} \text{ cm}^{-2}$ and we can observe proper quantization in a 2 T range for

$I_{sd} = 10 \mu\text{A}$ but for $I_{sd} = 20 \mu\text{A}$, R_{xx} is in the $\text{m}\Omega$ range and the device becomes unquantized (see below). When the carrier density is set even higher (see figure 5 (c)), quantization becomes stronger but the usable magnetic field range shrinks to around 0.5 T. The bottom graph in figure 5 shows a high-resolution measurement of R_{xx} in this range demonstrating longitudinal resistance of order $10 \mu\Omega$ and confirming proper quantization.

Using the magnetic field dependent charge-transfer model it is straightforward to estimate the optimum charge carrier density for maximum breakdown current [28]. Assuming that the maximum breakdown current will occur when $\nu = 2$ filling factor coincides with our maximum magnetic field of 5 T [29], gives a carrier density of $\approx 2.4 \times 10^{11} \text{ cm}^{-2}$. Setting this density as n_∞ in the model calculation of [28] allows us to obtain the zero field carrier density. $n_\infty = \frac{A\gamma}{1 + e^{2\gamma/c_e}} - n_g$ in which A is the difference in work function between graphene and the donor states in SiC, γ is the density of donor states, c_e is the classical capacitance and n_g is the deposited corona gate charge. Using γ as a fit parameter we obtain a value for the optimum carrier density of $n_s \approx 1.3 \times 10^{11} \text{ cm}^{-2}$ (see figure 6).

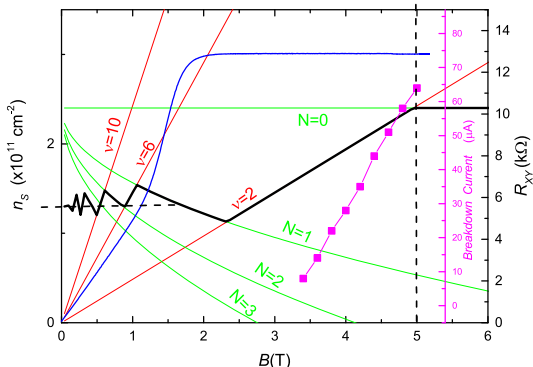


Figure 6. n_s versus magnetic field using the model from [28] (thick black line). Red lines are constant filling factors and green lines are $n_s(B, N)$. Blue line is R_{xy} measured for a device with $n_s \approx 1.3 \times 10^{11} \text{ cm}^{-2}$ (right hand axis) together with the measured breakdown current (purple squares and second purple right hand axis). Vertical dashed line indicates maximum magnetic field of 5 T and horizontal dashed line indicates zero field carrier density of $1.3 \times 10^{11} \text{ cm}^{-2}$.

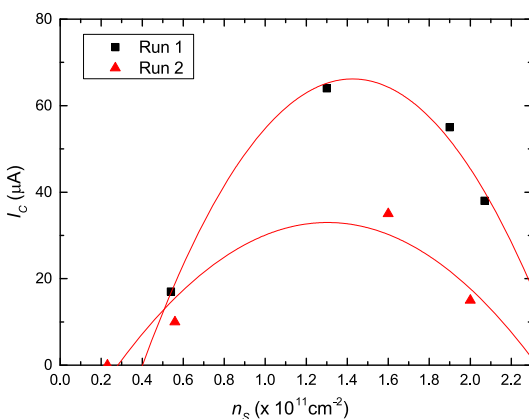
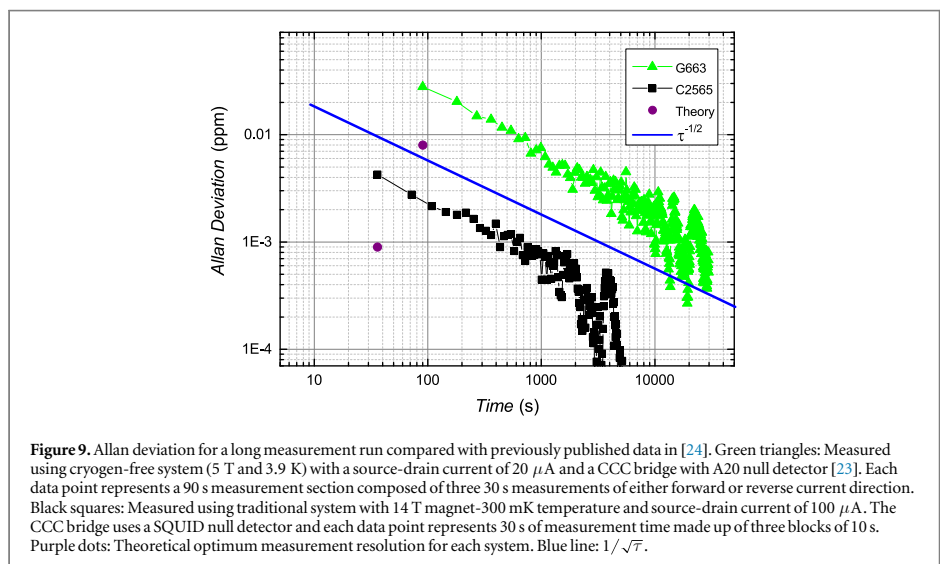
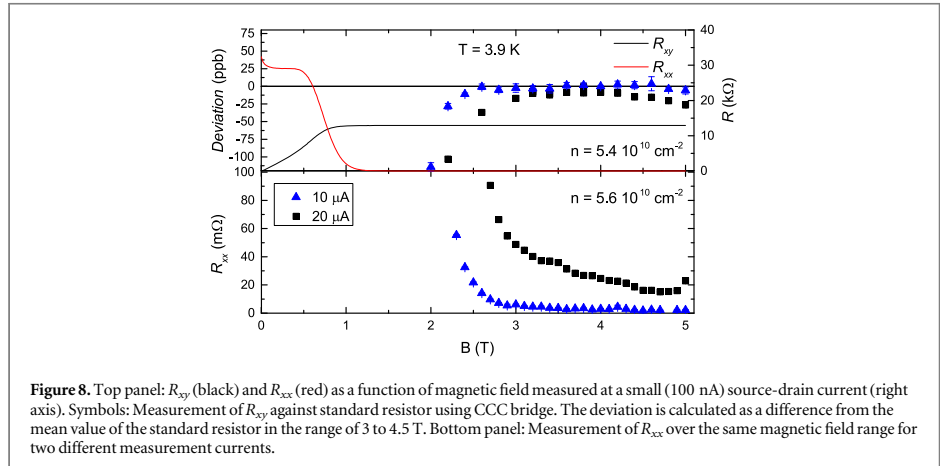


Figure 7. Breakdown current, I_c , versus carrier density n_s at $B = 5 \text{ T}$ and $T = 3.9 \text{ K}$. Black squares are for the first measurement run when the device was new and red triangles are for the second run 3 months later. Red lines are polynomial fits which serve as guide to the eye.

Figure 7 shows the measured maximum breakdown current measured at $B = 5 \text{ T}$ as a function of zero field charge carrier density for two sets of data 3 months apart. The graph confirms that optimum carrier density is around $n_s = 1.3 \times 10^{11} \text{ cm}^{-2}$. For the later data set the breakdown current was almost half the original breakdown current which could be related to the degradation of one of the current contacts on the device after repeated thermal cycling and re-wiring. The cause of this degradation is yet unclear and needs to be investigated further because QHR devices for quantum resistance metrology need to be stable and reproducible over long periods of time. The original maximum breakdown current is $60 \mu\text{A}$ which for our channel width of $30 \mu\text{m}$ implies a current density of 2 Am^{-1} density which is close to the theoretical maximum [29].

5. Quantum Hall resistance measurements

Figure 8 shows the central result of this paper. Here we measured the quantum Hall resistance in terms of a nominally 100Ω temperature controlled standard resistor using the CCC bridge. The data in figure 8 is normalized to the mean value of the resistor since we are not concerned with the absolute accuracy of the QHE in graphene which was established earlier [9]. The measurements are made at two different source-drain currents (≈ 10 and $\approx 20 \mu\text{A}$) as a function of magnetic field. Comparing the data for $10 \mu\text{A}$ with that for $20 \mu\text{A}$ it is clear that for the larger measurement current, the device is not properly quantized. This fact is also confirmed by the measurement of R_{xx} which show a significant deviation from zero for this larger current. The low breakdown current is not a



major issue because the sample chip contains a number of devices with a larger width ($100 \mu\text{m}$) in which the breakdown current will be correspondingly larger (to be published). For the smaller measurement current, accurate quantization is observed over a 2 T magnetic field range which is perfectly adequate for primary resistance measurements.

The measurement resolution obtained for most individual measurements of R_{xy} in figure 8 is 5 parts in 10^9 for a 15 min measuring time. A few measurements are made over a longer time (several hours) and are of order 5 part in 10^{10} . This compares very well with traditional QHR systems, especially considering that for the cryogen-free system, there is in principle no limit on the available measurement time.

Figure 9 shows an Allan deviation plot of the measurement resolution for a long measurement run together with results obtained from a previous measurement using our standard quantum Hall system [24]. Both curves show the expected $1/\sqrt{\tau}$ behaviour for uncorrelated white noise. The lower measurement resolution of the cryogen-free system can be explained by the lower measurement current used ($20 \mu\text{A}$ versus $100 \mu\text{A}$) and the higher current noise of the null detector (A20 null-detector versus SQUID null detector), resulting in a factor of 10 difference. For both the cryogen-free system and the traditional system the theoretical optimum measurement resolution is still a factor of 5 better. This is caused by the fact that the noise of CCC-SQUID combination in our systems is about a

factor of 5 higher than that of the bare SQUID sensor [24].

6. Summary/outlook

The results presented here demonstrate that with epitaxial graphene on SiC it is possible to achieve part per billion accuracy in primary resistance metrology using a simple cryogen-free system. Measurements are presented as a function of magnetic field and different source-drain current densities which demonstrate that the operational parameters are sufficiently wide for easy and reliable use. Care has to be taken to adjust the charge carrier density to the optimum value to ensure a maximum breakdown current density. Corona gating at room temperature and subsequent freezing of the doping is beneficial compared to applying a gate voltage during QHR measurements because no additional noise is injected into the system, but this comes at the expense of the practical inconvenience of thermal cycling the system.

Another practical aspect which needs addressing is the CCC bridge. At the moment this bridge requires a liquid helium dewar to provide the low temperature for the superconducting shield and SQUID. In a separate cryogen-free cryostat we have recently demonstrated that a CCC can be operated in such an environment (to be published). The challenge is to integrate the CCC in the same cryogen-free cryostat as the QHE system and our plan is to do this in the next design iteration of the system.

An alternative to a CCC would be a room temperature comparator bridge. In order to obtain the required ppb-accuracy a large (at least $100 \mu\text{A}$) source drain current through the quantum Hall device is needed which is beyond the breakdown current of a single SiC/G device at low magnetic field and high temperature. In a quantum Hall array many devices can be operated in parallel, lowering the resistance value and increasing the total measurement current. The epitaxial graphene needs to be sufficiently homogeneous so that the operational parameters of all QHR devices overlap and all contacts need to be low ohmic. Recently, the first SiC/G quantum Hall array at $R_K/200$ has been demonstrated [31].

Dissemination and proliferation of primary quantum standards is one of the key objectives of fundamental metrology. The results presented in this paper could be transformative for future resistance metrology by creating the opportunity for many more metrology and calibration laboratories to realize their own primary resistance traceability. This will shorten the calibration chain and lower the uncertainty which can be provided to end users with all its implicit benefits. A number of technical issues remain to be addressed but the basic principle of operation has been demonstrated.

Acknowledgments

This work was supported by the NPL Proof-of-Concept fund, NMS Programme, European Union Seventh Framework Programme under Grant Agreement No. 604391 Graphene Flagship, and EMRP Project GraphOhm.

References

- [1] See for example the BIPM CMC Website at <http://kcdb.bipm.org>
- [2] Klitzing K V, Dorda G and Pepper M 1980 New method for high-accuracy determination of the fine-structure constant based on quantized hall resistance *Phys. Rev. Lett.* **45** 4
- [3] Jeckelmann B and Jeanneret B 2003 The quantum hall effect as an electrical resistance standard *Meas. Sci. Technol.* **14** 1229–36
- [4] Novoselov K S, Geim A K, Morozov S V, Jiang D, Katsnelson M I, Grigorieva I V, Dubonos S V and Firsov A A 2005 Two-dimensional gas of massless dirac fermions in graphene *Nature* **438** 197–200
- [5] Zhang Y B, Tan Y W, Stormer H L and Kim P 2005 Experimental observation of the quantum hall effect and berry's phase in graphene *Nature* **438** 201–4
- [6] Novoselov K S, Jiang Z, Zhang Y, Morozov S V, Stormer H L, Zeitzer U, Maan J C, Boebinger G S, Kim P and Geim A K 2007 Room-temperature quantum hall effect in graphene *Science* **315** 1379
- [7] Giesbers A J M, Rietveld G, Houtzager E, Zeitzer U, Yang R, Novoselov K S, Geim A K and Maan J C 2008 Quantum resistance metrology in graphene *Appl. Phys. Lett.* **93** 222109
- [8] Tzalenchuk A, Lara-Avila S, Kalaboukhov A, Paolillo S, Syvajarvi M, Yakimova R, Kazakova O, Janssen T J B M, Fal'ko V and Kubatkin S 2010 Towards a quantum resistance standard based on epitaxial graphene *Nat. Nanotechnology* **5** 186–9
- [9] Janssen T J B M, Fletcher N E, Goebel R, Williams J M, Tzalenchuk A, Yakimova R, Lara-Avila S, Kubatkin S and Fal'ko V I 2011 Graphene, universality of the quantum hall effect and redefinition of the si system *New J. Phys.* **13** 6
- [10] Satrapinski A, Novikov S and Lebedeva N 2013 Precision quantum hall resistance measurement on epitaxial graphene device in low magnetic field *Appl. Phys. Lett.* **103** 173509
- [11] Kalmbach C C, Schurr J, Ahlers F J, Muller A, Novikov S, Lebedeva N and Satrapinski A 2014 Towards a graphene-based quantum impedance standard *Appl. Phys. Lett.* **105** 073511
- [12] Lafont F et al 2015 Quantum hall resistance standards from graphene grown by chemical vapour deposition on silicon carbide *Nat. Commun.* **6** 6806
- [13] Kopylov S, Tzalenchuk A, Kubatkin S and Fal'ko V I 2010 Charge transfer between epitaxial graphene and silicon carbide *Appl. Phys. Lett.* **97** 3
- [14] Tanabe S, Sekine Y, Kageshima H, Nagase M and Hibino H 2010 Half-integer quantum hall effect in gate-controlled epitaxial graphene devices *Appl. Phys. Lett.* **3** 3
- [15] Lara-Avila S, Moth-Poulsen K, Yakimova R, Bjornholm T, Fal'ko V, Tzalenchuk A and Kubatkin S 2011 Non-volatile photochemical gating of an epitaxial graphene/polymer heterostructure *Adv. Mater.* **23** 5
- [16] Waldmann D, Jobst J, Speck F, Seyller T, Krieger M and Weber H B 2011 Bottom-gated epitaxial graphene *Nat. Mater.* **10** 357–60
- [17] Lartsev A, Yager T, Bergsten T, Tzalenchuk A, Janssen T J B M, Yakimova R, Lara-Avila S and Kubatkin S 2014 Tuning carrier density across dirac point in epitaxial graphene on sic by corona discharge *Appl. Phys. Lett.* **105** 063106
- [18] Martin J, Akerman N, Ulbricht G, Lohmann T, Smet J H, von Klitzing K and Yacoby A 2008 Observation of electron-hole puddles in graphene using a scanning single-electron transistor *Nat. Phys.* **4** 144–8
- [19] Huang J et al 2015 Disorder induced Dirac-point physics in epitaxial graphene from temperature-dependent magneto-transport measurements *Phys. Rev. B* **92** 075407

- [20] Delahaye F and Jeckelmann B 2003 Revised technical guidelines for reliable dc measurements of the quantized hall resistance *Metrologia* **40** 217–23
- [21] Virojanadara C, Virojanadara C, Syvajarvi M, Yakimova R, Johansson L I, Zakharov A A and Balasubramanian T 2008 Homogeneous large-area graphene layer growth on 6h-sic (0001) *Phys. Rev. B* **78** 6
- Yakimova R, Iakimov T and Syvjarvi M 2014 Process for growth of graphene *Patent Granted CN103097283A* p 5
- [22] Yager T *et al* 2015 Low contact resistance in epitaxial graphene devices for quantum metrology *AIP Adv.* **5** 087134
- [23] Williams J M, Janssen T J B M, Rietveld G and Houtzager E 2010 An automated cryogenic current comparator resistance ratio bridge for routine resistance measurements *Metrologia* **47** 167–74
- [24] Janssen T J B M, Williams J M, Fletcher N E, Goebel R, Tzalenchuk A, Yakimova R, Lara-Avila S, Kubatkin S and Fal'ko V I 2012 Precision comparison of the quantum hall effect in graphene and gallium arsenide *Metrologia* **49** 294–306
- [25] Schopfer F and Poirier W 2013 Quantum resistance standard accuracy close to the zero-dissipation state *J. Appl. Phys.* **114** 064508
- [26] Wu X S, Hu Y K, Ruan M, Madiomanana N K, Hankinson J, Sprinkle M, Berger C and de Heer W A 2009 Half integer quantum hall effect in high mobility single layer epitaxial graphene *Appl. Phys. Lett.* **95** 3
- [27] Shen T, Gu J J, Xu M, Wu Y Q, Bolen M L, Capano M A, Engel L W and Ye P D 2009 Observation of quantum-hall effect in gated epitaxial graphene grown on sic (0001) *Appl. Phys. Lett.* **95** 3
- [28] Janssen T J B M, Tzalenchuk A, Yakimova R, Kubatkin S, Lara-Avila S, Kopylov S and Fal'ko V I 2011 Anomalously strong pinning of the filling factor $\nu = 2$ in epitaxial graphene *Phys. Rev. B* **83** 4
- [29] Alexander-Webber J A, Baker A M R, Janssen T J B M, Tzalenchuk A, Lara-Avila S, Kubatkin S, Yakimova R, Piot B A, Maude D K and Nicholas R J 2013 Phase space for the breakdown of the quantum hall effect in epitaxial graphene *Phys. Rev. Lett.* **111** 096601
- [30] Jeckelmann B and Jeanneret B 2001 The quantum hall effect as an electrical resistance standard *Rep. Prog. Phys.* **64** 1603–55
- [31] Lartsev A *et al* 2015 A prototype of $R_K/200$ quantum hall array resistance standard on epitaxial graphene *J. Appl. Phys.* **118** 044506

Paper B

Fabrication of graphene quantum hall resistance standard in a cryogen-free table-top system

Fabrication of graphene quantum Hall resistance standard in a cryogen-free table-top system

H He¹, T J B M Janssen², S Rozhko², A Tzalenchuk^{2,3}, S Lara-Avila¹, R Yakimova⁴ and S Kubatkin¹

¹Department of Microtechnology and Nanoscience, Chalmers University of Technology, S-41296 Göteborg, Sweden

²National Physical Laboratory, Hampton Road, Teddington TW110LW, UK

³Royal Holloway, University of London, Egham TW200EX, UK

⁴Department of Physics, Chemistry and Biology (IFM), Linköping University, S-58183 Linköping, Sweden

Email: hanshe@chalmers.se

Abstract — We have demonstrated quantum Hall resistance measurements with metrological accuracy in a relatively easy to use and compact cryogen-free system operating at a temperature of around 3.8 K and magnetic field below 5 T. This advance in technology is due to the unique properties of epitaxial graphene on silicon carbide (SiC) which lifts the stringent requirements for quantum hall effect seen in conventional semiconductors. This paper presents the processes involved in fabrication and characterization of metrologically viable epitaxial graphene samples.

Index Terms — Epitaxial layers, Graphene, measurement standards, microfabrication, quantum hall effect

I. INTRODUCTION

One of the challenges of modern-day metrology is to shorten the traceability chain by bringing quantum standards closer to the end-user. Solving this problem will lead to improved calibration accuracy for users and is highly beneficial for projects where accurate measurements are an issue. Advancement towards this goal was done by utilizing the special properties of epitaxial graphene on silicon carbide to make a small cryogen-free table-top system which is relatively easy to operate and shows quantum hall resistance quantization with metrological accuracy below 4 K and 5 T [1]. This work will focus on the fabrication and characterization of epitaxial graphene samples used in the table-top system.

II. EPITAXIAL GRAPHENE ON SILICON CARBIDE

The most accurate resistance standards are based on the quantum Hall effect (QHE) which can be achieved in conventional semiconductors, e.g. GaAs, at temperature below 1 K and in magnetic fields around 10 T. The harsh constraints make these measurements quite complicated and expensive to perform. After graphene was first experimentally isolated in 2004 the discovery of QHE in graphene followed quickly [2]. Owing to its unique Landau level quantization the low temperature and high magnetic field constraints are relaxed for QHE in graphene systems which facilitate measurements.

The possibility of highly accurate quantum hall measurements in epitaxial graphene on silicon carbide (SiC) was originally demonstrated in 2010 [3]. The graphene samples compared favorably to GaAs systems by reaching resistance quantization accuracy of a few parts per billion.

Using graphene on SiC comes with many advantages such as: accurate quantization can be achieved at 4 K and 5 T, the resistance plateau (typically filling factor $n=2$) is stable over a wide range of magnetic fields, critical currents are high which improves signal-to-noise ratio, high quality monolayer graphene can be grown on a wafer scale on SiC and no graphene transfer is needed since SiC is a wide-gap semiconductor. Some disadvantages, which can be mitigated, are: strong intrinsic n-doping from the substrate and bilayer inclusions which can be detrimental to device performance.

III. SAMPLE PREPARATION

A. Graphene Growth

Graphene samples are grown epitaxially on the Si-face (0001) of SiC using thermal decomposition. The SiC substrate is heated to 2000 °C while being kept in an argon environment at 1 atm pressure [4]. Typical samples sizes are 7x7 mm SiC chips covered uniformly by monolayer graphene.

B. Optical Characterization

After growth samples are inspected using a simple optical microscopy technique to look for surface inhomogeneities [5]. While the entire chip is covered by monolayer graphene (without grain boundaries) there are places where patches of bilayer exist which could spoil device performance depending on their size and orientation. This is due to the fact that when the monolayer graphene enters the quantum hall regime bilayer patches can stay normal or even become insulating. Using optical microscopy with real-time digital filtering and image post-processing it is possible to identify bilayer patches and choose the optimal location for graphene Hall bars which typically have channel widths around 30-100 μm.

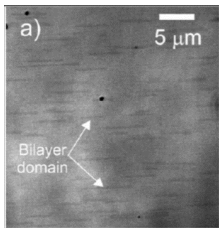


Fig. 1. Optical micrograph taken in transmission mode. The bilayer patches appear as dark streaks. Reprinted with permission from [5].

C. Electron Beam Lithography

The quantum hall devices are fabricated using standard electron beam lithography techniques. Typically two layers of PMMA based positive resists are used. In the first lithography layer graphene is etched away using oxygen plasma and Ti/Au metal pads are deposited directly on top of SiC. These serve as anchoring points for metallic contacts to graphene since adhesion between metal and SiC is much stronger than metal and graphene. In the second layer the Ti/Au contacts, which connect to the legs of the hall bar, are deposited. In the final layer oxygen plasma is used to define the hall bar and isolate devices from each other. Typically 20 quantum hall devices are made simultaneously on the same chip.

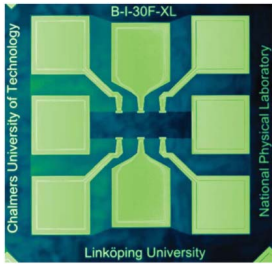


Fig. 2. Optical micrograph taken of a finished graphene hall device with a 100 μm wide channel. The dark part is graphene and the light part is SiC [1].

D. Electrical Characterization

After finishing fabrication the sample is quickly tested to see if quantum hall transition occurs at 4 K and below 5 T. Epitaxial graphene on SiC is intrinsically n-doped (up to 10^{13} cm^{-2}) due to substrate interactions and coronal discharge gating is used to bring the carrier density to a more desired level (10^{11} cm^{-2}), optimized with respect to maximum critical current [1][6]. The sample is then inserted into a cryostat and

tested to see if the QHE appears at the desired temperatures and fields. For optimal performance the longitudinal resistance and contact resistances should be as close to zero as possible. The longitudinal resistance is easily measured using a four-probe setup and in quantum hall regime three-probe techniques are used to determine contact resistances.

IV. CONCLUSION

A method to fabricate quantum hall resistance standards on epitaxial graphene grown on SiC was developed. The samples produced using this process were used to measure resistance quantization with metrological accuracy up to a few parts per billion at relaxed conditions 4 K and 5 T compared to standard semiconductor systems. Such samples are integrated into a cryogen-free table-top system aimed to improving usability and calibration accuracy for the end-user.

ACKNOWLEDGEMENT

This work was supported by the NPL Proof-of-Concept fund, NMS Program, European Union Seventh Framework Program under Grant Agreement No. 604391 Graphene Flagship, VINNOVA and EMRP Project GraphOhm. The EMRP is jointly funded by the EMRP participating countries within EURAMET and the European Union.

REFERENCES

- [1] T. J. B. M. Janssen, S. Rozhko, I. Antonov, A. Tzalenchuk, J. M. Williams, Z. Melhem, H. He, S. Lara-Avila, S. Kubatkin and R. Yakimova, "Operation of graphene quantum Hall resistance standard in a cryogen-free table-top system," *2D Mater.*, vol. 2, no. 4, p. 035015, July 2015.
- [2] K. S. Novoselov, A. K. Geim, S. V. Morozov, D. Jiang, M. I. Katsnelson, I. V. Grigorieva, S. V. Dubonos and A. A. Firsov, "Two-dimensional gas of massless Dirac fermions in graphene", *Nature*, vol. 348, pp. 197-200, November 2005.
- [3] A. Tzalenchuk, S. Lara-Avila, A. Kalaboukhov, S. Paolillo, M. Syväjärvi, R. Yakimova, O. Kazakova, T. J. B. M. Janssen, V. Fal'ko and S. Kubatkin "Towards a quantum resistance standard based on epitaxial graphene," *Nat. Nanotechnology*, vol. 5, pp. 186-189, January 2010.
- [4] C. Virojanadara, M. Syväjärvi, R. Yakimova, L. I. Johansson, A. A. Zakharov and T. Balasubramanian, "Homogeneous large-area graphene layer growth on 6H-SiC(0001)", *Phys. Rev. B*, vol. 78, p. 245403, December 2008.
- [5] T. Yager, A. Lartsev, S. Mahashabde, S. Charpentier, D. Davidvojkj, A. Danilov, R. Yakimova, V. Panchal, O. Kazakova, A. Tzalenchuk, S. Lara-Avila and S. Kubatkin, "Express Optical Analysis of Epitaxial Graphene on SiC: Impact of Morphology on Quantum Transport", *Nano Letters*, vol. 13, pp. 4217-4223, August 2013.
- [6] A. Lartsev, T. Yager, T. Bergsten, A. Tzalenchuk, T. J. B. M. Janssen, R. Yakimova, S. Lara-Avila and S. Kubatkin, "Tuning carrier density across dirac point in epitaxial graphene on SiC by corona discharge", *Appl. Phys. Lett.*, vol. 105, p. 063106, July 2014.

Paper C

Uniform doping of graphene close to the Dirac point
by polymer-assisted assembly of molecular dopants

ARTICLE

DOI: 10.1038/s41467-018-06352-5

OPEN

Uniform doping of graphene close to the Dirac point by polymer-assisted assembly of molecular dopants

Hans He¹, Kyung Ho Kim^{1,2}, Andrey Danilov¹, Domenico Montemurro¹, Liyang Yu³, Yung Woo Park^{2,4,5}, Floriana Lombardi¹, Thilo Bauch¹, Kasper Moth-Poulsen¹, Tihomir Iakimov⁶, Rositsa Yakimova⁶, Per Malmberg¹, Christian Müller¹, Sergey Kubatkin¹ & Samuel Lara-Avila^{1,7}

Tuning the charge carrier density of two-dimensional (2D) materials by incorporating dopants into the crystal lattice is a challenging task. An attractive alternative is the surface transfer doping by adsorption of molecules on 2D crystals, which can lead to ordered molecular arrays. However, such systems, demonstrated in ultra-high vacuum conditions (UHV), are often unstable in ambient conditions. Here we show that air-stable doping of epitaxial graphene on SiC—achieved by spin-coating deposition of 2,3,5,6-tetrafluoro-tetracyano-quino-dimethane (F4TCNQ) incorporated in poly(methyl-methacrylate)—proceeds via the spontaneous accumulation of dopants at the graphene-polymer interface and by the formation of a charge-transfer complex that yields low-disorder, charge-neutral, large-area graphene with carrier mobilities $\sim 70\,000\,\text{cm}^2\,\text{V}^{-1}\,\text{s}^{-1}$ at cryogenic temperatures. The assembly of dopants on 2D materials assisted by a polymer matrix, demonstrated by spin-coating wafer-scale substrates in ambient conditions, opens up a scalable technological route toward expanding the functionality of 2D materials.

¹Department of Microtechnology and Nanoscience, Chalmers University of Technology, 412 96 Gothenburg, Sweden. ²Department of Physics and Astronomy, Seoul National University, Seoul 08826, Korea. ³Department of Chemistry and Chemical Engineering, Chalmers University of Technology, 41296 Göteborg, Sweden. ⁴Institute of Applied Physics, Seoul National University, Seoul 08826, Korea. ⁵Department of Physics and Astronomy, University of Pennsylvania, Philadelphia, PA 19104, USA. ⁶Department of Physics, Chemistry and Biology, Linköping University, 581 83 Linköping, Sweden. ⁷National Physical Laboratory, Hampton Road, Teddington TW11 OLW, UK. Correspondence and requests for materials should be addressed to S.L.-A. (email: samuel.lara@chalmers.se)

Homogeneous doping of graphene down to low carrier densities enables the study of delicate and fascinating physics at the Dirac point. The prime experimental archetypes for the study of Dirac physics in solid-state devices are van der Waals (VdW) hetero-structures of graphene and hexagonal boron nitride (hBN). In these, extremely low carrier densities in graphene are attainable, especially when prepared on atomically flat, electrically conductive substrates that screen long-range potential fluctuations (i.e. disorder) in the graphene layer^{1,2}. Typically microscopic in size, VdW hetero-structures are prone to size-induced mesoscopic effects that obscure novel physical effects expected in graphene at charge neutrality. Large-area graphene, uniformly doped to the Dirac point as in the case of VdW hetero-structures, is required to unveil the intimate details of, for instance, metal-insulator transitions³, interacting Dirac fermions⁴, and Zitterbewegung of electrons in graphene⁵. Atomically flat, large-scale epitaxial graphene on SiC (SiC/G) has demonstrated its potential for scalability in applications that demand extremely high-quality graphene over large areas, including quantum metrology^{6,7} and high-frequency electronics^{8,9}. Yet, in practice, carrier density control of SiC/G remains a challenge because of high intrinsic n-doping ($n > 10^{13} \text{ cm}^{-2}$) due to interaction with the substrate, making it difficult to substantially tune its carrier concentration¹⁰. While numerous gating techniques have been applied to SiC/G to reduce its carrier density^{8,9}, such approaches introduce carrier density fluctuations, which prevent further explorations of Dirac physics in this material.

Here we show a molecular approach to control the carrier density of epitaxial graphene homogeneously over macroscopic areas, yielding graphene with low carrier density ($n < 10^{10} \text{ cm}^{-2}$), low charge fluctuations (at the level of $\Delta n \approx \pm 6 \times 10^9 \text{ cm}^{-2}$), and carrier mobilities up to $70\,000 \text{ cm}^2 \text{ V}^{-1} \text{ s}^{-1}$ at low temperatures. So far, such electron transport properties have only been attained in microscopic single-crystal graphene flakes encapsulated by hBN¹¹ or in suspended graphene¹². The doping method described here was applied to samples over $5 \times 5 \text{ mm}^2$, resulting in epitaxial graphene devices that display quantum Hall effect at magnetic fields $B < 1 \text{ T}$. These measurements indicate, as we elaborate below, a highly homogeneous spatial distribution of charge carriers on graphene. Chemical analysis reveals that air-stable molecular doping of graphene is achieved when organic molecules, embedded in a polymer matrix, diffuse through the matrix and spontaneously accumulate at the graphene surface due to formation of a charge-transfer complex. High-electron-affinity 2,3,5,6-tetrafluoro-tetracyano-quinino-dimethane (F4TCNQ) molecules are mixed in a liquid solution with poly(methyl-methacrylate) (PMMA) and spin-coated at ambient conditions on SiC/G, with graphene being used both as the target substrate for molecular assembly and, simultaneously, as a charge sensor. The stability of the samples allows us to study the chemical composition as well as electronic transport properties of the F4TCNQ/graphene system. We expect this method to open up a scalable route toward expanding the properties and functionality of graphene and other two-dimensional (2D) materials well beyond doping control.

Results

Doping schemes. The different chemical doping schemes of graphene devices are shown in Fig. 1b. Our devices include large ($W = 5 \text{ mm} \times L = 5 \text{ mm}$) (Fig. 1a) and small ($W = 2\text{--}100 \mu\text{m} \times L = 10\text{--}180 \mu\text{m}$) epitaxial graphene Hall bars fabricated by conventional electron beam lithography (see Methods section). When PMMA is used as a spacer between graphene and the molecular dopant layer, the carrier density decreases three orders of magnitude from its pristine value, $n \approx 1 \times 10^{13} \text{ cm}^{-2}$ to

near charge neutrality, $n \approx 1 \times 10^{10} \text{ cm}^{-2}$ (Fig. 1c). Importantly, even at such low carrier densities the carrier mobility remains high, with the largest measured value exceeding $\mu \approx 50\,000 \text{ cm}^2 \text{ V}^{-1} \text{ s}^{-1}$ at $T = 2 \text{ K}$. The effect of doping is homogeneous over millimeter scale and large samples display quantum Hall effect at magnetic fields $B < 1 \text{ T}$ (Fig. 1a), retaining their low carrier density over the course of 2 years, even under ambient conditions (Supplementary Fig. 1). To achieve this, a 200-nm-thick layer of the PMMA-F4TCNQ dopant blend is spin-coated onto a PMMA-protected sample, followed by thermal annealing above the PMMA glass transition temperature. The resulting carrier density could be fine-tuned by the total annealing time. For a concentration of 7% of F4TCNQ in PMMA by weight, charge-neutral graphene is achieved after annealing at $T = 160^\circ\text{C}$ for 5 min. Shorter annealing times yield hole-doping and longer times yield electron-doping (Supplementary Fig. 1). Using the optimal time, we have consistently observed a decrease in electron density by three orders of magnitude together with a tenfold increase of carrier mobility at $T = 2 \text{ K}$ in more than 20 devices on 11 different chips (Supplementary Table 1 and Supplementary Fig. 2). Typical carrier concentrations in doped samples are of the order of $5 \times 10^{11} \text{ cm}^{-2}$ at room temperature. They decrease to values $\sim 1 \times 10^{10} \text{ cm}^{-2}$ at $T = 2 \text{ K}$, due to freezing of thermally activated carriers¹³. The corresponding carrier mobilities are in the range of $30\,000\text{--}50\,000 \text{ cm}^2 \text{ V}^{-1} \text{ s}^{-1}$ (Fig. 1d). The PMMA spacer layer plays a crucial role in achieving high carrier mobilities. While both PMMA and the dopant blend act independently as moderate p-dopants when deposited directly on SiC/G, it is only when the PMMA spacer layer is added between graphene and the dopant blend that we observe the near to charge neutrality doping effect. Similarly, carrier mobilities exceed $10\,000 \text{ cm}^2 \text{ V}^{-1} \text{ s}^{-1}$ only if the PMMA spacer and dopant blend operate in tandem (Supplementary Fig. 3).

Chemical analysis of graphene-polymer hetero-structure. We demonstrate that the doping of graphene is the result of F4TCNQ molecules diffusing through the PMMA layer and accumulating at the graphene surface. Figure 2a, b shows the chemical depth profile of the polymer stack, obtained by using time-of-flight secondary ion mass spectrometry (ToF-SIMS), revealing both diffusion of F4TCNQ through the PMMA spacer and the accumulation of molecules at the graphene surface. From this we estimate the diffusion coefficient of F4TCNQ through PMMA to be of the order of $10^{14} \text{ cm}^2 \text{ s}^{-1}$ and by integrating the areas under the ion current intensity curves, we estimate the density of F4TCNQ molecules near the graphene surface to be $\sim 4.6 \times 10^{14} \text{ cm}^{-2}$ (Supplementary Fig. 4, Supplementary Note 1). Graphene and metallic surfaces promote the accumulation of F4TCNQ, while there are virtually no dopant molecules at the polymer/SiC interface. The surface density of F4TCNQ is roughly 50% greater on graphene (and sixfold higher on gold) compared to that in the dopant blend layer (Fig. 2c). We attribute the accumulation of F4TCNQ on the graphene surface and the measured p-doping effect to the formation of a charge transfer complex, with partially charged F4TCNQ remaining at the graphene interface to preserve overall charge neutrality. F4TCNQ is known to be mobile in thin polymer films^{14,15}, with its diffusion depending on polarity and glass transition temperature of the polymer. When using an inert PMMA as a host matrix, F4TCNQ remains neutral both in the doping layer and as it diffuses through PMMA spacer layer¹⁶. The formation of a charge transfer complex takes place only when encountering an electron donor, such as graphene. Once charged, the F4TCNQ anion is bound to graphene, stabilized by Coulomb interaction¹⁷.

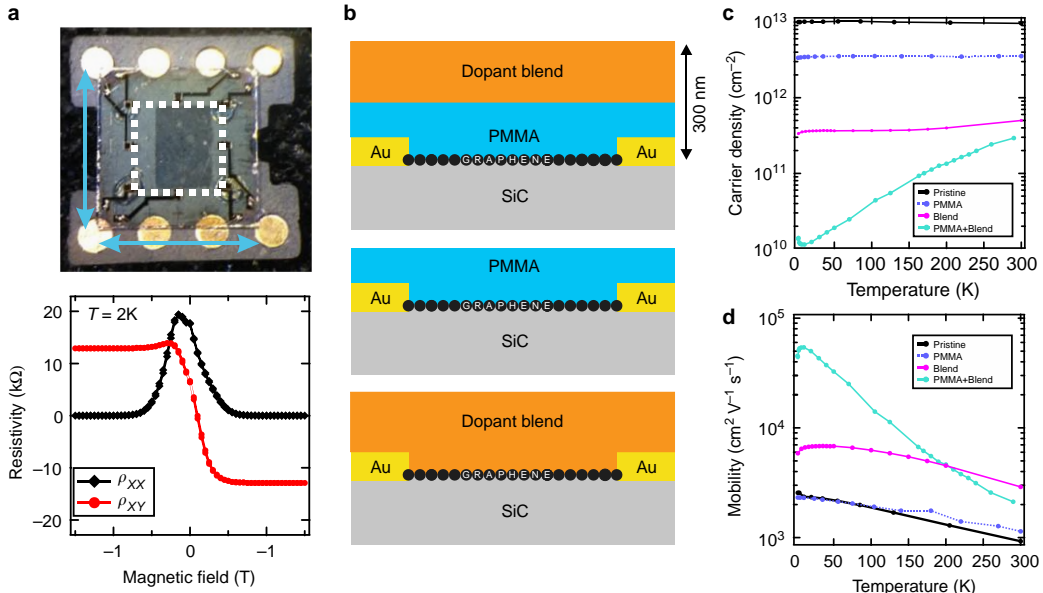


Fig. 1 Magnetotransport characterization of chemically doped SiC/G. **a** Top: macroscopic graphene Hall bar device (white dotted outline, $W = 5 \text{ mm} \times L = 5 \text{ mm}$). Bottom: low field magnetoresistance and fully developed quantum Hall effect indicating low charge disorder in chemically doped graphene, even over macroscopic areas. For this device, the measured carrier density $p = 9 \times 10^9 \text{ cm}^{-2}$ and mobility $\mu = 67\,000 \text{ cm}^2 \text{ V}^{-1} \text{ s}^{-1}$. **b** The different encapsulation schemes with a polymer stack consisting of PMMA-F4TCNQ dopant blend, which comprises of F4TCNQ molecules in a PMMA matrix (F4TCNQ 7 wt%). The three schemes are dopant blend separated from graphene by a PMMA spacer (top), only PMMA layer (middle), and the dopant blend directly on the surface of graphene (bottom). **c** Carrier density as a function of temperature extracted from Hall measurements on small epitaxial graphene devices ($W = 2\text{--}50 \mu\text{m} \times L = 4\text{--}180 \mu\text{m}$). **d** The corresponding Hall carrier mobility showing the highest $\mu \sim 55\,000 \text{ cm}^2 \text{ V}^{-1} \text{ s}^{-1}$ at $T = 10 \text{ K}$ for sample prepared with PMMA spacer and dopant layer. The downturn in mobility at lower temperatures is due to quantum corrections to the Drude resistance. Carrier concentration n and mobilities μ were extracted from Hall measurements as $n = 1/eR_H$ and $\mu = R_H/\rho_{XX}$, with e the elementary charge, the Hall coefficient $R_H = dR_{XY}/dB$, the longitudinal sheet resistance $\rho_{XX} = R_{XX}W/L$, and R_{XY} the transversal resistance.

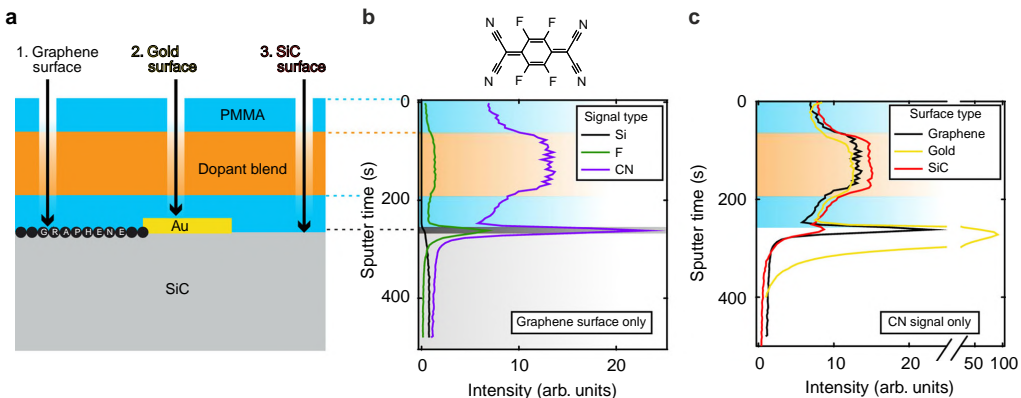


Fig. 2 Chemical profiling of the polymer layers using ToF-SIMS to detect fingerprints of the F4TCNQ molecule (F and CN ions) as one probes deeper into the polymer stack. **a** Samples were prepared with PMMA spacer, dopant blend, and PMMA encapsulation layer. Three distinct spots on the substrate have been investigated: (1) graphene, (2) gold, and (3) SiC surfaces. **b** When analyzing the polymer layers on spot 1, above the graphene surface, the ion intensity for F and CN ions (top inset shows a schematic representation of a F4TCNQ molecule) vs. sputter time reveals significant accumulation of F4TCNQ at the graphene/PMMA interface, as well as the spatial distribution of F4TCNQ molecules through the spacer and encapsulation PMMA layers. The onset of the silicon signal (Si) is the marker, which indicates that the SiC substrate has been reached. The shaded regions denote the extent of each layer, from top PMMA layer down to SiC substrate. **c** Here we focus only on the CN signal measured at all three different spots. This analysis shows accumulation of F4TCNQ on the conductive surfaces of graphene and gold, but virtually no accumulation on SiC.

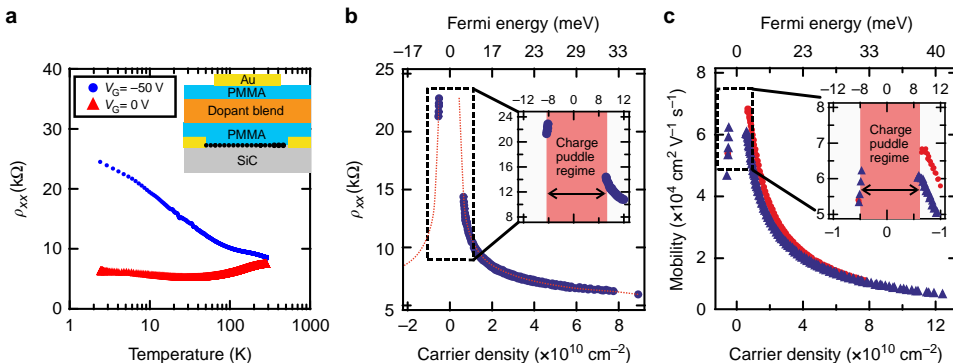


Fig. 3 Electrostatic gating of chemically doped graphene ($30\ \mu\text{m} \times 180\ \mu\text{m}$ Hall bar). **a**, Temperature dependence of longitudinal resistance for graphene in the metallic limit (red) and gated to Dirac point (blue). (Inset) Schematic representation of a chemically doped graphene device with a metallic gate (the topmost Au layer). **b**, ρ_{xx} vs. carrier concentration shows the characteristic Dirac peak around the charge neutrality point (red dotted line serves as a guide to the eye). The Dirac point is crossed below $V_G = -40\ \text{V}$, and the device has well-defined carrier densities within $\pm 6 \times 10^9\ \text{cm}^{-2}$ at $T = 2\ \text{K}$, which corresponds to a Fermi energy of $\pm 9\ \text{meV}$. **c**, Corresponding charge carrier mobilities, with values up to $70\,000\ \text{cm}^2\ \text{V}^{-1}\ \text{s}^{-1}$. Each point in **b** and **c** represents data of magnetic field scans where R_{XY} is linear in the low magnetic field limit and the device shows fully developed quantum Hall effect at high magnetic fields ($\rho_{xx} = 0$ and exactly quantized R_{XY} plateaus). The gap in data around zero carrier concentration corresponds to omitted data points where graphene is in the charge puddle regime. For comparison, in **c**, red circles and blue triangles correspond to Hall measurements from two different Hall probe pairs on the same device. The gate voltage was applied at cryogenic temperatures; the measured leakage current did not exceed 50 pA, with the bias current on graphene of 100 nA

Low charge disorder in SiC/G doped close to Dirac point. We investigated further electron transport details of the F4TCNQ-graphene charge-transfer complex system by introducing a top electrostatic gate (Fig. 3a, inset) on top of a $30\ \mu\text{m} \times 180\ \mu\text{m}$ Hall bar. The top gate enables additional fine tuning of the carrier concentration within $\Delta n \sim 5 \times 10^{11}\ \text{cm}^{-2}$ using gate voltages $V_G = -100$ to $+200\ \text{V}$. At $V_G = 0\ \text{V}$ the carrier density is $n = 5 \times 10^{11}\ \text{cm}^{-2}$ at room temperature and graphene is in the metallic limit. In this case, $\rho_{xx}(T, V_G = 0\ \text{V})$ decreases linearly with temperature from its room temperature value, due to suppression of acoustic phonon scattering. Quantum corrections to resistance result in a $\log(T)$ dependence below the Bloch-Grüneisen temperature $T_{BG} = 2v_{ph}E_F/(k_Bv_F) = 2v_{ph}\hbar v_F\sqrt{\pi n}/(k_Bv_F) \approx 38\ \text{K}$, with the phonon velocity $v_{ph} = 2 \times 10^4\ \text{m s}^{-1}$ ($E_F = \hbar v_F\sqrt{\pi n}$ the Fermi level of graphene, \hbar the reduced Planck's constant, k_B the Boltzmann constant, and $v_F = 10^6\ \text{m s}^{-1}$ the Fermi velocity in graphene¹⁸). In contrast, when graphene is gated to the Dirac point, the sheet resistance $\rho_{xx}(T, V_G = -50\ \text{V})$ monotonically increases as the temperature drops, though remains finite with no indication of a transport gap in the current voltage characteristics down to $T = 2\ \text{K}$ (Fig. 3a).

To characterize the magnitude of carrier density fluctuations (i.e. how precisely one can approach the Dirac point) we conducted low-temperature magnetotransport measurements on chemically and electrostatically gated devices and found these fluctuations to be on the level of $\Delta n \sim \pm 6 \times 10^9\ \text{cm}^{-2}$ ($\Delta E_F \sim \pm 9\ \text{meV}$). Figure 3b shows longitudinal resistance vs. carrier concentration in which every data point, extracted from individual measurements of $\rho_{xx}(B)$, $R_{XY}(B)$ at a fixed gate voltage, corresponds to devices behaving as a system with a single electronic band and spatially homogenous carrier density^{19–23}. That is, data points in Fig. 3b fulfill simultaneously the criteria of linear $R_{XY}(B)$ at low fields^{19–22}, and fully developed half-integer quantum Hall Effect at high fields²³, i.e. $\rho_{xx}(B) = 0\ \Omega$ and strictly quantized R_{XY} plateau over the entire available range of magnetic field (Supplementary Fig. 5). The gap in data around zero carrier

concentration thus corresponds to data points where graphene is in the charge puddle regime. Under quantizing conditions, the residual disorder in the sample causes non-zero and oscillatory $\rho_{xx}(B)$ once the magnetic length approaches the average charge puddle size^{23,24}. In our samples with low carrier density concentration $\sim 10^{10}\ \text{cm}^{-2}$ we have observed no deviation from $\rho_{xx}(B) = 0$ to the largest magnetic field available in our setup ($B = 14\ \text{T}$) (Supplementary Fig. 5). Thus, we establish an upper limit for the puddle size of about $l_B = \sqrt{\hbar/eB} \approx 7\ \text{nm}$. The charge puddle magnitude is directly connected to disorder introduced by, e.g., topography or inhomogeneous doping²⁵. The small magnitude of charge puddles measured in our devices indicate that SiC/G doped with F4TCNQ molecules is homogeneous also at the microscopic scale, with carrier density fluctuations comparable to those in high-quality, hBN-encapsulated single-crystal graphene flakes obtained by exfoliation¹¹ or by chemical vapor deposition growth²⁶ (Supplementary Fig. 6).

It is remarkable that epitaxial graphene displays such low disorder even at extreme dopant coverage, being decorated with a dense layer of molecules of about 3–4 molecules per nm^2 ($c \approx 3 \times 10^{14}\ \text{cm}^{-2}$, comparable to the molecular coverage of $c \approx 4.6 \times 10^{14}\ \text{cm}^{-2}$ from SIMS). We estimated the molecular density at the graphene surface from the shift in carrier density measured in doped graphene with respect to its pristine concentration ($\Delta n \approx 1 \times 10^{13}\ \text{cm}^{-2}$), and assuming that 0.3 electrons are withdrawn from epitaxial graphene per molecule^{27,28} with 1/10 gate efficiency¹⁰. The homogeneity in doping is in part enabled by the high degree of F4TCNQ dispersion inside the PMMA matrix, shown by room temperature grazing-incidence wide-angle X-ray scattering (GIWAXs). The diffractogram in Fig. 4a, b reveals a broad amorphous halo with a distinct diffraction peak at $q = 9.6\ \text{nm}^{-1}$ from PMMA (Supplementary Note 2). The absence of diffraction spots from F4TCNQ implies the lack of molecular aggregation (i.e. crystallites) inside the matrix. Given the size of the F4TCNQ molecule, we propose that at this packing density a

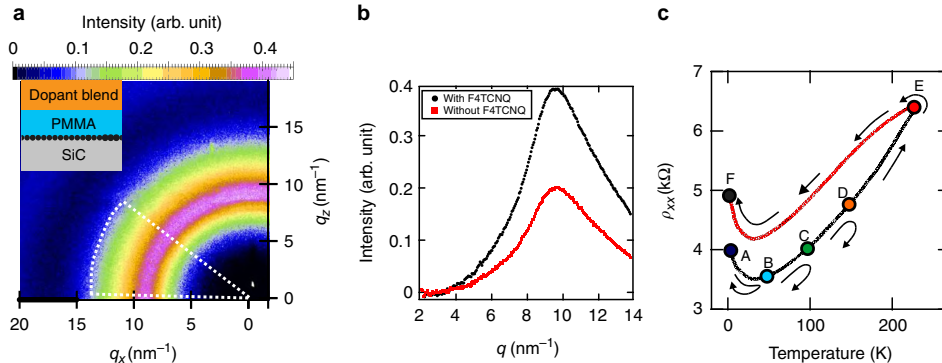


Fig. 4 F4TCNQ in PMMA matrix. **a** Grazing-incidence wide-angle x-ray scattering (GIWAXS) measurements taken on SiC/G with dopant blend and PMMA spacer (inset) (ambient condition, room temperature, 0.15° incident angle). The diffraction ring with radius $q = 9.6 \text{ nm}^{-1}$ from PMMA and the absence of F4TCNQ diffraction spots suggests a good molecular solubility in the polymer matrix. The color bar shows the normalized intensity, after a constant diffuse scattering background has been subtracted. The white dotted region denotes over which azimuthal angles the intensity profile in **b** has been averaged. **b** The reference sample, without F4TCNQ in the dopant blend displays a clear peak diffraction ring with radius $q = 9.6 \text{ nm}^{-1}$; the addition of F4TCNQ molecules enhances the signal twofold. **c** Stability of doping at low temperature in a device that has been cooled down from room temperature. Starting at $T = 300 \text{ K}$ we applied a gate voltage $V_G = +50 \text{ V}$ during cool down. Once we reached $T = 2 \text{ K}$, the gate terminal is set to $V_G = 0 \text{ V}$ and sample sheet resistance acquires a value of $\rho_{xx} = 4 \text{ k}\Omega$ (point A). Thermal excursions to $T = 50 \text{ K}$ (B), 100 K (C), and 150 K (D) result in reversible $\rho_{xx}(T)$ along the black curve. Once temperature exceeds $T = 150 \text{ K}$ (E), $\rho_{xx}(T)$ irreversibly changes to a higher resistive value (red curve), and on cooling down back to $T = 2 \text{ K}$, the sample resistance takes a value of $\rho_{xx} = 5 \text{ k}\Omega$ (F). In the absence of the gate voltage, the sample resistance remains in the higher resistance $\rho_{xx}(T)$ branch

feasible molecular orientation of F4TCNQ is close to that of molecules standing up on the graphene surface²⁸. Yet, we do not rule out molecular re-orientation or thermally induced redistribution of charges in the dopant layer under the effect of electric field, even at low temperatures. Such charge redistribution in the dopants in close vicinity to graphene may be responsible for screening charge inhomogeneities that facilitate highly uniform doping¹. Thermally activated motion of charges in the dopant layer is a plausible source of the hysteresis in $\rho_{xx}(T)$ when devices are subjected to thermal excursion from $T = 2$ to 230 K (Fig. 4c). This is also suggested by more accurate resistance measurements, which reveal that charges in the dopant layer are mobile down to $T \approx 113 \text{ K}$ (Supplementary Fig. 7), in notable coincidence with the energy scale of the measured charge inhomogeneity in doped epitaxial graphene ($\Delta E_F \sim \pm 9 \text{ meV}$). The charge homogeneity of the samples is thus determined by the temperature at which the screening charges freeze.

Discussion

A possible explanation for the observed low disorder and high charge carrier mobility of SiC/G at large molecular coverage is a high degree of spatial correlation between adsorbed F4TCNQ and impurities present on bare graphene. Together with the low charge carrier density fluctuations, increasing impurity (e.g. F4TCNQ) density can lead to suppression of charge scattering in graphene if there is sufficient inter-impurity correlation present in the system^{29,30} (Supplementary Fig. 8). The actual organization and conformation of charged molecules on graphene is the result of delicate balance between molecule-graphene interactions as well as the intermolecular many-body dispersion forces³¹ in the presence of polymer. While the exact arrangement of molecules on graphene is difficult to probe through the thick polymer layers with surface science techniques, the graphene layer itself utilized as detector allows gaining an insight of such molecular reorganization at the polymer-graphene interface.

In summary, we presented a method of guiding the assembly of molecular dopants onto the surface of graphene by using an organic polymer matrix. With the doping stability observed in our samples, the tuneability of molecular coverage, and given the vast catalog of polymers and organic/organo-metallic molecules, we expect this method to open up a scalable route toward expanding the properties and functionality of graphene and other 2D materials well beyond doping control. Moreover, the presented analysis of chemical and electron transport properties of doped graphene sheds light on the complex processes that molecular dopants undergo when embedded in polymers. This is relevant to the understanding of performance, materials, and interfaces in organic electronic devices, especially when combined with 2D materials. This method can be explored in the future to create and study electron transport properties of novel 2D systems of ordered molecular arrays templated by 2D crystals^{32–35}.

Methods

Sample fabrication. Monolayer SiC/G was grown on the Si-face of SiC using thermal decomposition of $7 \text{ mm} \times 7 \text{ mm}$ 4H(0001)-SiC substrates. The samples were grown in argon atmosphere of 800 mbar, and kept at a temperature of around 1700°C for 5 min³⁶. Optical microscopy³⁷ revealed a typical surface coverage of >95% monolayer graphene.

Epitaxial graphene Hall bars were fabricated using electron beam lithography described in detail elsewhere³⁸. The electrical contacts were fabricated using physical vapor deposition of Ti and Au, 5 and 80 nm thick, respectively. After fabrication samples were cleaned using isopropyl alcohol, acetone, and dried using nitrogen gas. For pristine SiC/G (shown in Fig. 1b) a hBN flake was exfoliated and transferred to pristine SiC/G using a polydimethylsiloxane stamp. To clean the interface the sample was annealed in argon 800 mbar at 755°C , after which standard lithography was performed.

The dopant blend consisted of a mixture of F4TCNQ (Sigma-Aldrich) and PMMA (Microlithography Chemicals Corp., molecular weight 950 000). A unit of 25 mg of dry F4TCNQ powder was mixed with 3 ml anisole solvent. A volume of 0.5 ml of this solution was then mixed with 1 ml PMMA A6 (6% PMMA by weight in anisole). The PMMA spacer layer and encapsulation layers used either PMMA A4 (5% by weight in anisole) or PMMA-based copolymer (MMA (8.5) MAA) EL6 (6% by weight in ethyl lactate solvent). All polymer layers were deposited on graphene using spin-coating at 6000 rpm for 1 min. After each spin-coating step a

5 min baking step on a hotplate set at 160 °C follows. The dopant blend is an exception, since the baking time dictates the final doping level.

The electrostatic top gate was fabricated using a shadow mask, and physical vapor deposition of Au in order to avoid disruption of the chemically doped sample. In order to preserve the integrity of the doping strength of graphene, additional layers of dopant blend and PMMA encapsulation layers were deposited before fabrication of the gate. The samples with the full stack of five polymer layers are the most resilient to drift in carrier concentrations in ambient conditions.

Electrical measurements. Standard electrical characterization was performed in a liquid ^4He gas flow cryostat, which allowed for temperatures down to 2 K and magnetic fields up to 14 T. All reported values of charge carrier mobility and charge carrier concentration were extracted from four-probe Hall and quantum Hall measurements. The standard measurement setup used current biased samples at maximum of 100 nA DC (Keithley 6221 DC and AC current source, Agilent 34420 A nanovolt meter), in this range samples showed linear IV characteristics down to cryogenic temperatures. The electrostatic top gate was DC biased with voltages ranging from -100 mV to +200 V, where leakage current was <0.05 nA.

Secondary ion mass spectrometry. ToF-SIMS analysis was performed using a ToF-SIMS 5 instrument (ION-TOF GmbH, Münster, Germany). The instrument is equipped with a 25 keV Bi_3^{+} cluster ion gun as the primary ion source and a 10 keV C_{60}^{++} ion source for sputtering and etching. The samples were analyzed using a pulsed primary ion beam (Bi_3^{++} , 0.34 pA at 50 keV) with a focus of approximately 2 μm at a field of view of 150 $\mu\text{m} \times 150 \mu\text{m}$. The mass resolution using this setup was at least $M/\Delta M = 5000$ full width at half maximum at m/z 500. All spectra were acquired and processed with the Surface Lab software (version 6.4, ION-TOF GmbH). Depth profile analysis was performed using a C_{60}^{++} beam at 20 keV with a current of 0.2 nA in a non-interlaced mode with 1 s of analysis, 1 s of sputtering, and a pause of 1 s for each sputter cycle at 350 $\mu\text{m} \times 350 \mu\text{m}$. The maximum ion dose density of Bi_3^{++} was kept between 4×10^{12} and $7 \times 10^{12} \text{ cm}^{-2}$ over the whole depth profiling experiment, while the ion dose for C_{60}^{++} ranged from 2×10^{14} to 4×10^{14} ions per cm^2 . Low-energy electrons were used for charge compensation during analysis.

Grazing-incidence wide-angle X-ray scattering. Data were obtained at the D1-beam line at the Cornell High Energy Synchrotron Source at Cornell University. The measurements used a positron beam with synchrotron radiation of a wavelength of 1.162 Å. Pilatus 200K detector with pixel size of 172 $\mu\text{m} \times 172 \mu\text{m}$ and sample to detector distance of 177.2 mm. Measurements were done in ambient conditions at room temperature. The exposure time for each individual measurement was 20 s.

Data availability

The authors declare that the main data supporting the findings of this study are available within the article and its Supplementary Information files. Extra data are available from the corresponding author upon request.

Received: 8 August 2018 Accepted: 31 August 2018

Published online: 27 September 2018

References

- Ponomarenko, L. A. et al. Tunable metal–insulator transition in double-layer graphene heterostructures. *Nat. Phys.* **7**, 958–961 (2011).
- Hunt, B., Taniguchi, T., Moon, P., Koshino, M. & Ashoori, R. C. Massive Dirac Fermions and hofstadter butterfly in a van der Waals heterostructure. *Science* **340**, 1427–1431 (2013).
- Evers, F. & Mirlin, A. D. Anderson transitions. *Rev. Mod. Phys.* **80**, 1355–1417 (2008).
- Müller, M., Fritz, L. & Sachdev, S. Quantum-critical relativistic magnetotransport in graphene. *Phys. Rev. B* **78**, 115406 (2008).
- Katsnelson, M. I. Zitterbewegung, chirality, and minimal conductivity in graphene. *Eur. Phys. J. B* **51**, 157–160 (2006).
- Tzalenchuk, A. et al. Towards a quantum resistance standard based on epitaxial graphene. *Nat. Nanotechnol.* **5**, 186–189 (2010).
- Janssen, T. et al. Operation of graphene quantum Hall resistance standard in a cryogen-free table-top system. *2D Mater.* **2**, 35015 (2015).
- Wu, Y. et al. State-of-the-art graphene high-frequency electronics. *Nano Lett.* **12**, 3062–3067 (2012).
- Lin, Y. M. et al. 100-GHz transistors from wafer-scale epitaxial graphene. *Science* **327**, 662 (2010).
- Kopylov, S., Tzalenchuk, A., Kubatkin, S. & Fal'ko, V. I. Charge transfer between epitaxial graphene and silicon carbide. *Appl. Phys. Lett.* **97**, 11–14 (2010).
- Xue, J. et al. Scanning tunnelling microscopy and spectroscopy of ultra-flat graphene on hexagonal boron nitride. *Nat. Mater.* **10**, 282–285 (2011).
- Mayorov, A. S. et al. How close can one approach the dirac point in graphene experimentally? *Nano Lett.* **12**, 4629–4634 (2012).
- Li, Q., Hwang, E. H. & Das Sarma, S. Disorder-induced temperature-dependent transport in graphene: puddles, impurities, activation, and diffusion. *Phys. Rev. B Condens. Matter Mater. Phys.* **84**, 115442 (2011).
- Li, J. et al. Measurement of small molecular dopant F4TCNQ and C60F36 diffusion in organic bilayer architectures. *ACS Appl. Mater. Interfaces* **7**, 28420–28428 (2015).
- Jacobs, I. E. & Moul, A. J. Controlling molecular doping in organic semiconductors. *Adv. Mater.* **29**, 1703063 (2017).
- Pingel, P. & Neher, D. Comprehensive picture of p-type doping of P3HT with the molecular acceptor F₄TCNQ. *Phys. Rev. B* **87**, 115209 (2013).
- Li, J. et al. Quantitative measurements of the temperature-dependent microscopic and macroscopic dynamics of a molecular dopant in a conjugated polymer. *Macromolecules* **50**, 5476–5489 (2017).
- Lara-Avila, S. et al. Disordered Fermi liquid in epitaxial graphene from quantum transport measurements. *Phys. Rev. Lett.* **107**, 166602 (2011).
- Cho, S. & Fuhrer, M. S. Charge transport and inhomogeneity near the minimum conductivity point in graphene. *Phys. Rev. B Condens. Matter Mater. Phys.* **77**, 081402 (2008).
- Tiwari, R. P. & Stroud, D. Model for the magnetoresistance and Hall coefficient of inhomogeneous graphene. *Phys. Rev. B Condens. Matter Mater. Phys.* **79**, 165408 (2009).
- Ping, J. et al. Disorder-induced magnetoresistance in a two-dimensional electron system. *Phys. Rev. Lett.* **113**, 047206 (2014).
- Knap, M., Sau, J. D., Halperin, B. I. & Demler, E. Transport in two-dimensional disordered semimetals. *Phys. Rev. Lett.* **113**, 186801 (2014).
- Yang, M. et al. Puddle-induced resistance oscillations in the breakdown of the graphene quantum Hall effect. *Phys. Rev. Lett.* **117**, 1–5 (2016).
- Poumirol, J. M. et al. Electron–hole coexistence in disordered graphene probed by high-field magneto-transport. *New J. Phys.* **12**, 083006 (2010).
- Zhang, Y., Brar, V. W., Girit, C., Zettl, A. & Crommie, M. F. Origin of spatial charge inhomogeneity in graphene. *Nat. Phys.* **5**, 722–726 (2009).
- Banszerus, L. et al. Ultrahigh-mobility graphene devices from chemical vapor deposition on reusable copper. *Sci. Adv.* **1**, e1500222–e1500222 (2015).
- Chen, W., Chen, S., Dong, C. Q., Xing, Y. G. & Wee, A. T. S. Surface transfer p-type doping of epitaxial graphene. *J. Am. Chem. Soc.* **129**, 10418–10422 (2007).
- Coletti, C. et al. Charge neutrality and band-gap tuning of epitaxial graphene on SiC by molecular doping. *Phys. Rev. B Condens. Matter Mater. Phys.* **81**, 235401 (2010).
- Li, Q., Hwang, E. H., Rossi, E. & Das Sarma, S. Theory of 2D transport in graphene for correlated disorder. *Phys. Rev. Lett.* **107**, 156601 (2011).
- Yan, J. & Fuhrer, M. S. Correlated charged impurity scattering in graphene. *Phys. Rev. Lett.* **107**, 206601 (2011).
- Yang, S., Jiang, Y., Li, S. & Liu, W. Many-body dispersion effects on the binding of TCNQ and F₄-TCNQ with graphene. *Carbon N. Y.* **111**, 513–518 (2017).
- Mao, J. et al. Tunability of supramolecular kagomé lattices of magnetic phthalocyanines using graphene-based moiré patterns as templates. *J. Am. Chem. Soc.* **131**, 14136–14137 (2009).
- Cho, J. et al. Structural and electronic decoupling of C 60 from epitaxial graphene on sic. *Nano Lett.* **12**, 3018–3024 (2012).
- Wang, Q. H. & Hersam, M. C. Room-temperature molecular-resolution characterization of self-assembled organic monolayers on epitaxial graphene. *Nat. Chem.* **1**, 206–211 (2009).
- Tsai, H.-Z. et al. Molecular self-assembly in a poorly screened environment: F 4 TCNQ on graphene/BN. *ACS Nano* **9**, 12168–12173 (2015).
- Virojanadara, C. et al. Homogeneous large-area graphene layer growth on 6H-SiC(0001). *Phys. Rev. B* **78**, 245403 (2008).
- Yager, T. et al. Express optical analysis of epitaxial graphene on SiC: impact of morphology on quantum transport. *Nano Lett.* **13**, 4217–4223 (2013).
- Yager, T. et al. Low contact resistance in epitaxial graphene devices for quantum metrology. *AIP Adv.* **5**, 87134 (2015).

Acknowledgements

We thank Dmitry Golubev, Alexander Tzalenchuk, and Tord Claeson for useful discussion and critical reading of the manuscript. This work was jointly supported by the Swedish Foundation for Strategic Research (SSF) (No. IS14-0053, GMT14-0077, and RMA15-0024), Knut and Alice Wallenberg Foundation, Chalmers Area of Advance NANO, the Swedish Research Council (VR) 2015-03758 and 2016-048287, the Swedish-Korean Basic Research Cooperative Program of the NRF (No. NRF-2017R1A2A1A8070721), and European Union's Horizon 2020 research and innovation program (grant agreement No. 766714/HiTMe). We thank Cornell

High Energy Synchrotron Source (CHESS) for providing time for GIWAXS measurements. CHESS is supported by the NSF & NIH/NIGMS via NSF award DMR-1332208.

Author contributions

H.H. and S.L.-A. fabricated samples, performed transport measurements, and analyzed data. K.H.K., A.D., D.M., F.L., Y.W.P. and T.B. performed transport experiments. P.M. performed and analyzed SIMS measurements. K.M.-P., L.Y. and C.M. analyzed GIWAXS measurements. H.H. and S.L.A. wrote the manuscript, with contributions from all of the authors. S.K. and S.L.A. conceived and designed the experiment.

Additional information

Supplementary Information accompanies this paper at <https://doi.org/10.1038/s41467-018-06352-5>.

Competing interests: The authors declare no competing interests.

Reprints and permission information is available online at <http://npg.nature.com/reprintsandpermissions/>

Publisher's note: Springer Nature remains neutral with regard to jurisdictional claims in published maps and institutional affiliations.



Open Access This article is licensed under a Creative Commons Attribution 4.0 International License, which permits use, sharing, adaptation, distribution and reproduction in any medium or format, as long as you give appropriate credit to the original author(s) and the source, provide a link to the Creative Commons license, and indicate if changes were made. The images or other third party material in this article are included in the article's Creative Commons license, unless indicated otherwise in a credit line to the material. If material is not included in the article's Creative Commons license and your intended use is not permitted by statutory regulation or exceeds the permitted use, you will need to obtain permission directly from the copyright holder. To view a copy of this license, visit <http://creativecommons.org/licenses/by/4.0/>.

© The Author(s) 2018

Paper D

Polymer-encapsulated molecular doped epigraphene for quantum resistance metrology



PAPER • OPEN ACCESS

Polymer-encapsulated molecular doped epigraphene for quantum resistance metrology

To cite this article: Hans He *et al* 2019 *Metrologia* **56** 045004

View the [article online](#) for updates and enhancements.

Polymer-encapsulated molecular doped epigraphene for quantum resistance metrology

Hans He¹, Samuel Lara-Avila^{1,2}, Kyung Ho Kim¹, Nick Fletcher²,
Sergiy Rozhko², Tobias Bergsten³, Gunnar Eklund³, Karin Cedergren³,
Rositsa Yakimova⁴, Yung Woo Park^{5,6}, Alexander Tzalenchuk^{2,7}
and Sergey Kubatkin¹

¹ Department of Microtechnology and Nanoscience, Chalmers University of Technology,
S-41296 Göteborg, Sweden

² National Physical Laboratory, Hampton Road, Teddington TW11 0LW, United Kingdom

³ RISE Research Institutes of Sweden, Box 857, S-50115 Borås, Sweden

⁴ Department of Physics, Chemistry and Biology (IFM), Linköping University,
S-58183 Linköping, Sweden

⁵ Institute of Applied Physics, Seoul National University, Seoul 08826, Republic of Korea

⁶ Department of Physics and Astronomy, University of Pennsylvania, Philadelphia, PA 19104,
United States of America

⁷ Royal Holloway, University of London, Egham TW20 0EX, United Kingdom

E-mail: hanshe@chalmers.se

Received 25 March 2019, revised 29 May 2019

Accepted for publication 10 June 2019

Published 28 June 2019



Abstract

One of the aspirations of quantum metrology is to deliver primary standards directly to end-users thereby significantly shortening the traceability chains and enabling more accurate products. Epitaxial graphene grown on silicon carbide (epigraphene) is known to be a viable candidate for a primary realisation of a quantum Hall resistance standard, surpassing conventional semiconductor two-dimensional electron gases, such as those based on GaAs, in terms of performance at higher temperatures and lower magnetic fields. The bottleneck in the realisation of a turn-key quantum resistance standard requiring minimum user intervention has so far been the need to fine-tune the carrier density in this material to fit the constraints imposed by a simple cryo-magnetic system. Previously demonstrated methods, such as via photo-chemistry or corona discharge, require application prior to every cool-down as well as specialist knowledge and equipment. To this end we perform metrological evaluation of epigraphene with carrier density tuned by a recently reported permanent molecular doping technique. Measurements at two National Metrology Institutes confirm accurate resistance quantisation below $5 \text{ n}\Omega \text{ }\Omega^{-1}$. Furthermore, samples show no significant drift in carrier concentration and performance on multiple thermal cycles over three years. This development paves the way for dissemination of primary resistance standards based on epigraphene.

Keywords: molecular doping, graphene, measurement standards, quantum Hall effect

(Some figures may appear in colour only in the online journal)



Original content from this work may be used under the terms of the [Creative Commons Attribution 3.0 licence](#). Any further distribution of this work must maintain attribution to the author(s) and the title of the work, journal citation and DOI.

1. Introduction

Epitaxial graphene on silicon carbide (epigraphene) can be grown as a high quality monocrystalline film on a wafer-scale, allowing for scalable production of electronic devices. The metrological viability of epigraphene as a quantum Hall resistance (QHR) standard was first shown experimentally in 2010 [1]. Epigraphene has since proven itself superior to the conventional two-dimensional electron gas (2DEG) systems based on GaAs/AlGaAs (henceforth simply GaAs) due to its unique electronic properties, which result in a robust quantum Hall effect (QHE) measurable at higher probing currents, higher temperatures and lower magnetic fields [2, 3]. The quantum Hall effect in epigraphene is so robust that the filling factor $\nu = 2$ plateau has been shown to extend over nearly 50 T [4]. Universality of the quantum Hall effect has been demonstrated to better than $0.1 \text{ n}\Omega \text{ }\Omega^{-1}$ via comparison of resistance quantisation in epigraphene and GaAs [3, 5]. Finally, an epigraphene QHR standard was successfully operated at 4 K and 5 T in a small cryogen-free table-top system [2]. However, one major problem that remains is exerting control over the charge carrier density, which is necessary in order to achieve proper quantization and optimal operation for a chosen range of temperatures and magnetic fields. Under the above conditions, the empirically found [2] optimal carrier density yielding the maximum breakdown current is $(1.4 \pm 0.2) \times 10^{11} \text{ cm}^{-2}$, whereas metrologically useful currents $\gtrsim 10 \mu\text{A}$ can be achieved in 10 s μm wide devices in the approximate range of densities $0.5\text{--}2.5 \times 10^{11} \text{ cm}^{-2}$. Due to the presence of an insulating interface layer (buffer layer) between the SiC substrate and graphene, epigraphene shows both high n-doping on the order of 10^{13} electrons per cm^2 and Fermi level pinning. These two factors in combination make tuning the carrier density to the useful range a challenge [6]. Previously tested methods such as photochemical gating [7, 8] and corona discharge [9] are suitable but lack the reliability and stability required for real-world applications. An interesting method of tuning the carrier density in epigraphene specifically for resistance metrology was demonstrated at NIST [10]. The method involves deposition of chromium tri-carbonyl on top of graphene followed by exposure to atmospheric air which relatively quickly reduces the carrier density to some usefully low level. However, according to [10] the carrier density continues to drift down by as much as 75% in one year and by then precision measurements suggest that the devices deviate from accurate quantisation by more than $10 \text{ n}\Omega \text{ }\Omega^{-1}$. Ideally we would like to adjust the carrier density to the desired level once and for all during the epigraphene fabrication, as indeed is the situation for conventional GaAs devices.

A possible solution, involving polymer-assisted assembly of molecular dopants on the surface of epigraphene, has recently been proposed by the Chalmers group [11]. In this paper we demonstrate that this approach affords stable and controllable tuning of the charge carrier density in epigraphene while maintaining all of its major advantages for the realisation of a quantum resistance standard. We have explored long-term stability of molecularly doped epigraphene samples and

compared the resistance quantisation to conventional GaAs resistance standards using cryogenic current-comparators (CCC) in two National Metrology Institutes (NMIs). We have also demonstrated stability upon repeated thermal cycles and operation of the standard in a dry table-top cryo-magnetic system.

2. Polymer-assisted molecular doping of epigraphene

2.1. Sample preparation

We have followed the procedure for sample fabrication and polymer-assisted assembly of molecular dopants as described in [11]. Here we summarise it briefly.

Epitaxial graphene was grown on the silicon face of an insulating 4H-SiC substrate using thermal decomposition of SiC at 2000 °C and in an 850 mbar argon atmosphere [12, 13]. The size of the SiC chips are $7 \times 7 \text{ mm}^2$. Prior to microfabrication the highest quality of monolayer graphene chips, i.e. lowest amount of bilayer inclusions, are selected using transmission mode optical microscopy techniques [14]. The device fabrication was performed using standard electron beam lithography techniques to define electrical contacts and Hall bar devices. Excess graphene was removed using oxygen plasma etching and the resulting epigraphene Hall bars have typical dimensions of $30 \times 150 \mu\text{m}^2$ and are electrically contacted using 80 nm Au with 5 nm of Ti as an adhesion layer (see figure 1(a)).

The intrinsic n-doping of pristine epigraphene is on the order of 10^{13} electrons cm^{-2} . After microfabrication and exposure to ambient the carrier density tends to decrease, moving slightly towards neutrality [15]. However, the carrier density is usually too high to reliably observe fully developed quantum Hall effect below applied magnetic fields of 10 T, even at 2 K (see figure 2(b)). To achieve the desired carrier density, we apply polymer-assisted assembly of molecular dopants [11], which proceeds as follows: a 100 nm thick layer of the PMMA-F4TCNQ dopant blend is spin-coated onto a PMMA-protected sample, with a PMMA encapsulation layer on top. This sequence is then repeated to provide additional encapsulation and reduce drift of the carrier density (see figure 1(b)). The deposition of each polymer layer is followed by thermal annealing at 160 °C, above the PMMA glass transition temperature. The resulting carrier density can be fine-tuned through the total annealing time. For a concentration of 7% of F4TCNQ in PMMA by weight, and using the standardized annealing time, we have consistently observed a decrease in electron density by three orders of magnitude together with a tenfold increase of carrier mobility reaching $30000\text{--}50000 \text{ cm}^2 \text{ V}^{-1} \text{ s}^{-1}$. Several chemically doped epigraphene samples were prepared and measured in this study. Samples used to explore homogeneity of the doping were prepared with a deliberately low carrier density $\sim 10^{10} \text{ cm}^{-2}$ and these measurements are described in section 2.2. For the investigation of metrological viability samples were controllably tuned to $\sim 1.5 \times 10^{11} \text{ cm}^{-2}$ in order to maximize the critical current in the desired operating regime for table-top systems

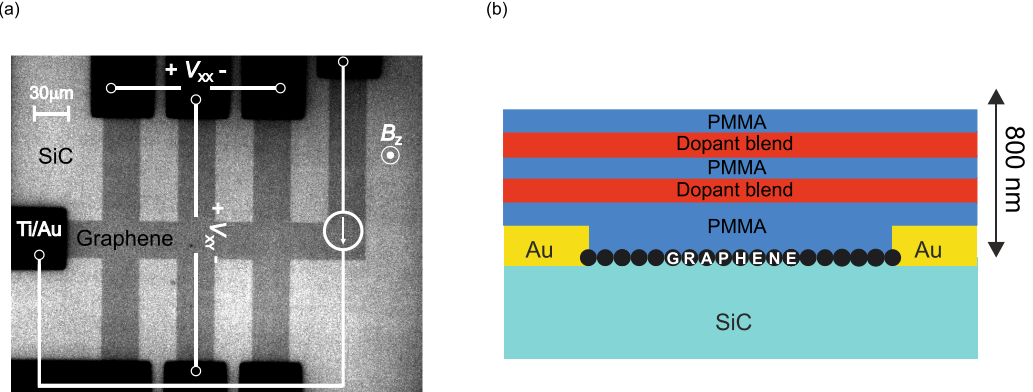


Figure 1. (a) Optical micrograph of a typical epigraphene Hall bar device taken in transmission mode. The overlay shows a schematic representation of the standard measurement setup for quantum Hall measurements with bias current direction, the direction of the perpendicular magnetic field, and connections for longitudinal voltage V_{xx} and Hall voltage V_{xy} . (b) Schematic representation of the chemical doping scheme consisting of an acceptor molecule encapsulated in organic polymers.

[2]. Figure 2(c) shows the long-time drift of the carrier density in two samples: one initially tuned to $5.4 \times 10^{10} \text{ cm}^{-2}$ and the other tuned to $1.63 \times 10^{11} \text{ cm}^{-2}$. The electron density increased at an average relative rate 0.02% and 0.05% per day for the two samples respectively. The estimated lifetime of the two samples, that is the time they are expected to yield the breakdown current $\gtrsim 10 \mu\text{A}$, is over 20 and 4 years respectively. Since the two samples differed not only in the initial carrier density but were also kept in different environments, dry nitrogen and vacuum, at room temperature between measurements, it is premature to speculate regarding the somewhat different, albeit by any measure very low, drift rate. The stability can potentially be improved even further by hermetic sealing or by storing the sample at low temperatures.

2.2. Large scale homogeneity

Understanding doping uniformity is important if the described fabrication method is to be used for reliable manufacturing of epigraphene QHR samples on a wafer scale. Figure 3 shows a comparison between molecular doping of microscopic and macroscopic Hall bars. Both devices have similar carrier densities, which in this case is low p-doping on the order $p \approx 10^{10} \text{ cm}^{-2}$, but drastically different surface areas (similarly n-doped samples show qualitatively similar behaviour). At such low carrier concentrations, where Fermi energy level is close to the Dirac point in graphene, the influence of the charge inhomogeneities on the measured resistance is more noticeable. The longitudinal and Hall resistance measurements were performed at 2 K using bias current 100 nA. For standard microscopic Hall bars with typical size $30 \times 150 \mu\text{m}^2$ we observe fully developed quantum Hall effect below 1 T, with a carrier density $p = 5.7 \times 10^9 \text{ cm}^{-2}$ and mobility $\mu = 52000 \text{ cm}^2 \text{ V}^{-1} \text{ s}^{-1}$. For the macroscopic Hall bar of $5 \times 5 \text{ mm}^2$ we also observe fully developed quantum Hall effect below 1 T, with carrier density $p = 9.1 \times 10^9 \text{ cm}^{-2}$

and mobility $\mu = 39000 \text{ cm}^2 \text{ V}^{-1} \text{ s}^{-1}$. Note that we attribute the asymmetries in the low-field data to defects in graphene itself, such as bilayer inclusions and SiC steps, which can be avoided for smaller geometries [14] but not for macroscopic devices [16].

3. Metrological viability

For precision measurements we produced the following two samples: one sample G-RISE was measured at the Research Institutes of Sweden (RISE) in a liquid helium cryostat with an 11 T superconducting magnet and base temperature of 1.9 K, another sample G-NPL was tested at the National Physical Laboratory (NPL) in a small table-top mechanical refrigerator with the base temperature of 4 K and magnetic field 5 T [2]. The samples were manufactured at the same time but measured at different times over the span of almost two years. This time delay, and the different type of the cryogenic system could be considered as an additional test of reliability and stability of the molecularly gated graphene Hall devices. The electron concentration for G-RISE was initially tuned to around $1.3 \times 10^{11} \text{ cm}^{-2}$, and $1.6 \times 10^{11} \text{ cm}^{-2}$ for G-NPL. The device geometries are identical to that of figure 1(a).

To evaluate the metrological viability of the epigraphene devices we have generally followed the technical guidelines for reliable DC measurements of the quantised Hall resistance initially developed for metal-oxide semiconductor field-effect transistors (MOSFETs) and GaAs devices [17]. Here we will consider the properties of the Hall devices which have the strongest effect on the precision of the Hall resistance measurements, such as the geometrical homogeneity of the 2D layer, the residual longitudinal resistance, the contact resistance, critical breakdown current, and finally analysis of the Quantum Hall resistance measurements using the CCC technique.

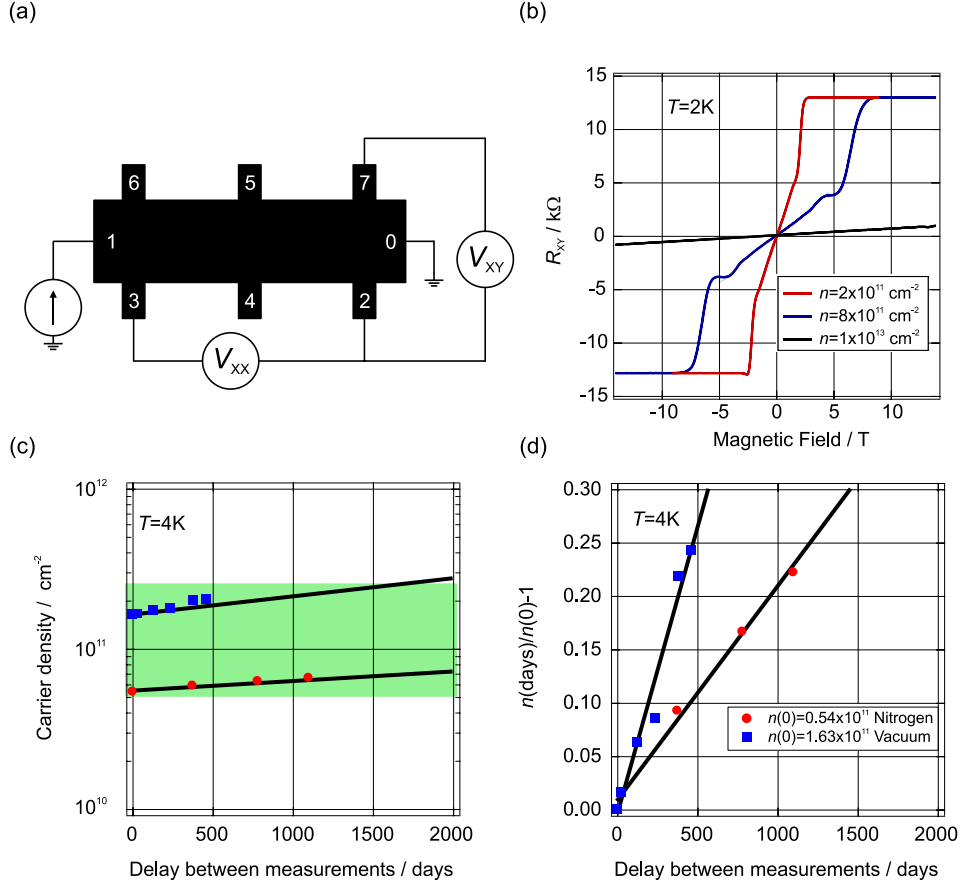


Figure 2. (a) Schematic sample layout and contact notations (b) measurements of Hall resistance R_{xy} performed at $T = 2\text{ K}$ with 100 nA bias, showing the different minimum magnetic field needed to reach the $\nu = 2$ plateau. The sample with the highest n-doping (black curve) corresponds to pristine epigraphene encapsulated by hexagonal boron nitride. The medium doped sample (blue curve), covered by polymer, shows the effect of partial compensation doping resulting mainly from polymer contaminants. The residual n-doping is typically above 10^{12} cm^{-2} . The sample with the lowest doping (red curve) was produced using chemical doping with an acceptor molecule. It has been controllably tuned to $n = 2 \times 10^{11} \text{ cm}^{-2}$. (c) Long term stability of carrier density measured in two samples described in the text. The green area indicates the limits of the carrier density set by the metrologically useful currents $\gtrsim 10 \mu\text{A}$. The solid black lines are linear fits to the drift in carrier density. (d) The same data as (c) but plotted on the relative scale to highlight the linear drift.

3.1. Contact resistances measurements

All contact resistances were measured in the three-terminal configuration, in the magnetic field adjusted to the quantum Hall plateau (5 T). For illustration, the contact resistance for the sample G-NPL against DC current is presented in figure 4. Contact number is indicated on the graph. Note that pad #5 is not shown due to wire bond failure. All measured contact resistances were in the range of 0.1 to 1 Ω up to bias currents about 100 μA independent of current polarity, well below the recommended 10 Ω [18]. The sharp increase in resistance above 100 μA is due to the breakdown of the quantum Hall state. The same check was performed for sample G-RISE.

3.2. Critical current measurements

The critical breakdown current is the maximum non-dissipative current that the sample can sustain in the quantum Hall state. The onset of dissipation is seen in the abrupt increase of longitudinal resistance. Figure 5(a) shows R_{23} and R_{67} measured on both sides of the sample G-NPL against DC source-drain current of both polarities at $B = 5\text{ T}$ and $T = 4\text{ K}$. The red points were measured on the ‘low’ potential side of the device and the black points—on the ‘high’ side. The apparent residual resistance $R_{23} \approx 1 \text{ m}\Omega$ in the QHE regime disappeared when contact 1 instead of contact 0 was grounded [18]. It follows that the breakdown happens at $I_{SD} \approx 60 \mu\text{A}$ with the accuracy of these measurements (at 10 nV level) for this

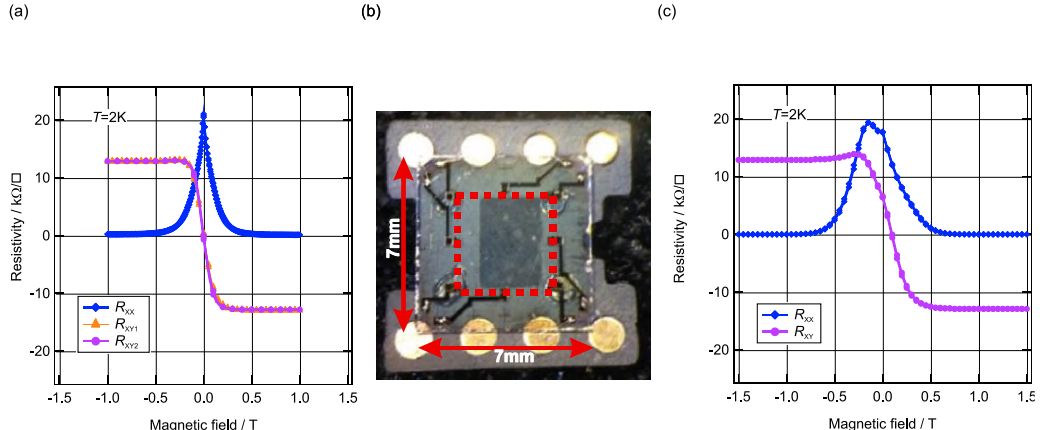


Figure 3. Chemical doping of epigraphene with low p-doping for both microscopic and macroscopic Hall bar geometries (a) quantum Hall measurements performed on $30 \mu\text{m}$ wide Hall bar, as seen in figure 1(a), displays fully quantized plateaus below 1 T . (b) Optical micrograph of a macroscopic Hall bar $5 \times 5 \text{ mm}^2$. The red dotted square outlines the epigraphene region. Even at this scale the device is seemingly uniformly covered by the chemical dopant, as verified by (c) which shows quantization below 1 T . Adapted from [11]. CC BY 4.0.

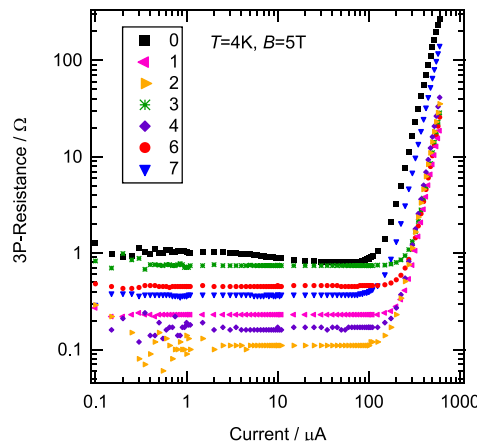


Figure 4. The contact resistance for sample G-NPL against DC current measured in three-probe configuration (3P). Numbers on the graph indicate the contact number, see figure 2(a).

particular sample. Figure 5(b) shows the critical currents for both measured samples, extracted as stated above, as a function of magnetic field. The difference in the critical currents is attributed to discrepancies between the two samples such carrier densities, charge homogeneity etc.

4. Precision measurements

The measurements described in the previous section (meeting the recommended guidelines for reliable QHR measurements) are in principle sufficient to demonstrate that the sample is fit for metrological use as a calibration reference. However, as the molecular gating represents a new fabrication technology,

it is valuable to demonstrate the equivalence with an independent QHR realization in a proven GaAs sample. One possible cause of error that is not easily detected by the standard tests is a resistive leakage error in parallel with the quantized resistance, which might arise due to the surface dopant layer in our epigraphene device. A ratio comparison of the $\nu = 2$ and $\nu = 4$ plateaux in a GaAs sample can reveal this error, but this is not possible in a graphene device. In order to eliminate this or other possible undetected errors in the epigraphene sample we carried out a precision comparison to the GaAs reference using a cryogenic current comparator (CCC) based bridge.

The CCC bridges used for this comparison have been evaluated for absolute accurate measurements of the ratio $100 \Omega : 12.906 \text{ k}\Omega$ to a relative uncertainty of at least $10 \text{ n}\Omega \Omega^{-1}$ [19]. The CCC device with its superconducting windings and shielding plus SQUID magnetic null detector provides the accurate dc current ratio required to achieve this. In this test, however, we are using the same instrument twice in almost identical conditions to make a substitution comparison between two QHR devices. Most of the uncertainty contributions and possible errors in the resistance measurement (for example ratio errors, imperfect detector linearity) cancel in this configuration, and the uncertainty budget for the comparison result is dramatically simplified. Ideally the type A (statistical) uncertainty of the measurements will be the limiting remaining component. The CCC bridge circuit is immune to most leakage paths (particularly leakage to screen) due to the use of an ‘active Wagner’ technique [19], but leakage directly across the QHR device is impossible to separate from the resistance being measured.

Similar measurements were carried out at both NPL and RISE and below we describe them in detail. Each NMI deliberately followed their own measurement protocol to maintain independent comparison.

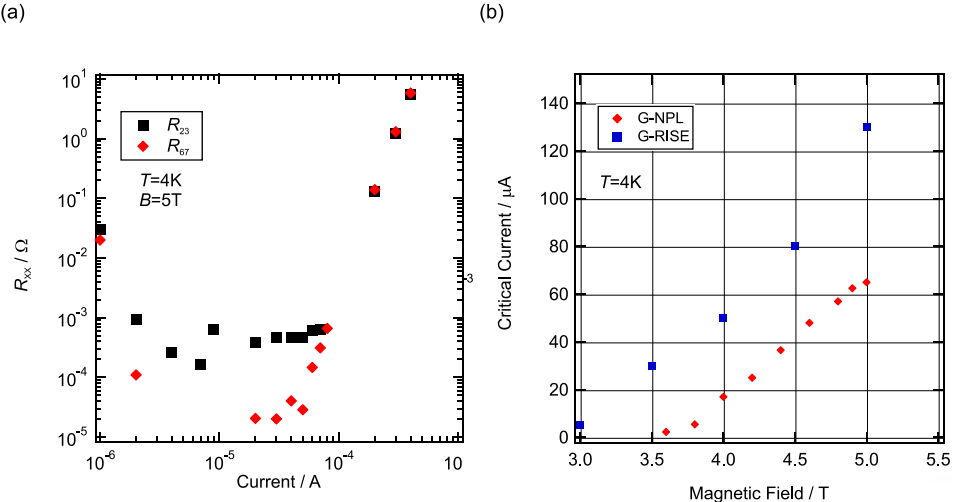


Figure 5. (a) Longitudinal resistance R_{XX} measured from the both sides of the sample using connections R_{23} and R_{67} for G-NPL plotted against DC source-drain current. (b) Critical current measured for sample G-NPL and G-RISE as a function of magnetic field.

4.1. CCC measurements on G-NPL

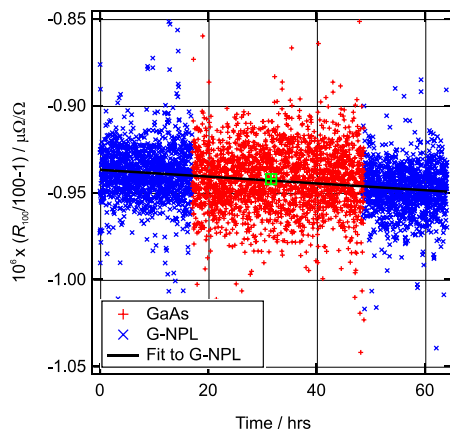
The comparison measurements at NPL use two separate cryo-magnetic systems for epigraphene and GaAs. This allowed us to perform resistor calibration against one QHE device quickly followed by calibration against the other, and the first one again. The temperature and short term stability of the $100\ \Omega$ standard is then easily included in the type A evaluation via the ‘A-B-A’ measurement pattern and linear fit. As the QHR devices are in separate cryogenic systems, one effect that is independent and does not cancel is any leakage in the cryogenic wiring that appears in parallel with the QHR sample. The leakage in the GaAs system probe has previously been evaluated to contribute $10\ \text{p}\Omega\ \Omega^{-1}$ relative uncertainty on a QHR measurement (i.e. to be $\geq 10^{15}\ \Omega$) [5]. The wiring in the table-top graphene system has been tested to $\geq 10^{14}\ \Omega$ ($0.1\ \text{n}\Omega\ \Omega^{-1}$ relative uncertainty contribution).

The GaAs device used in the measurements at NPL was originally supplied by the Physikalisch-Technische Bundesanstalt (PTB), and has been in use for routine resistance traceability at NPL for over 20 years (and was one of the GaAs devices used in a previous comparison [5]). It has a carrier concentration of $4.6 \times 10^{11}\ \text{cm}^{-2}$ and mobility $400\,000\,\text{cm}^2\ \text{V}^{-1}\ \text{s}^{-1}$, and was operated on the $\nu = 2$ plateau at a temperature of $<0.3\text{ K}$ and a magnetic field of 9.4 T in a conventional liquid helium cryostat. The comparison between this and the epigraphene device was performed via an intermediate $100\ \Omega$ conventional resistance standard, measured using the CCC bridge described in [19] with a 16:2065 turns ratio on the CCC. The current in the QHR device was $23\ \mu\text{A}$, giving nominally $3\ \text{mA}$ or $1\ \text{mW}$ power dissipation in the $100\ \Omega$ standard, which matches the regular calibration conditions. The epigraphene device was operated at 4.9 T and 4 K in the ‘desktop’ liquid free system described above.

Measurements were performed on several different $100\ \Omega$ standards, some of which were found to have short term instabilities that limited the overall uncertainty of the comparison. We give the results here of one comparison over 3 d (approximately 70 h of measurements) where the resistor showed a small linear drift. The resistor used was a Tinsley type wire wound Evanohm standard enclosed in a custom built thermostated enclosure with temperature stability of a few mK over the measurement period. The measurement sequence was graphene-GaAs-graphene in order to be able to cancel the effect of linear change of the $100\ \Omega$ standard. Figure 6(a) shows the results, plotted as the measured relative deviation of the unknown resistor from its nominal $100\ \Omega$ value, in $\mu\Omega\ \Omega^{-1}$. The CCC measurements consist of repeated forward and reverse current energization, with the bridge null detector reading analysed in forward-reverse-forward groups to eliminate offsets and drifts in the electronics. Each individual point on figure 6(a) is the result of this fitting for approximately 54 s of data, which is the shortest section that can be analysed in this way to give a calculated resistance value. To calculate the mean difference between the graphene and GaAs measurements we take a linear fit to the graphene data (two groups of blue points) and compare the value of this fit at the mean time of the GaAs data to the mean value of the GaAs data.

As the type A uncertainty contribution is effectively the total uncertainty for the comparison results, we need to take care that the usual expression for the standard uncertainty of the mean is a reliable estimate. Figure 6(b) presents the Allan deviation of the residuals to the linear fit for the three groups of data in figure 6(a). The Allan deviation in each case reduces as the square root of the measurement time (as expected for white noise with no time correlation) to below $1\ \text{n}\Omega\ \Omega^{-1}$ (relative). This confirms the current reversal in the CCC measurements is successfully eliminating offset drifts and instabilities,

(a)



(b)

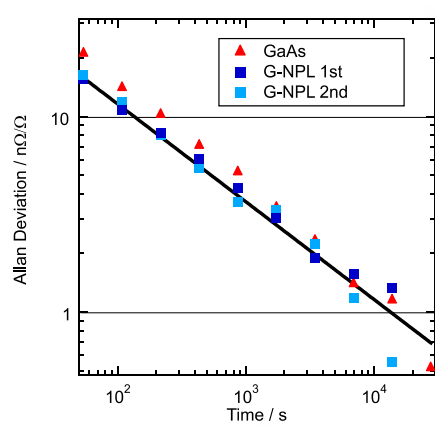


Figure 6. (a) Relative deviation of the $100\ \Omega$ standard resistor from its nominal $100\ \Omega$ value demonstrating linear drift. The linear fit to G-NPL data is shown by the solid black curve. The green square marks the mean value of GaAs at mean measurement time (b) Allan deviation of the residuals to the linear fit to data in (a). G-NPL 1st and 2nd denote the measurement using G-NPL before and after GaAs. The solid black line shows that the Allan deviation decreases with time τ as $\sim 1/\sqrt{\tau}$.

and that the linear drift model for the resistor is adequate. Although the reduction in uncertainty with increasing averaging time is as we would wish, the absolute level is larger than optimal. The ideal case measurement for our CCC bridge in this configuration should approach the Johnson noise limit for the resistors; for a cold QHR resistor and a room temperature $100\ \Omega$ this theoretical limit is around $2\text{ nV}(\sqrt{\text{Hz}})^{-1}$ voltage noise, which translates to a relative uncertainty of $1\text{ n}\Omega\ \Omega^{-1}$ for a 100s measurement at 1 mW measurement power. We observe a noise level approximately ten times worse than this, which is at least partly due to excess electromagnetic interference present in our laboratory. Despite this limitation, the extended measurement time with the automated bridge running continuously over 3 d does allow us to reach $<1\text{ n}\Omega\ \Omega^{-1}$ final uncertainty, which is adequate to demonstrate the QHR device accuracy for all requirements in resistance traceability.

The final expanded uncertainty contains the root-sum-square of type A standard error of the mean for GaAs (σ/\sqrt{N} here σ is standard deviation and N is number of samples), along with the uncertainty from the linear fit to G-NPL data. In summary, the difference in deviation from nominal of the $100\ \Omega$ resistor, Δ , as measured against the different QHR references is

$$\Delta_{\text{Gr-GaAs}} = 1.02 \pm 1.42\text{ n}\Omega\ \Omega^{-1}(k=2).$$

Epigraphene is shown to be in good agreement with standard GaAs.

4.2. CCC measurements on sample G-RISE

RISE performed calibrations of a $100\ \Omega$ standard resistor against QHE devices, epigraphene and GaAs, sequentially in the same cryo-magnetic system. As mentioned, the advantage

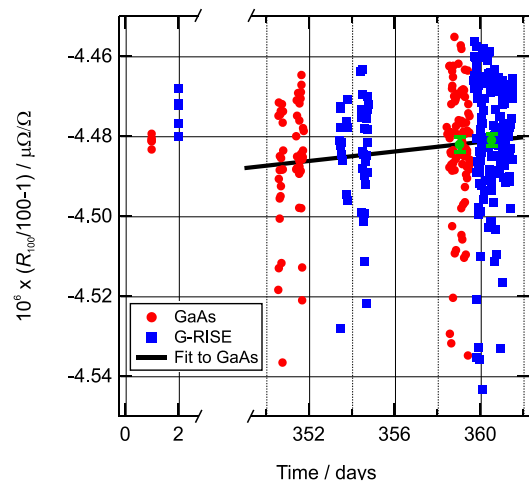


Figure 7. Comparison between sample G-RISE and a GaAs QHR device via a standard resistor with the nominal value of $100\ \Omega$ over the span of one year. The y-axis denotes the relative deviation from the nominal value of the $100\ \Omega$ resistor measured with the epigraphene and GaAs devices. The x-axis denotes the time in days from initial characterization. Each point is a 12 min long CCC measurement. The solid black line is a linear fit to the GaAs data taken from Day 350 onwards. The green dots show the mean value at mean time for the last two GaAs and G-RISE measurement blocks. The bars represent the standard error of the means.

of this approach is that any leakage in the wiring of this measurement system will be cancelled out in the substitution measurement. The disadvantage is that swapping QHE devices over and repeating the measurements takes considerable time over which the comparison resistor may drift. The $100\ \Omega$ standard

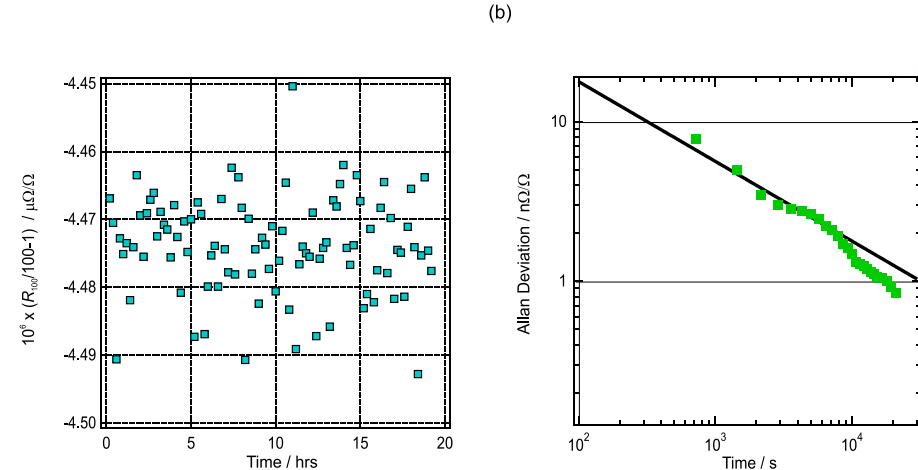


Figure 8. Extended CCC measurement of G-RISE compared to 100Ω standard at 4.2 K , 8 T , and $23\text{ }\mu\text{A}$ bias. (a) Measured deviation from nominal value as a function of time, up to 20 h continuous measurements. Each data point corresponds to 12 min of measurement time. (b) Allan deviation calculated from the data in (a). The solid black line shows that the Allan deviation decreases with time $\sim 1/\sqrt{\tau}$.

resistor is a Tinsley AC/DC type 5685A which is stored in an oil bath kept at $25\text{ }^\circ\text{C}$, with a temperature stability of $\sim 1\text{ mK}$. Its short-term instability can be accounted for by introducing a significant type B uncertainty of $3\text{ n}\Omega\text{ }\Omega^{-1}$, or compensated for using ‘A-B-A’ type measurement as described above. The GaAs device used in these measurements at RISE also comes from PTB and has been in use for routine resistance traceability at RISE since 1999. The device has a carrier concentration of $5.2 \times 10^{11}\text{ cm}^{-2}$, mobility $430\,000\text{ cm}^2\text{ V}^{-1}\text{ s}^{-1}$. It was operated on the $\nu = 2$ plateau at a temperature of $1.6\text{--}1.9\text{ K}$ and a magnetic field range between $9.65\text{--}9.95\text{ T}$ in a conventional liquid helium cryostat. The comparison was performed using a CCC bridge with a 32:4130 turns ratio on the CCC.

Figure 7 shows the two measurement campaigns of comparisons between sample G-RISE and GaAs performed over the span of one year. Each point takes 12 min to measure, which is the standard time for the CCC to finish one full, current reversed, measurement with the present setup.

From the initial set of measurements, up to Day 2, we can calculate that the difference between the mean relative deviations resulting from the G-RISE- 100Ω and GaAs- 100Ω CCC measurements as $\Delta_{\text{Gr-GaAs}} = 7.2 \pm 7.4\text{ n}\Omega\text{ }\Omega^{-1}$ ($k = 2$), including the root-sum-square of the type A standard error of the two means and an estimated type B error from instability of the 100Ω standard. Figure 8(a) shows an extended measurement series where we continuously monitor the CCC measurement of G-RISE and 100Ω standard over 20 h , with each point representing 12 min of measurement time. Figure 8(b) shows the Allan deviation which demonstrates how the precision improves over measurement time. The black dotted line shows that the Allan deviation predominately decreases with time $\sim 1/\sqrt{\tau}$ which indicates that uncorrelated white noise is the main source [20]. After six hours of continuous measurements we can reach $<1\text{ n}\Omega\text{ }\Omega^{-1}$ final uncertainty, which

is a suitable level of device accuracy for all requirements in resistance traceability. This measurement shows agreement between G-RISE and GaAs within the expanded measurement error but can be improved by performing ‘A-B-A’ sequence to account for the short time linear drift component of the instability of the 100Ω standard.

From day 350 and onwards an ‘A-B-A-B’ measurement was carried out. Since there is only one cryostat available, samples have to be exchanged in sequence, which takes a considerable time. However, the drift of the 100Ω reference resistor appears to be linear inside these 10 d . Since the data blocks are more spread out in time compared to NPL the analysis is slightly different. A linear fit is performed on both blocks of GaAs data to estimate the drift in the resistor. We only look at the last two GaAs and G-RISE measurement blocks for two reasons. Firstly, they are closest in time and therefore, by comparing these two, the contribution of the uncertainty of the estimated linear drift is reduced. Secondly, they contain more than 71% of the measurement points which reduces the uncertainty of the mean value for these two points, compared to the others. We calculate the difference between the mean of GaAs points and mean of G-RISE points, with the linear drift of the 100Ω standard subtracted. The final expanded uncertainty then contains the root-sum-square of type A standard error of the mean for both GaAs and G-RISE, along with the uncertainty of the estimated slope of the GaAs data acquired from fitting. In summary, the difference in deviation from nominal of the 100Ω resistor, Δ , as measured against the different QHR references is

$$\Delta_{\text{Gr-GaAs}} = 0.19 \pm 4.81\text{ n}\Omega\text{ }\Omega^{-1} (k = 2).$$

Epigraphene is again shown to be in good agreement with GaAs standard. It is also shown to retain its performance in CCC measurements for at least one year.

5. Conclusions

The new molecular doping scheme enables uniform precision control of the carrier density in epitaxial graphene on SiC, which remains stable over at least several years despite numerous thermal cycles. Independent measurements in two NMIs confirmed that the molecularly gated epigraphene devices are suitable for realization of the SI resistance unit at the level of uncertainty required in any metrology laboratory.

Acknowledgment

This work was jointly supported by the Swedish-Korean Basic Research Cooperative Program of the NRF (No. NRF-2017R1A2A1A18070721), the Swedish Foundation for Strategic Research (SSF) (No. IS14-0053, GMT14-0077, and RMA15-0024), Swedish Research Council (VR), VINNOVA, Knut and Alice Wallenberg Foundation, Chalmers Area of Advance NANO, the UK Department of Business, Energy and Industrial Strategy (BEIS), and the European Union's Horizon 2020 research and innovation programme under Grant Agreement GrapheneCore2 No 785219.

ORCID iDs

Nick Fletcher  <https://orcid.org/0000-0002-9653-1580>
 Yung Woo Park  <https://orcid.org/0000-0003-2046-8025>
 Sergey Kubatkin  <https://orcid.org/0000-0001-8551-9247>

References

- [1] Tzalenchuk A, Lara-Avila S, Kalaboukhov A, Paolillo S, Syväjärvi M, Yakimova R, Kazakova O, Janssen T J B M, Fal'ko V and Kubatkin S 2010 Towards a quantum resistance standard based on epitaxial graphene *Nat. Nanotechnol.* **5** 186–9
- [2] Janssen T J B M, Rozhko S, Antonov I, Tzalenchuk A, Williams J M, Melhem Z, He H, Lara-Avila S, Kubatkin S and Yakimova R 2015 Operation of graphene quantum Hall resistance standard in a cryogen-free table-top system *2D Mater.* **2** 035015
- [3] Ribeiro-Palau R et al 2015 Quantum Hall resistance standard in graphene devices under relaxed experimental conditions *Nat. Nanotechnol.* **10** 1–18
- [4] Alexander-Webber J A et al 2016 Giant quantum Hall plateaus generated by charge transfer in epitaxial graphene *Sci. Rep.* **6** 30296
- [5] Janssen T J B M, Fletcher N E, Goebel R, Williams J M, Tzalenchuk A, Yakimova R, Kubatkin S, Lara-Avila S, Fal'ko V I and Yakimova R 2011 Graphene, universality of the quantum Hall effect and redefinition of the SI system *New J. Phys.* **9** 93026
- [6] Kopylov S, Tzalenchuk A, Kubatkin S and Fal'ko V I 2010 Charge transfer between epitaxial graphene and silicon carbide *Appl. Phys. Lett.* **97** 112109
- [7] Lara-Avila S, Moth-Poulsen K, Yakimova R, Bjaðrholm T, Fal'ko V, Tzalenchuk A and Kubatkin S 2011 Non-volatile photochemical gating of an epitaxial graphene/polymer heterostructure *Adv. Mater.* **23** 878–82
- [8] Tzalenchuk A et al 2011 Engineering and metrology of epitaxial graphene *Solid State Commun.* **151** 1094–9
- [9] Lartsev A, Yager T, Bergsten T, Tzalenchuk A, Janssen T J B M, Yakimova R, Lara-Avila S and Kubatkin S 2014 Tuning carrier density across Dirac point in epitaxial graphene on SiC by corona discharge *Appl. Phys. Lett.* **105** 063106
- [10] Rigosi A F et al 2018 Gateless and reversible Carrier density tunability in epitaxial graphene devices functionalized with chromium tricarbonyl *Carbon* **142** 468–74
- [11] He H et al 2018 Uniform doping of graphene close to the Dirac point by polymer-assisted assembly of molecular dopants *Nat. Commun.* **9** 3–9
- [12] Emtsev K V et al 2009 Towards wafer-size graphene layers by atmospheric pressure graphitization of silicon carbide *Nat. Mater.* **8** 203–7
- [13] Virojanadara C, Syväjärvi M, Yakimova R, Johansson L, Zakharov a and Balasubramanian T 2008 Homogeneous large-area graphene layer growth on 6H-SiC(0001) *Phys. Rev. B* **78** 245403
- [14] Yager T et al 2013 Express optical analysis of epitaxial graphene on SiC: impact of morphology on quantum transport *Nano Lett.* **13** 4217–23
- [15] Panchal V, Giusca C E, Lartsev A, Martin N A, Cassidy N, Myers-Ward R L, Gaskill D K and Kazakova O 2016 Atmospheric doping effects in epitaxial graphene: correlation of local and global electrical studies *2D Mater.* **3** 015006
- [16] Yager T, Lartsev A, Yakimova R, Lara-Avila S and Kubatkin S 2015 Wafer-scale homogeneity of transport properties in epitaxial graphene on SiC *Carbon* **87** 409–14
- [17] Delahaye F 1989 Technical guidelines for reliable measurements of the quantized hall resistance *Metrologia* **26** 63–8
- [18] Delahaye F and Jeckelmann B 2003 Revised technical guidelines for reliable dc measurements of the quantized Hall resistance *Metrologia* **40** 217–23
- [19] Williams J M, Janssen T J B M, Rietveld G and Houtzager E 2010 An automated cryogenic current comparator resistance ratio bridge for routine resistance measurements *Metrologia* **47** 167–74
- [20] Allan D W 1987 Should the classical variance be used as a basic measure in standards metrology? *IEEE Trans. Instrum. Meas.* **IM-36** 646–54

Paper E

The performance limits of Epigraphene Hall sensors
doped across the Dirac point

The performance limits of epigraphene Hall sensors

H. He¹, N. Shetty¹, T. Bauch¹, S. Kubatkin¹, T. Kaufmann², M. Cornils², R. Yakimova³, and S. Lara-Avila^{1,4}

¹ Department of Microtechnology and Nanoscience, Chalmers University of Technology, 412 96 Gothenburg, Sweden.

² TDK-Micronas GmbH, Hans-Bunte-Strasse 19, D-79108 Freiburg, Germany

³ Department of Physics, Chemistry and Biology, Linköping University, 581 83 Linköping, Sweden.

⁴ National Physical Laboratory, Hampton Road, Teddington TW11 OLW, UK

Epitaxial graphene on silicon carbide, or epigraphene, provides an excellent platform for Hall sensing devices in terms of both high electrical quality and scalability. However, the challenge in controlling its carrier density has thus far prevented systematic studies of epigraphene Hall sensor performance. In this work we investigate epigraphene Hall sensors where epigraphene is doped across the Dirac point using molecular doping. Depending on the carrier density, molecular-doped epigraphene Hall sensors reach room temperature sensitivities $S_V=0.23 \text{ V}/\text{VT}$, $S_I=1440 \text{ V}/\text{AT}$ and magnetic field detection limits down to $B_{\text{MIN}}=27 \text{ nT}/\sqrt{\text{Hz}}$ at 20 kHz. Thermally stabilized devices demonstrate operation up to 150 °C with $S_V=0.12 \text{ V}/\text{VT}$, $S_I=300 \text{ V}/\text{AT}$ and $B_{\text{MIN}}\sim 100 \text{ nT}/\sqrt{\text{Hz}}$ at 20 kHz.

Based on the classical Hall Effect, solid-state Hall sensors represent a large portion of magnetometers which are extensively used in automotive, marine and consumer electronics applications. Hall sensors based on silicon see widespread use owing to well-established and low-cost production methods,¹⁻³ but increasing requirements placed on improved magnetic performance or resilience to harsh conditions like high temperatures, demand the exploration of other, even more suitable materials.⁴

Hall sensors detect magnetic fields by measuring the Hall voltage V_H induced by an external field B . High device sensitivity implies a large magnitude of V_H response to an external field, for a given bias current I_B or voltage V_B . This leads to two important material-related metrics: the current-related sensitivity $S_I=|V_H/(BI_B)|$ (V(AT)), which is essentially determined by the Hall coefficient R_H (Ω/T), and the voltage-related sensitivity $S_V=|V_H/(BV_B)|$ (V(VT)) which is ultimately limited by the carrier mobility μ ($\text{m}^2/(\text{Vs})$), where ρ_{xx} is sheet resistance.

Graphene appears to be a natural candidate for highly sensitive Hall elements due to its high mobility, and the possibility to tune carrier density n down to zero towards charge neutrality (Dirac point). Low carrier density is desirable because it increases the Hall coefficient, $R_H = 1/(ne)$ ^{5,6}. Moreover, since the mobility $\mu = R_H/\rho_{xx}$ of graphene is inversely proportional to carrier density as $\mu \propto 1/\sqrt{n}$,⁷ decreasing n towards neutrality would increase both S_I and S_V . In principle, low n leads to an increase in ρ_{xx} , which follows the relation $\rho_{xx} \propto 1/n$, in the limit where charged impurity scattering dominates (Supplementary S1).^{8,9} Yet, decreasing n can actually lead to a lower magnetic field detection limit, $B_{\text{MIN}} = V_N/(I_B R_H)$ (T/ $\sqrt{\text{Hz}}$), where V_N is the voltage noise spectral density (V/ $\sqrt{\text{Hz}}$). If Johnson-Nyquist noise dominates, then $V_N = V_{TH} \propto \sqrt{4k_B T \rho_{xx}}$, with

Boltzmann constant k_B , temperature T , and the detection limit scales as $B_{\text{MIN}} \propto V_N/R_H \propto \sqrt{n}$ for a fixed I_B . Disorder in real graphene samples prevents it from reaching true charge neutrality, but high-quality graphene can approach low carrier densities.¹⁰

The highest quality graphene is obtained by mechanical exfoliation of graphite and encapsulation in hexagonal boron nitride (hBN-G). As Hall sensor, hBN-G has shown ultra-high device sensitivities, and detection limits comparable to that of silicon.¹¹ However, this approach serves only as a proof of principle of the capabilities of graphene Hall sensors since device fabrication cannot be scaled-up. Graphene grown using chemical vapor deposition (CVD) is a more scalable technology which also can reach high sensitivities, but reported performance varies greatly,^{12–14} perhaps due to variability in material growth and the need for subsequent transfer to suitable substrates.¹⁵

Epitaxial graphene on SiC substrate (epigraphene) is another attractive scalable technology. The insulating substrate allows for direct mass-fabrication of devices over wafer-scales,^{16,17} forgoing the need for graphene-transfer thus increasing reproducibility and yield. Epigraphene is also compatible with operation at temperatures exceeding common industrial requirements.^{18,19} Despite these advantages, epigraphene remains relatively unexplored for Hall sensing in literature,¹⁸ possibly owing to the difficulties in tuning carrier density due to high intrinsic n-doping, pinned by the substrate.^{20–22}

We report the exploration of the performance limits of epigraphene Hall sensors for varying doping levels across the Dirac point. Carrier density control is enabled by a molecular doping method using electron acceptors F4TCNQ assembled on the surface of epigraphene.²³ Devices doped using this method have already shown excellent electrical properties and low charge-disorder, albeit at low temperatures.^{24,25} We investigate Hall sensor figures of merit B_{MIN} , S_V , and S_I , and finally thermal stability in ambient conditions from room temperature and just above 200 °C. Furthermore, we establish the limits for optimal operation of epigraphene Hall devices under realistic operational conditions.

Epigraphene was grown on 4H-SiC chips encased in a graphite crucible and heated using RF heating to around 1850 °C in an inert atmosphere of 1 bar argon.¹⁶ Transmission mode microscopy was used to select only samples with over 90 % monolayer coverage.²⁶ Device fabrication used standard electron beam lithography. Epigraphene is removed using oxygen plasma etching and the metal contacts are deposited using physical vapor deposition of 5 nm Ti and 80 nm Au. The finished device is spin-coated with molecular dopants and the final carrier density is tuned by annealing at T=160 °C, with varying annealing time depending on the desired final doping level.²³ Electrical characterization was performed primarily using the Van der Pauw (VdP) method, with samples measured at room temperature and under ambient conditions unless otherwise stated. A magnetic field perpendicular to the chip surface was applied using a coil electromagnet up to 100 mT). Noise measurements were performed by taking the power spectral density (PSD) using a voltage amplifier DLPVA-100-F-D from Femto, with bandwidth limited to 100 kHz and measured input noise level of 9 nV/√Hz. High-field measurements were performed in PPMS (Quantum design) cryostat (2–300 K) with a superconducting magnet providing fields up to 14 T. For heating

experiments, the sample was mounted using epoxy on a ceramic heater, and temperature was monitored using a Pt100-resistor.

Seven epigraphene Hall sensors (Fig. 1(a)), spread across four chips, were investigated in total. They were designed using symmetric square or cross shaped geometries optimized with respect to S_V .^{27,28} Cryogenic measurements on a molecular-doped sensor demonstrates a full transition to half-integer Quantum Hall regime, with vanishing sheet resistance ρ_{XX} and quantized Hall resistance $R_{XY} = h/2e^2$ (Fig. 1(b)). These measurements verify that the devices are made of high-quality monolayer graphene with uniform doping.

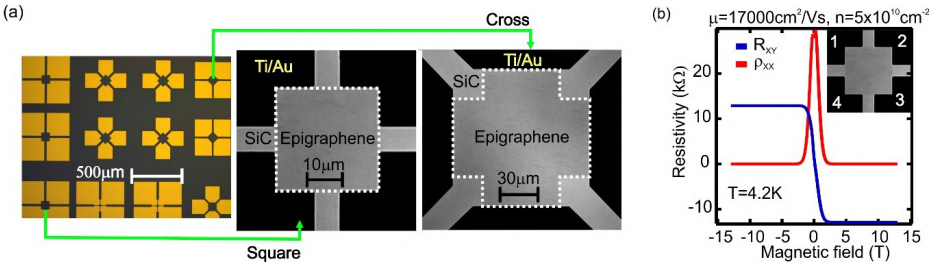


FIG. 1. (a) Optical micrographs of the layout epigraphene Hall sensors. Each chip contains an array of sensors with square and cross shaped geometries. (b) Molecular-doped Hall sensor displays the half-integer quantum Hall effect at cryogenic temperatures. R_{XY} used e.g. contacts 1-3 for bias current and 2-4 to measure Hall voltage. ρ_{XX} used e.g. 1-2 for bias and 4-3 for voltage measurement.

Hall measurements of the transversal resistance $R_{XY} = V_H/I_B$ serve as basis for the evaluation of epigraphene Hall magnetometers. Hall coefficient, carrier densities, and mobilities are calculated from measurements in low magnetic fields ($B < 0.5$ T) as $R_H = dR_{XY}/dB$, $n = 1/(eR_H)$, and $\mu = R_H/\rho_{XX}$, respectively. For the low-field range, the linearity error of R_{XY} is below 1 %, which is determined by the percentage deviation of the raw data from the low-field linear fit (Fig. 2(a)). The samples were tested up to $B=13$ T at room temperature. For low doping ($R_H=1284 \Omega/T$, $n=4.9 \times 10^{11} \text{ cm}^{-2}$) the transversal resistance remains within 5% error in a range of $B=\pm 1.2$ T, but for higher doping ($R_H=949 \Omega/T$, $n=6.6 \times 10^{11} \text{ cm}^{-2}$) the 5% error range increases to $B=\pm 6$ T. Figure 2(b) shows a summary of the carrier densities achieved in our experiments. The gap in data near charge neutrality ($n=0$) indicates the disordered charge-puddle regime, characterized by a nonlinear low-field R_{XY} .²³ At room temperature the maximum measured values of R_H and μ are $R_H=1440 \Omega/T$ and $\mu=2300 \text{ cm}^2/(\text{Vs})$, respectively. In terms of charge disorder, at room temperature, epigraphene is in puddle regime for doping levels $|n| < 5 \times 10^{11} \text{ cm}^{-2}$ thus setting the maximum R_H attainable in our epigraphene samples.

Fig. 2(c) shows the linearity of V_H at 100 mT up to 6 mA bias current, measured for highly ($n=1.6 \times 10^{12} \text{ cm}^{-2}$) and lowly ($n=4.5 \times 10^{12} \text{ cm}^{-2}$) doped devices. We find that for all carrier densities the current-voltage (I-V) characteristic is linear within 5% error for $I_B < 2.5$ mA. The non-linearity is expected to be due to self-heating. For all subsequent measurements we limit the bias current to below 1.5mA to ensure a linear I-V behavior within 2% error.

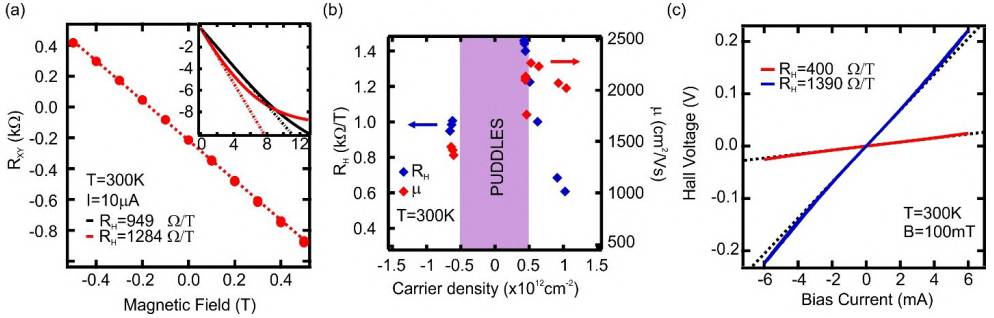


FIG. 2. (a) Hall measurements showing linearity of R_{XY} vs applied magnetic field. Inset shows behavior up to 13 T for different doping. The dotted lines are linear fits to low-field data $|B|<0.5$ T. (b) Carrier densities n and mobilities μ are extracted from low-field Hall measurements. (c) Linearity of Hall voltage measured at fixed field of 100 mT vs applied bias current. The dotted lines are linear fits to low-bias data $|I_B|<0.5$ mA. The offset in V_H at zero field can be compensated by orthogonal VdP measurements and spinning current.²⁹ Typically observed offsets are on the order of 1 mV for a bias current $I_B=10$ μ A (Supplementary S2).

The measurements in magnetic fields are complemented with noise measurements to unveil the minimum detection limit B_{MIN} . Fig. 3(a) shows the low-bias ($I_B=10$ μ A) voltage noise spectral density V_N measured at the Hall voltage terminals for different doping levels. In the low bias regime, the corner frequency of $1/f$ noise is around ~ 30 Hz. As epigraphene approaches the Dirac point, the sheet resistance of the devices increases as $\rho_{XX} \propto 1/n$, and consequently the larger input and output resistance of the devices increases thermal noise. Dotted lines in Fig. 3 are the thermal voltage noise V_{TH} calculated using measured input resistance. The agreement with experimental noise data points to the fact that, at low bias, thermal noise dominates in our sensors. Fig. 3(b) shows the increase of the $1/f$ noise contribution at larger bias currents, which nearly follows the Hooge's empirical relation with Hooge parameter $\alpha_H \approx 0.015$ (Fig 3(b) inset),³⁰ implying that the excess noise is mostly due to resistance fluctuations. In practical devices, the excess noise can be alleviated by using spinning Hall current measurement techniques.²⁹

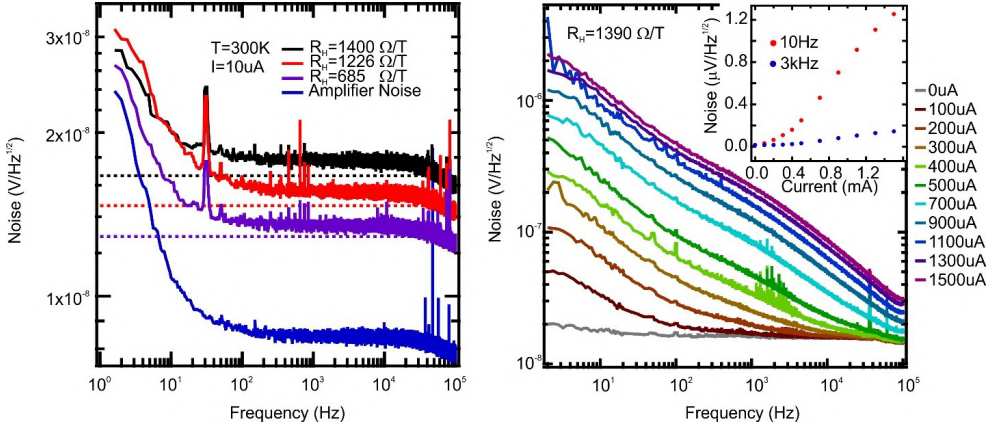


FIG. 3. (a) Noise performance for one Hall sensor measured at different doping levels. The dotted lines are calculated noise levels assuming pure thermal noise of a resistor. (b) Measured voltage noise spectral density vs bias current in another lowly doped device. Inset: The noise amplitude vs bias current at two different frequencies.

The measured sensitivities for epigraphene Hall sensors and their dependence on doping, collected across all measured devices, are summarized in Fig. 4(a). The highest S_I is reached for low doping levels, close to the puddle regime ($n \sim 5 \times 10^{11} \text{ cm}^{-2}$). The highest S_V occurs slightly outside the puddle regime, at doping levels $n \sim 6 \times 10^{11} \text{ cm}^{-2}$. We have performed full noise spectrum characterization (e.g. Fig. 3b) for four doping levels to obtain $B_{\text{MIN}} = V_N / (I_B R_H)$, which includes not only intrinsic noise of epigraphene (thermal and 1/f noise) but also amplifier noise. Fig. 4(b) shows B_{MIN} as a function of I_B , measured at a frequency of 3 kHz for fair comparison to other graphene devices reported in literature. The best $B_{\text{MIN}} = 47 \text{ nT}/\sqrt{\text{Hz}}$ is attained at lowest doping $n \sim 5 \times 10^{11} \text{ cm}^{-2}$, for $I_B = 400 \mu\text{A}$. At higher frequencies, where the 1/f noise contribution is lower, B_{MIN} can be naturally lower with $B_{\text{MIN}} = 27 \text{ nT}/\sqrt{\text{Hz}}$, for $n \sim 5 \times 10^{11}$ at 20 kHz (inset Fig. 4(b)).

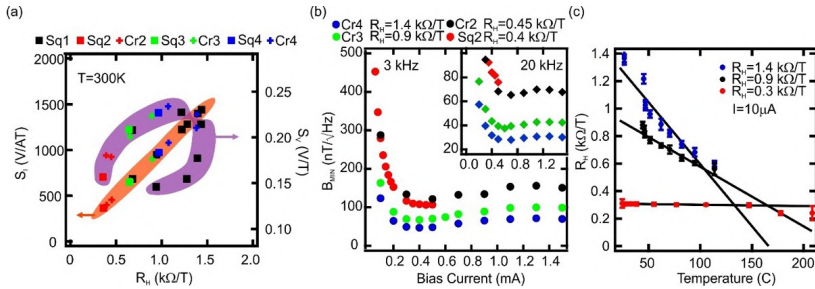


FIG. 4. (a) S_I (orange region) and S_V (purple region) versus R_H compiled from 7 Hall sensors across 4 chips (Sq=square shaped, Cr=cross shaped). The sequence of data points span high to low doping (starting from the leftmost point). (b) B_{MIN} versus bias current calculated directly from measured noise data for 3 kHz. Inset also shows data for 20 kHz. (c) Investigation of B_{MIN} versus temperature (C) for three different Hall resistances: $R_H = 1.4 \text{ k}\Omega/\text{T}$, $R_H = 0.9 \text{ k}\Omega/\text{T}$, and $R_H = 0.3 \text{ k}\Omega/\text{T}$.

thermal stability of R_H by measuring R_H at elevated sample temperatures, for different initial room temperature doping. The error bars represent 2 standard deviations for measured R_H averaged over 10-15 min of measurements. The solid lines are linear fits taken at the lower temperatures before permanent doping change is induced.

Finally, we describe the thermal stability of the molecular-doped Hall sensor through the temperature coefficient Δ_T , defined as the percentage change of R_H from its room temperature value per degree Celsius. Fig. 4(c) shows that samples doped close to neutrality ($R_H=1400 \Omega/T$) are stable up to $T=80^\circ\text{C}$ (Supplementary S3), with a temperature coefficient $\Delta_T=-0.6\%/\text{C}$. We achieve highest thermal stability with samples annealed for ~4 hours at $T=160^\circ\text{C}$, after which the R_H reached a stable value of $R_H\sim 300 \Omega/T$ due to partial desorption of dopants.²³ After this curing step at 160°C , samples showed a fairly low $\Delta_T=-0.03\%/\text{C}$ up to $T=150^\circ\text{C}$, while still displaying respectable performance at this temperature, with $S_V\sim 0.12 \text{ V}/(\text{V}T)$, $S_I\sim 300 \text{ V}/(\text{A}T)$, and $B_{\text{MIN}}\sim 100 \text{ nT}/\sqrt{\text{Hz}}$.

Type	S_I (V/(AT))	S_V (V/(VT))	B_{MIN} (nT/ $\sqrt{\text{Hz}}$)	Freq (kHz)
InSb ^{29,31-33}	140-700	1-7.2	1-60	0-50
GaAs ^{29,31-33}	30-3200	0.6-1	10-6000	0-50
hBN-G ¹¹	4100	2.6	50	3
CVD ¹⁴	2093	0.35	100	3
CVD ¹²	1200	N/A	300000	3
CVD ¹³	97	0.03	400000	1
Epi ³⁴	1021	0.3	2000	3
Epi (this)	1080	0.23	60, 40	3, 20
Epi (this)	1442	0.21	47, 27	3, 20

Table I. Figures of merit for room temperature Hall sensor performance, compared between both graphene-based Hall sensors and III-V commercially available sensors.

Table 1 shows a comparison of our devices with other Hall sensors reported in literature. The maximum current-related sensitivity in doped epigraphene is found to be on the order of $S_I\sim 1.500 \text{ V}/(\text{A}T)$ at room temperature. This value is limited by minimum n attained in our sample ($|n|<5\times 10^{11} \text{ cm}^{-2}$), and is set by the disorder present in the as-grown material, combined with additional contributions from external doping and thermally excited carriers in the dopant layer and the SiC substrate. Decoupling epigraphene and substrate by hydrogen intercalation has led to high μ at cryogenic temperatures. However, at room temperature, the lowest n reported for H-intercalated epigraphene are all above $1\times 10^{12} \text{ cm}^{-2}$, with $\mu\sim 1300-1700 \text{ cm}^2/(\text{Vs})$.³⁵ These mobilities are lower than the highest reported for epigraphene at room temperature ($\mu=5500 \text{ cm}^2/(\text{Vs})$)^{22,36} and the ones achieved in this work ($\mu=2300 \text{ cm}^2/(\text{Vs})$). Above room temperature, interactions between epigraphene and the substrate via longitudinal-acoustic and remote interfacial phonon scattering further degrades mobility. The stable temperature range ($T<80^\circ\text{C}$) for samples doped close to Dirac point is determined by our current choice of doping method.²³ A high thermal

stability up to T=150°C is achieved after curing the samples at a temperature of 160°C for 4 hours. The resulting temperature coefficient $\Delta_T = -0.03\%/\text{°C}$ could then be understood as the intrinsic thermal drift of epigraphene, and not due to desorption of dopants. This implies that by using an alternate thermally-stable doping scheme, epigraphene could well outperform Hall elements based III-V at high temperatures.^{29,31-33} Our work paves the way for development of epigraphene Hall sensors for real-world applications which require durable, controllable and sensitive devices produced in a scalable way.

We thank Alexander Tzalenchuk for insightful discussions. This work was jointly supported by the Swedish Foundation for Strategic Research (SSF) (nos. GMT14-0077, RMA15-0024), Chalmers Excellence Initiative Nano, and VINNOVA (nos. 2017-03604 and 2019-04426). This work was performed in part at Myfab Chalmers.

The authors declare that the main data supporting the findings of this study are available within the article and supplementary information. Additional data are available from the corresponding author upon request.

References

- ¹ J. Heremans, J. Phys. D. Appl. Phys. **26**, 1149 (1993).
- ² G. Boero, M. Demierre, P.-. A. Besse, and R.S. Popovic, Sensors Actuators A Phys. **106**, 314 (2003).
- ³ P. Kejik, G. Boero, M. Demierre, and R.S. Popovic, Sensors Actuators A Phys. **129**, 212 (2006).
- ⁴ I. Shibaasaki, J. Cryst. Growth **175–176**, 13 (1997).
- ⁵ K.S.S.K.S. Novoselov, A.K. a. K. Geim, S.V.S. V Morozov, D. Jiang, Y. Zhang, S.V. V Dubonos, I.V. V Grigorieva, and a. a. A. Firsov, Science (80-.). **306**, 666 (2004).
- ⁶ K.S. Novoselov, A.K. Geim, S. V Morozov, D. Jiang, M.I. Katsnelson, I. V Grigorieva, S. V Dubonos, and A.A. Firsov, Nature **438**, 197 (2005).
- ⁷ W. Zhu, V. Perebeinos, M. Freitag, and P. Avouris, Phys. Rev. B - Condens. Matter Mater. Phys. **80**, 1 (2009).
- ⁸ V. Cheianov and V. Fal'ko, Phys. Rev. Lett. **97**, 1 (2006).
- ⁹ J.-H. Chen, C. Jang, S. Adam, M.S. Fuhrer, E.D. Williams, and M. Ishigami, Nat. Phys. **4**, 377 (2008).
- ¹⁰ J. Martin, N. Akerman, G. Ulbricht, T. Lohmann, J.H. Smet, K. von Klitzing, and A. Yacoby, Nat. Phys. **4**, 13 (2007).
- ¹¹ J. Dauber, A.A. Sagade, M. Oellers, K. Watanabe, T. Taniguchi, D. Neumaier, and C. Stampfer, Appl. Phys. Lett. **106**, (2015).
- ¹² C.-C. Tang, M.-Y. Li, L.J. Li, C.C. Chi, and J.C. Chen, Appl. Phys. Lett. **99**, 112107 (2011).
- ¹³ A. Dankert, B. Karpiak, and S.P. Dash, Sci. Rep. **7**, 15231 (2017).
- ¹⁴ L. Huang, Z. Zhang, B. Chen, X. Ma, H. Zhong, and L.M. Peng, Appl. Phys. Lett. **104**, (2014).
- ¹⁵ J. Chan, A. Venugopal, A. Pirkle, S. McDonnell, D. Hinojos, C.W. Magnuson, R.S. Ruoff, L. Colombo, R.M. Wallace, and E.M. Vogel, ACS Nano **6**, 3224 (2012).

- ¹⁶ C. Virojanadara, M. Syväjarvi, R. Yakimova, L. Johansson, a. Zakharov, and T. Balasubramanian, Phys. Rev. B **78**, 245403 (2008).
- ¹⁷ K. V Emtsev, A. Bostwick, K. Horn, J. Jobst, G.L. Kellogg, L. Ley, J.L. McChesney, T. Ohta, S. a Reshanov, J. Röhrl, E. Rotenberg, A.K. Schmid, D. Waldmann, H.B. Weber, and T. Seyller, Nat. Mater. **8**, 203 (2009).
- ¹⁸ T. Ciuk, B. Stanczyk, K. Przyborowska, D. Czolak, A. Dobrowolski, J. Jagiello, W. Kaszub, M. Kozubal, R. Kozlowski, and P. Kaminski, IEEE Trans. Electron Devices **66**, 3134 (2019).
- ¹⁹ K.H. Kim, S. Lara-Avila, H. He, H. Kang, Y.W. Park, R. Yakimova, and S. Kubatkin, Crystals **7**, (2017).
- ²⁰ S. Kopylov, A. Tzalenchuk, S. Kubatkin, and V.I. Fal'Ko, Appl. Phys. Lett. **97**, (2010).
- ²¹ A. Lartsev, T. Yager, T. Bergsten, A. Tzalenchuk, T.J.B.M. Janssen, R. Yakimova, S. Lara-Avila, and S. Kubatkin, Appl. Phys. Lett. **105**, 063106 (2014).
- ²² S. Lara-Avila, K. Moth-Poulsen, R. Yakimova, T. Bjaðrnholm, V. Fal'Ko, A. Tzalenchuk, and S. Kubatkin, Adv. Mater. **23**, 878 (2011).
- ²³ H. He, K.H. Kim, A. Danilov, D. Montemurro, L. Yu, Y.W. Park, F. Lombardi, T. Bauch, K. Moth-poulsen, T. Iakimov, and R. Yakimova, (n.d.).
- ²⁴ H. He, S. Lara-Avila, K.H. Kim, N. Fletcher, S. Rozhko, T. Bergsten, G. Eklund, K. Cedergren, R. Yakimova, Y.W. Park, A. Tzalenchuk, and S. Kubatkin, Metrologia **56**, 045004 (2019).
- ²⁵ S. Lara-Avila, A. Danilov, D. Golubev, H. He, K.H. Kim, R. Yakimova, F. Lombardi, T. Bauch, S. Cherednichenko, and S. Kubatkin, Nat. Astron. **3**, (2019).
- ²⁶ T. Yager, A. Lartsev, S. Mahashabde, S. Charpentier, D. Davidovikj, A. Danilov, R. Yakimova, V. Panchal, O. Kazakova, A. Tzalenchuk, S. Lara-Avila, and S. Kubatkin, Nano Lett. **13**, 4217 (2013).
- ²⁷ M. Cornils and O. Paul, in *Proc. IEEE Int. Conf. Micro Electro Mech. Syst.* (IEEE, 2008), pp. 940–943.
- ²⁸ M. Cornils, *Sheet Resistance and Hall Mobility Determination Beyond Van Der Pauw* (Der Andere Verlag, 2009).
- ²⁹ R.S. Popović, *Hall Effect Devices* (Institute of Physics Pub, 2004).
- ³⁰ F.N. Hooge, Phys. B+C **83**, 14 (1976).
- ³¹ Y. Sugiyama and S. Kataoka, Sensors and Actuators **8**, 29 (1985).
- ³² F.W Bell, Bell Technol. Inc., a SYPRIS Co. (n.d.).
- ³³ AKM, Akahi Kasei Microdevices (2020).
- ³⁴ V. Panchal, K. Cedergren, R. Yakimova, A. Tzalenchuk, S. Kubatkin, and O. Kazakova, J. Appl. Phys. **111**, 8 (2012).
- ³⁵ E. Pallecchi, F. Lafont, V. Cavaliere, F. Schopfer, D. Mailly, W. Poirier, and A. Ouerghi, Sci. Rep. **4**, 1 (2014).
- ³⁶ J.L. Tedesco, B.L. VanMil, R.L. Myers-Ward, J.M. McCrate, S.A. Kitt, P.M. Campbell, G.G. Jernigan, J.C. Culbertson, C.R. Eddy, and D.K. Gaskill, Appl. Phys. Lett. **95**, 122102 (2009).

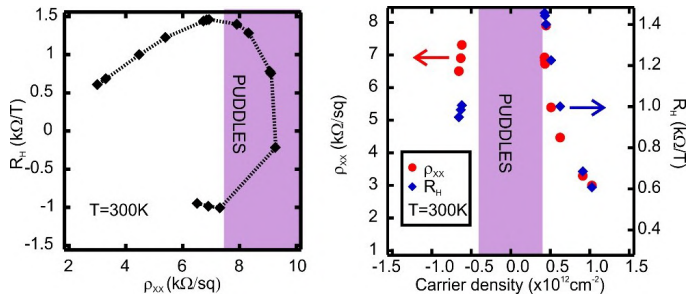


Fig. S1. Left: Relationship between Hall coefficient R_H and sheet resistance ρ_{xx} . Sheet resistance is the highest in the puddle regime, while R_H is the highest just outside the puddle regime. Right: R_H and ρ_{xx} vs carrier density n . ρ_{xx} scales with carrier density n in the same way as $R_H \sim 1/n$. Note that several R_H -values in the left plot have been omitted from the carrier density x-axis in right plot because the carrier density $n=1/(eR_H)$ is not well-defined in the puddle regime.

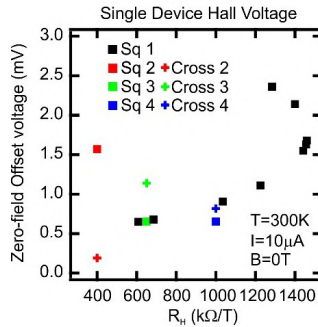


Fig. S2. Left: Uncompensated offset in Hall voltages at zero magnetic field measured for 7 different devices. In general, the offset voltages are on the order 1 mV, and tends to increase as samples are doped towards neutrality (puddle regime). Note that we estimate that the residual magnetization of the coil magnet is on the order of $\sim\text{mT}$, further skewing the data to high offset values. In this limited dataset there is no observed correlation between device geometry and offset. The lowest offset voltage is achieved for cross geometry and high doping levels. Offset compensation can be achieved using orthogonal coupling of two or more Hall elements, in combination with Van der Pauw averaging, and can reduce the final offset to below 1 μV . Note that this requires very homogeneously doped devices, which we do achieve when using molecular dopant F4TCNQ mixed with PMMA.

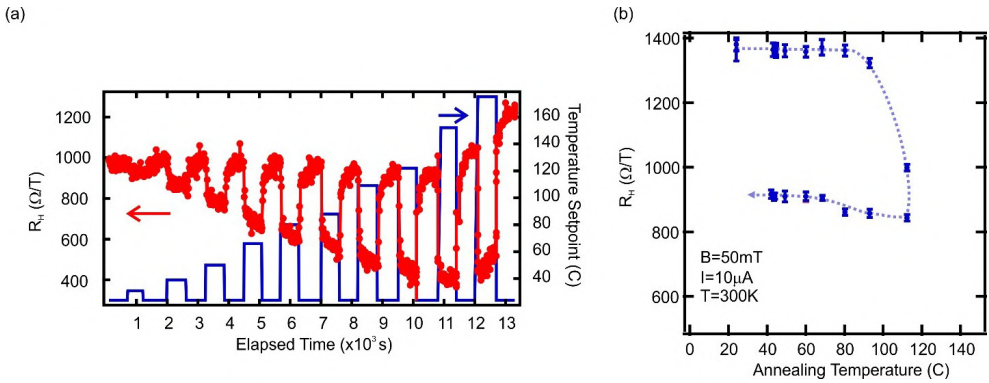


Fig. S3. (a) Example of investigation of thermal stability of a Hall sensor using in-situ heating sweeps. The red curve shows the Hall coefficient versus time and the blue curve shows the temperature set-point versus time. Sample behavior is monitored in real-time during heating and cooling. Fast sweeps (< 1 min) of magnetic field (± 10 mT) are used to deduce R_H . The blue curve shows the temperature set-point versus time. (b) We study the thermal stability of the molecular-doped Hall sensor by measuring the room temperature performance of devices after repeated annealing. Initially, the devices is doped close to the Dirac point ($n < 5 \times 10^{11} \text{ cm}^{-2}$) and is kept at elevated temperatures for 15 min, and left to cool down back to room temperature. Performance is assessed in real-time like in (a). This heating process is repeated, moving to successively higher temperatures. Only when the sample is annealed to above 80 $^\circ\text{C}$, close to glass transition temperature of the polymer using for doping, does significant permanent change of room temperature n occur. There is a permanent increase in n-doping leading to a decrease in R_H . Subsequent heating above 80 $^\circ\text{C}$ induces further permanent change in doping toward even higher n-doping.

Paper F

Towards quantum-limited coherent detection of terahertz waves in charge-neutral graphene

Towards quantum-limited coherent detection of terahertz waves in charge-neutral graphene

S. Lara-Avila^{1,2*}, A. Danilov¹, D. Golubev³, H. He¹, K. H. Kim¹, R. Yakimova⁴, F. Lombardi¹, T. Bauch¹, S. Cherednichenko¹ and S. Kubatkin¹

Spectacular advances in heterodyne astronomy^{1,2} have been largely due to breakthroughs in detector technology³. To exploit the full capacity of future terahertz (~ 300 GHz– 5 THz) telescope space missions⁴, new concepts of terahertz coherent receivers are needed, providing larger bandwidths and imaging capabilities with multipixel focal plane heterodyne arrays⁵. Here we show that graphene uniformly doped to the Dirac point, with material resistance dominated by quantum localization and thermal relaxation governed by electron diffusion, enables highly sensitive and wideband coherent detection of signals from 90 to 700 GHz and, prospectively, across the entire terahertz range. We measure on proof-of-concept graphene bolometric mixers an electron diffusion-limited gain bandwidth of 8 GHz (corresponding to a Doppler shift of 480 km s⁻¹ at 5 THz) and intrinsic mixer noise temperature of 475 K (which would be equivalent to $-2hf/k_B$ at $f=5$ THz, where h is Planck's constant, f is the frequency and k_B is the Boltzmann constant), limited by the residual thermal background in our setup. An optimized device will result in a mixer noise temperature as low as 36 K, with the gain bandwidth exceeding 20 GHz, and a local oscillator power of <100 pW. In conjunction with the emerging quantum-limited amplifiers at the intermediate frequency^{6,7}, our approach promises quantum-limited sensing in the terahertz domain, potentially surpassing superconducting technologies, particularly for large heterodyne arrays.

Observations in the terahertz (THz; or submillimetre wavelength) frequency range are of great importance for understanding physics and chemistry in the star- and planet-forming regions^{8,9}. With the dawn of space and airborne submillimetre-wavelength telescopes, rotational transitions of atomic and molecular tracers in the THz range, blocked for ground-based telescopes by atmospheric attenuation, can now be accessed in full. Moreover, the high spectral resolution provided by coherent (that is heterodyne) receivers ($>\lambda/\Delta\lambda=10^7$, where λ is wavelength), allows for measurements of fine spectral line structure and Doppler shifts, hence obtaining valuable information about kinematics in the observed regions.

To recover information carried by faint celestial signals, THz frequency mixers—the core of coherent detection—have to fulfil stringent requirements on both sensitivity and, not less importantly, on a broad intermediate frequency (IF) bandwidth. The latter is required to enable line surveys and to accommodate the broad lines coming from our Galactic Centre and other extragalactic sources. For instance, a Doppler width of 300 km s⁻¹ corresponds to 5 GHz for the O I line (4.7 THz). For frequencies <1 THz and restricted by

the superconducting energy gap, superconductor-insulator-superconductor mixers have been the workhorse of THz heterodyne astronomy, reaching the fundamental detection limit and broad detection bandwidth. For the supra-THz range, superconducting hot-electron bolometers (HEB) form the baseline for modern astronomical receivers, offering sensitivities in the range of $10hf/k_B$ at a bandwidth of few GHz. In these mixers, the wave beating between the incoming THz signal and detuned local oscillator (LO) causes temperature oscillations at the IF, enabling readout through changes in electrical resistance R (resistive readout) as long as the temperature in the material can follow the signal modulation. The upper limit for the IF frequency is determined by either the electron–phonon relaxation time τ_{e-ph} (phonon cooling) or the out-diffusion time $\tau_D=L^2/(\pi^2D)$ of hot electrons from the superconductor into the cold electrical contacts (diffusion cooling), with L the length of the device and D the diffusion constant^{10–12}. Despite great efforts, NbN superconducting HEB mixers are limited in terms of instantaneous bandwidth to ~ 4 – 5 GHz (refs. ^{3,13}). Higher bandwidths are possible in new superconductors¹⁴, but at the expense of forbiddingly high LO power requirements, which is particularly detrimental for array applications. New materials and concepts are needed to go beyond few-pixel THz detectors, available today, to the large-format detector arrays required to enable further cosmic quests^{4,5,8}.

Here, we explore the resistive readout of the bolometric response of graphene, where quantum effects introduce the long-sought-after temperature dependence of graphene's resistance^{15–17}. Both long phase-coherence times and poor screening of carriers in two dimensions favour quantum interference and electron–electron interactions^{8–20}. These effects introduce logarithmic-in-temperature T dependence of the conductivity σ of graphene, of the order of $\sigma_1 \sim e^2/h \approx 3.9 \times 10^{-5} \text{ S}$, where e is the elementary charge:

$$\sigma(T) = \sigma_0 + \sigma_1(T/1\text{K}) \quad (1)$$

With graphene at high carrier density n , these effects are relatively small. Yet, as n approaches the Dirac point, the sheet conductance of graphene σ_0 decreases, and the relative contribution of quantum effects grows. This scenario, appealing for the use of graphene as a thermometer, can however be spoiled by charge disorder. Close to charge neutrality, disorder leads to doping inhomogeneity, resulting in charge puddles that can effectively shunt quantum transport and cause the resistance of graphene to saturate at low temperatures^{21–23}. In contrast, for high-quality graphene, such as flakes encapsulated by boron nitride^{24,25}, reduced disorder results in monotonically increasing resistance at low temperatures. As we

¹Department of Microtechnology and Nanoscience, Chalmers University of Technology, Gothenburg, Sweden. ²National Physical Laboratory, Teddington, UK. ³Department of Applied Physics, Aalto University, Aalto, Finland. ⁴Department of Physics, Chemistry and Biology, Linköping University, Linköping, Sweden. *e-mail: samuel.lara@chalmers.se

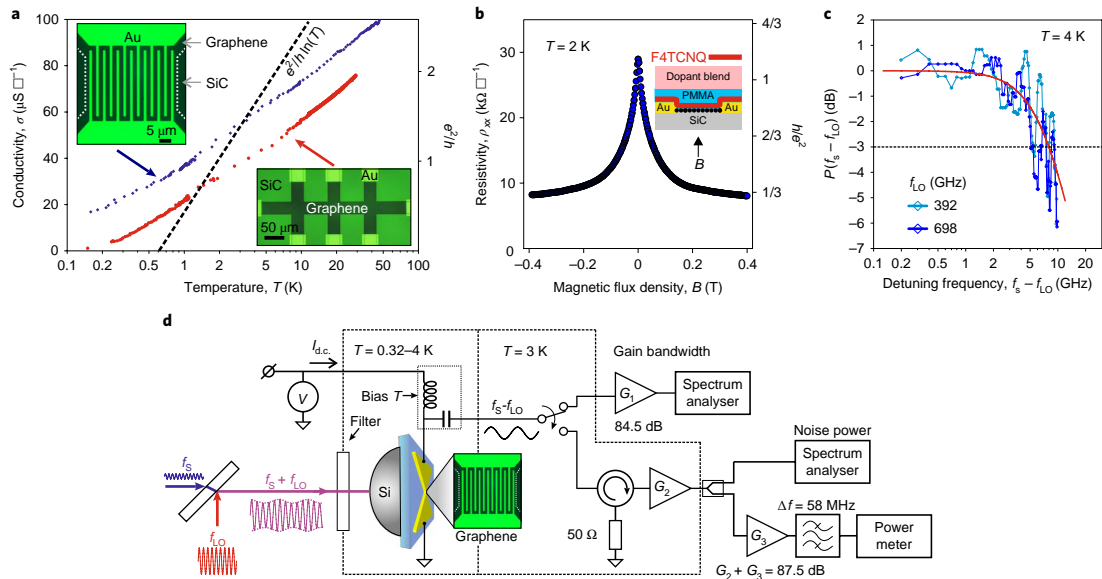


Fig. 1 | Graphene doped to the Dirac point as bolometric mixer. **a**, Zero-bias differential conductivity $\sigma(T) = dI/dV|_{V=0}$, measured in a dark (optically tight) cryostat for both a Hall bar ($L=180\text{ }\mu\text{m} \times W=30\text{ }\mu\text{m}$, red) and the interdigitized THz mixer ($L=1.5\text{ }\mu\text{m}$, blue), display a logarithmic temperature dependence $\sigma(T) = \sigma_0 + \sigma_1 \ln(T/1\text{ K})$, confirming our interdigitized device retains the properties of the ‘bulk’ chemically doped graphene. We attribute the offset in σ_0 between the Hall bar and the THz mixer to an extra temperature-independent conductance channel, coming from the contribution of bilayer patches that shunt the monolayer graphene conductivity in the narrow gap³⁹. The dashed line indicates slope $\sigma_1 = e^2/h$. **b**, Suppression of quantum interference effects by perpendicular magnetic field B breaking time-reversal symmetry (inset shows the cross-section of the device). **c**, The gain bandwidth of 8 GHz for our graphene mixer, extracted via measurements of the power at the intermediate frequency P_{IF} as a function of detuning frequency between the signal f_s and the local oscillator f_{LO} . The solid line is a fit to $P(f_{\text{IF}}) = 1/[1 + (f_{\text{IF}}/f_{\text{LO}})^2]$, the dashed line indicates $P(f_{\text{IF}}) = -3\text{ dB}$. Resonances are due to interferences in the optical path and the IF chain. **d**, Schematic of the experimental setup: the THz signal at frequency f_s is combined with a monochromatic wave emitted by a local oscillator at a nearby frequency f_{LO} , and both are fed into graphene via an integrated bow-tie antenna through a silicon lens. G_1 , G_2 , and G_3 are the gain of the IF amplifiers, and $\Delta f = 58\text{ MHz}$ refers to the bandwidth of the bandpass filter.

recently demonstrated²⁶, a similar physical situation occurs when epitaxial graphene on SiC is brought close to the Dirac point by chemical doping. The spontaneous accumulation and assembly of molecular dopants 2,3,5,6-tetrafluorotetracyanoquinodimethane (F4TCNQ) on graphene via diffusion through poly(methyl methacrylate) (PMMA) results in a molecular adlayer that dopes epitaxial graphene to the vicinity of the Dirac point and flattens charge inhomogeneity, translating into an effectively reduced disorder. As a result, equation (1) holds even when graphene is doped to the Dirac point ($n < 5 \times 10^9\text{ cm}^{-2}$) (Fig. 1a), arising primarily from quantum interference in the presence of strong intervalley scattering (Fig. 1b)^{18,24}, thus making this material an effective thermometer down to $T=0.2\text{ K}$.

But, from the point of view of bolometric mixer operation, how fast and sensitive can this thermometer be, while based on charge-neutral graphene? Dependence (1) implies a diverging sensitivity of the resistive readout $dR/dT \sim T^{-1}\ln^{-2}(T)$, favouring measurements at low temperatures. The low heat capacity of graphene translates into fast device operation²⁷ as long as a proper heat-link is provided. However, the electron–phonon cooling time $\tau_{\text{e-ph}} \sim n^{-0.5}T^{-2}$, diverges at charge neutrality and low temperature^{28,29}. Therefore, other cooling pathways, such as electron diffusion cooling, will be required. Although the residual charge puddles do not shunt quantum interference effects, the exact chemical potential landscape and microscopic scattering details are not known for the studied material, and these may greatly modify charge and heat transport

of graphene at the Dirac point^{30–33}. Summarizing, it is a priori not clear how quantum interference and strong electron–electron interactions in epitaxial graphene, chemically doped to the vicinity of the Dirac point, will affect the device speed and noise—it has to be tested experimentally.

We conducted THz mixing experiments to unveil both the response time and mixer sensitivity in epitaxial graphene chemically doped to the Dirac point. Figure 1c, the central result of this experiment, shows a mixing gain bandwidth of $f_0 = 8\text{ GHz}$, corresponding to a time constant of $1/(2\pi f_0) = 20\text{ ps}$ (for temperature independence of the gain bandwidth, see Supplementary Fig. 1). As we elaborate below, the high Fermi velocity in graphene and highly transparent metallic contacts³⁴ in our impedance-matched, interdigitated device ($L=1.5\text{ }\mu\text{m}$) allow the heat load in the device to be quickly dissipated by hot electrons diffusing into the metallic leads. Figure 1d shows a schematic of our setup, which simultaneously allows for direct current (d.c.), THz response and noise thermometry measurements down to $T=0.32\text{ K}$ (see also Supplementary Fig. 2). Thorough calibration of the THz power reaching graphene and the gain of the GHz chain was performed using noise thermometry (see Supplementary Figs. 3 and 4).

Remarkably, the d.c. transport characteristics, and both the THz direct and mixing response of our device—with transport properties dominated by quantum effects—can all be understood within a simple thermal model of diffusion cooling of electrons. In essence, the effect of THz radiation on our device is that of a

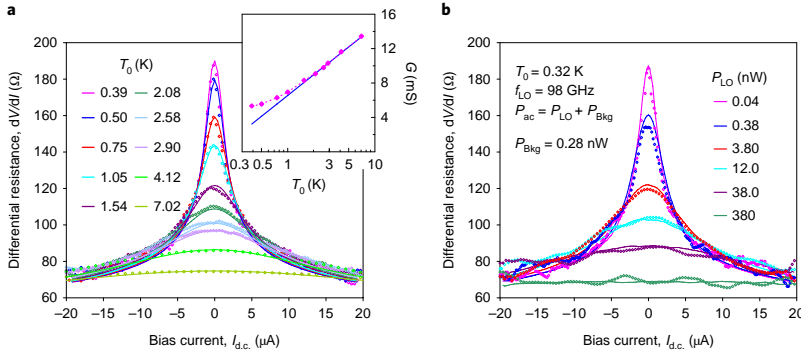


Fig. 2 | Equivalence of THz radiation, Joule heating and base temperature effects on the graphene bolometer. **a**, Effect of temperature on the measured differential resistance $dV/dI(I)$ with the THz source OFF. Inset: zero-bias conductance for the same device. Deviation from $G(T) = G_0 + G_1 \ln(T/1K)$ at low temperature, absent in measurements in a dark cryostat (Fig. 1a), is due to background heat load P_{Bkg} . **b**, Effect of THz power ($f_{\text{LO}}=98\text{ GHz}$) on the dV/dI response of our device at $T_0=0.32\text{ K}$. In both cases, dots correspond to measurements and solid lines to the DCM prediction.

temperature increase, with a diffusion cooling rate dominating over phonon cooling of hot electrons (see Supplementary Section 1 and Supplementary Fig. 5). Figure 2a shows the differential resistance dV/dI (where V is voltage and I is current) of the device, measured in the optical cryostat with the THz source OFF, as a function of the bias current at different temperatures. Figure 2b complements this, with the dV/dI of the device at the base temperature $T_0=0.32\text{ K}$ for increasing THz power P_{ac} . In both figures, solid lines correspond to calculations within a diffusion cooling model (DCM), which considers that the heat induced by both d.c. current and THz radiation is transferred by charge carriers into the metallic leads kept at the cryostat temperature T_0 (see also Supplementary Figs. 5 and 6 and Supplementary Section 2). The power P_{ac} refers to the THz input power that is dissipated in graphene, and through the rest of the paper we thus focus on the intrinsic mixer parameters that describe the detector's response to P_{ac} . Our model assumes the validity of Wiedeman–Franz law and considers that, for temperatures below 6 K, phonon cooling of electrons can be neglected. For the particular case of logarithmic temperature dependence of the bridge conductance, the device I – V characteristic $I(V)$ under a THz power P_{ac} can be obtained within the DCM as a recursive expression:

$$I(V) = G(T_0)V + G_1 V \left(\frac{\sqrt{1+u^2}}{u} \left(\sqrt{1+u^2} + u \right) - 1 \right) \quad (2)$$

with $u = \frac{1}{V_T} \sqrt{V^2 + \frac{V}{T} P_{\text{ac}}}$ and $V_T = \sqrt{\mathcal{L}} \times T_0$. Here, $G(T) = G_0 + G_1 \ln(T/1K)$ is the experimentally determined temperature-dependent conductance, yielding $G_0 = 6.55\text{ mS}$ and $G_1 = 3.50\text{ mS}$. From the family of differential resistance curves measured with the THz source OFF in Fig. 2a, we extract as a fitting parameter the radiation background power $P_{\text{Bkg}} = 0.28\text{ nW}$ in our cryostat, which leads to apparent saturation of conductance at low temperatures (Fig. 2a, inset). Additionally, the fit returns the Lorenz number $\mathcal{L} = 3.1 \times 10^{-8}\text{ W}\Omega\text{K}^{-2}$ remarkably close to its theoretical value, $\mathcal{L} = \pi^2/3(k_B/e)^2 \approx 2.44 \times 10^{-8}\text{ W}\Omega\text{K}^{-2}$. Next, we use the same P_{Bkg} and \mathcal{L} to predict a set of curves for the dV/dI response under THz irradiation at base temperature $T_0=0.32\text{ K}$, considering that the total absorbed THz power (P_{ac}) includes contribution from both the LO and P_{Bkg} . Figure 2b shows, with no extra fitting parameters involved, that the DCM precisely reproduces the observed response to radiation. Having established the bolometric nature of the THz response in our device, we investigated its performance as a THz

mixer. We irradiated the device with two THz sources, a weak signal S, and the stronger LO, measuring the mixer gain $G_{\text{mix}} = P_{\text{IF}}/P_S$, which is the ratio of the power at the output (P_{IF}) to the signal power coupled into the device, P_S (Fig. 3a). The latter one was obtained from experimental $I(V)$ curves with and without the THz signal applied. Solid lines in Fig. 3a show that, within all of our tested parameter space (T_0 , local oscillator power P_{LO} , bias current $I_{\text{d.c.}}$), G_{mix} is well described by the classical bolometric mixer expression³⁵, which also follows from the DCM:

$$G_{\text{mix}} = \frac{1}{2} \frac{P_{\text{LO}}}{P_{\text{d.c.}}} \frac{50\Omega}{V/I} \left[\frac{1 - \left(\frac{V}{I} \right) \left(\frac{dI}{dV} \right)}{1 + 50\Omega \left(\frac{dI}{dV} \right)} \right]^2 \quad (3)$$

The maximum measured mixer gain is $G_{\text{mix}} = -27\text{ dB}$ ($P_{\text{IF}}/P_S = 2\%$) at optimum mixing conditions ($P_{\text{LO}} = 3.8\text{ nW}$, $I_{\text{d.c.}} = 5\mu\text{A}$). At this operating point, the electronic temperature in graphene, measured by noise thermometry, is elevated above the base temperature due to the d.c. bias and the LO and background radiation powers, reaching an effective noise-equivalent temperature $T_s \approx 1.9\text{ K}$, as shown in Fig. 3b. Solid lines in Fig. 3b correspond to the DCM considering that the microwave noise of graphene is purely thermal (Johnson noise) (see also Supplementary Section 3 and Supplementary Fig. 7). For a mixer, the ultimate sensitivity is determined by its noise temperature T_{mix} , and for our device we find, using experimental values, $T_{\text{mix}} = T_s/(2G_{\text{mix}}) = 475\text{ K}$ (the factor 2 accounts for the double side-band nature of mixing).

With the validity of the DCM demonstrated, we extrapolated the intrinsic performance of our device for zero background radiation conditions ($P_{\text{Bkg}} = 0$), as expected on a space-borne mission. Figure 3c shows that zero background would allow for operation at reduced d.c. bias, resulting in the increase of the achievable mixing gain $G_{\text{mix}}(I_{\text{d.c.}}, P_{\text{LO}})$ by a few decibels compared with the gain we measured in our cryostat (Fig. 3a). Combining the mixer gain and the T_s corresponding to maximum conversion conditions, we show the calculated mixer noise temperature as a function of the base temperature T_0 in Fig. 3d (see also Supplementary Section 4 and Supplementary Fig. 8). Under these considerations, cooling the device down to $T_0 = 0.2\text{ K}$, a limit set by the validity of logarithmic fit in our model and achievable in refrigerators for satellite missions³⁶, would lead to $T_{\text{mix}} = 36\text{ K}$. Remarkably, this implies that the graphene bolometer mixer can operate in a quantum-limited regime at all frequencies above $k_B T_{\text{mix}}/h = 0.75\text{ THz}$.

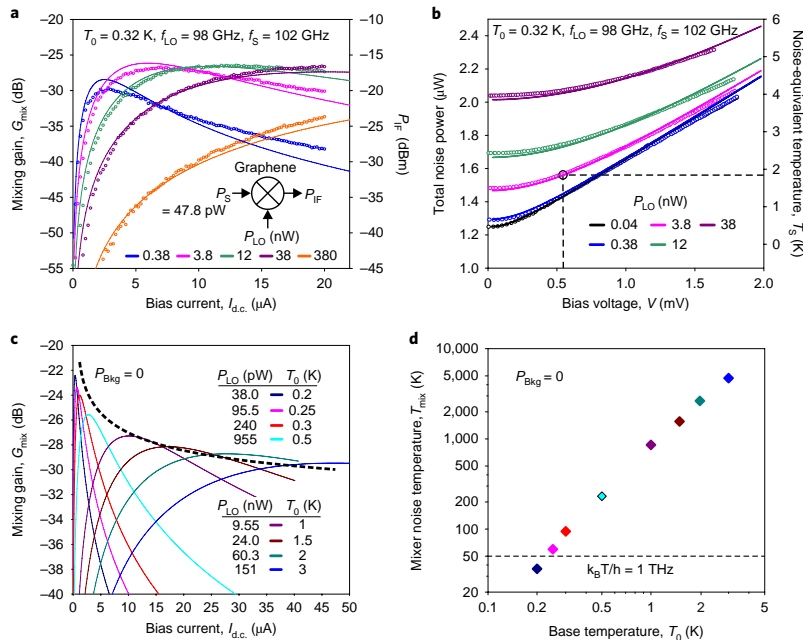


Fig. 3 | Measured and projected (for zero background radiation) THz mixing performance of our graphene bolometric mixer. **a,b,** Mixing gain ($f_{\text{IF}} = 4 \text{ GHz}$, $P_{\text{S}} = 47.8 \text{ pW}$) (**a**) and thermal noise power (**b**) measurements for different LO power levels P_{LO} ($f_{\text{IF}} = 4 \text{ GHz}$). Dots correspond to measurements. With a radiation background $P_{\text{Bkg}} = 0.5 \text{ nW}$, solid lines in **a** correspond to equation (3) and the right y axis is the measured output power at the IF. In **b**, solid lines are fits to the DCM, and the right y axis displays the graphene noise equivalent temperature T_s , calculated with the DCM. **c,** Mixing performance for different operating temperatures T_0 . For each temperature, the curve corresponding to an optimum LO power (highest possible gain) is shown. Dashed line represents an approximated expression for the mixing gain $G_{\text{mix}} \propto (G_{\text{IF}} V / I)^2$. **d,** Mixer noise temperature ($T_{\text{mix}} = T_{\text{noise}} / 2G_{\text{mix}}$) under optimal conditions as a function of the base temperature T_0 .

Table 1 | Summary of graphene bolometric mixer parameters

	$L (\mu\text{m})$	$f_0 (\text{GHz})$	$f_{\text{LO}} (\text{GHz})$	$P_{\text{LO}} (\text{nW})$	$I_{\text{d.c.}} (\mu\text{A})$	$P_{\text{Bkg}} (\text{nW})$	$T_s (\text{K})$	$G_{\text{mix}} (\text{dB})$	$T_{\text{mix}} (\text{K})$
Measured	1.5	8	98, 392, 698	3.8	5	0.28	1.9	-27	475
Projected	0.8	20	Entire THz range	0.04	1	0	0.4	-22	36 ($T_{\text{Amp}} \sim 0.3 \text{ K}$)

The observed and expected parameters under optimal conditions include: device channel length (L), gain bandwidth (f_0), local oscillator frequency (f_{LO}), local oscillator power (P_{LO}), bias current ($I_{\text{d.c.}}$), background radiation power (P_{Bkg}), effective noise-equivalent temperature (T_s), mixer gain (G_{mix}) and mixing noise temperature (T_{mix}). The measured mixer gain (G_{mix}) and mixing noise temperature (T_{mix}) are extracted from the measurements at $f_{\text{LO}} = 98 \text{ GHz}$. The validity of the bolometric model ensures that the same values hold for $f_{\text{LO}} = 392 \text{ GHz}$ and 698 GHz . The projected (calculated values) reflect the intrinsic performance of the device in an optimized setup (zero background radiation power, $P_{\text{Bkg}} = 0$). Zero background radiation would allow for operation at reduced d.c. bias, resulting in the increase of the achievable mixing gain G_{mix} by a few decibels compared with the gain that we measured in our cryostat. The projected T_{mix} is provided for an intrinsic device performance as well as for the mixer-amplifier chain using the best available commercial amplifiers ($T_{\text{Amp}} \sim 1 \text{ K}$). The operational mixing parameters P_{LO} , G_{mix} and T_{mix} refer to the intrinsic sensor performance that is referred to the THz signal power coupled into the mixer.

The performance of our THz mixer, summarized in Table 1, improves drastically at lower temperatures and thus can take full advantage of space-oriented cryocoolers providing sub-Kelvin temperatures³⁶. In our experiments, the graphene temperature at optimum operation conditions was limited by the background radiation power. However, with the present device at zero radiation background, we expect $T_s \sim 0.4 \text{ K}$; if combined with the best available commercial amplifiers ($T_{\text{Amp}} \sim 1 \text{ K}$), this translates into a mixing noise figure of 125 K for the mixer-amplifier chain. Thus, unleashing the full potential of the presented mixer requires a wideband amplifier with sub-Kelvin noise and high-performance circulators. Such devices are emerging on the wave of progress in quantum technologies⁷.

For an IF amplifier with an added noise of about 1 photon at 10 GHz , the mixer input-referred noise will be $1/G_{\text{mix}} \approx 100$ in units of 10 GHz photons, or ~ 1 in units of 1 THz photons.

Our results are based on our ability to decrease the carrier density in graphene without degrading its transport properties. In this scenario, quantum transport in graphene at the Dirac point enables highly sensitive and broadband terahertz coherent mixing. Currently demonstrating a gain bandwidth of 8 GHz for a $L = 1.5 \text{-}\mu\text{m}$ -long device, and with its operation fully described by a diffusion cooling model, we expect the bandwidth of the device to scale as $\sim L^{-2}$ (refs. ^{10–12}). Thus, for a device length of $0.8\text{--}1.0 \mu\text{m}$ (attainable with current microfabrication technologies), the bandwidth can in principle be extended

to 20 GHz, far superior to what is achievable in superconducting mixers. Our large interdigitated device geometry, chosen for our proof-of-concept experiments, can present challenges for operation at supra-THz frequencies. Future devices, optimized for operation at supra-THz frequencies, might thus require geometry different from the interdigitated device with more elaborate signal coupling schemes, for example, distributed bolometers in a coplanar waveguide^{37,38}. Combining wafer-scale epitaxial graphene on SiC and subnanowatt LO power requirements, this mixing platform is appealing for implementing large focal-plane arrays of THz mixers. Finally, the achievable mixing gain $G_{\text{mix}} \propto (G_V V/I)^2$ is set by the strength of quantum effects, which in our material are quantified as $\sigma_i \approx 0.3 e^2/h$ (Fig. 1a). Further efforts will unveil whether a different combination of polymers and molecular dopants can lead to an increased σ_i , as a result of an even more homogeneous doping closer to the Dirac point or by tuning a particular interplay of microscopic scattering mechanisms.

Methods

Sample fabrication. Monolayer SiC/G was grown on the Si face of SiC using thermal decomposition of 7 mm × 7 mm SiC substrates. The samples were grown in argon atmosphere at 800 mbar, and at a temperature of around 1,700 °C for 5 min. Optical microscopy reveals a typical surface coverage of >95% monolayer graphene. Devices were fabricated using conventional electron beam lithography, using only PMMA resist (Microlithography Chemicals) bilayer and lift-off. The electrical contacts were fabricated using physical vapour deposition of Ti/Au, 5 nm and 80 nm thick, respectively. After fabrication, samples were cleaned using isopropyl alcohol, acetone and dried using nitrogen gas. After this step, the samples were spin-coated with a 100-nm-thick PMMA layer (Microlithography Chemicals), followed by spin coating of a 170-nm-thick chemical dopant blend. The dopant blend consists of a mixture of F4TCNQ (Sigma-Aldrich) and PMMA (Microlithography Chemicals). In detail, 25 mg of dry F4TCNQ powder was mixed with 3 ml anisole solvent. Subsequently, 0.5 ml of this solution was then mixed with 1 ml PMMA A6 (6% PMMA by weight in anisole). The resulting ratio of PMMA to F4TCNQ was roughly 93:7 by weight. All polymer layers are deposited on graphene using spin coating at 6,000 r.p.m. for 1 min. A 5 min baking step on a hotplate at 160 °C followed each spin-coating step. This process consistently yielded a carrier density $|n| < 1 \times 10^{10} \text{ cm}^{-2}$ and sheet resistance of about $\rho = 50 \text{ k}\Omega \text{ sq}^{-1}$ at $T = 1 \text{ K}$. At this temperature, the mean free path (MFP) in this material is of the order of $l_{\text{MFP}} = h/(2e\rho_{xx}\sqrt{\pi n}) \approx 20 \text{ nm}$ at low temperatures, anticipating diffusive electron transport in micrometre-scale devices. To match the resistance of the graphene sample to both the THz impedance of the antenna and the impedance of the IF readout amplifier, we used interdigitated electrodes, with a graphene length of $L = 1.5 \mu\text{m}$ and a device width of $W = 345 \mu\text{m}$, resulting in nominally 230 squares of graphene in parallel. This approach allows graphene bolometer integration in a simple bow-tie antenna, suitable for experiments from the millimetre waves up to 1 THz.

Gain bandwidth measurements. Frequency mixing experiments were done with the two-wave mixing approach, where the frequency of one THz source is kept constant, while the frequency of the second source is changed. The resulting THz current through the device becomes amplitude modulated with the beating frequency $f_{\text{be}} = f_{\text{LO}} - f_{\text{IF}}$. The output signal from the device under test is amplified and its power is measured with a spectrum analyser. Measurements were conducted with THz generators in all three frequency bands (100, 400 and 700 GHz). For broadband measurements, with the beating frequency f_{be} at least up to 10 GHz, both the bias tee and the amplifiers were held at room temperature. Gain calibration for the readout chain was conducted separately. The only factors that were not included in the calibration were the effect of the mixer block and the THz standing waves in the optical path. These residuals lead to some ripples in the measured signal. The fitting curve $P(f_{\text{IF}}) = 1/[1 + (f_{\text{IF}}/f_0)^2]$ in Fig. 1c of the main text provides a roll-off frequency of $f_0 = 8 \text{ GHz}$.

Data availability

The authors declare that the main data supporting the findings of this study are available within the article and its Supplementary Information files. Additional data is available from the corresponding author upon request.

Received: 11 December 2018; Accepted: 11 June 2019;
Published online: 5 August 2019

References

- Rowan-Robinson, M. Probing the cold Universe. *Science* **325**, 546–547 (2009).
- Young, E. T. et al. Early science with SOFIA, the Stratospheric Observatory for Infrared Astronomy. *Astrophys. J. Lett.* **749**, L17 (2012).
- de Graauw, T. et al. The Herschel-Heterodyne Instrument for the Far-Infrared (HIFI). *Astron. Astrophys.* **518**, L6 (2010).
- Battersby, C. et al. The Origins Space Telescope. *Nat. Astron.* **2**, 596–599 (2018).
- Goldsmith, P. F. Sub-millimeter heterodyne focal-plane arrays for high-resolution astronomical spectroscopy. *Radio Sci. Bull.* **362**, 53–73 (2017).
- White, T. C. et al. Traveling wave parametric amplifier with Josephson junctions using minimal resonator phase matching. *Appl. Phys. Lett.* **106**, 242601 (2015).
- Ho Eom, B., Day, P. K., Leduc, H. G. & Zmuidzinas, J. A wideband, low-noise superconducting amplifier with high dynamic range. *Nat. Phys.* **8**, 623–627 (2012).
- Blain, A. W., Smail, I., Ivison, R. J., Kneib, J. P. & Frayer, D. T. Submillimeter galaxies. *Phys. Rep.* **369**, 111–176 (2002).
- Madau, P. & Dickinson, M. Cosmic star formation history. *Annu. Rev. Astron. Astrophys.* **52**, 415–486 (2014).
- Klapwijk, T. M. & Semenov, A. V. Engineering physics of superconducting hot-electron bolometer mixers. *IEEE Trans. Terahertz Sci. Technol.* **7**, 627–648 (2017).
- Prober, D. E. Superconducting terahertz mixer using a transition-edge microbolometer. *Appl. Phys. Lett.* **62**, 2119–2121 (1993).
- Gershenson, E. M. et al. Millimeter and submillimeter range mixer based on electronic heating of superconducting films in the resistive state. *Sov. Phys. Supercond.* **3**, 1582–1597 (1990).
- Krause, S. et al. Noise and IF gain bandwidth of a balanced waveguide NbN/GaN hot electron bolometer mixer operating at 1.3 THz. *IEEE Trans. Terahertz Sci. Technol.* **8**, 365–371 (2018).
- Novoselov, E. & Cherednichenko, S. Low noise terahertz MgB₃ hot-electron bolometer mixers with an 11 GHz bandwidth. *Appl. Phys. Lett.* **110**, 032601 (2017).
- El Fatimi, A. et al. Epitaxial graphene quantum dots for high-performance terahertz bolometers. *Nat. Nanotechnol.* **11**, 335–338 (2016).
- Cai, X. et al. Sensitive room-temperature terahertz detection via the photothermoelectric effect in graphene. *Nat. Nanotechnol.* **9**, 814–819 (2014).
- Mittendorff, M. et al. Ultrafast graphene-based broadband THz detector. *Appl. Phys. Lett.* **103**, 021113 (2013).
- McCann, E. et al. Weak-localization magnetoresistance and valley symmetry in graphene. *Phys. Rev. Lett.* **97**, 146805 (2006).
- Aleiner, I. L. & Efetov, K. B. Effect of disorder on transport in graphene. *Phys. Rev. Lett.* **97**, 236801 (2006).
- Lara-Avila, S. et al. Disordered Fermi liquid in epitaxial graphene from quantum transport measurements. *Phys. Rev. Lett.* **107**, 166602 (2011).
- Novoselov, K. S. et al. Electric field effect in atomically thin carbon films. *Science* **306**, 666–669 (2004).
- Novoselov, K. S. et al. Two-dimensional gas of massless Dirac fermions in graphene. *Nature* **438**, 197–200 (2005).
- Zhang, Y., Tan, Y.-W., Stormer, H. L. & Kim, P. Experimental observation of the quantum Hall effect and Berry's phase in graphene. *Nature* **438**, 201–204 (2005).
- Ponomarenko, L. A. et al. Tunable metal-insulator transition in double-layer graphene heterostructures. *Nat. Phys.* **7**, 958–961 (2011).
- Efetov, D. K. et al. Fast thermal relaxation in cavity-coupled graphene bolometers with a Johnson noise read-out. *Nat. Nanotechnol.* **13**, 797–801 (2018).
- He, H. et al. Uniform doping of graphene close to the charge neutrality point by polymer-assisted spontaneous assembly of molecular dopants. *Nat. Commun.* **9**, 3956 (2018).
- Balandin, A. A. Thermal properties of graphene and nanostructured carbon materials. *Nat. Mater.* **10**, 569–581 (2011).
- Kubakaddi, S. S. Interaction of massless Dirac electrons with acoustic phonons in graphene at low temperatures. *Phys. Rev. B* **79**, 075417 (2009).
- Baker, A. M. R. et al. Energy loss rates of hot Dirac fermions in epitaxial, exfoliated, and CVD graphene. *Phys. Rev. B* **87**, 045414 (2013).
- Nazozhny, B. N., Gornyi, I. V., Titov, M., Schütt, M. & Mirlin, A. D. Hydrodynamics in graphene: linear-response transport. *Phys. Rev. B* **91**, 035414 (2015).
- Foster, M. S. & Aleiner, I. L. Slow imbalance relaxation and thermoelectric transport in graphene. *Phys. Rev. B* **79**, 085415 (2009).
- Müller, M., Fritz, L. & Sachdev, S. Quantum-critical relativistic magnetotransport in graphene. *Phys. Rev. B* **78**, 115406 (2008).
- Crossno, J. et al. Observation of the Dirac fluid and the breakdown of the Wiedemann-Franz law in graphene. *Science* **351**, 1058–1061 (2016).
- Wang, L. et al. One-dimensional electrical contact to a two-dimensional material. *Science* **342**, 614–617 (2013).
- Ekström, H., Karasik, B. S., Kollberg, E. L. & Yngvesson, K. S. Conversion gain and noise of niobium superconducting hot-electron-mixers. *IEEE Trans. Microw. Theory Tech.* **43**, 938–947 (1995).
- Martin, F., Vermeulen, G., Camus, P. & Benoit, A. A closed cycle ³He–⁴He dilution refrigerator insensitive to gravity. *Cryogenics* **50**, 623–627 (2010).

37. Yates, S. J. C. et al. Photon noise limited radiation detection with lens-antenna coupled microwave kinetic inductance detectors. *Appl. Phys. Lett.* **99**, 073505 (2011).
38. Bichel, D. et al. 4.7-THz superconducting hot electron bolometer waveguide mixer. *IEEE Trans. Terahertz Sci. Technol.* **5**, 207–214 (2015).
39. Yager, T. et al. Express optical analysis of epitaxial graphene on SiC: impact of morphology on quantum transport. *Nano Lett.* **13**, 4217–4223 (2013).

Acknowledgements

We thank J. Conway and E. De Beck for illuminating discussions, and A. Tzalenchuk, J. F. Schneiderman and T. Claeson for critical reading of the manuscript. This work was jointly supported by the Swedish Foundation for Strategic Research (SSF) (nos. IS14-0053, GMT14-0077, RMA15-0024), Knut and Alice Wallenberg Foundation, Chalmers Area of Advance NANO, the Swedish Research Council (VR) 2015-03758 and 2016-04828, the Swedish-Korean Basic Research Cooperative Program of the NRF (no. NRF-2017R1A2A1A18070721) and the European Union's Horizon 2020 research and innovation programme (grant agreement no. 766714/HiTMe).

Author contributions

S.L.-A., H.H., K.H.K. and R.Y. contributed to sample growth and device fabrication. S.L.-A., H.H., K.H.K., F.L. and T.B. performed the d.c. characterization of the device.

D.G. developed the theoretical calculations. A.D. and S.C. characterized the sample at THz and microwave frequency ranges. D.G., S.L.-A., A.D., S.C. and S.K. contributed to the interpretation of the experiments. S.K., S.L.-A. and S.C. conceived and designed the experiment. All the authors contributed to the writing of the manuscript.

Competing interests

The authors declare no competing interests.

Additional information

Supplementary information is available for this paper at <https://doi.org/10.1038/s41550-019-0843-7>.

Reprints and permissions information is available at www.nature.com/reprints.

Correspondence and requests for materials should be addressed to S.L.

Peer review information: *Nature Astronomy* thanks Peter Roelfsema and the other, anonymous, reviewer(s) for their contribution to the peer review of this work.

Publisher's note: Springer Nature remains neutral with regard to jurisdictional claims in published maps and institutional affiliations.

© The Author(s), under exclusive licence to Springer Nature Limited 2019

